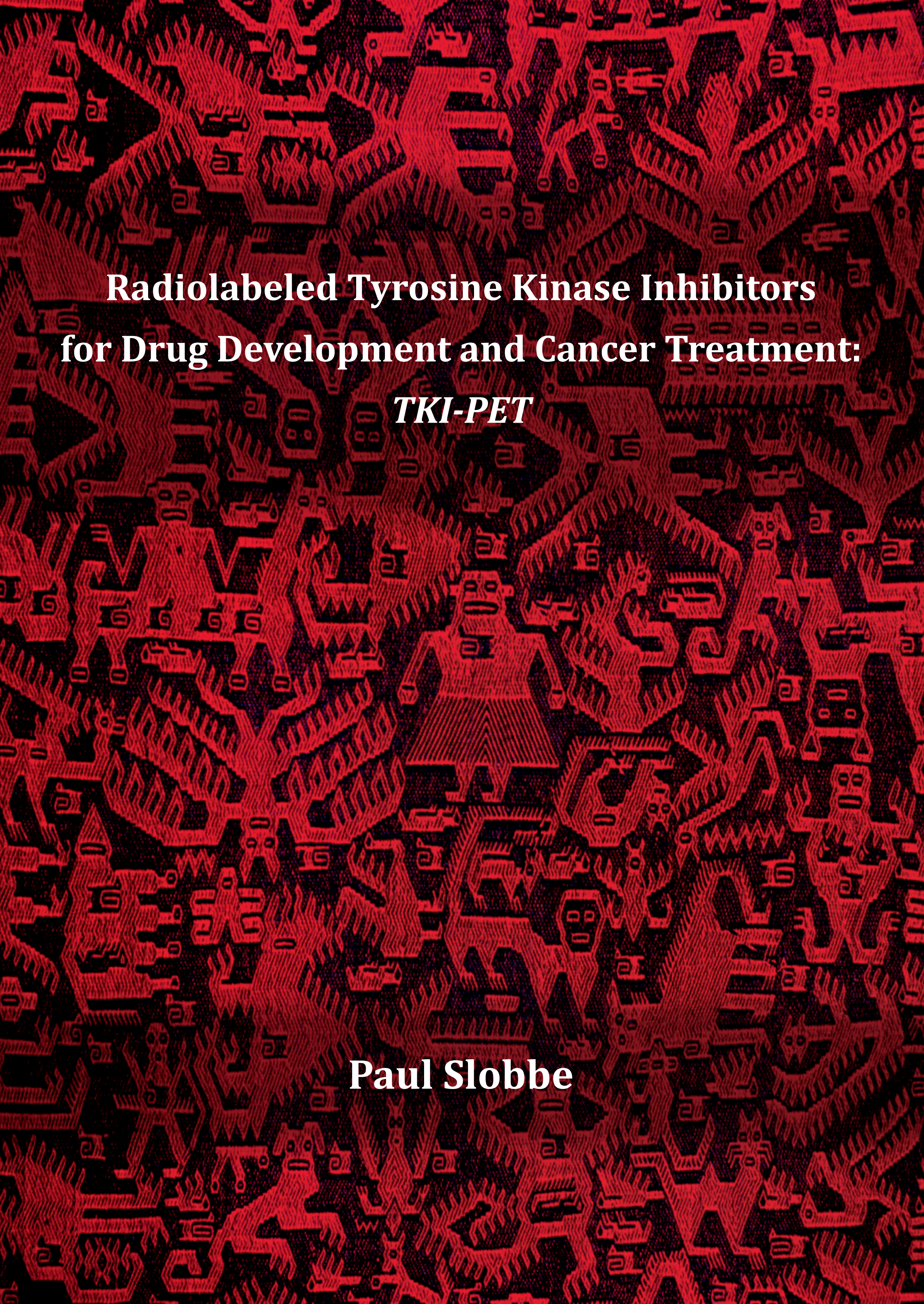

Radiolabeled Tyrosine Kinase Inhibitors for Drug Development and Cancer Treatment: *TKI-PET*

Paul Slobbe

Radiolabeled Tyrosine Kinase Inhibitors for Drug Development and Cancer treatment: *TKI-PET*

Paul Slobbe

2016

The work described in this thesis was financially supported by the VUmc Cancer Center Amsterdam (CCA) and by Boehringer Ingelheim.

ISBN: 978-94-6299-407-2

Boehringer Ingelheim, BV Cyclotron VU and Lahringen are kindly acknowledged for their financial support for the printing of this thesis.

VRIJE UNIVERSITEIT

Radiolabeled Tyrosine Kinase Inhibitors for Drug Development and Cancer treatment: *TKI-PET*

ACADEMISCH PROEFSCHRIFT

ter verkrijging van de graad Doctor aan
de Vrije Universiteit Amsterdam,
op gezag van de rector magnificus
prof.dr. V. Subramaniam,
in het openbaar te verdedigen
ten overstaan van de promotiecommissie
van de Faculteit der Geneeskunde
op donderdag 17 november 2016 om 11.45 uur
in de aula van de universiteit
De Boelelaan 1105

door

Paul Slobbe

geboren te Amstelveen

promotoren:	prof.dr. G.A.M.S. van Dongen
	prof.dr. A.D. Windhorst
copromotor:	dr. A.J. Poot

“Je kunt de moleculen niet dwingen”

Table of Contents

Chapter 1

Preface: PET-imaging as a tool in drug discovery and personalized medicine

P. Slobbe, A.J. Poot, A.D. Windhorst and G.A.M.S. van Dongen

Therapeutic advances in cancer care have revolutionized the oncological landscape, increasing the survival of cancer patients from months to years. Arguably one of the major advancement in this regard is owed to the development of targeted therapies by the pharmaceutical industry in the last 20 years. Targeted therapy has experienced a tremendous boost owing to the elucidation of the cellular biology fueling tumors. Moreover, the discovery of specific (mutated) genes driving cancer growth, the so-called oncogenes, has provided extremely selective and in some cases particularly effective pharmaceuticals.[1]

Treatment with targeted drugs is inherently different from traditional cancer treatment. These include: surgery, radiotherapy and/or (aggressive) chemotherapy. Surgery and radiotherapy, while often very effective for treatment of locoregional disease, are extremely burdensome for patients and have associated side-effects and/or complications. In the case of radiotherapy these may be relatively minor side-effects, such as fatigue or nausea but can also include late side effects as a consequence of radiation dose. Surgery is generally very effective as complete cures can be obtained but the operation can have more risk associated with it in the form of complications. Chemotherapy has found broad application in various forms of cancer and is a very effective systemic treatment strategy (e.g. in the case of metastatic disease). The major disadvantage is the fact that the cytotoxic drugs used lack selectivity for tumor cells. Chemotherapy acts on all rapidly dividing cells and is therefore very effective in many different types of cancer. However, fast dividing healthy tissue cells are targeted equally effective, leading to a plethora of side-effects. Targeted therapy, in contrast, is developed to specifically block tumor cell growth, by targeting tumor-associated or tumor specific antigens [2].

Among the most exploited tumor targets in this regard is without doubt the class of kinases. As key-players in the pathways controlling cell growth, differentiation and proliferation, aberrant signaling or mutated variants of these enzymes often lead to tumor formation. The increased structural understanding of proteins and their specific molecular interactions and expression levels, combined with high throughput screening, medicinal chemistry efforts and antibody engineering, have led to major breakthroughs in drug discovery. Together this has led to the development of tailor-made targeted pharmaceuticals as anti-cancer drugs [3].

Targeted therapy has initiated a shift in cancer treatment paradigms. Where it used to be the case that there was a single drug used for a large subset of patients with a certain type of cancer, current development is becoming more personalized. Specific genomic abnormalities are detected in a tumor and a matching targeted therapeutic is selected for this particular patient. This concept of personalized medicine is becoming increasingly important and will shape cancer care in the years to come [1].

Kinases comprise a family of proteins that play a pivotal role in the signal transduction pathways of the cell. Receptor kinases consist of an extracellular domain capable of ligand binding and an intracellular domain for downstream signaling. Prominent members of this family include the epidermal growth factor receptor (EGFR) and the vascular endothelial growth factor receptor (VEGFR). Non receptor kinases (or cytosolic kinases) have a comparable function, but are expressed in the cytosol and therefore have no membrane spanning domain and are usually activated by phosphorylation of an upstream (receptor) kinase. Examples of cystolic kinases include: RAF kinase (rapidly accelerated fibrosarcoma) or JAK (janus kinase).

Two main categories of kinase targeting drugs are currently on the market; the first are monoclonal antibody (mAb) based drugs that bind to the extracellular domain of the kinase and thereby compete with the endogenous ligand for receptor activation. These antibodies can be modified with various payloads such as radioactive isotopes or toxic drugs to increase their efficacy. The second type of drugs consists of small molecule inhibitors that act intracellularly by competition with ATP (adenosine triphosphate) for binding at the catalytic kinase domain, thereby disrupting downstream signaling.

Currently 19 naked mAbs have been approved by the FDA for the treatment of various oncological indications (end of 2015, Table 1). Although characterized by very high target affinity (usually in the subnanomolar range), antibodies, in some cases lack potency in cell killing [4]. Good clinical benefit is achieved, however, with for example rituximab in non-Hodgkin lymphoma and with bevacizumab in a variety of solid malignancies [5]. An iconic example of personalized medicine is the application of trastuzumab in HER2-positive breast cancer patients. HER2 regulates cell proliferation and is overexpressed in 20-25% of breast cancer patients. HER2-positive status confers a poor prognosis but is also a good biomarker for prediction of response to trastuzumab [6, 7].

Despite the clinical successes with mAbs the need for tumor cell toxicity is becoming more apparent. While antibodies enjoy excellent selectivity for tumor unique antigens, they often suffer from a lack of cell-killing capacity. This is driving the need for innovative combination therapies or introduction of a toxic payload such as a radionuclide (e.g. ^{90}Y) as used in Ibritumomab (Zevalin ®) in Non-Hodgkin's lymphoma or a highly potent small molecules attached to the antibody, like in the antibody-drug-conjugate (ADC) approach, to achieve efficient tumor killing. After internalization of the ADC the toxic small molecule is released, leading to selective tumor killing. Thereby avoiding the toxicity associated with such small molecules as a consequence of their lack of selectivity when administered systemically. Currently two ADCs have been approved by the FDA, being ado-trastuzumab emtansine (TDM-1, Kadcyla ®), which consists of trastuzumab conjugated to cytotoxic emtansine (DM1) for the treatment of HER2-positive breast cancer and brentuximab vedotin (Adcetris ®), which consists of brentuximab conjugated to the antimitotic agent monomethyl auristatin E, targeting CD30, for the treatment of Hodgkin’s lymphoma and anaplastic large cell lymphoma.

Table 1: FDA approved mAbs, radioimmunoconjugates and ADCs, used for cancer treatment

Generic Name (approval)	**Trade Name**	**Target**	**Cancer Indication**
Alemtuzumab (2001)	Campath	CD52	B-cell chronic lymphocytic leukemia
Bevacizumab (2004)	Avastin	VEGF	Cervical cancer Colorectal cancer Fallopian tube cancer Glioblastoma Non-small cell lung cancer Ovarian cancer Peritoneal cancer Renal cell carcinoma
Cetuximab (2004)	Erbitux	EGFR	Colorectal cancer (KRAS wild type) Squamous cell cancer of the head and neck
Daratumumab (2015)	Darzalex	CD38	Multiple myeloma
Denosumab (2009)	Xgeva	RANKL	Giant cell tumor of the bone
Dinutuximab (2015)	Unituxin	GD2	Pediatric neuroblastoma
Elotuzumab (2015)	Empliciti	CD319	Multiple myeloma
Ipilimumab (2011)	Yervoy	CTLA-4	Melanoma

Necitumumab (2015)	Portrazza	EGFR	Squamous non-small cell lung cancer
Nivolumab (2014)	Opdivo	PD-1	Melanoma Non-small cell lung cancer
Obinutuzumab (2013)	Gazyva	CD20	Chronic lymphocytic leukemia
Ofatumumab (2009)	Azerra	CD20	Chronic lymphocytic leukemia
Panitumumab (2006)	Vectibix	EGFR	Colorectal cancer (KRAS wild type)
Pembrolizumab (2014)	Keytruda	PD-1	Melanoma
Pertuzumab (2012)	Perjeta	HER2	Breast cancer (HER2+)
Ramucirumab (2014)	Cyramza	VEGFR2	Gastric cancer or Gastroesophageal junction (GEJ) adenocarcinoma Non-small cell lung cancer
Rituximab (1997)	Rituxan	CD20	Non-Hodgkin’s lymphoma Chronic lymphocytic leukemia Rheumatoid arthritis Granulomatosis with polyangiitis
Siltuximab (2014)	Sylvant	IL-6	Multicentric Castleman's disease
Trastuzumab (1998)	Herceptin	HER2	Breast cancer (HER2+)

			Gastric cancer (HER2+)
Radioimmunoconjugates			
Ibritumomab-^{90}Y (2002)	Zevalin	CD20	Non-Hodgkin's lymphoma
Tositumomab-^{131}I (2003)	Bexxar	CD20	Non-Hodgkin's lymphoma
Antibody Drug Conjugates			
Ado-trastuzumab emtansine (2013)	Kadcyla (TDM-1)	HER2	Breast cancer (HER2+)
Brentuximab vedotin (2011)	Adcetris	CD30	Hodgkin lymphoma Anaplastic large cell lymphoma

EGFR: epidermal growth factor receptor, VEGF: Vascular endothelial growth factor, RANKL: Tumor necrosis factor (ligand) superfamily member 11, CD20: B-lymphocyte antigen CD20, CTLA-4: cytotoxic T-lymphocyte-associated protein 4, PD-1: programmed cell death 1, HER2: human epidermal growth factor receptor 2, VEGFR: vascular endothelial growth factor receptor, IL-6 interleukin-6, MEK: MAP kinase kinase.

The second class of targeted therapies consists of the small molecule inhibitors, which is the biggest group of FDA approved targeted therapeutics. Predominantly protein kinase inhibitors have been developed (summarized in Table 2), although also histone deacetylase inhibitors, proteasome inhibitors and PARP inhibitors are classed as targeted anti-cancer therapy. Due to the key role fulfilled by kinases in various growth related processes of cancer cells, they are very attractive as drug targets. The pharmaceutical industry has spent the last few decades developing small molecules to target various kinases. Especially tyrosine kinases have found great interest and many compounds have been approved for this type of kinase. Regardless still circa 70% of the kinome remains “undrugged” [8].

Especially mutated kinases can be effectively treated with small molecule kinase inhibitors. For example imatinib for the treatment of multiple hematologic malignancies, which are positive for the so called Philadelphia chromosome. This is a result of a reciprocal translation between chromosomes 9 and 22 leading to expression of an oncogenic fusion protein BCR-ABL. This can be effectively targeted by imatinib and related kinase inhibitors [9]. Another example is found in the EGFR inhibitors (gefinib, erlotinib and afatinib) for non-small cell lung cancer harboring oncogenic mutations in the ATP binding site of the EGF receptor [10] or vemurafenib for V600E mutated BRAF in melanomas [11]. This demonstrates that kinase inhibitors are excellent tools for personalized cancer treatment.

Table 2: FDA approved small molecule kinase inhibitors used for cancer treatment

Generic Name (approval)	**Trade Name**	**Target**	**Cancer Indication**
		Receptor tyrosine kinase inhibitors	
Afatinib (2013)	Gilotrif	EGFR, HER2	Non-small cell lung cancer (with EGFR exon 19 deletions or exon 21 substitution (L858R) mutations)
Axitinib (2012)	Inlyta	KIT, PDGFRβ, VEGFR1/2/3	Renal cell carcinoma
Cabozantinib (2012)	Cometriq	FLT3, KIT, MET, RET, VEGFR2	Medullary thyroid cancer
Erlotinib (2005)	Tarceva	EGFR	Non-small cell lung cancer Pancreatic cancer
Gefitinib (2003)	Iressa	EGFR	Non-small cell lung cancer (with EGFR exon 19 deletions or exon 21 substitution (L858R) mutations)
Lapatinib (2007)	Tykerb	EGFR, HER2	Breast cancer (HER2+)

Lenvatinib (2012)	Lenvima	VEGFR2	Thyroid cancer
Nintedanib (2014)	Vargatef	VEGFR1/2/3, FGFR, PDGFR	Non-small cell lung cancer Iodopathic pulmonary fibrosis
Osimeritinib (2015)	Targrisso	EGFR	Non-small cell lung cancer (with EGFR exon 20 T790M mutation)
Pazopanib (2009)	Votrient	VEGFR, PDGFR, KIT	Renal cell carcinoma Soft tissue carcinoma
Regorafenib (2012)	Stivarga	KIT, PDGFRβ, RAF RET, VEGFR1,2,3	Colorectal cancer Gastrointestinal stromal tumors
Sorafenib (2005)	Nexavar	VEGFR, PDGFR, KIT, RAF	Hepatocellular carcinoma Renal cell carcinoma Thyroid carcinoma
Sunitinib (2006)	Sutent	VEGFR, KIT, PDGFR, RET, CSF1R, FLT3	Renal cell carcinoma GI stromal tumor
Vandetanib (2011)	Caprelsa	EGFR, RET, VEGFR2	Medullary thyroid cancer
Non receptor tyrosine kinase inhibitors			
Alectinib (2011)	Alecensa	ALK	Non-small cell lung cancer (with ALK fusion)
Bosutinib (2012)	Bosulif	ABL	Chronic myelogenous leukemia (Philadelphia

			chromosome positive)
Ceritinib (2014)	Zykadia	ALK	Non-small cell lung cancer (with ALK fusion)
Cobimetinib (2015)	Cotellic	MEK	Melanoma (with BRAF V600 mutation)
Crizotinib (2011)	Xalkori	ALK, MET	Non-small cell lung cancer (with ALK fusion)
Dabrafenib (2013)	Tafinlar	BRAF	Melanoma (with BRAF V600 mutation)
Dasatinib (2010)	Sprycel	ABL, Src	Chronic myelogenous leukemia (Philadelphia chromosome positive) Acute lymphoblastic leukemia (Philadelphia chromosome positive)
Ibrutinib (2013)	Imbruvica	BTK	Mantle cell lymphoma Chronic lymphocytic leukemia Waldenstrom's macroglobulinemia
Idelalisib (2014)	Zydelig	PI3Kδ	Chronic lymphocytic leukemia Follicular B-cell non-Hodgkin lymphoma Small lymphocytic lymphoma
Imatinib (2002)	Glivec	ABL, KIT, PDGFR,	GI stromal tumor (KIT+) Dermatofibrosarcoma

			protuberans Multiple hematologic malignancies including Philadelphia chromosome-positive ALL and CML
Nilotinib (2007)	Tasigna	ABL	Chronic myelogenous leukemia (Philadelphia chromosome positive)
Palbociclib (2015)	Ibrance	CDK4, CDK6	Breast cancer (ER+, HER2-)
Ponatinib (2012)	Iclusig	ABL, FGFR1/2/3, FLT3, VEGFR2	Chronic myelogenous leukemia Acute lymphoblastic leukemia (Philadelphia chromosome positive)
Ruxolitinib (2011)	Jakafi	JAK1,2	Myelofibrosis
Trametinib (2013)	Mekinist	MEK	Melanoma (with BRAF V600 mutation)
Vermurafenib (2011)	Zelboraf	BRAF	Melanoma (with BRAF V600 mutation)

ABL: v-abl Abelson murine leukemia viral oncogenes homolog, ALK: anaplastic lymphoma kinase, BCR: breakpoint cluster region gene, BRAF: serine/threonine-protein kinase B-Raf, BTK: Burton's tyrosine kinase, CD: cluster of differentiation, CDK4: Cyclin-dependent kinase 4, CDK6: Cyclin-dependent kinase 6, CSF1R: colony stimulating factor 1 receptor, EGFR: epidermal growth factor receptor, Erk: extracellular regulated kinase, FGFR: Fibroblast growth factor receptor, FLT3: Fms-like tyrosine kinase-3, HER2: human epidermal growth factor receptor 2, JAK: Janus Kinase, KIT: Mast/stem cell growth factor receptor, MEK: MAP kinase kinase, MET: MNNG HOS transforming gene, PDGFR: platelet derived growth factor receptor, PhC: Philadelphia chromosome, PI3Kδ: Phosphoinositide 3-kinase, RAF: Rapidly Accelerated Fibrosarcoma, RET, rearranged during transfection proto-oncogene, Src: Proto-oncogene tyrosine-protein kinase, VEGFR: vascular endothelial growth factor receptor.

Generally kinase inhibitors function as ATP mimetics and occupy the ATP binding site at the intracellular kinase domain, therefore they first have to pass the cell membrane, as opposed to the mAbs which generally bind extracellularly.

Furthermore, high affinity and long lasting binding to the target is required to effectively compete with the high intracellular ATP concentration [12]. Although the approval rate of small molecule kinase inhibitors is high and substantial patient benefit is achieved, there is a lack of efficacy in certain patient populations. Moreover, patients responding to treatment often develop resistance to a certain kinase inhibitor, mainly by mutation of the target or by activation of escape signaling pathways that are not dependent on the targeted kinase for proliferation.

One of the major caveats of targeted therapy is its associated economic burden. The cost of cancer care in the United States alone is projected to reach $173 billion dollars in 2020 up from $125 billion in 2010. Targeted therapies currently dominate the anti-cancer spending, indicating the keen interest in this field. This observation, however, is offset by the increasing costs of delivering targeted therapies to the market and the ensuing high price of these drugs [13].

Combining all these factors with the lack of clinical efficacy, the need for effective patient selection and therapy monitoring becomes increasingly important in an era of precision medicine. The increased development of these targeted drugs raises the question how to test all these new pharmaceuticals in an efficient way, as it would require many clinical trials and thereby a substantial investment and patient burden. Furthermore, approximately 90% of these drugs are likely to fail in clinical trials and do not reach the market, eventually escalating the costs of drugs that do reach the market [14].

To address these issues, molecular imaging and especially Positron Emission Tomography (PET), is ideally suited. PET is a non-invasive *in vivo* imaging technique that allows the visualization and quantification of the distribution of molecules labeled with positron-emitting isotopes at a picomolar level. This method allows for the evaluation of biochemical and physiological processes by monitoring the distribution and kinetics of the labeled molecule *in vivo*. Often combined with an anatomical imaging modality such as computed tomography or magnetic resonance imaging, PET-CT and PET-MRI, for simultaneous monitoring of anatomical (CT/MRI) and biological (PET) effects, providing an extremely valuable diagnostic tool for drug developers and clinicians.

PET with radiolabeled drugs can be of great value to determine pharmacokinetic parameters of drugs or drug candidates, as well as interpatient variability. Basic questions such as biodistribution of a therapeutic can be determined (at tracer level) quantitatively and over time. Target engagement can be assessed by PET, thereby indicating if the desired therapeutic target is expressed and whether or not the drug reaches the target site or binds an off-target position, which might be predictive for toxicity. Furthermore binding kinetics can be determined, possibly providing valuable information with regard to dosing and therapy scheduling. Early drug leads can be radiolabeled and directly applied in phase-0 clinical studies, rapidly providing vital information about tumor-targeting, pharmacokinetic and –dynamics. This can possibly facilitate go/no-go decisions in drug development early on, thereby avoiding large clinical trials and the associated costs and patient burden and streamlining the drug development process.

One particular category of anti-cancer drugs where imaging has demonstrated its value is antibody imaging. Immuno-PET, or PET imaging of radiolabeled antibodies, has become increasingly popular over the last years. Labeling of an antibody with a positron emitting isotope in an inert way is essential for this purpose. The standard short lived PET-isotopes such as carbon-11 or fluorine-18 (half–life 20 and 109 minutes respectively) are unsuitable for radiolabeling of a mAb due to its long circulation time. There are a number of positron emitting radionuclides that have a matching half-life when compared to the biological half-life of a mAb [15]. The most popular radionuclides for this purpose currently include copper-64, iodine-124 and zirconium-89. Copper-64 (half-life: 12.7 h) is employed for imaging of intact antibodies but has a few drawbacks such as high liver uptake, that might be associated with hepatobiliary excretion of copper. Furthermore copper binding proteins found in the liver and the blood pool negatively influence the signal-to-noise ratio. Additionally it has a β^- emission of (E_{max}: 573 KeV) leading to a higher radiation burden for the patient, finally the half-life is not matched to the biological half-life of an antibody. Iodine-124 (half-life: 100.2 h) has also been employed in several immuno-PET studies, however, the positron decay of this isotope is characterized by high energy (E_{max}: 2.14 MeV) which leads to a lower spatial resolution. In addition iodine-124 also emits a γ of 603 KeV, which coincides with the annihilation photon detection window, hampering proper detection of positron decay and thereby reducing image quality. Zirconium-89 (half-life: 78.4 h) has risen to the forefront as radionuclide of choice for immuno-PET. It has a relatively low energy positron (E_{max}: 897 KeV) and an additional γ (E= 909 KeV) with high energy that does not interfere with positron annihilation photon detection, making it an ideal isotope for conjugation to an antibody. With the advent of facile labeling techniques and increased commercial availability of clinical grade zirconium-89 its use has become increasingly widespread in both preclinical and clinical studies [16].

Many excellent preclinical and clinical studies have been reported and reviews have appeared summarizing the field of zirconium-89 immuno-PET [16-19]. Selected examples of the successes achieved with clinically approved mAbs will be discussed below to demonstrate the value of immuno-PET.

Two examples of EGFR targeting mAbs are cetuximab and panitumumab and both have been employed as immuno-PET tracer in a preclinical setting. ^{89}Zr-cetuximab was evaluated for scouting the biodistribution of ^{90}Y- and ^{177}Lu-cetuximab biodistribution, allowing the estimation of radiation dose to tumors and normal organs. This study demonstrated that this was indeed feasible with the caveat that a higher bone-uptake was observed for ^{89}Zr-cetuximab [20]. An interesting disparity was observed between EGFR expression levels and tumor uptake of this ^{89}Zr-cetuximab, indicating that in additional to target expression and pharmacokinetics also other factors are affecting tumor delivery of cetuximab [21].

Trastuzumab targets the HER2 receptor, which is closely related to the EGF receptor (HER1) and involved in proliferation, differentiation and metastasis. ^{89}Zr-trastuzumab was employed for the selective detection of HER2-positive xenograft in nude mice. In Figure 1 representative PET-scans are depicted of a mouse bearing a HER2-postive tumor (left flank) and a HER2-negative xenograft (right flank). Both [^{18}F]FDG (metabolic marker) and [^{18}F]FLT (proliferation marker) are able to clearly delineate the tumors but neither is able to detect HER2-status. However, ^{89}Zr-trastuzumab very clearly detects the HER2-positive tumor and shows no accumulation in the HER2-negative xenograft. Furthermore as evidenced by the PET-image, excellent signal-to-noise ratios are achieved. Finally ^{89}Zr-trastuzumab was able to monitor HER2 expression and monitor afatinib treatment as uptake was of ^{89}Zr-trastuzumab decreased as HER2 downregulation was observed in tumor bearing mice [22].

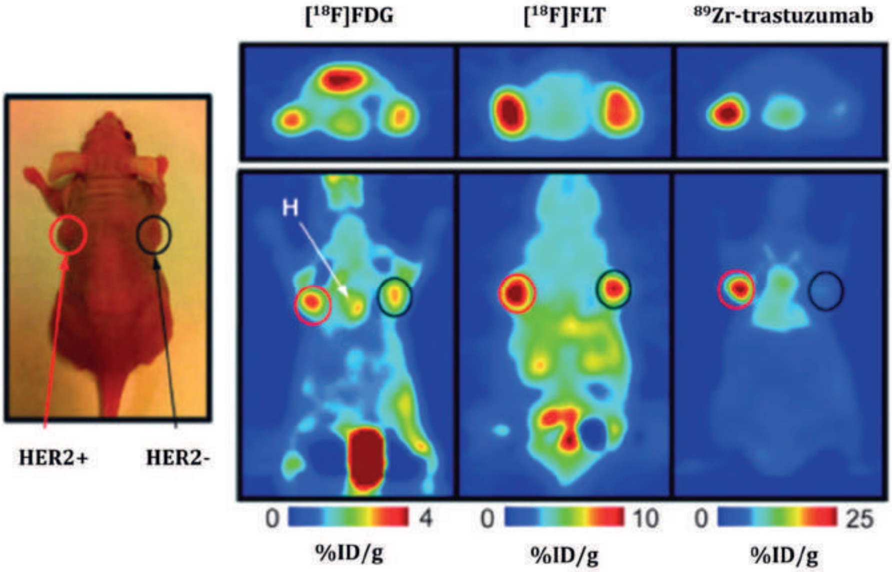

Figure 1: [^{18}F]FDG, [^{18}F]FLT and ^{89}Zr-trastuzumab PET images of a nude mouse bearing a HER2-postive (left, NCI-87) and a HER2-negative (right, MKN-47) xenograft.

Bevacizumab, in contrast to the previously discussed antibodies, does not target a kinase receptor, but a growth factor, in this case the Vascular Endothelial Growth Factor (VEGF). This endogenous ligand of the VEGF receptor family, is heavily involved in angiogenesis. Due to the fact that this is a circulating growth factor, imaging of VEGF specifically in tumor tissue might be challenging. The tumor micro-environment, however, will have high levels of VEGF due to the active angiogenesis process and the association of VEGF with the extracellular matrix, providing a potential imaging target. ^{89}Zr-bevacizumab uptake was demonstrated in mice bearing SKOV-3 xenografts (ovarian carcinoma, Figure 2) and accumulation was significantly higher when compared to ^{89}Zr-IgG (non-specific antibody) uptake. Indicating that imaging of VEGF-levels in the tumor micro-environment is feasible [23].

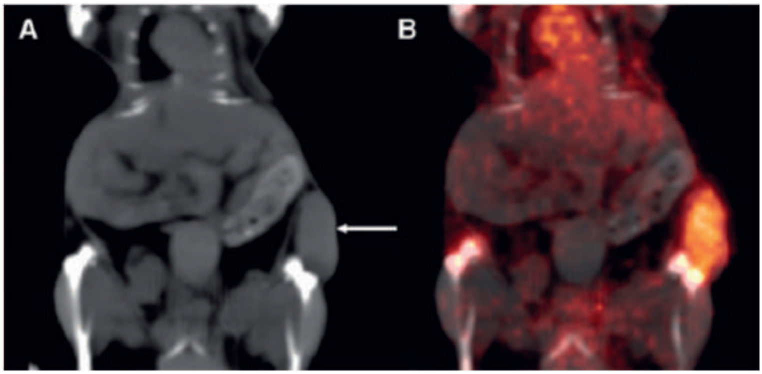

Figure 2: CT-image (A) and ^{89}Zr-bevacizumab PET-CT image (B) of a mouse bearing a SKOV-3 xenograft. Image adapted from [23].

Clinically immuno-PET has also demonstrated success in several types of cancer. ^{89}Zr-trastuzumab has been applied in breast cancer patients. In this study three groups of patients were imaged with ^{89}Zr-trastuzumab. The first two groups consisted of trastuzumab naïve patients receiving a dose of 10 or 50 mg cold trastuzumab co-injected with tracer and the third group consisted of patients already on trastuzumab therapy, receiving 10 mg cold trastuzumab with ^{89}Zr-trastuzumab administration. The 10 mg, trastuzumab-naïve patients, showed rapid clearance of ^{89}Zr-trastuzumab when compared to the 50 mg cohort. This demonstrated that pre-dosing was required to avoid rapid clearance of the tracer and obtain high quality images. The HER2-positive lesions were identified using immuno-PET with ^{89}Zr-trastuzumab and imaging results were in good agreement with other imaging modalities. Finally metastatic lesions of the liver, lung, bone and even brain were observed (Figure 3) [24].

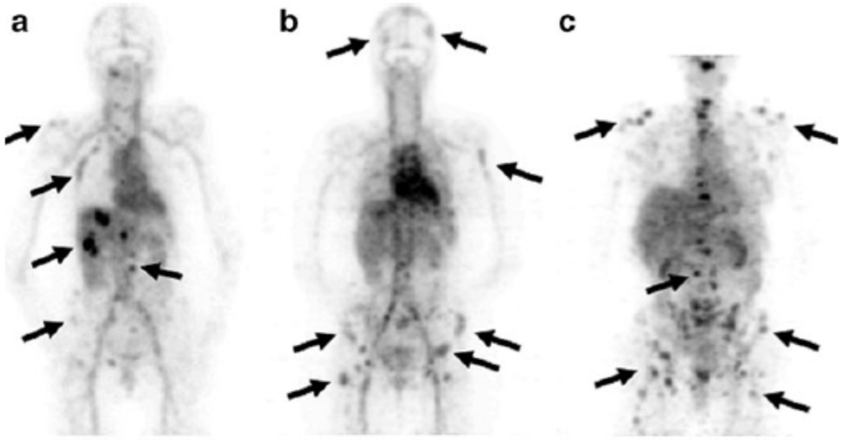

Figure 3: Examples of ^{89}Zr-trastuzumab uptake (5 days p.i.) in a patient with liver and bone metastases (a), and two patients with bone metastases (b and C). Arrows indicate selected tumor lesions. Figure adapted from [24].

Gaykema *et al.* applied ^{89}Zr-bevacizumab immuno-PET in a cohort of 23 breast cancer patients for imaging of VEGF-A levels. This study included a total of 26 tumors, of which 25 showed good uptake for ^{89}Zr-bevacizumab (Figure 4 a). VEGF-A levels were determined in 17 available biopsy samples and this correlated to the uptake of ^{89}Zr-bevacizumab (Pearson $r = 0.49$, $P = 0.04$). This report provides evidence that it is possible to monitor VEGF-A levels *in vivo* using ^{89}Zr-bevacizumab immuno-PET, which could be a valuable tool to predict and monitor VEGF targeting therapies [25].

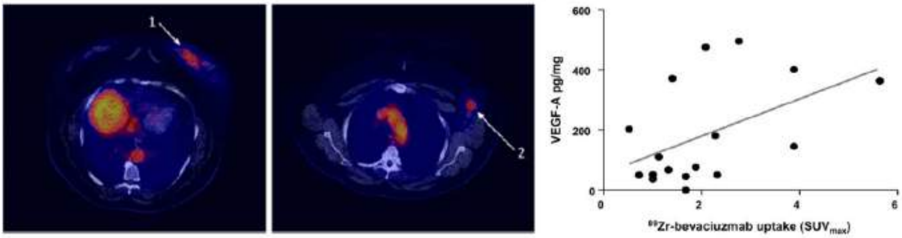

Figure 4: left: axial slices of a ^{89}Zr-bevacizumab PET-CT scan of patients with primary breast tumor (1) and lymph node metastasis (2). Right: Correlation between ^{89}Zr-bevacizumab uptake (SUV$_{max}$) with VEGF-A levels as determined by ELISA. Figure adapted from [25].

^{89}Zr-cetuximab was recently evaluated in a small patient cohort of advanced colorectal cancer (mCRC), in which approximately 50% of the patients respond to EGFR targeted mAb therapy, despite selection for RAS wild type. Patients harboring mutated K-RAS or N-RAS are unresponsive to EGFR targeted treatment, because these mutations occur downstream of the kinase receptor. Further selection of responsive patients, apart from RAS mutational status, is ongoing. In this setting ^{89}Zr-cetuximab was administered to 10 cetuximab eligible patients (mCRC with wt Ras) and PET scans were acquired over time (1 to 10 days post injection) after start of therapy (patients received a dose of cetuximab less than 2h before ^{89}Zr-cetuximab injection). 6 out of 10 patients showed uptake was detected in tumor lesions and from these six patients, four demonstrated clinical benefit from cetuximab treatment. In the three out of four patients without ^{89}Zr-cetuximab uptake, progressive disease was observed. These results, demonstrate a good relation between tracer uptake and response to treatment and therefore ^{89}Zr-cetuximab warrants evaluation in larger clinical trials in patients with mCRC which is wild type for RAS [26].

From the above presented examples it is clear that imaging with ^{89}Zr-labeled antibodies provides a unique tool to assess antibody biodistribution and tumor targeting by means of PET. High resolution images with excellent tumor-to-background ratios can be obtained and antigen expression can be characterized *in vivo* in a non-invasive manner. Together this provides a tool to aid in prediction and monitoring of treatment, moreover immuno-PET has the potential to aid in the drug discovery process by early identification of clinical leads. Complex constructs (such as ADCs or mAbs modified with an optical dye) can also be tracked *in vivo* in this manner, confirming that antibody modifications are well tolerated and tumor targeting remains optimal.

The aim of this thesis is to extend the concept of immuno-PET to the small molecule kinase inhibitors, particularly the tyrosine kinase inhibitors. As evidenced by Table 2 a keen interest is present in this field and we aim to develop (T)KI-PET as a tool for response prediction, therapy monitoring and drug discovery. **Chapter 2** describes the status of the TKI-PET field at the start of the research described in this thesis. This chapter summarizes radiochemical development of TKI-PET tracers known in literature. Evaluation in both preclinical and in some cases clinical studies is described and a summary is provided of important aspects with regard to TKI-PET tracer development. **Chapter 3** describes the radiosynthesis, metabolic stability and biodistribution in tumor bearing mice of fluorine-18 labeled afatinib, a second generation, irreversible EGFR inhibitor approved for the treatment of non-small cell lung cancer with activating mutations of EGFR. **Chapter 4** describes a comparative pre-clinical imaging study, where [^{11}C]erlotinib and [^{18}F]afatinib are compared in a panel of non-small cell lung cancer bearing mice, expressing a clinically relevant set of mutations of the EGF receptor. Furthermore, the effect of blocking the efflux transporters (P-gp and BCRP) on the biodistribution of both tracers are explored. **Chapter 5** covers the synthesis of [^{11}C]vemurafenib a mutant selective Sr/Thr-kinase inhibitor approved for the treatment of melanoma, in which the tumor expresses V600E mutated BRAF. [^{11}C]vemurafenib is prepared by a carbonylative Stille coupling using [^{11}C]carbonmonoxide and evaluated in a panel of melanoma xenografts. The aim of this chapter was partly to extend the concept of TKI-PET to non-tyrosine kinases. **Chapter 6** deals with the development of two carbon-11 labeled antiangiogenic kinases, namely [^{11}C]axitinib and [^{11}C]nintedanib, where the first is a selective inhibitor and the second a triple kinase inhibitor. A thorough metabolite analysis is performed and the major metabolites are identified using LC-MS/MS techniques at tracer level.

References

[1] Jackson SE and Chester JD. Personalised cancer medicine *Int. J. Cancer* **2015**, *137*, 262-266.

[2] Sledge GW. What is targeted therapy? *J. Clin. Oncol.* **2005**, *23*, 1614-1615.

[3] Zhang J, Yang PL, and Gray NS. Targeting cancer with small molecule kinase inhibitors *Nat. Rev. Cancer.* **2009**, *9*, 28-39.

[4] Scott AM, Wolchok JD, and Old LJ. Antibody therapy of cancer *Nat. Rev. Cancer* **2012**, *12*, 278-287.

[5] Oldham RK and Dillman RO. Monoclonal antibodies in cancer therapy: 25 years of progress *J. Clin. Oncol.* **2008**, *26*, 1774-1777.

[6] Goldenberg MM. Trastuzumab, a recombinant DNA-derived humanized monoclonal antibody, a novel agent for the treatment of metastatic breast cancer *Clin. Ther.* **1999**, *21*, 309-318.

[7] Balduzzi S, Mantarro S, Guarneri V, Tagliabue L, Pistotti V, Moja L, et al. Trastuzumab-containing regimens for metastatic breast cancer *Cochrane Database of Systematic Reviews* **2014**.

[8] Fabbro D. 25 years of small molecular weight kinase inhibitors: potentials and limitations *Mol. Pharmacol.* **2015**, *87*, 766-775.

[9] Capdeville R, Buchdunger E, Zimmermann J, and Matter A. Glivec (STI571, imatinib), a rationally developed, targeted anticancer drug *Nat. Rev. Drug Discovery* **2002**, *1*, 493-502.

[10] Kobayashi K and Hagiwara K. Epidermal growth factor receptor (EGFR) mutation and personalized therapy in advanced nonsmall cell lung cancer (NSCLC) *Target. Oncol.* **2013**, *8*, 27-33.

[11] Bollag G, Tsai J, Zhang J, Zhang C, Ibrahim P, Nolop K, et al. Vemurafenib: the first drug approved for BRAF-mutant cancer *Nat. Rev. Drug Discov.* **2012**, *11*, 873-886.

[12] Garuti L, Roberti M, and Bottegoni G. Non-ATP competitive protein kinase inhibitors *Curr. Med. Chem.* **2010**, *17*, 2804-2821.

[13] Shih Y-CT, Smieliauskas F, Geynisman DM, Kelly RJ, and Smith TJ. Trends in the cost and use of targeted cancer therapies for the privately insured nonelderly: 2001 to 2011 *J. Clin. Oncol.* **2015**.

[14] Mano M. The burden of scientific progress: growing inequalities in the delivery of cancer care *Acta Oncol.* **2006**, *45*, 84-86.

[15] Zhou Y, Baidoo KE, and Brechbiel MW. Mapping biological behaviors by application of longer-lived positron emitting radionuclides *Adv. Drug Delivery Rev.* **2013**, *65*, 1098-1111.

[16] van de Watering FCJ, Rijpkema M, Perk L, Brinkmann U, Oyen WJG, and Boerman OC. Zirconium-89 labeled antibodies: a new tool for molecular imaging in cancer patients *BioMed Res. Int.* **2014**, *2014*, 13.

[17] Vugts DJ, Visser GWM, and van Dongen GAMS. Zr-89-PET radiochemistry in the development and application of therapeutic monoclonal antibodies and other biologicals *Curr. Top. Med. Chem.* **2013**, *13*, 446-457.

[18] van Dongen GAMS, Poot AJ, and Vugts DJ. PET imaging with radiolabeled antibodies and tyrosine kinase inhibitors: immuno-PET and TKI-PET *Tumor Biol.* **2012**, *33*, 607-615.

[19] Van Dongen GAMS, Huisman MC, Boellaard R, Hendrikse NH, Windhorst AD, Visser GWM, et al. Zr-89-immuno-PET for imaging of long circulating drugs and disease targets: why, how and when to be applied? *Q. J. Nucl. Med. Mol. Im.* **2015**, *59*, 18-38.

[20] Perk LR, Visser GWM, Vosjan MJWD, Stigter-van Walsum M, Tijink BM, Leemans CR, et al. ^{89}Zr as a PET surrogate radioisotope for scouting biodistribution of the therapeutic radiometals ^{90}Y and ^{177}Lu in tumor-bearing nude mice after coupling to the internalizing antibody cetuximab *J. Nucl. Med.* **2005**, *46*, 1898-1906.

[21] Aerts H, Dubois L, Perk L, Vermaelen P, van Dongen G, Wouters BG, et al. Disparity between *in vivo* EGFR expression and ^{89}Zr-Labeled cetuximab uptake assessed with PET *J. Nucl. Med.* **2009**, *50*, 123-131.

[22] Janjigian YY, Viola-Villegas N, Holland JP, Divilov V, Carlin SD, Gomes-DaGama EM, et al. Monitoring afatinib treatment in HER2-positive gastric cancer with ^{18}F-FDG and ^{89}Zr-trastuzumab PET *J. Nucl. Med.* **2013**, *54*, 936-943.

[23] Nagengast WB, de Vries EG, Hospers GA, Mulder NH, de Jong JR, Hollema H, et al. *In vivo* VEGF imaging with radiolabeled bevacizumab in a human ovarian tumor xenograft *J. Nucl. Med.* **2007**, *48*, 1313-1319.

[24] Dijkers EC, Oude Munnink TH, Kosterink JG, Brouwers AH, Jager PL, de Jong JR, et al. Biodistribution of ^{89}Zr-trastuzumab and PET imaging of HER2-positive lesions in patients with metastatic breast cancer *Clin. Pharmacol. Ther.* **2010**, *87*, 586-592.

[25] Gaykema SBM, Brouwers AH, Lub-de Hooge MN, Pleijhuis RG, Timmer-Bosscha H, Pot L, et al. ^{89}Zr-Bevacizumab PET imaging in primary breast cancer *J. Nucl. Med.* **2013**, *54*, 1014-1018.

[26] der Houven CWM-v, Gootjes EC, Huisman MC, Vugts DJ, Roth C, Luik AM, et al. ^{89}Zr-cetuximab PET imaging in patients with advanced colorectal cancer *Oncorget* **2015**, *6*, 30384-30393.

Chapter 2

PET imaging with small-molecule tyrosine kinase inhibitors: TKI-PET

P. Slobbe, A.J. Poot, A.D. Windhorst and G.A.M.S. van Dongen

Published in: *Drug Discovery Today,* **2012**, *17*, 1175-1187

Clinical Pharmacology & Therapeutics, **2013**, *93*, 239-241 (partly)

Abstract

The discovery and increased understanding of tumor targets has led to the development and approval of 22 small molecule tyrosine kinase inhibitors (TKI). Despite tremendous efforts in TKI development, treatment efficacies with these therapeutics are still too low and improvements require a personalized medicine approach. Positron Emission Tomography (PET) with radiolabeled TKIs (TKI-PET) is a tracking, quantification and imaging method, which provides a unique understanding of the behavior of these drugs *in vivo* and of the interaction with their target(s). An overview is provided of tracer synthesis and development as each TKI requires a tailor made approach. Moreover, current preclinical work and the first proof-of-principle clinical studies on the application of TKI-PET are described, illustrating the potential of this approach for improving therapy efficacy and personalized cancer treatment.

2.1 Introduction

Recent advances in cellular biology have led to an increased understanding of signaling transduction pathways in cancer. Crucial molecular targets have been identified involved in e.g. proliferation, differentiation, angiogenesis and metastases. This knowledge has led to the development of tailor-made targeted pharmaceuticals designed particularly to be effective anti-cancer agents. One of the most rapidly expanding fields in this respect is without doubt the development of tyrosine kinase inhibitors (TKIs).

Receptor tyrosine kinases (RTKs) form a family of transmembrane proteins which play a pivotal role in signal transduction processes of the cell (Figure 1). They consist of an extracellular domain for ligand binding and an intracellular domain for signaling. Members of this family include, amongst others, the epidermal growth factor receptor (EGFR), vascular endothelial growth factor receptor (VEGFR) and platelet derived growth factor receptor (PDGFR). Upon ligand binding RTKs oligomerize and autophosphorylation of intracellular tyrosine residues occurs, which in turn stimulate downstream signaling leading to various cell growth related processes [1-3]

Two main categories of RTK targeting drugs are currently on the market, namely monoclonal antibody-based drugs that bind to the extracellular domain of the receptor and compete with the natural ligands, thereby blocking the down-stream signal transduction cascade. Next are the small molecule inhibitors acting intracellularly by competing with ATP for its binding site in the intracellular domain of the receptor, which results in blocking of the down-stream signal transduction cascade as well [4]. This chapter focuses on small molecule (T)KIs that have been approved by the US Food and Drug Administration (FDA, Table 1), their relative limited efficacy in today's cancer treatment and the role that Positron Emission Tomography with radiolabeled TKIs (TKI-PET) can play in a personalized treatment approach and improvement of the therapeutic successes.

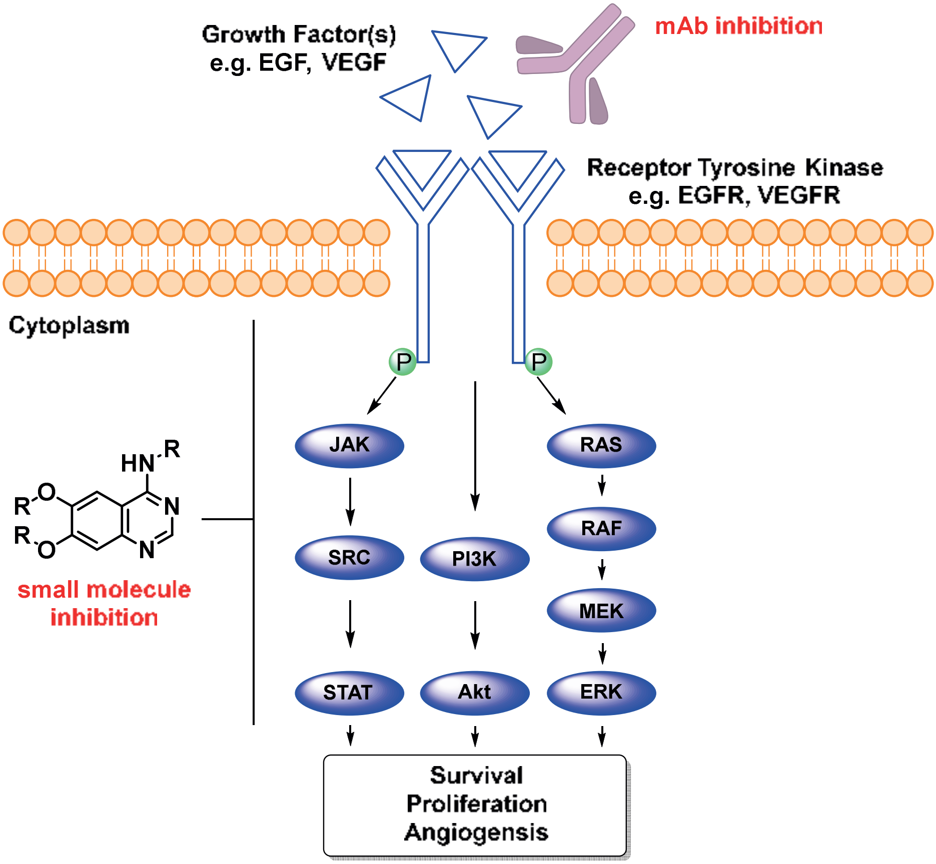

Figure 1: Receptor tyrosine kinase structure, associated downstream signalling and inhibition opportunities

From 2002-2015, thirty small molecule (T)KIs (Table 1) have been approved by the FDA. Moreover, hundreds of new (T)KIs are under clinical development. The effectiveness of these drugs is attributed to the high degree of conservation of the ATP binding region of RTKs and the distinguished ability of these small molecules to bind to this region [5]. Many of these inhibitors act against one specific kinase, making them very selective, but also susceptible for drug resistance by mutation of the target receptor [4]. In addition, broad-spectrum TKIs that target multiple kinases, such as sorafenib and sunitinib, as well as irreversible inhibitors that covalently bind to the target kinase are being developed as well [6, 7].

Table 1*:* FDA approved small molecule kinase inhibitors used for cancer treatment

Generic Name (approval)	**Trade Name**	**Target**	**Cancer Indication**
		Receptor tyrosine kinase inhibitors	
Afatinib (2013)	Gilotrif	EGFR, HER2	Non-small cell lung cancer (with EGFR exon 19 deletions or exon 21 substitution (L858R) mutations)
Axitinib (2012)	Inlyta	KIT, PDGFRβ, VEGFR1/2/3	Renal cell carcinoma
Cabozantinib (2012)	Cometriq	FLT3, KIT, MET, RET, VEGFR2	Medullary thyroid cancer
Erlotinib (2005)	Tarceva	EGFR	Non-small cell lung cancer Pancreatic cancer
Gefitinib (2003)	Iressa	EGFR	Non-small cell lung cancer (with EGFR exon 19 deletions or exon 21 substitution (L858R) mutations)
Lapatinib (2007)	Tykerb	EGFR, HER2	Breast cancer (HER2+)
Lenvatinib (2012)	Lenvima	VEGFR2	Thyroid cancer
Nintedanib (2014)	Vargatef	VEGFR1/2/3, FGFR, PDGFR	Non-small cell lung cancer Iodopathic pulmonary

			fibrosis
Osimeritinib (2015)	Targrisso	EGFR	Non-small cell lung cancer (with EGFR exon 20 T790M mutation)
Pazopanib (2009)	Votrient	VEGFR, PDGFR, KIT	Renal cell carcinoma Soft tissue carcinoma
Regorafenib (2012)	Stivarga	KIT, PDGFRβ, RAF RET, VEGFR1,2,3	Colorectal cancer Gastrointestinal stromal tumors
Sorafenib (2005)	Nexavar	VEGFR, PDGFR, KIT, RAF	Hepatocellular carcinoma Renal cell carcinoma Thyroid carcinoma
Sunitinib (2006)	Sutent	VEGFR, KIT, PDGFR, RET, CSF1R, FLT3	Renal cell carcinoma GI stromal tumor
Vandetanib (2011)	Caprelsa	EGFR, RET, VEGFR2	Medullary thyroid cancer

Non receptor kinase inhibitors

Alectinib (2011)	Alecensa	ALK	Non-small cell lung cancer (with ALK fusion)
Bosutinib (2012)	Bosulif	ABL	Chronic myelogenous leukemia (Philadelphia chromosome positive)
Ceritinib (2014)	Zykadia	ALK	Non-small cell lung cancer (with ALK fusion)

Cobimetinib (2015)	Cotellic	MEK	Melanoma (with BRAF V600 mutation)
Crizotinib (2011)	Xalkori	ALK, MET	Non-small cell lung cancer (with ALK fusion)
Dabrafenib (2013)	Tafinlar	BRAF	Melanoma (with BRAF V600 mutation)
Dasatinib (2010)	Sprycel	ABL, Src	Chronic myelogenous leukemia (Philadelphia chromosome positive) Acute lymphoblastic leukemia (Philadelphia chromosome positive)
Ibrutinib (2013)	Imbruvica	BTK	Mantle cell lymphoma Chronic lymphocytic leukemia Waldenstrom's macroglobulinemia
Idelalisib (2014)	Zydelig	PI3Kδ	Chronic lymphocytic leukemia Follicular B-cell non-Hodgkin lymphoma Small lymphocytic lymphoma
Imatinib (2002)	Glivec	ABL, KIT, PDGFR,	GI stromal tumor (KIT+) Dermatofibrosarcoma protuberans Multiple hematologic malignancies including Philadelphia chromosome-

			positive ALL and CML
Nilotinib (2007)	Tasigna	ABL	Chronic myelogenous leukemia (Philadelphia chromosome positive)
Palbociclib (2015)	Ibrance	CDK4, CDK6	Breast cancer (ER+, HER2-)
Ponatinib (2012)	Iclusig	ABL, FGFR1/2/3, FLT3, VEGFR2	Chronic myelogenous leukemia Acute lymphoblastic leukemia (Philadelphia chromosome positive)
Ruxolitinib (2011)	Jakafi	JAK1,2	Myelofibrosis
Trametinib (2013)	Mekinist	MEK	Melanoma (with BRAF V600 mutation)
Vermurafenib (2011)	Zelboraf	BRAF	Melanoma (with BRAF V600 mutation)

ABL: v-abl Abelson murine leukemia viral oncogenes homolog, ALK: anaplastic lymphoma kinase, BCR: breakpoint cluster region gene, BRAF: serine/threonine-protein kinase B-Raf, BTK: Burton's tyrosine kinase, CD: cluster of differentiation, CDK4: Cyclin-dependent kinase 4, CDK6: Cyclin-dependent kinase 6, CSF1R: colony stimulating factor 1 receptor, EGFR: epidermal growth factor receptor, Erk: extracellular regulated kinase, FGFR: Fibroblast growth factor receptor, FLT3: Fms-like tyrosine kinase-3, HER2: human epidermal growth factor receptor 2, JAK: Janus Kinase, KIT: Mast/stem cell growth factor receptor, MEK: MAP kinase kinase, MET: MNNG HOS transforming gene, PDGFR: platelet derived growth factor receptor, PhC: Philadelphia chromosome, PI3Kδ: Phosphoinositide 3-kinase, RAF: Rapidly Accelerated Fibrosarcoma, RET, rearranged during transfection proto-oncogene, Src: Proto-oncogene tyrosine-protein kinase, VEGFR: vascular endothelial growth factor receptor.

The increased development of these targeted drugs raises the question how to test all these new pharmaceuticals in an efficient way, as it would require many clinical trials and thereby a substantial investment and patient burden. Furthermore, approximately 90% of these drugs are likely to fail in clinical trials and do not reach the market, eventually escalating the costs of drugs that do reach the market [8]. Even approved small molecule TKIs have limited efficacy with response rates varying between 10-30%. Therefore it is becoming increasingly important to distinguish between effective and ineffective drugs at an early stage. Questions that arise are: how to improve the efficacy of therapy with targeted TKIs and how to identify patients with the highest chance of benefit from treatment with TKIs?

Aforementioned questions become increasingly important with respect to the drug discovery process of personalized medicines. The traditional concept of large, randomized clinical trials becomes obsolete in personalized TKI-development. When maximally 30% of the patient population will respond to a targeted drug, 70% of the subjects in a routine blinded randomized clinical trial will never respond, e.g. due to inefficient tumor targeting. The results of these trials will therefore automatically be biased towards the negative. A method to confirm target expression and selective targeting of TKIs to the tumor is therefore of extreme value in the drug discovery process. This selection method can then be used to include patients into a clinical trial.

Currently the method of choice to assess the target expression level or target mutation status is to obtain a biopsy of the tumor material. However, obtaining a biopsy is an invasive method and even not always possible. When a biopsy is available, it is questionable whether this is sufficient to obtain a representative overview of the whole (often genetically heterogeneous) tumor. Moreover, expression of a target does not guarantee efficient targeting by the particular TKI.

PET is uniquely qualified to address these issues. PET is a non-invasive *in vivo* imaging technique that allows the visualization and quantification of the distribution of molecules labeled with positron-emitting isotopes at a picomolar level. This method allows for the evaluation of biochemical and physiological processes by monitoring the distribution and kinetics of the labeled molecule *in vivo*. PET has found broad application in clinical practice (personalized treatments), research and pharmaceutical development [9, 10]. PET with radiolabeled drugs can serve as a tool to answer several vital questions during drug development. Fundamental issues such as the distribution of a drug in the body can be assessed quantitatively and over time, indicating if the desired target is present (target expression), whether the target site is reached by the drug, and how the kinetics of binding are *in vivo*. Discrepancy between tumor uptake of a drug and the therapeutic response might be indicative for the presence of resistance mechanisms. Furthermore, uptake in normal organs might be predictive for toxicity. Interpatient variation of tumor targeting can be assessed, providing a method to preselect patients which will or will not benefit the most from treatment. In this context TKI-PET can be extremely valuable since only a minority of the potential patient population benefits from the treatment, while the majority only suffers from the treatment side effects. Starting point of TKI-PET is the design and development of a suitable TKI-PET tracer. In setting up a suitable labeling strategy the following aspects are critical: (1) the chemical structure of the TKI-PET tracer, which dictates the options for radiolabeling, (2) the short physical half-life of the decaying PET radionuclide, (3) the formation of radioactive metabolites and (4) the specific activity of the TKI-PET tracer.

First, to avoid a difference in their *in vivo* behavior it is of vital importance that the radiotracer and the parent compound have exactly the same chemical structure. Only when the native chemical structure is employed as a tracer, the results of the PET study will represent the behavior of the corresponding drug. This requires a unique tracer development approach for each individual TKI. The purpose of TKI-PET is to study the behavior of FDA approved drugs *in vivo*. The pharmacological properties of these TKIs, such as affinity and lypophilicity, have already been established in the past, before considering tracer development. Moreover, by using the same chemical structure for PET tracer and approved TKI, additional toxicity studies and regulatory hurdles can be avoided, providing a fast track to clinical application.

Second, the labeling of TKIs requires a drug-specific strategy. Usually a TKI can be labeled with carbon-11 and sometimes with fluorine-18. The challenge in the radiosynthesis of PET-tracers lies in the short half-life of PET-isotopes, being 20 minutes for carbon-11 and 110 minutes for fluorine-18. As a consequence the synthesis of a PET tracer should be performed in the shortest time possible after production of these PET-isotopes with a cyclotron. In general, the total preparation time should not exceed 3 half-lifes (60 minutes for carbon-11 and 6 hours for fluorine-18).

The third important consideration in the design of a TKI-PET tracer is the metabolism of the drug. Radiolabeled metabolites will not represent the biodistribution of the drug. Therefore, quantification of receptor binding and associated kinetic modeling becomes more difficult and has to be corrected for the presence of radiometabolites. To this end, it is interesting to label a TKI at several positions (when possible) and to select the most suitable tracer for clinical application on the basis of metabolite formation.

Fourth, the specific activity of a TKI-PET tracer can be of importance. Specific activity is defined as the amount of radioactivity per mole of product. From the origin of PET imaging it was generally thought that this should be as high as possible (a lower limit is 18.5 GBq/μmol is generally accepted) to avoid any pharmacological effects of the tracer itself. This concept is known as the tracer principle of George de Hevesy. While this rule remains commonly accepted it might well be that TKI-PET imaging at a therapeutic dose (resulting in low specific activity) might give superior information. To date, this question remains unanswered since most PET tracers are evaluated at tracer dose only. Thorough studies comparing these two imaging options are required to establish the differences [11-13].

In recent years seven out of twenty-two FDA approved TKIs have been radiolabeled and *in vivo* evaluations have been performed. This chapter aims to provide an overview of the exciting field of small-molecule TKI-PET. Radiosynthesis strategies and *in vivo* evaluations regarding tumor targeting will be discussed. Many TKIs are known to bind to efflux-pumps like P-glycoprotein (P-gp) and the use of radiolabeled TKIs for imaging of efflux-pumps in the blood brain barrier has been published as well, however, this overview will mainly focus on the potential of TKI-PET in cancer treatment. To date, some excellent general reviews have been published. However, most of them address broad topics covering RTK biology, PET imaging with antibodies (immuno-PET) as well as with TKIs, and/or the use of radiolabeled TKI analogs [14-24]. TKIs like gefitinib and erlotinib are monospecific and target just one tyrosine kinase, while most other FDA approved TKIs are dual- or multispecific (see Table 1). Next to (approved) reversible TKIs, more recently also irreversible TKIs are under investigation like the EGFR and HER2 inhibitors afatinib and neratinib. TKI-PET can be key in understanding the *in vivo* of the behavior of these next generation inhibitors. Furthermore TKI-PET could contribute to the dosimetry of novel therapeutic agents as well as be an indication whether monospecific, multispecific, reversible or irreversible inhibitors are best suited to use in cancer therapy. This chapter primarily touches upon the chemistry to develop radiolabeled TKIs that still have the native chemical structure of the FDA approved drugs and (pre)clinical evaluation of these tracers. Challenges in chemistry development will be discussed as well as the possibility to use TKI-PET in a clinical setting to boost personalized patient care.

2.2 Imatinib (Glivec®)

Imatinib was the first selective TKI approved by the FDA in 2001 for the treatment of several types of cancer, predominantly Chronic Myelogenous Leukemia (CML) and gastrointestinal stromal (GIST) tumors. Its development is rooted in the discovery of the so-called oncogenes, which are genes that are drivers of human cancer [25]. CML is characterized by a reciprocal translocation between chromosomes 9 and 22. This shortened chromosome discovered in 1960 is known as the Philadelphia chromosome and was the first specific genetic change directly related to cancer [26]. The result of this altered gene is the expression of the BCR-ABL protein, which is a protein with increased tyrosine kinase activity. Expression of the BCR-ABL protein in mice resulted in the advent of leukemia, making this protein attractive for drug targeting [27]. Medicinal chemistry optimization by a high-throughput screen resulted in imatinib, which was found to be effective not only to inhibit the BCR-ABL kinase (IC_{50} = 0.025 μM), but also c-KIT (IC_{50} = 0.1 μM, another receptor kinase) and PDGFR (IC_{50} = 0.1 μM)

[25]. Clinical studies revealed modest side-effects and a clear effect in patients with CML and GIST tumors leading to the approval of imatinib.

The therapeutic advantage of broad spectrum TKI imatinib is that several signal transduction pathways can be blocked simultaneously. Since the RTKs targeted by imatinib have different affinities, one RTK might be targeted more efficient than the others. Moreover, due to its multi-specificity imatinib can potentially be applied for multiple tumor types. A possible disadvantage in the application of broad spectrum TKIs is that normal tissues might be targeted as well, resulting in additional toxicities. Because of these complex binding characteristics, TKI-PET can be particularly useful in elucidating the targeting potential of broad spectrum TKIs.

2.2.1 Tracer synthesis

Radiolabeled imatinib was described by Fowler and co-workers in 2007, employing a straightforward methylation procedure [28]. Desmethyl precursor **1** is reacted with [^{11}C]methyl iodide in DMSO for 10 minutes to obtain [^{11}C]imatinib in 76.7 ± 6.9% radiochemical yield (decay corrected) with a specific activity of 40.7 to 51.8 GBq/μmol and a radiochemical purity of >98% (Scheme 1). Total synthesis time is 1 hour from the end of cyclotron bombardment (EOB) to formulation of the final product. Other positions for labeling are not readily available in this molecule, with the possible exception of the carbonyl position. Labeling at this position can theoretically be achieved by a palladium mediated [^{11}C]carbonmonoxide insertion, however, this option is radiochemically more challenging [29]. Furthermore, having the label on the amide position could lead to unwanted radiometabolites as *N*-demethylation occurs as a major metabolic pathway [30, 31].

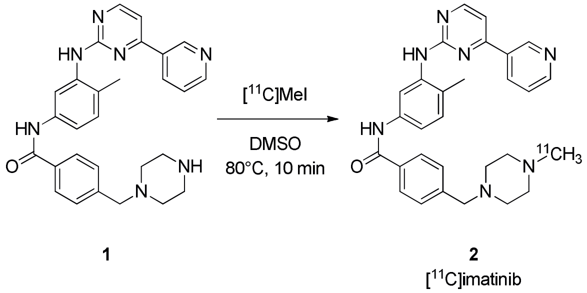

Scheme 1. Radiosynthesis of [^{11}C]imatinib

2.2.2 In vivo evaluation

[^{11}C]Imatinib has been evaluated *in vivo* in baboons. Biodistribution studies indicated that [^{11}C]imatinib does not accumulate in the brain, most likely due to efflux effects via the P-glycoprotein [28, 32]. [^{11}C]imatinib and/or its radioactive metabolites were found mainly in the liver, kidneys and gallbladder. This is an expected result as these organs are involved in the metabolism and excretion of xenobiotics.

Unfortunately, it was not investigated whether radioactive metabolites are formed. Furthermore, no tumor models were used in this study, so it cannot be judged whether selective tumor targeting occurs. As imatinib was specifically designed to target the BCR-ABL protein it would be of interest to assess the imaging performance of [^{11}C]imatinib in animal models bearing tumors that over-express this protein. It is of note, however, that it is challenging to image leukemia since this is not a solid tumor. Nevertheless, a clinical example of imaging leukemia has been reported with [^{18}F]FLT, a PET tracer for imaging cell proliferation. This exciting result indicates that imaging leukemia with TKI-PET might be feasible as well [33].

2.3 Gefitinib (Iressa®)

Gefitinib (IC_{50}= 33 nM [34], Scheme 2), a reversible EGFR inhibitor, was approved for the treatment of NSCLC in 2003. NSCLC accounts for 80% of all lung cancers, the leading cause of cancer mortality, and the 5-year survival of patients with this disease is only 10% [35]. Moreover, a modest 10% of the patient population show a clinical response upon treatment with gefitinib, but those responding patients often benefit significantly. Small gene alterations around the ATP binding site of the EGF receptor have been associated with the therapeutic effectiveness of gefitinib in NSCLC patients. A similar correlation was found with the other EGFR inhibitor erlotinib. Predominantly 2 gene alterations have been correlated with striking clinical responses to EGFR kinase inhibitors such as gefitinib and erlotinib. The first concerns an exon 19 deletion (around E746-A750) and the second a point mutation in exon 21 (L858R). Both alterations result in constituent activation of EGFR signaling by disruption of the auto inhibitory conformation. Moreover, these alterations decrease the affinity for ATP and thereby increase affinity for competitive inhibitors such as gefitinib and erlotinib [36-40]. Unfortunately, most responders eventually develop drug resistance. Resistance is frequently associated with a secondary EGFR mutation, namely T790M, which increases the affinity for ATP [41].

For assessment of EGFR expression and mutation status a tumor biopsy has to be taken, which is not always possible. Even when a biopsy is available, it is questionable whether this is sufficient to obtain a representative overview of the whole (often heterogeneous) tumor. Moreover, it is possible that expression and mutation status differ in primary tumor and metastatic lesions and change during the course of disease, for example upon chemo- or radiotherapy. Taking this into account, it might be that PET imaging with the radiolabeled EGFR TKI itself gives a more comprehensive overview of EGF receptor status, and the interaction of the drug with this receptor.

The discovery of gefitinib and related TKIs is rooted in the potency of the 4-anilinoquinazoline (Scheme 2a) moiety to bind to the ATP binding site of the EGFR [42, 43]. A structure-activity relationship study to determine the optimal substituents in terms of bio-availability and potency resulted in the drug candidate gefitinib [44].

Gefitinib (Scheme 2b) was found to be effective in several types of EGFR expressing cancer cell lines with IC_{50} values ranging from 0.2-0.6 μM [45].

2.3.1 Tracer synthesis

Several papers have appeared dealing on the radiolabeling of gefitinib. The first report in 2005 by Seimbille *et al.* describes a general approach for the radiolabeling of gefitinib and related anilinoquinazoline structures with fluorine-18 [46]. The key step in the synthesis is the preparation of a 3-chloro-4[^{18}F]-fluoro-aniline derivative [^{18}F]**6**, which can be reacted with a variety of substrates to obtain radiolabeled compounds such as [^{18}F]gefitinib ([^{18}F]**8**) (Scheme 2b). The synthesis starts with the nucleophilic substitution with [^{18}F]fluoride of the trimethyl triflate group of **4** to provide [^{18}F]**5**. Reduction of the nitro-group using sodium borohydride in the presence of palladium on activated carbon affords the 3-chloro-4[^{18}F]-fluoroaniline ([^{18}F]**6**) in 25-40% radiochemical yield (decay corrected). Reaction with precursor **7** and subsequent HPLC purification furnishes [^{18}F]gefitinib (**8**) in 60-70% radiochemical yield (based on 3-chloro-4[^{18}F]-fluoroaniline) with >222 GBq/μmol of specific activity (purity not reported). Total synthesis time is about 2 hours from EOB, excluding formulation. Moreover, recently a fully automated synthesis of [^{18}F]gefitinib ([^{18}F]**8**) was reported providing the tracer in 17.2% radiochemical yield, high purity (>99%) and a specific activity of 14.1 GBq/μmol in 2.5 hours of total synthesis time [47].

In 2006 two reports were published simultaneously covering the synthesis of carbon-11 labeled gefitinib. In the first report by Wang *et al.* [^{11}C]gefitinib is prepared using a straightforward methylation of hydroxyl precursor **9** using [^{11}C]methyltriflate (Scheme 2c). This procedure afforded [^{11}C]gefitinib, after HPLC purification, in 30-40% radiochemical yield with a specific activity of 148-222 GBq/μmol and a purity of >98% in a synthesis time of only 20-30 minutes from EOB [48]. In the second report by Holt *et al.* the same procedure is used affording [^{11}C]gefitinib in similar yields and purity but with a higher specific activity of 359 GBq/μmol) [49].

Finally in 2010 Zhang *et al*. reported a synthesis using [^{11}C]methyl iodide, which is a less reactive methylating reagent than [^{11}C]MeOTf [50]. [^{11}C]Gefitinib was obtained in a relatively low radiochemical yield of 11±7% (decay corrected) and a specific activity of 61-159 GBq/µmol with a radiochemical purity of >98%. Total synthesis time is 23 minutes.

Clearly, using the more reactive [^{11}C]MeOTf is the preferred method of synthesis for [^{11}C]gefitinib as yields and specific activities are higher at similar synthesis times. Other labeling positions are not readily available in this molecule.

2.3.2 In vivo evaluation

[^{18}F]Gefitinib ([^{18}F]**8**) was evaluated *in vivo* in vervet monkeys and in tumor-free and tumor bearing mice by Su *et al.* [51]. In tumor-free mice administration of [^{18}F]gefitinib resulted in high uptake in the lungs after 5 minutes followed by a fast uptake in the liver and finally hepatobiliar and renal excretion. The biodistribution in vervet monkeys was essentially similar to that of mice, however, excretion was slower. Next, [^{18}F]gefitinib was evaluated in mice bearing human tumor xenografts. Several human tumor types were chosen: U87 (gliobastoma cell line, showing low expression of EGFR), U87-EGFR (overexpressing EGFR), H3255 (NSCLC cell line, carrying the exon 21 point mutation L858R [40]) and H1975 (NSCLC cell line, carrying the exon 21 point mutation L858R as well as the secondary mutation T790M [40]). Unexpectedly, none of the selected xenograft lines showed increased tracer uptake as assessed by PET-imaging and ex vivo biodistribution analysis, whereas every xenograft line with the exception of U87 was expressing EGFR (Figure 2). [^{18}F]Gefitinib appeared metabolically stable in mice for the duration of the scans, ruling out the option that metabolism is the reason for the lack of tumor targeting.

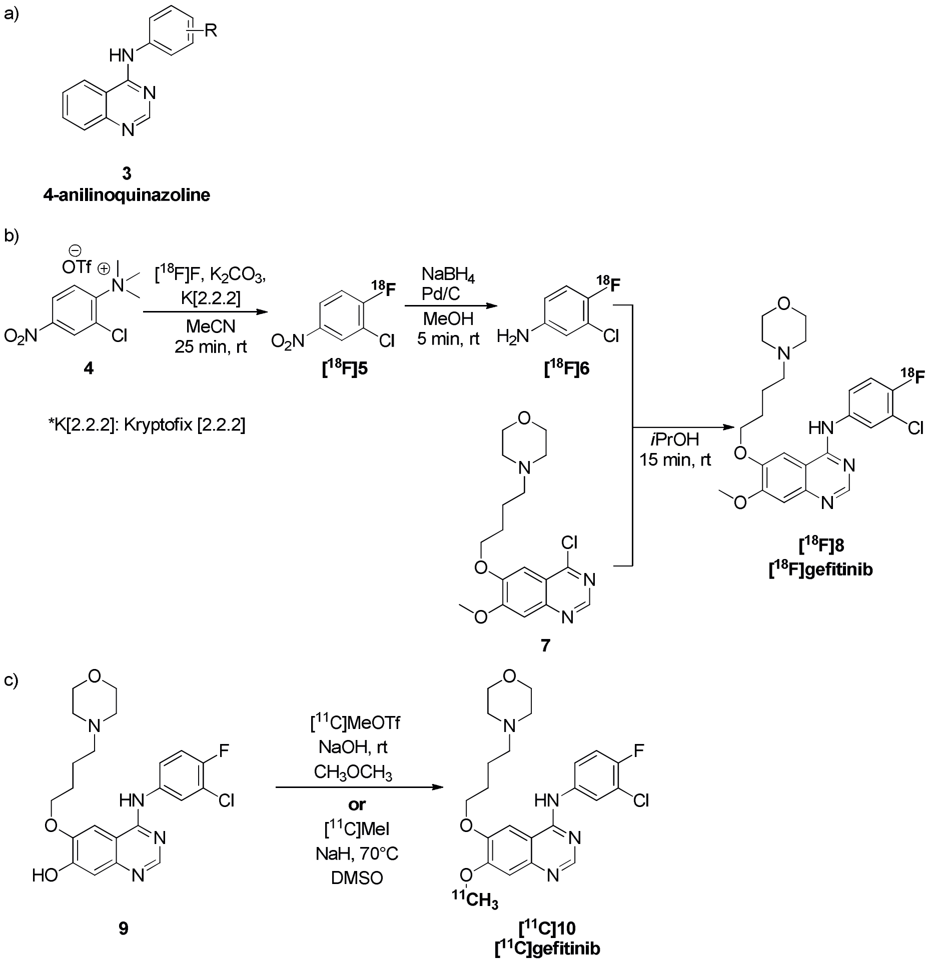

Scheme 2. Synthesis of radiolabeled gefitinib; a) 4-anilinoquinazoline scaffold; b) Synthesis of [^{18}F]gefitinib; c) Synthesis of [^{11}C]gefitinib

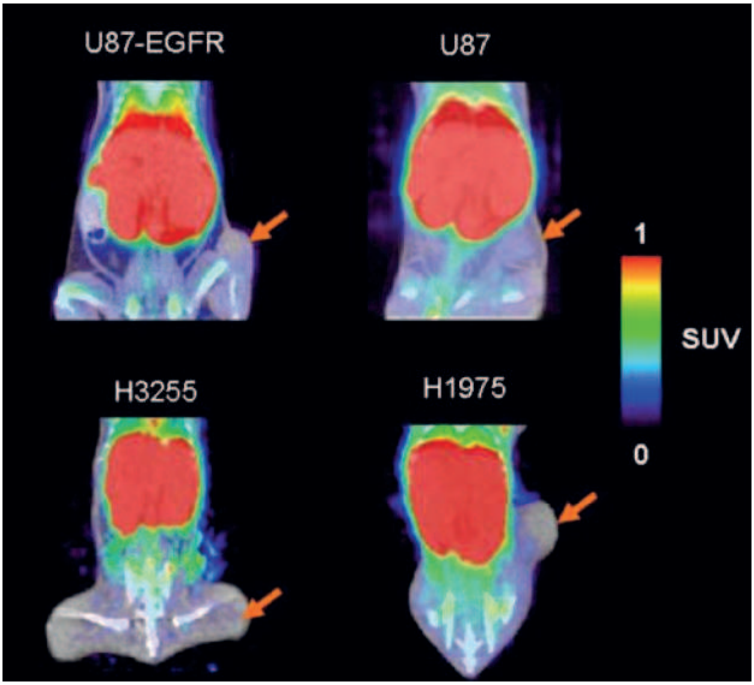

Figure 2: µPET/CT images of tumor bearing mice at 1 hour post intravenous injection of [^{18}F]gefitinib. (Arrows indicate tumor location, *SUV:* standardized uptake value) showing no significant uptake in tumor tissue. Figure adapted from [51]

The lack of uptake of [^{18}F]gefitinib in tumors expressing wild type EGFR could explain the lack of clinical efficacy in these tumors (*vide infra)*. However, it should be mentioned that the cell line H3255 contain activated EGFR and this mutation is clinically sensitive to treatment with gefitinib and therefore tracer accumulation in the tumor would have been expected. *In vitro* experiments confirmed that the cells take up [^{18}F]gefitinib, most probably, tumor accumulation is too low or the retention of [^{18}F]gefitinib is too short for imaging purposes.

The observed limited tumor uptake might be due to other mechanisms. It has been shown that gefitinib is a substrate for P-gp and/or the Breast Cancer Resistance Protein (BCRP), both members of the ATP binding cassette (ABC) transporters. These transmembrane proteins actively reduce the intracellular concentration of substrates (xenobiotics such as drugs) by pumping them out of the cell. By doing so these proteins are heavily involved in drug resistance against cancer [52]. Using [^{11}C]gefitinib in BCRP/P-gp knock-out mice it was demonstrated that gefitinib is a substrate for BCRP and/or P-gp as the knock-out mice showed uptake in the brain region, whereas the wild-type mice did not [53]. Tumor cells often express these types of drug efflux pumps and therefore this could be the reason for the low tumor uptake of [^{11}C]gefitinib as observed in aforementioned experiments. It is likely that the tracer amounts of [^{18}F]gefitinib are rapidly pumped out of the tumor via P-gp and this might explain the lack of tracer accumulation in gefitinib sensitive tumors. This hypothesis can readily be confirmed by performing biodistribution experiments or PET imaging while co-injecting a P-gp blocker (such as tariquidar or loperamide) together with [^{18}F]gefitinib. Moreover, it can be considered to evaluate the imaging performance of radiolabeled gefitinib at tracer dose as well as at therapeutic dose. It might be that imaging at therapeutic dose is much more informative to predict the TKIs therapeutic efficacy, especially when drug resistance mechanisms play a role. To date, little is known about this kind of imaging at therapeutic dosis and future research is required to confirm or reject this hypothesis.

Another factor which could be of importance is the lipophilicity of the tracer. If the passage of the cell membrane is too slow this becomes the critical and rate limiting step. However, gefitinib and erlotinib have a similar lipophilicity, and erlotinib does accumulate in tumor cells (*vide supra*).

[^{11}C]Gefitinib ([^{11}C]**10**) was also evaluated in mice bearing murine fibrosarcoma (NFSa), and was found to be an effective imaging agent for this kind of tumors [50]. As is depicted in Figure 3 [^{11}C]gefitinib accumulated in the tumor tissue efficiently, with a maximum of 3.5% injected dose per gram (%ID/g) of tumor tissue at 60 min. Furthermore, blocking studies were performed which showed that the uptake of [^{11}C]gefitinib could be reduced in a dose dependent manner. A high signal-to-noise ratio was observed indicating that the tracer can be used as imaging agent for murine fibrosarcoma tumors.

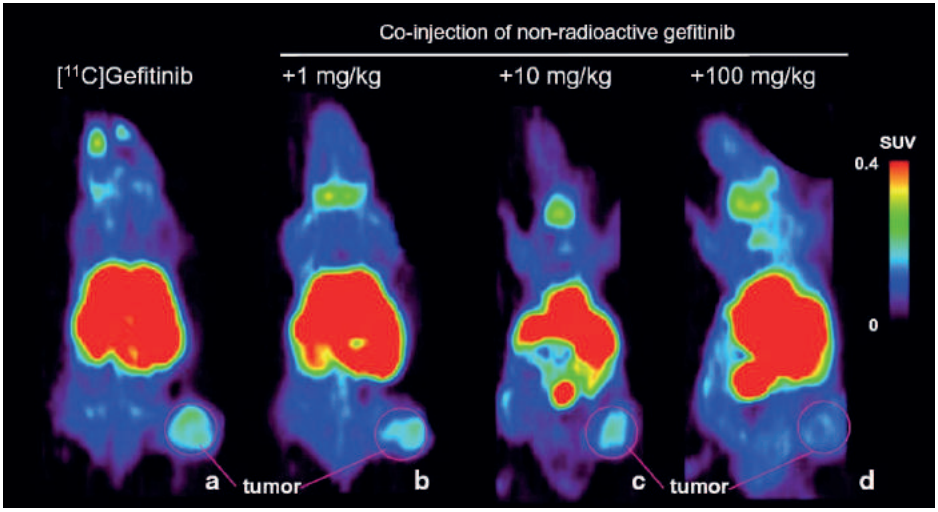

Figure 3: PET imaging of tumor bearing mice (summation 30-60 min). a) [^{11}C]gefitinib only; b) [^{11}C] gefitinib coinjected with gefitinib (1mg/kg); c) [^{11}C] gefitinib coinjected with gefitinib (10 mg/kg); c) [^{11}C] gefitinib coinjected with gefitinib (100 mg/kg); showing uptake of [^{11}C]gefitinib which could be blocked by saturation with cold gefitinib. Figure adapted from [50].

It is of note that these tumors are not derived from a human cell line and have been extracted from a naturally occurring murine fibrosarcoma. This raises the question whether or not this is a suitable preclinical model for the use of TKIs in man.

Finally, comparative studies on [^{18}F]gefitinib and [^{11}C]gefitinib revealed that both are metabolically stable for the duration of PET scanning, making [^{18}F]gefitinib a more attractive tracer due to the longer half-life.

2.4 Erlotinib (Tarceva®)

Erlotinib (IC_{50} = 20 nM [54]) is a similar, albeit more potent, inhibitor as gefitinib in the sense that it also competes with ATP for its binding site in EGFR. Erlotinib is also based on the 4-anilinoquinazoline scaffold and the product of classical medicinal chemistry optimization [55]. Moreover, mutations associated with gefitinib sensitivity are also important for erlotinib sensitivity [56, 57]. After significantly increasing survival of patients in clinical trials, erlotinib (12) was approved in 2004 as a second line treatment for patients with advanced NSCLC, after failure of at least one prior chemotherapy regimen. In 2005 approval followed for the treatment of pancreatic carcinoma in combination with gemcitabine. However, erlotinib is only effective in 10-20% of the patient population, therefore a straightforward imaging method to predict response can be of immense value [58]. In the following years it became clear that EGFR mutations are of great importance for efficacy of erlotinib (and other first generation EGFR TKIs, such as gefitinib) and erlotinib was subsequently approved in 2013 as a first-line treatment for patients whose tumors harbor an exon 19 deletion or an exon 20 point mutation [59].

2.4.1 Tracer synthesis

A straightforward methylation procedure for the preparation of [^{11}C]erlotinib was reported by Memon and co-workers, employing [^{11}C]methyl iodide [60]. [^{11}C]erlotinib was obtained by reacting desmethyl precursor **11** with [^{11}C]methyl iodide in the presence of sodium hydride (Scheme 3). Although the radiochemical yield was not reported, the product was obtained with a radiochemical purity of >95% and a moderate specific activity of 20-100 GBq/µmol. Alternatively, [^{11}C]erlotinib was obtained via methylation on the other hydroxyl functionality on precursor **13** in good yield (2183-3476 MBq), high radiochemical purity (>98%) and excellent specific activity of 184-587 GBq/µmol [61]. Other positions for straightforward labeling are not available in this molecule.

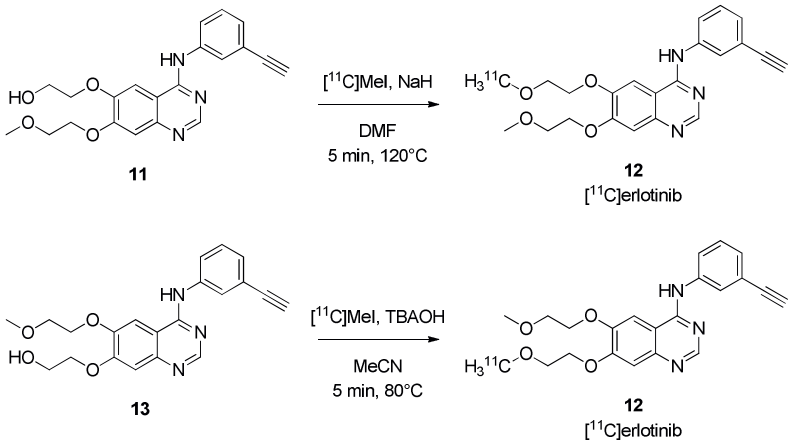

Scheme 3: Synthesis of [^{11}C]erlotinib via carbon-11 methylation of a terminal alcohol

2.4.2 In vivo evaluation

[^{11}C]Erlotinib was evaluated in three lung cancer cell lines namely HCC827, A549 and NCI358 [60]. All of these cell lines over-express EGFR, however, only HCC827 is sensitive to erlotinib *in vitro*. The HCC827 cells harbor the exon 19 activating mutation in EGFR, rendering it sensitive to erlotinib. Mice were grafted with tumors from each of these cell lines and the uptake of [^{11}C]erlotinib was evaluated using µPET imaging (Figure 4). The results of this study are striking as the highest tumor uptake was observed in the erlotinib sensitive HCC827 tumors (Figure 4a,b). Liver and kidney uptake was also high, which is expected as excretion occurs via these organs. In contrast, erlotinib insensitive NCI358 tumors did not show any tracer uptake (Figure 4c,d). Ex vivo biodistribution analysis confirmed these results. In HCC827 bearing mice a high tumor-to-blood ratio was observed while in NCI358 bearing mice the tumor-to-blood ratio was almost 1. Clearly in contrast to the previously described results on [^{18}F]gefitinib, [^{11}C]erlotinib accumulates at the highest level in the most sensitive xenograft line, indicating that [^{11}C]erlotinib PET can indeed identify erlotinib sensitive tumors.

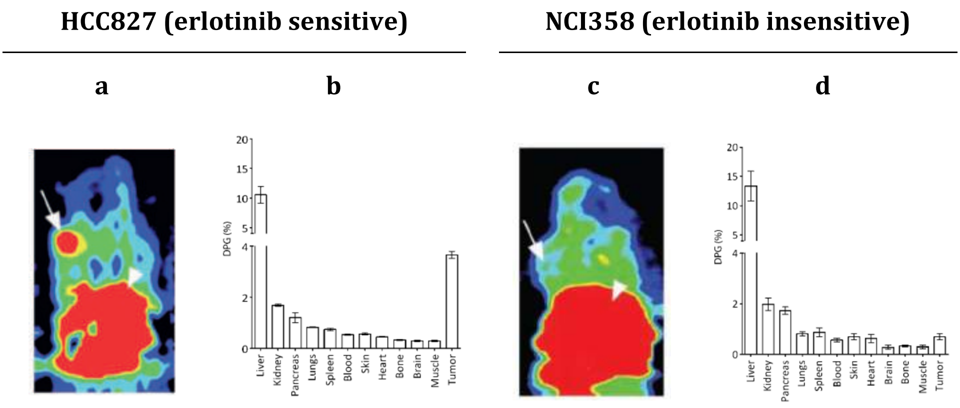

Figure 4: a) µPET image of HCC827 tumor xenograft bearing mouse, arrow indicates tumor position; b) biodistribution of [^{11}C]Erlotinib in HCC827 tumor bearing mice; c) µPET image of NCI358 tumor xenograft bearing mouse, arrow indicates tumor position; d) biodistribution of [^{11}C]erlotinib in NCI358 tumor bearing mice. (results for A549 cell line are comparable to the NCI358). Indicating clear uptake in mutated EGFR compared to wild-type. Figure adapted from [60].

A similar study was performed by Petrulli *et al*. in which a µPET analysis was performed on tumor bearing mic [62]. In this case several xenograft types were used, namely two exon 19 deleted variants: HCC827 and PC9, two wild type: SW620 and U87 and finally an EGFR V3 mutated variant of the latter (which has a mutation in exon 2-8, thereby rendering it unable to bind ligands extracellularly). The PET-data revealed uptake in the exon 19 deleted lines and not in any of the other xenografts. Kinetic analysis revealed the highest binding potential (BP) in the HCC827 tumors, which was a 2-3 fold higher than in the PC9 cells, however, this appears to correlate with the EGFR expression level in both lines. Furthermore imaging was performed at high specific activity (159.1 ± 48.1 GBq/µmol, 5.9 ± 4.4 MBq and 9.3 ± 5.2 nmol of erlotinib) or at low specific activity where cold erlotinib (10 mg/kg) was co-injected with the tracer (2.2 ± 1.1 MBq). Significantly higher binding of [^{11}C]erlotinib was observed in the high specific activity group when compared to the low specific activity group. This demonstrated that imaging should be performed at high specific activity with [^{11}C]erlotinib.

The final pre-clinical report on [^{11}C]erlotinib appeared in 2015 by the group of Mishani [63]. Mice bearing a panel of NSCLC tumor xenografts with different mutations of EGFR were subjected to PET imaging. The following mutations were analyzed in this study: wild type (QG56), exon 19 deletion (HCC827), exon 21 point mutation L858R (H3255) and a double mutant L8585R/T790M associated with acquired resistance to TKI therapy (H1975). Sensitivity to erlotinib treatment was determined and the HCC827 and H3225 were found to be sensitive. Imaging results were similar, with regard to the exon 19 deleted xenograft (HCC827) and the wild-type (QG56) as in previous studies, however the L858R xenograft expressing a sensitizing mutation demonstrated uptake of [^{11}C]erlotinib higher than WT but significantly lower than in the HCC827 xenograft. Finally, the double mutant demonstrated uptake similar to WT. This report indicates that erlotinib uptake can also be found in other mutants then the exon 19 deleted variant of EGFR, which are also sensitive to treatment.

The first-in-human application of TKI-PET was reported by the Weber *et al.* in 2011 [64]. This case study was performed with a 32-year old NSCLC patient who presented with a primary tumor and multiple brain metastases. The patient was responsive to erlotinib treatment and a biopsy of the primary lung tumor revealed the exon 19 deletion of EGFR. Using MRI (Magnetic Resonance Imaging) metastatic lesion were identified in the cerebellum of the brain and a [^{11}C]erlotinib PET scan revealed clear uptake of the tracer in these metastases (Figure 5) with little to no uptake in the surrounding brain tissue. This study clearly demonstrates that [^{11}C]erlotinib accumulates in erlotinib sensitive tumor lesions, although the authors did not report on uptake in the primary tumor.

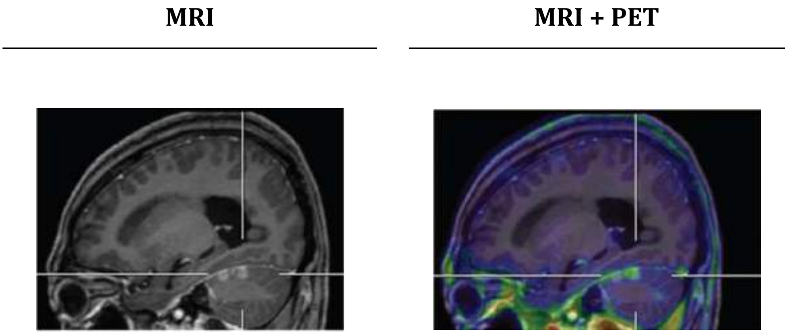

MRI

MRI + PET

Figure 5: MRI-PET images of two brain metastatic lesions in the cerebellum, showing [^{11}C]erlotinib hot spot in the metastatic lesions. Figure adapted from [64].

Another report on clinical PET imaging with [^{11}C]erlotinib to predict responsiveness appeared in 2011. In this study of Memon *et al.*, 13 NSCLC patients were included and grouped into responders and non-responders to erlotinib treatment. At the start of the study a PET/CT scan using [^{18}F]FDG and [^{11}C]erlotinib was performed, followed by treatment with erlotinib for a period of twelve weeks. After the treatment period again a PET/CT scan using [^{18}F]FDG was performed for response evaluation. In four out of the thirteen patients, [^{11}C]erlotinib PET revealed uptake in one or more of their lung tumors or lymph node metastases (Figure 6c). Furthermore, [^{11}C]erlotinib PET was capable to visualize tumor-positive lymph nodes that could not be visualized by [^{18}F]FDG PET. Of the four patients with tumor accumulation of [^{11}C]erlotinib, one died before follow-up, whereas the other three responded to erlotinib treatment. Of the nine patients without tracer accumulation three died before follow-up, four showed progressive disease while two had stable disease after 12 weeks treatment. These results indicate that responders and non-responders show different uptake of [^{11}C]erlotinib PET, but the discriminating value of [^{11}C]erlotinib to decide on erlotinib treatment for individual patients still has to be demonstrated in larger studies. To this end, it is informative to correlate [^{11}C]erlotinib uptake in tumors with their mutational status, this will provide important insight into the working mechanism of erlotinib treatment. This analysis was not performed in aforementioned trial.

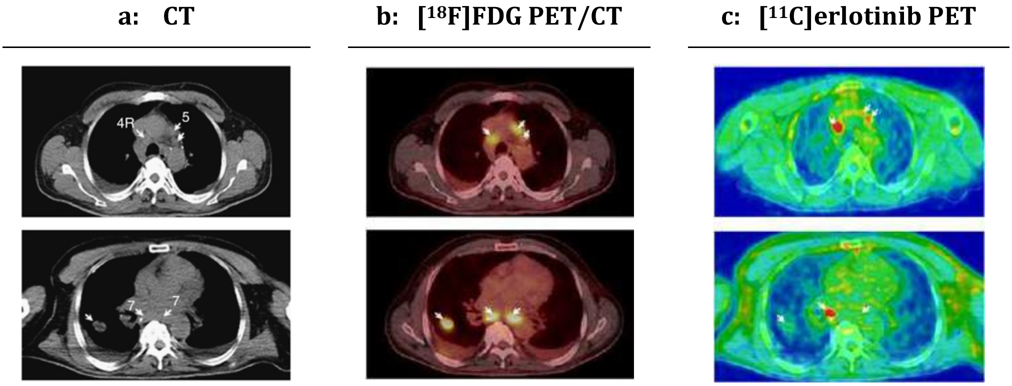
a: CT

b: $[^{18}F]$FDG PET/CT

c: $[^{11}C]$erlotinib PET

Figure 6: Transaxial PET-CT images of 2 erlotinib responsive patients showing $[^{11}C]$erlotinib positive lymph nodes (red). Figure adapted from [65].

In a landmark study performed by Bahce *et al*. 10 NSCLC patients were included and the mutational status of EGFR in the tumors determined via biopsy [61]. Subsequently these patients were grouped either for activating mutation (exon 19 deletion) or wild type EGFR. Both groups underwent a $[^{15}O]H_2O$ (for tumor perfusion) scan and a $[^{11}C]$erlotinib scan in a test-retest setting on the same day. During the $[^{11}C]$erlotinib scan blood sampling was performed to determine plasma input function and tracer metabolism. Figure 7 depicts representative PET-CT scans of both an exon 19 deleted patient and a wild type patient. The exon 19 deleted patient clearly demonstrates uptake in the tumor, whereas this is not observed for the wild type patient. $[^{15}O]H_2O$ scans revealed that higher tracer uptake was not related to increased perfusion. Of the 5 patients in the mutated EGFR group, demonstrating uptake of $[^{11}C]$erlotinib, 3 were subsequently treated with a full regimen of erlotinib therapy and achieved a partial response. This pilot study clearly demonstrates the potential predictive value of $[^{11}C]$erlotinib PET and these findings therefore warrant larger clinical studies to determine the complete potential of $[^{11}C]$erlotinib PET, for example in genomic heterogeneous tumors.

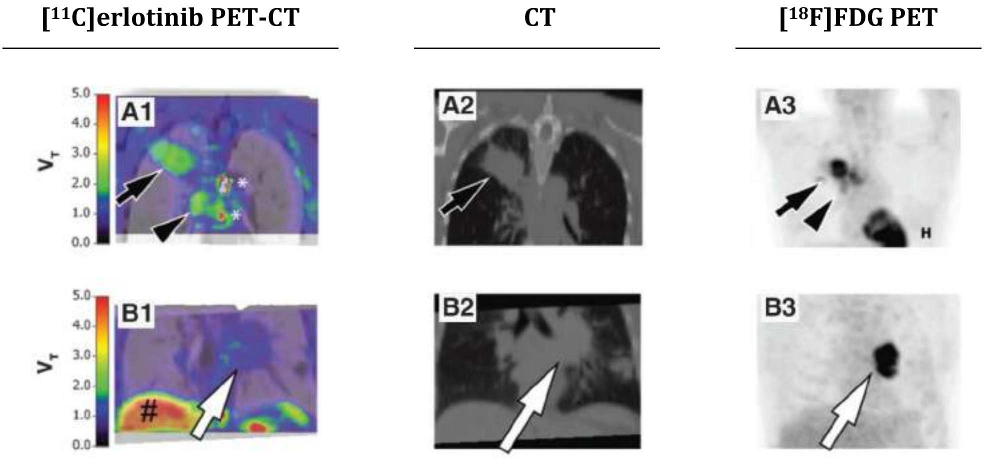

Figure 7: [^{11}C]erlotinib PET-CT scan (A1), CT-scan (A2) and [^{18}F]FDG PET scan (A3) of a patient harboring an exon 19 deleted tumor; [^{11}C]erlotinib PET-CT scan (B1), CT-scan (B2) and [^{18}F]FDG PET scan (B3) of a patient harboring a wild type tumor, where the mutated tumor shows clear uptake of [^{11}C]erlotinib. Figure adapted from [61].

Recently Bahce *et al*. also reported on a clinical PET study in NSCLC patients expressing mutated EGFR, in which [^{11}C]erlotinib uptake was compared in patients on erlotinib therapy and patients who were erlotinib naïve [66]. To our knowledge this is the first clinical example in which a radiolabeled TKI is dosed to patients on therapy with the same TKI. 10 patients were included, who either were planned to start erlotinib therapy or patients who stopped erlotinib therapy due to disease progression. This study demonstrated that therapeutically administered erlotinib (150 mg/kg) decreased [^{11}C]erlotinib uptake (although with high inter patient variability) consistent with the hypothesis that the therapeutic dose of erlotinib saturates the available binding sites. Preclinical studies with radiolabeled TKI show similar results with regard to decrease of uptake when therapeutic doses are co-administered [62]. Interestingly in patients on therapy residual tumor uptake could still be observed, which may indicate that heterogenous tumor targeting with erlotinib can be imaged with [^{11}C]erlotinib.

2.5 Lapatinib (Tykerb/Tyverb®)

Lapatinib is a reversible, dual EGFR/HER2 (IC_{50}: 10.8 / 9.2 nM) selective tyrosine kinase inhibitor used in the treatment of breast cancer. As with the previously discussed EGFR targeting molecules the core scaffold is in this case again a 4-anilinoquinazoline (**4**), the main structural difference is the bulky head group introduced on anilinoquinazoline moiety improving HER2 binding. It is hypothesized that this expansion is responsible for a relatively slow disassociation rate from the ATP binding pocket and subsequent prolonged inhibition of downstream signalling [67]. Lapatinib received FDA approval in 2007 for the treatment of advanced HER2-positive breast cancer in combination with capecitabine and is under investigation in other tumor types. Furthermore, recently it was demonstrated that mutations of HER2 in the kinase domain, analogous to EGFR mutations, demonstrate different sensitivity to lapatinib treatment. TKI-PET with radiolabeled lapatinib might therefore be a valuable tool for patient selection [68].

2.5.1 Tracer synthesis

Two reports on the radiolabeling of lapatinib (**19,** Scheme 4) have appeared in the literature employing multistep radiosynthethic sequences. The first concerns a 5 step synthesis starting with the preparation of *meta*-[^{18}F]fluorobenzylbromide [69, 70]. Microwave assisted nucleophilic fluorination on iodonium salt **14** provides *meta*-[^{18}F]fluorobenzaldehyde ([^{18}F]1**5**) which is purified and reduced to the corresponding alcohol [^{18}F]**16** (using $NaBH_4$) on one solid phase extraction cartridge and subsequently eluted for the final bromination to *meta*-[^{18}F]fluorobenzylbromide ([^{18}F]**17).** [^{18}F]Lapatinib is obtained by ether bond formation between [^{18}F]**17** and **18,** subsequent removal of the Boc protecting group, affording the product, after semi-preparative purification in decent radiochemical yield (8-12%, not corrected for decay), high radiochemical purity (>98%) and low specific activity (exact value not reported) in 140 minutes of synthesis time. The low specific activity could become a problem when imaging tumors with low receptor density.

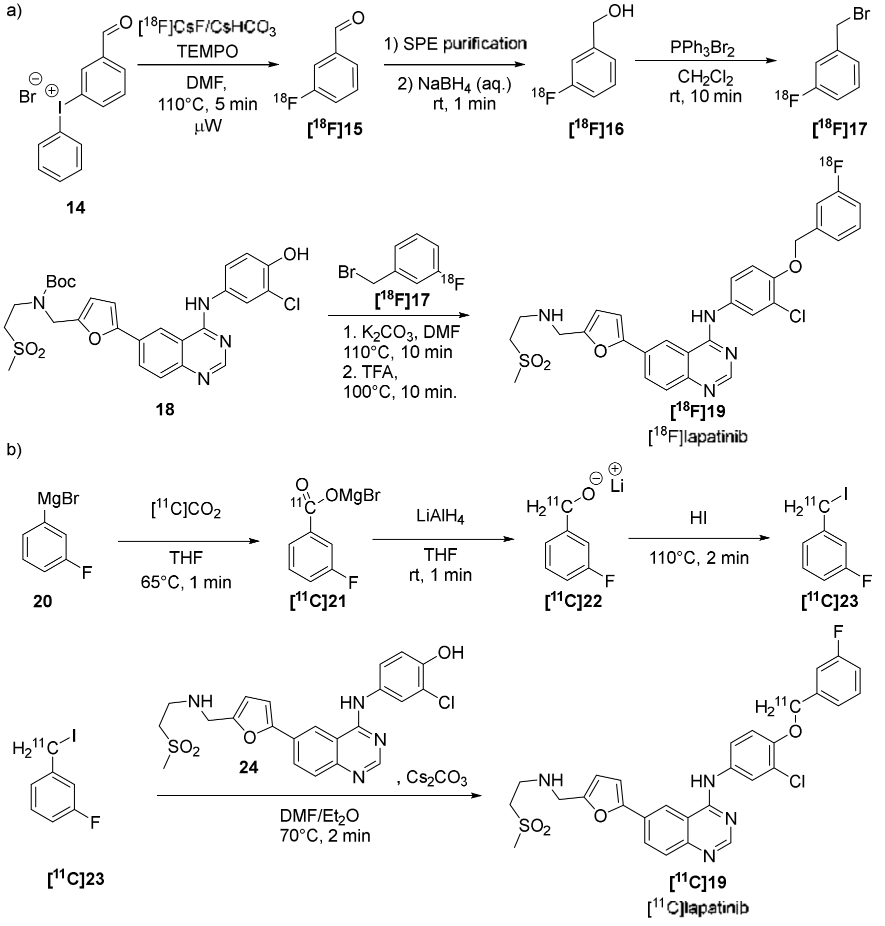

Scheme 4. Synthesis of radiolabeled lapatinib; a) synthesis of [^{18}F]lapatinib; b) Synthesis of [^{11}C]lapatinib

The second report concerns a carbon-11 labeled variant of lapatinib and starts with the synthesis of [^{11}C]*meta*-fluorobenzyliodide [71]. Cyclotron produced [^{11}C]CO_2 was reacted with *meta*-fluorophenylmagnesiumbromide (**20**), to obtain carboxylic acid [^{11}C]**21** which was subsequently reduced with lithiumaluminum hydride and directly iodinated to obtain [^{11}C]*meta*-fluorobenzyliodide ([^{11}C]**23**) after solid phase extraction. [^{11}C]**23** was reacted with **24** to afford [^{11}C]lapatinib in a yield of 1286 ± 572 MBq, 100% radiochemical purity and a specific activity of 66 ± 24 GBq/mmol.

2.5.2 In vivo evaluation

[^{11}C]lapatinib was evaluated in a small clinical trial to determine penetration in brain metastases of HER2-positive breast cancer patients [71]. In this study 6 patients were included, al diagnosed with HER2-positive breast cancer, however 3 with and 3 without brain metastases (determined by MRI). The patients received a baseline [^{11}C]lapatinib scan followed by therapeutic dosing with lapatinib (1500 mg, once daily) and another [^{11}C]lapatinib scan on day 8. Plasma analysis revealed excellent stability of the tracer with a mean of >83% intact tracer after 60 minutes. Brain uptake in normal brain tissue was not observed. Cranial metastases demonstrated higher uptake of [^{11}C]lapatinib on both baseline as well as follow-up scans compared to healthy brain tissue. Similar uptake on day 8 is remarkable as saturation of the receptor system could have been expected due to therapeutic dosing. The uptake in brain-metastases is most likely attributed to disruption of the Blood-Brain-Barrier (BBB) in these patients allowing for better tissue-penetration. Kinetic modelling was performed on the scans to correct for the blood contribution as a consequence of increased perfusion in the cranial metastasis (Figure 8). This indicated that the higher uptake in metastases was not related to an increase in perfusion due to loss of BBB integrity. Together this data suggest that lapatinib can play a role in the treatment of brain metastasis, however, this needs to be confirmed in larger clinical trials and the authors do not report on patient follow-up. Ostentatiously missing from this study is the evaluation of primary tumor uptake [^{11}C]lapatinib in the breast cancer lesions.

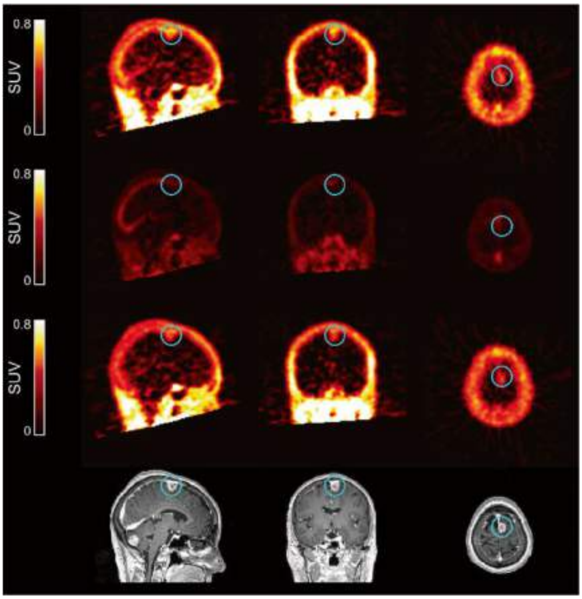

Figure 8: left: [^{11}C]lapatinib PET images of a patient with cranial metastasis (blue circle). Top: radioactivity distribution (uncorrected) and separated into non-blood (middle top) and blood (middle bottom). Bottom: contrast enhanced MRI delineating cranial metastasis. Figure adapted from [71].

2.6 Sorafenib (Nexavar®)

Sorafenib (**28**) is a broad spectrum kinase inhibitor approved for the treatment of advanced renal cell and hepatocellular carcinoma. Clinical studies regarding other solid tumors such as NSCLC are in progress. Sorafenib was discovered via a high throughput screen of 200.000 compounds, while searching for Raf (serine/threonine kinases), ERK (extracellular-signal related kinases) and MEK (involved in the MAPK pathway) inhibitors. A lead optimization study led to sorafenib (**28**) which proved to be a highly potent inhibitor of several kinases (amongst others: Raf1 kinase IC_{50} = 6 nM, wild-type B-Raf IC_{50} = 25 nM and VEGFR1 IC_{50} = 26 nM, for an overview see [7, 72]). After obtaining promising *in vivo* results in tumor bearing mice, sorafenib entered into a clinical trial comprising patients with several kinds of solid tumors.

Approval for the treatment of renal cell carcinoma came in 2005 followed by hepatocellular carcinoma in 2007 and thyroid cancer in 2013 [73, 74]. As sorafenib targets multiple kinases with different affinity, also for this drug TKI-PET can be very informative to learn about its targeting potential.

2.6.1 Tracer synthesis

A radiolabeled variant of sorafenib was reported first by Asakawa *et al.*, using [^{11}C]phosgene to introduce the label on the urea moiety of sorafenib (Scheme 5) [75]. The unsymmetrical urea moiety was constructed by reaction of two aniline derivatives (**25** and **27**) with phosgene in a stepwise manner. Initially the free amine of **25** was reacted with phosgene but this resulted in symmetrically substituted urea products due to the nucleophilicity of **25.** Reacting the less reactive hydrochloric acid salt of **25** afforded **26**, which smoothly afforded [^{11}C]sorafenib ([^{11}C]**28**) after reaction with aniline **27.** The product [^{11}C]**28** was obtained in 44% radiochemical yield (decay corrected), a radiochemical purity of >99%, and a specific activity of 20-56 GBq/μmol. Total synthesis time for [^{11}C]sorafenib was 40 minutes starting from EOB. Poot *et al.* reported two additional radiosyntheses for [^{11}C]sorafenib (Scheme 5) [76]. The first, a straightforward methylation reaction on desmethylsorafenib (**29**), with [^{11}C]MeI in the presence of a base, proceeding in a good radiochemical yield of 60% (decay corrected) affording the product in high purity (>99% radiochemical purity) and high specific activity (150-210 GBq/μmol) in 35 minutes of synthesis time. The second radiosynthesis concerns a carbonylation reaction to introduce the label on the urea moiety. In this case a rhodium mediated carbonylation was performed reacting azide **30** with analine **27** at 350 bar in a microautoclave to obtain [^{11}C]sorafenib in good yields for a carbonylation reaction (27% decay corrected). After purification the product is obtained in good purity (>95% radiochemical purity) and average specific activity (30-50 GBq/μmol) in 50 minutes of synthesis time. While the urea position of sorafenib is a chemically interesting position to radiolabel, this position could lead to the generation of radio-metabolites as this is more metabolically stabile then for example the methylamide. Interestingly, a method for labeling of the aromatic trifluoromethoxy group was recently reported, opening up avenues for a fluorine-18 labeled variant of sorafenib.[77, 78]

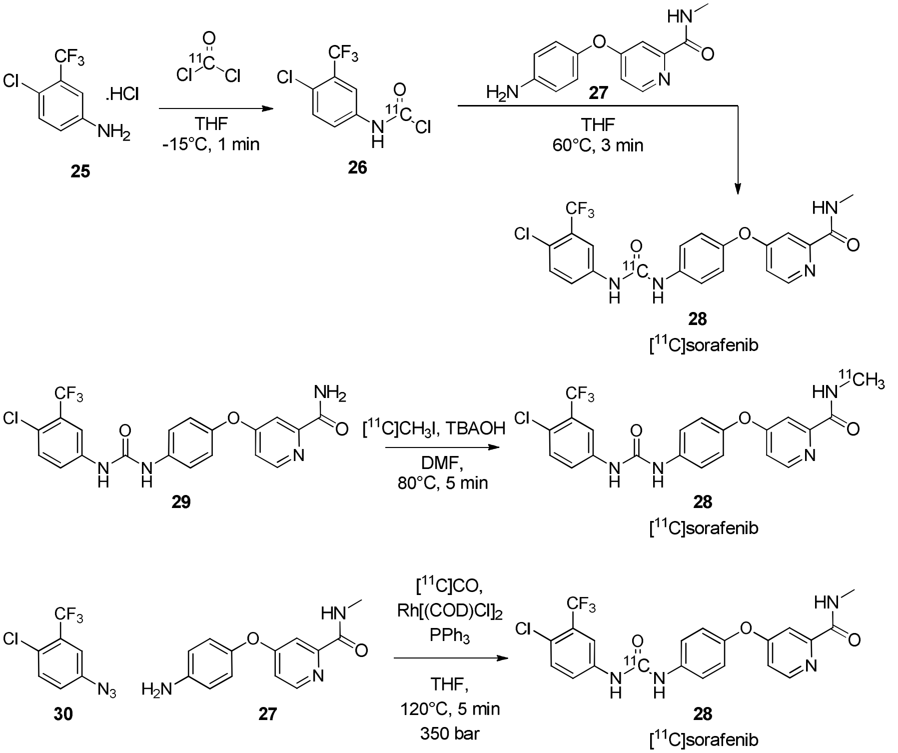

Scheme 5: Radiosyntheses of [^{11}C]sorafenib

2.6.2 In vivo evaluation

A metabolite analysis was not performed by Asakawa *et al.*, however, *in vivo* stability for both tracers developed by Poot *et al.* was determined and this demonstrated that [^{11}C]sorafenib labeled on either the urea- or methylamide moiety was intact for >90% at 45 minutes p.i.. Based on the higher specific activity, radiochemical yield and comparable stability, the methylamide was chose as a preferred labeling position and this tracer was subjected to *in vivo* evaluation.

[^{11}C]Sorafenib was evaluated *in vivo*, however, initially Asakawa *et al*. only performed a brain-uptake study using wild-type mice and P-gp/BCRP knock-out mice. A clear difference in brain uptake was observed with [^{11}C]sorafenib showing only uptake in the brain of knock-out mice. From these results the authors conclude that sorafenib is likely a substrate for BCRP as it was previously shown that it is not a good substrate for P-gp [75].

[^{11}C]sorafenib was more extensively evaluated by Poot *et al*. for its tumor targeting potential [76]. The main target of sorafenib is Raf-1 kinase and therefore tumor xenografts were selected based on the expression of this particular kinase via immunohistochemical analysis. Three xenografts lines were selected namely, FaDu, MDA-MB-231 and RXF393, all demonstrated expression of Raf-1 while it was most intense for the latter.

PET-imaging and biodistribution studies were performed with [^{11}C]sorafenib in mice bearing xenografts of the three mentioned cell lines. [^{18}F]FDG was used to delineate tumors and to check tumor viability. PET data analysis demonstrated the highest uptake in the RXF393 xenografts (Figure 9; 2.04 ± 0.37 %ID/g at 60 minutes p.i.), whereas no significant uptake (compared to reference tissue) was observed in the other xenograft lines. The PET data was confirmed by *ex-vivo* biodistribution data. This data demonstrates that [^{11}C]sorafenib has the potential as a PET-tracer for imaging Raf-1 kinase *in vivo* and warrants further evaluation as TKI-PET tracer clinically.

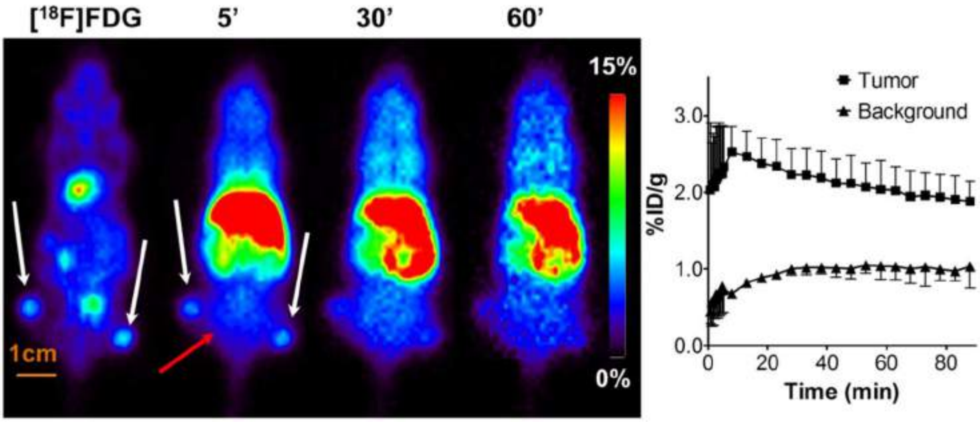

Figure 9: left: $[^{18}\text{F}]$FDG and $[^{11}\text{C}]$sorafenib PET images of a mouse bearing two RXF393 xenografts (white arrow indicates tumor position and background is indicated by a red arrow). right: Time-activity-curve of tumor and background tissue. Figure adapted from [76]

2.7 Other tyrosine kinase inhibitors

Two additional TKIs have been radiolabeled being sunitinib ([^{18}F]**32**), via a direct fluorination with fluorine-18 [79] and vandetanib via two carbon-11 methylations ([^{11}C]34) [80], radiosyntheses depicted in Scheme 6a,b. *In vivo* evaluation of these tracers has not been reported yet, but given the novelty of this field papers can be expected to appear in the coming years. Since 2005 seven of the twenty-two FDA approved TKI's have been radiolabeled for PET and (pre)clinical analyses are appearing in the literature, indicating the keen interest in the field of TKI-PET.

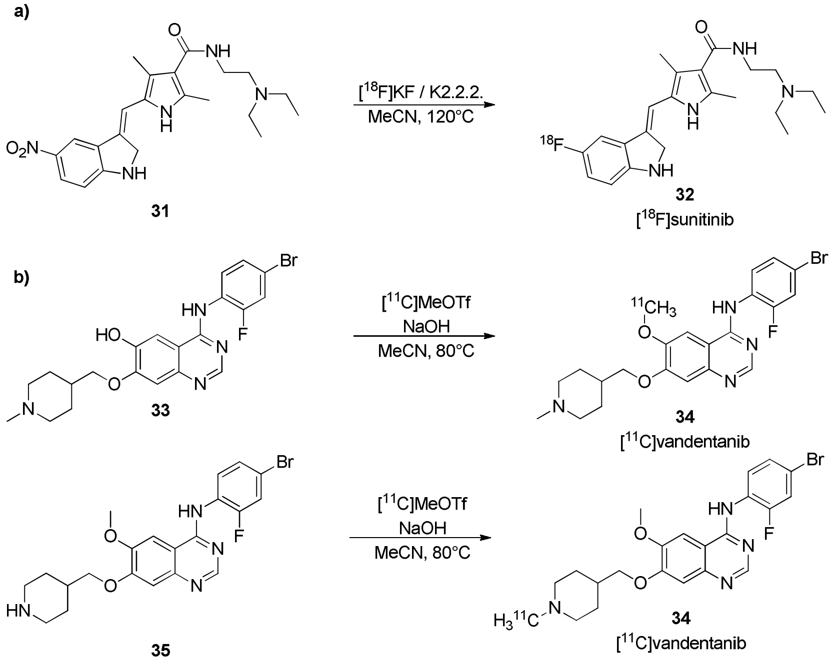

Scheme 6: Radiosynthesis of a) [^{18}F]sunitinib; b) [^{11}C]-*O*-vandetanib and [^{11}C]-*N*-vandetanib

2.8 Discussion

Several TKI-PET tracers have been developed, but unfortunately in some cases detailed evaluation of these tracers is lacking. [^{11}C]imatinib has been evaluated *in vivo*, however, the presence of radio-metabolites was not evaluated, neither the targeting properties of the tracer since the target was not present in the particular animal models. In the case of [^{11}C]sorafenib, a brain-uptake study has been performed and the preclinical tumor targeting has been established, making [^{11}C]sorafenib a candidate for clinical application. Thorough pre-clinical studies have been performed with [^{11}C]gefitinib, [^{18}F]gefitinib and [^{11}C]erlotinib, demonstrating the potential of these tracers. First, gefitinib was labeled both with fluorine-18 and carbon-11, providing the choice of the optimum tracer with respect to metabolism and half-life. Second, the preclinical validation experiments of gefitinib were designed very well, as the proper models were used to evaluate this tracer *in vivo*. The results of these studies indicate that clinical work with gefitinib would have poor perspectives and that labeled gefitinib is unsuitable for human use, as the human tumor xenografts show no uptake of the tracer. In contrast, preclinical experiments with [^{11}C]erlotinib showed very promising results, revealing higher accumulation in tumors with activating EGFR mutations than in tumors with wild-type EGFR. Next these promising pre-clinical results were confirmed in first proof-of-principle clinical trials [61, 65]. The ability to distinguish between responders and non-responders in this non-invasive manner can open new avenues towards personalized medicine. In the case of [^{11}C]lapatinib the first patient study has been reported, demonstrating targeting in cranial metastasis, however, primary tumor evaluation is lacking in this case [71].

It is vital that novel TKI-PET tracers are designed with care, retaining the native chemical structure but also successfully passing thorough metabolite analyses and biodistribution studies in relevant animal models before performing clinical studies. Ideally a preclinical TKI-PET study should involve the following stages. First, based on the chemical structure a suitable labeling position should be selected with regard to the PET isotope (fluorine-18 when possible or carbon-11) and metabolism.

In the selected cases that several positions are available ideally all of them are labeled and evaluated. Second a thorough radiometabolite analysis should be performed (for each labeling position) and on the basis of these first two criteria a tracer can be selected for *in vivo* evaluation. The *in vivo* analysis should contain a biodistribution in relevant human tumor models. Namely, one with high expression of the target (which can be confirmed by techniques such as immunohistochemistry or fluorescence assisted cell sorting, FACS), a negative control (which does not express the target) and when applicable, cell lines that harbor activating mutations. Finally PET imaging studies need to be performed in mouse-models with all of these cell lines to compare the imaging properties of the tracer across the different cell lines. Only after such properly performed preclinical validation studies, evaluation of the clinical feasibility of PET studies with the new TKI-PET tracers are justified. In these studies specificity and kinetics of target binding can be assessed. Furthermore, dosimetric analyses can be performed to estimate the radiation burden for the patient.

2.9 Conclusion

The TKI development process as a whole can benefit from TKI-PET, as it provides a straightforward tool to assess distribution, kinetics and tumor targeting. It can also provide a non-invasive prediction method to select patients that have the highest chance of benefit from treatment. The clinical success with [^{11}C]erlotinib is a mere first example of the potential of TKI-PET.

2.10 References

[1] Arora A and Scholar EM. Role of tyrosine kinase inhibitors in cancer therapy *J. Pharmacol. Exp. Ther.* **2005**, *315*, 971-979.

[2] Blume-Jensen P and Hunter T. Oncogenic kinase signalling *Nature* **2001**, *411*, 355-365.

[3] Heldin C-H. Dimerization of cell surface receptors in signal transduction *Cell* **1995**, *80*, 213-223.

[4] Zhang J, Yang PL, and Gray NS. Targeting cancer with small molecule kinase inhibitors *Nature* **2009**, *9*, 28-39.

[5] Janne PA, Gray N, and Settleman J. Factors underlying sensitivity of cancer to small molecules *Nat. Rev. Drug Discovery* **2009**, *8*, 709-723.

[6] Chow LQM and Eckhardt SG. Sunitinib: From rational design to clinical efficacy *J. Clin. Oncol.* **2007**, *25*, 884-896.

[7] Wilhelm S, Carter C, Lynch M, Lowinger T, Dumas J, Smith RA, et al. Discovery and development of sorafenib: a multikinase inhibitor for treating cancer *Nat. Rev. Drug Discovery* **2006**, *5*, 835-844.

[8] Mano M. The burden of scientific progress: Growing inequalities in the delivery of cancer care *Acta Oncol.* **2006**, *45*, 84-86.

[9] Rohren EM, Turkington TG, and Coleman RE. Clinical applications of PET in oncology *Radiology* **2004**, *231*, 305-332.

[10] Rudin M and Weissleder R. Molecular imaging in drug discovery and development *Nat. Rev. Drug Discovery* **2003**, *2*, 123-131.

[11] Wagner CC and Langer O. Approaches using molecular imaging technology — use of PET in clinical microdose studies *Adv. Drug Deliv. Rev.* **2011**, *63*, 539-546.

[12] Bergström M, Grahnén A, and Långström B. Positron emission tomography microdosing: a new concept with application in tracer and early clinical drug development *Eur. J. Clin. Pharmacol.* **2003**, *59*, 357-366.

[13] Lappin G and Garner RC. Big physics, small doses: the use of AMS and PET in human microdosing of development drugs *Nat. Rev. Drug Discov.* **2003**, *2*, 233-240.

[14] Gelovani J. Molecular imaging of epidermal growth factor receptor expression–activity at the kinase level in tumors with positron emission tomography *Cancer Metast. Rev.* **2008**, *27*, 645-653.

[15] Vugts DJ and van Dongen GAMS. ^{89}Zr-labeled compounds for PET imaging guided personalized therapy *Drug Discov. Today Tech.* **2011**, *8*, e53-e61.

[16] Glekas AP, Pillarsetty NK, Punzalan B, Khan N, Smith-Jones P, and Larson SM. *In vivo* imaging of BCR-ABl overexpressing tumors with a radiolabeled imatinib analog as an imaging surrogate for imatinib *J. Nucl. Med.* **2011**, *52*, 1301-1307.

[17] Mishani E and Hagooly A. Strategies for molecular imaging of epidermal growth factor receptor tyrosine kinase in cancer *J. Nucl. Med.* **2009**, *50*, 1199-1202.

[18] Tolmachev V, Stone-Elander S, and Orlova A. Radiolabelled receptor-tyrosine-kinase targeting drugs for patient stratification and monitoring of therapy response: Prospects and pitfalls *Lancet Oncol.* **2010**, *11*, 992-1000.

[19] Pal A, Glekas A, Doubrovin M, Balatoni J, Beresten T, Maxwell D, et al. Molecular imaging of EGFR kinase activity in tumors with ^{124}I-labeled small molecular tracer and positron emission tomography *Mol. Imaging Biol.* **2006**, *8*, 262-277.

[20] Abourbeh G, Dissoki S, Jacobson O, Litchi A, Daniel RB, Laki D, et al. Evaluation of radiolabeled ML04, a putative irreversible inhibitor of epidermal growth factor receptor, as a bioprobe for PET imaging of EGFR-overexpressing tumors *Nucl. Med. Biol.* **2007**, *34*, 55-70.

[21] Heuveling DA, de Bree R, and van Dongen GAMS. The potential role of non-FDG-PET in the management of head and neck cancer *Oral Oncol.* **2011**, *47*, 2-7.

[22] Yeh HH, Ogawa K, Balatoni J, Mukhapadhyay U, Pal A, Gonzalez-Lepera C, et al. Molecular imaging of active mutant L858R EGF receptor (EGFR) kinase-expressing nonsmall cell lung carcinomas using PET/CT *Proc. Natl. Acad. Sci. U.S.A.* **2011**, *108*, 1603-1608.

[23] van Dongen G, Poot A, and Vugts D. PET imaging with radiolabeled antibodies and tyrosine kinase inhibitors: immuno-PET and TKI-PET *Tumor Biol.* **2012**, *33*, 607-615.

[24] Kniess T. Radiolabeled small molecule inhibitors of VEGFR - recent advances *Curr. Pharm. Des.* **2012**, *18*, 2867-2874.

[25] Capdeville R, Buchdunger E, Zimmermann J, and Matter A. Glivec (STI571, imatinib), a rationally developed, targeted anticancer drug *Nat. Rev. Drug Discovery* **2002**, *1*, 493-502.

[26] Nowell PC and Hungeford DA. A minute chromosome in human chronic granulocytic leukemia *Science* **1960**, *132*, 1497-1501.

[27] Daley G, Van Etten R, and Baltimore D. Induction of chronic myelogenous leukemia in mice by the P210BCR/ABl gene of the philadelphia chromosome *Science* **1990**, *247*, 824-830.

[28] Kil K-E, Ding Y-S, Lin K-S, Alexoff D, Kim SW, Shea C, et al. Synthesis and positron emission tomography studies of carbon-11-labeled Imatinib (Gleevec) *Nucl. Med. Biol.* **2007**, *34*, 153-163.

[29] Långström B, Itsenko O, and Rahman O. [^{11}C]Carbon monoxide, a versatile and useful precursor in labelling chemistry for PET-ligand development *J. Labelled Compd. Radiopharm.* **2007**, *50*, 794-810.

[30] Gschwind H-P, Pfaar U, Waldmeier F, Zollinger M, Sayer C, Zbinden P, et al. Metabolism and disposition of imatninb mesylate in healthy volunteers *Drug Metab. Dispos.* **2005**, *33*, 1503-1512.

[31] Rochat B, Fayet A, Widmer N, Lahrichi SL, Pesse B, Décosterd LA, et al. Imatinib metabolite profiling in parallel to imatinib quantification in plasma of treated patients using liquid chromatography–mass spectrometry *J. Mass Spectrom.* **2008**, *43*, 736-752.

[32] Breedveld P, Pluim D, Cipriani G, Wielinga P, van Tellingen O, Schinkel AH, et al. The effect of BCRP1 (ABCG2) on the *in vivo* pharmacokinetics and brain penetration of imatinib mesylate (Gleevec): implications for the use of breast cancer resistance protein and P-glycoprotein inhibitors to enable the brain penetration of imatinib in patients *Cancer Res.* **2005**, *65*, 2577-2582.

[33] Buck AK, Bommer M, Juweid ME, Glatting G, Stilgenbauer S, Mottaghy FM, et al. First demonstration of leukemia imaging with the proliferation marker ^{18}F-fluorodeoxythymidine *J. Nucl. Med.* **2008**, *49*, 1756-1762.

[34] Wakeling AE, Guy SP, Woodburn JR, Ashton SE, Curry BJ, Barker AJ, et al. ZD1839 (Iressa): an orally active inhibitor of epidermal growth factor signaling with potential for cancer therapy *Cancer Res.* **2002**, *62*, 5749-5754.

[35] Gorzalczany Y, Gilad Y, Amihai D, Hammel I, Sagi-Eisenberg R, and Merimsky O. Combining an EGFR directed tyrosine kinase inhibitor with autophagy-inducing drugs: A beneficial strategy to combat non-small cell lung cancer *Cancer Lett.* **2011**, *310*, 207-215.

[36] Amann J, Kalyankrishna S, Massion PP, Ohm JE, Girard L, Shigematsu H, et al. Aberrant epidermal growth factor receptor signaling and enhanced sensitivity to EGFR Inhibitors in lung cancer *Cancer Res.* **2005**, *65*, 226-235.

[37] Lynch TJ, Bell DW, Sordella R, Gurubhagavatula S, Okimoto RA, Brannigan BW, et al. Activating mutations in the epidermal growth factor receptor underlying responsiveness of non-small-cell lung cancer to Gefitinib *N. Engl. J. Med.* **2004**, *350*, 2129-2139.

[38] Yun C-H, Mengwasser KE, Toms AV, Woo MS, Greulich H, Wong K-K, et al. The T790M mutation in EGFR kinase causes drug resistance by increasing the affinity for ATP *Proc. Natl. Acad. Sci. U.S.A.* **2008**, *105*, 2070-2075.

[39] Paez JG, Jänne PA, Lee JC, Tracy S, Greulich H, Gabriel S, et al. EGFR mutations in lung cancer: Correlation with clinical response to Gefitinib therapy *Science* **2004**, *304*, 1497-1500.

[40] Sordella R, Bell DW, Haber DA, and Settleman J. Gefitinib-sensitizing EGFR mutations in lung cancer activate anti-apoptotic pathways *Science* **2004**, *305*, 1163-1167.

[41] Mulloy R, Ferrand A, Kim Y, Sordella R, Bell DW, Haber DA, et al. Epidermal growth factor receptor mutants from human lung cancers exhibit enhanced catalytic activity and increased sensitivity to gefitinib *Cancer Res.* **2007**, *67*, 2325-2330.

[42] Wakeling AE, Barker AJ, Davies DH, Brown DS, Green LR, Cartlidge SA, et al. Specific inhibition of epidermal growth factor receptor tyrosine kinase by 4-anilinoquinazolines *Breast Cancer Res. Treat.* **1996**, *38*, 67-73.

[43] Ward WHJ, Cook PN, Slater AM, Davies DH, Holdgate GA, and Green LR. Epidermal growth factor receptor tyrosine kinase: Investigation of catalytic mechanism, structure-based searching and discovery of a potent inhibitor *Biochem. Pharmacol.* **1994**, *48*, 659-666.

[44] Barker AJ, Gibson KH, Grundy W, Godfrey AA, Barlow JJ, Healy MP, et al. Studies leading to the identification of ZD1839 (Iressa™): An orally active, selective epidermal growth factor receptor tyrosine kinase inhibitor targeted to the treatment of cancer *Bioorg. Med. Chem. Lett.* **2001**, *11*, 1911-1914.

[45] Ciardiello F, Caputo R, Bianco R, Damiano V, Fontanini G, Cuccato S, et al. Inhibition of growth factor production and angiogenesis in human cancer cells by ZD1839 (Iressa), a selective epidermal growth factor receptor tyrosine kinase inhibitor *Clin. Cancer Res.* **2001**, *7*, 1459-1465.

[46] Seimbille Y, Phelps ME, Czernin J, and Silverman DHS. Fluorine-18 labeling of 6,7-disubstituted anilinoquinazoline derivatives for positron emission tomography (PET) imaging of tyrosine kinase receptors: synthesis of [^{18}F]Iressa and related molecular probes *J. Labelled Compd. Radiopharm.* **2005**, *48*, 829-843.

[47] Läppchen T, Vlaming MLH, Custers E, Lub J, Sio CF, DeGroot J, et al. Automated synthesis of [^{18}F]gefitinib on a modular system *Appl. Radiat. Isot.* **2012**, *70*, 205-209.

[48] Wang J-Q, Gao M, Miller KD, Sledge GW, and Zheng Q-H. Synthesis of [^{11}C]Iressa as a new potential PET cancer imaging agent for epidermal growth factor receptor tyrosine kinase *Bioorg. Med. Chem. Lett.* **2006**, *16*, 4102-4106.

[49] Holt DP, Ravert HT, Dannals RF, and Pomper MG. Synthesis of [^{11}C]gefitinib for imaging epidermal growth factor receptor tyrosine kinase with positron emission tomography *J. Labelled Compd. Radiopharm.* **2006**, *49*, 883-888.

[50] Zhang M-R, Kumata K, Hatori A, Takai N, Toyohara J, Yamasaki T, et al. [^{11}C]gefitinib ([^{11}C]Iressa): Radiosynthesis, *in vitro* uptake, and *in vivo* of imaging of intact murine fibrosarcoma *Mol. Imaging Biol.* **2010**, *12*, 181-191.

[51] Su H, Seimbille Y, Ferl G, Bodenstein C, Fueger B, Kim K, et al. Evaluation of [^{18}F]gefitinib as a molecular imaging probe for the assessment of the epidermal

growth factor receptor status in malignant tumors *Eur. J. Nucl. Med. Mol. Imaging* **2008**, *35*, 1089-1099.

[52] Doyle LA and Ross DD. Multidrug resistance mediated by the breast cancer resistance protein BCRP (ABCG2) *Oncogene* **2003**, *22*, 7340-7358.

[53] Kawamura K, Yamasaki T, Yui J, Hatori A, Konno F, Kumata K, et al. *In vivo* evaluation of P-glycoprotein and breast cancer resistance protein modulation in the brain using [^{11}C]gefitinib *Nucl. Med. Biol.* **2009**, *36*, 239-246.

[54] Moyer JD, Barbacci EG, Iwata KK, Arnold L, Boman B, Cunningham A, et al. Induction of apoptosis and cell cycle arrest by CP-358774, an inhibitor of epidermal growth factor receptor tyrosine kinase *Cancer Res.* **1997**, *57*, 4838-4848.

[55] Dowell J, Minna JD, and Kirkpatrick P. Erlotinib hydrochloride *Nat. Rev. Drug Discovery* **2005**, *4*, 13-14.

[56] Pao W, Miller V, Zakowski M, Doherty J, Politi K, Sarkaria I, et al. EGF receptor gene mutations are common in lung cancers from "never smokers" and are associated with sensitivity of tumors to Gefitinib and Erlotinib *Proc. Natl. Acad. Sci. U.S.A.* **2004**, *101*, 13306-13311.

[57] Pao W and Miller VA. Epidermal growth factor receptor mutations, small-molecule kinase inhibitors, and non–small-cell lung cancer: Current knowledge and future directions *J. Clin. Oncol.* **2005**, *23*, 2556-2568.

[58] Shepherd FA, Rodrigues Pereira J, Ciuleanu T, Tan EH, Hirsh V, Thongprasert S, et al. Erlotinib in previously treated non–small-cell lung cancer *N. Engl. J. Med.* **2005**, *353*, 123-132.

[59] Wang Y, Schmid-Bindert G, and Zhou C. Erlotinib in the treatment of advanced non-small cell lung cancer: an update for clinicians *Ther. Adv. Med. Oncol.* **2012**, *4*, 19-29.

[60] Memon AA, Jakobsen S, Dagnaes-Hansen F, Sorensen BS, Keiding S, and Nexo E. Positron emission tomography (PET) imaging with [^{11}C]-labeled erlotinib: A micro-PET study on mice with lung tumor xenografts *Cancer Res.* **2009**, *69*, 873-878.

[61] Bahce I, Smit EF, Lubberink M, van der Veldt AAM, Yaqub M, Windhorst AD, et al. Development of [^{11}C]erlotinib Positron Emission Tomography for *in vivo* evaluation of EGF receptor mutational status *Clin. Cancer Res.* **2013**, *19*, 183-193.

[62] Petrulli JR, Sullivan JM, Zheng M-Q, Bennett DC, Charest J, Huang Y, et al. Quantitative analysis of [^{11}C]-erlotinib PET demonstrates specific binding for activating mutations of the EGFR kinase domain *Neoplasia* **2013**, *15*, 1347-1353.

[63] Abourbeh G, Itamar B, Salnikov O, Beltsov S, and Mishina E. Identifying erlotinib-sensitive non-small cell lung carcinoma tumors in mice using [^{11}C]erlotinib PET *Eur. J. Nucl. Med. Mol. Imaging: Res* **2015**, *5*.

[64] Weber B, Winterdahl M, Memon A, Sorensen BS, Keiding S, Sorensen L, et al. Erlotinib accumulation in brain metastases from non-small cell lung cancer: Visualization by positron emission tomography in a patient harboring a mutation in the epidermal growth factor receptor *J. Thorac. Oncol.* **2011**, *6*, 1287-1289.

[65] Memon AA, Weber B, Winterdahl M, Jakobsen S, Meldgaard P, Madsen HHT, et al. PET imaging of patients with non-small cell lung cancer employing an EGF receptor targeting drug as tracer *Br. J. Cancer* **2011**, *105*, 1850-1855.

[66] Bahce I, Yaqub M, Errami H, Schuit RC, Schober P, Thunnissen E, et al. Effects of erlotinib therapy on [11C]erlotinib uptake in EGFR mutated, advanced NSCLC *EJNMMI Research* **2016**, *6*, 1-13.

[67] Tevaarwerk AJ and Kolesar JM. Lapatinib: A small-molecule inhibitor of epidermal growth factor receptor and human epidermal growth factor receptor—2 tyrosine kinases used in the treatment of breast cancer *Clin. Ther.* **2009**, *31, Part 2*, 2332-2348.

[68] Kancha RK, von Bubnoff N, Bartosch N, Peschel C, Engh RA, and Duyster J. Differential Sensitivity of ERBB2 Kinase Domain Mutations towards Lapatinib *PLoS ONE* **2011**, *6*, e26760.

[69] Basuli F, Wu H, Li C, Shi Z-D, Sulima A, and Griffiths GL. A first synthesis of ^{18}F-radiolabeled Lapatinib: a potential tracer for positron emission tomographic imaging of ErbB1/ErbB2 tyrosine kinase activity *J. Labelled Compd. Radiopharm.* **2011**, *54*, 633-636.

[70] Basuli F, Wu H, and Griffiths GL. Syntheses of meta-[^{18}F]fluorobenzaldehyde and meta-[^{18}F]fluorobenzylbromide from phenyl(3-Formylphenyl) iodonium salt precursors *J. Labelled Compd. Radiopharm.* **2011**, *54*, 224-228.

[71] Saleem A, Searle GE, Kenny LM, Huiban M, Koslowski K, Waldman AD, et al. Lapatinib access into normal brain and brain metastases in patients with Her-2 overexpressing breast cancer *Eur. J. Nucl. Med. Mol. Imaging: Res* **2015**, *5*.

[72] Wilhelm SM, Adnane L, Newell P, Villanueva A, Llovet JM, and Lynch M. Preclinical overview of sorafenib, a multikinase inhibitor that targets both Raf and VEGF and PDGF receptor tyrosine kinase signaling *Mol. Cancer Ther.* **2008**, *7*, 3129-3140.

[73] Takimoto C and Awada A. Safety and anti-tumor activity of sorafenib (Nexavar®) in combination with other anti-cancer agents: a review of clinical trials *Cancer Chemother. Pharmacol.* **2008**, *61*, 535-548.

[74] Brose MS, Nutting CM, Jarzab B, Elisei R, Siena S, Bastholt L, et al. Sorafenib in radioactive iodine-refractory, locally advanced or metastatic differentiated thyroid cancer: a randomised, double-blind, phase 3 trial *The Lancet*, *384*, 319-328.

[75] Asakawa C, Ogawa M, Kumata K, Fujinaga M, Kato K, Yamasaki T, et al. [^{11}C]Sorafenib: Radiosynthesis and preliminary PET study of brain uptake in P-gp/BCRP knockout mice *Bioorg. Med. Chem. Lett.* **2011**, *21*, 2220-2223.

[76] Poot AJ, van der Wildt B, Stigter-van Walsum M, Rongen M, Schuit RC, Hendrikse NH, et al. [^{11}C]Sorafenib: Radiosynthesis and preclinical evaluation in tumor-bearing mice of a new TKI-PET tracer *Nucl. Med. Biol.* **2013**, *40*, 488-497.

[77] Huiban M, Tredwell M, Mizuta S, Wan Z, Zhang X, Collier TL, et al. A broadly applicable [^{18}F]trifluoromethylation of aryl and heteroaryl iodides for PET imaging *Nat. Chem.* **2013**, *5*, 941-944.

[78] van der Born D, Sewing C, Herscheid JDM, Windhorst AD, Orru RVA, and Vugts DJ. A universal procedure for the [^{18}F]trifluoromethylation of aryl iodides and aryl boronic acids with highly improved specific activity *Angew. Chem. Int. Ed.* **2014**, *53*, 11046-11050.

[79] Wang J-Q, Miller KD, Sledge GW, and Zheng Q-H. Synthesis of [^{18}F]SU11248, a new potential PET tracer for imaging cancer tyrosine kinase *Bioorg. Med. Chem. Lett.* **2005**, *15*, 4380-4384.

[80] Gao M, Lola CM, Wang M, Miller KD, Sledge GW, and Zheng Q-H. Radiosynthesis of [^{11}C]vandetanib and [^{11}C]chloro-vandetanib as new potential PET agents for imaging of VEGFR in cancer *Bioorg. Med. Chem. Lett.* **2011**, *21*, 3222-3226.

Chapter 3

Development of [^{18}F]afatinib as new TKI-PET tracer for EGFR positive tumors

P. Slobbe, A.D. Windhorst, M. Stigter-van Walsum, R.C. Schuit, E.F. Smit,
H.G. Niessen, F. Solca, G. Stehle, G.A.M.S van Dongen and A.J. Poot

Published in: *Nuclear Medicine and Biology,* ***2014****, 41, 749-757*

Abstract

Background: Afatinib is an irreversible ErbB family blocker that was approved for the treatment of EGFR mutated non-small cell lung cancer in 2013. Positron emission tomography (PET) with fluorine-18 labeled afatinib provides a means to obtain improved understanding of afatinib tumor disposition *in vivo*. PET imaging with [^{18}F]afatinib may also provide a method to select treatment responsive patients. The aim of this study was to label afatinib with fluorine-18 and evaluate its potential as TKI-PET tracer in tumor bearing mice.

Methods: A radiochemically novel coupling, using peptide coupling reagent BOP, was explored and optimized to synthesize [^{18}F]afatinib, followed by a metabolite analysis and biodistribution studies in two clinically relevant lung cancer cell lines, xenografted in nude mice.

Results: A reliable [^{18}F]afatinib radiosynthesis was developed and the tracer could be produced in yields of 17.0 ± 2.5% calculated from [^{18}F]F$^-$ and >98% purity. The identity of the product was confirmed by co-injection on HPLC with non-labeled afatinib. Metabolite analysis revealed a moderate rate of metabolism, with >80% intact tracer in plasma at 45 minutes p.i.. Biodistribution studies revealed rapid tumor accumulation and good retention for a period of at least 2 h, while background tissues showed rapid clearance of the tracer.

Conclusions: We have developed a method to synthesize [^{18}F]afatinib and related fluorine-18 labeled 4-anilinoquinazolines. [^{18}F]afatinib showed good stability *in vivo*, justifying further evaluation as a TKI-PET tracer.

3.1 Introduction

Recent advances in molecular biology have led to an increased understanding of the signaling transduction pathways in cancer, where crucial molecular targets have been identified that are involved in cancer growth, survival and metastasis. This knowledge has led to the development of tailor-made targeted pharmaceuticals designed to be particularly effective as anticancer agents. Receptor tyrosine kinases (RTKs) form a family of transmembrane proteins that play a pivotal role in the signal transduction pathways of the cell. RTKs consist of an extracellular domain that activates the intracellular domain for downstream signaling upon ligand binding. Prominent members of this family include the epidermal growth factor receptor (EGFR) and the vascular endothelial growth factor receptor (VEGFR). Upon ligand binding the RTK oligomerizes and autophosphorylation of intracellular tyrosine residues occurs, which in turn stimulates downstream signalling leading to proliferation, angiogenesis and consequently affecting cell survival [1, 2].

Two main categories of RTK targeting drugs are currently on the market; the first are monoclonal antibody based drugs that bind to the extracellular domain and thereby compete with the endogenous ligand for receptor activation. The second type of drugs are small molecule inhibitors acting intracellularly mainly by competing for ATP (adenosine triphosphate) at its binding site on the catalytic kinase domain, thereby disrupting downstream signaling. To date, 22 small molecule tyrosine kinase inhibitors (TKIs) have been approved by the US Food and Drug Administration. Furthermore, several dozens of TKIs are estimated to be in (pre)-clinical development [3]. Therefore, methodologies allowing fast and efficient testing of these drug candidates are of great importance and can possibly accelerate drug development which ultimately will benefit patients in need of these new therapies. In general, tests that can predict which patient will respond to therapy, are rarely available with the exception of EGFR mutation testing that is associated with effectiveness in non-small cell lung cancer (NSCLC) [4-6]. However, for assessment of RTK expression and mutational status an invasive biopsy is required, which is not always possible. Even when a biopsy is available it may be questionable whether or not this is sufficient to obtain an overview of the complete, often genetically heterogeneous tumor. Moreover, it is possible that the mutation status differs between primary tumor and metastatic lesions. Finally, even when a RTK is overexpressed this does not guarantee efficient tumor targeting by the TKI of choice. Therefore, a non-invasive patient selection tool capable to surmount some of the shortcomings would be highly attractive in the age of precision medicine.

With respect to EGFR, several mutations associated with sensitivity and/or resistance to treatment with small molecules (such as erlotinib and gefitinib), have been identified. Chief amongst the sensitizing mutations are small in-frame deletions in exon 19 (45%) or the L858R missense mutation (40-45%) in exon 21 leading to favorable response rates to EGFR TKI's [7]. However, despite initial good response, most patients invariably develop resistance against TKIs, half of these by the occurrence of another point mutation, i.e. the exon 20 T790M mutation [8].

Several TKIs have been labeled with PET-isotopes, although the preclinical analysis is in some cases incomplete. Various reviews have been written on the opportunities and challenges of TKI-PET imaging [9-11]. In addition, studies were performed using analogs of clinically used TKIs [12-22]. Radiotracers that have the exact structure of FDA approved TKIs, however, can be quickly applied clinically without the need for additional toxicology studies, thereby boosting translational research [23, 24]. The best example is [^{11}C]erlotinib, that showed good tumor accumulation in xenograft bearing mice, but only in treatment sensitive tumor models harboring the relevant mutations in the ATP binding domain of the kinase. [25] Encouraged by these promising results first-in-human studies were performed, showing the ability to distinguish between responding and non-responding patients based on [^{11}C]erlotinib tumor accumulation [26, 27].

Afatinib (**1**, Giotrif/Gilotrif®, Boehringer Ingelheim) is a 4-anilinoquinazoline, designed as irreversible ErbB family blocker inhibiting the enzymatic activity of EGFR, HER2 and ErbB4 [28]. By virtue of its Michael acceptor moiety (Figure 1) it is an irreversible inhibitor of EGFR, which acts by covalent binding to a cysteine residue in the ATP binding domain of EGFR, HER2 and HER4 (Cys 797, Cys 805 and Cys 803 respectively) [28, 29].

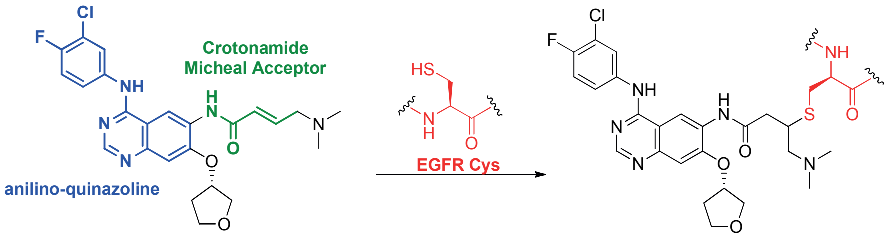

Afatinib, BIBW2992 (1)

2

Figure 1: Covalent modification of ATP-binding site of EGFR via a Michael addition of Cys797

Afatinib has been approved for the treatment of patients with metastatic NSCLC whose tumors harbor EGFR activating mutations. As indicated before, current clinical practice to determine the mutational status is by an invasive biopsy of the tumor tissue followed by DNA analysis using for instance the FDA approved *therascreen*® EGFR RGQ PCR Kit (QIAGEN). Clinical studies with afatinib have demonstrated that patients with EGFR mutations significantly benefit from treatment with afatinib compared to combination chemotherapy with pemetrexed and cisplatin [6].

Encouraged by previously reported results obtained in EGFR mutant NSCLC models [25], we envision that PET imaging of TKIs (TKI-PET) is a suitable and non-invasive tool to address tumor targeting and possibly patient selection. By labeling the native structure of a TKI with a PET-isotope, these compounds can be used to follow the *in vivo* biodistribution, pharmacokinetics (at tracer level), off-target binding and more importantly tumor targeting of the therapeutic itself. Therefore, it is of vital importance that the structure of the TKI is not altered by radiolabeling [3, 9, 10]. This can additionally provide direct access to clinical application of the tracer, which is of great value in an age of personalized medicine. Ultimately this strategy may provide insight into the *in vivo* behavior of these targeted therapeutics and their efficacy and might provide a manner to select patients that will benefit of treatment. For future drug development, TKI-PET imaging might also be applied to novel clinical candidates, possibly facilitating go/no-go decisions during a crucial stage of drug development. It is however of great importance that no structural alterations are introduced in the drug by labeling with a PET-isotope, to have a representative overview of the drugs behavior *in vivo.*

The aim of this study was to develop a reliable synthesis route to obtain fluorine-18 labeled afatinib and perform an initial preclinical analysis *in vivo* to ascertain whether this compound has potential as TKI-PET tracer.

3.2 Results and discussion

3.2.1 Chemistry

Initially our strategy for the synthesis of [^{18}F]afatinib was analogous to the procedure reported by Seimbille *et al.* for fluorine-18 labeling of 6,7 disubstituted anilinoquinazoline derivatives [30]. This strategy entails a three step radio-synthesis with as key step a condensation between a fluorine-18 labeled aniline and an aromatic chloride. Due to the effectiveness of this strategy as well as the availability of a completely automated synthesis [31], we set out to synthesize the required chloro-quinazoline **14** as desired precursor.

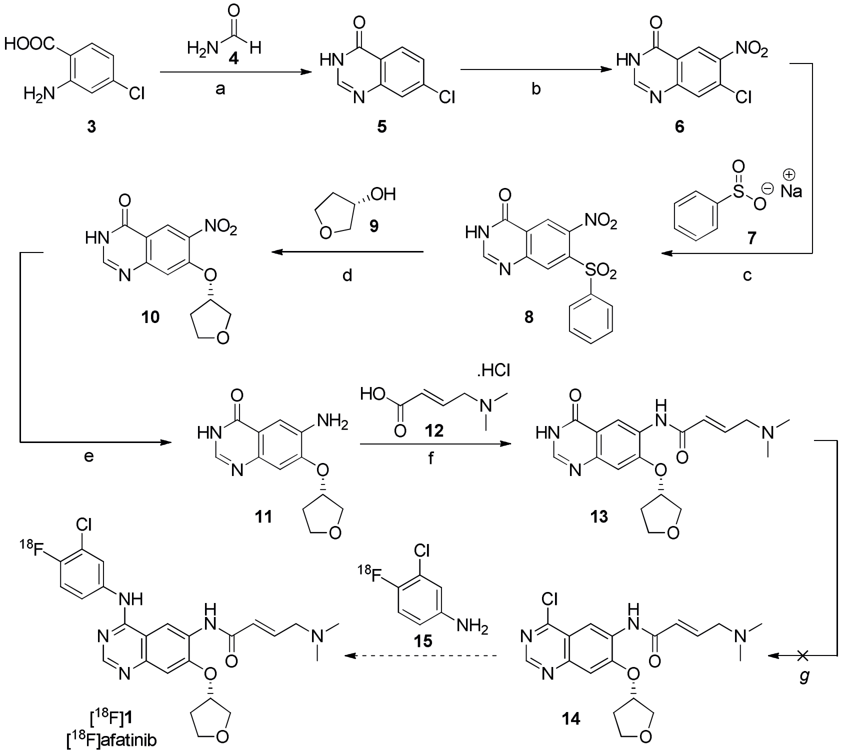

Scheme 1: Synthesis of [^{18}F]afatinib and precursor; reagents and conditions: (a) neat, 16 hours, 180°C, 78%; (b) HNO_3, H_2SO_4, 16 hours, rt, 67%; (c) DMF, 6 hours, 90°C, 97%; (d) KO*t*Bu, *t*BuOH, DMF; 24 hours, rt, 75%; (e) Fe(s), AcOH, EtOH, H_2O, 20 minutes, reflux, 99%; (f) First, 12 then $(COCl)_2$, then amine **11**, 4 hours, 0-25°C, 90%; (g) $SOCl_2$, $POCl_3$ or $(COCl)_2$

The synthesis of chloro-quinazoline **14** was adapted from the patented synthesis for afatinib [32]. Commercially available 2-amino-4-chloro-benzoic (**3**) acid was condensed with formamide at elevated temperatures to obtain de bicyclic quinazolone **5** in 78%. The subsequent nitration was achieved by a mixture of fuming nitric acid and sulfuric acid to obtain 2 regioisomers of the nitrated product. The desired regio-isomer **6** was readily obtained via recrystallization from hot acetic acid in 67% yield. The next step in the synthesis was the introduction of the enantiopure tetrahydrofuranoxy moiety. Initially we attempted a direct aromatic substitution on **6** in the presence of base, however, this proved to be unsuccessful. A more suitable leaving group was obtained by reaction of **6** with sodium benzenesulfinate (**7**) in quantitative yields and subsequent substitution with the alcohol provided the desired tetrafuranoxyquinazolone derivative **10** in 75% yield. The nitro-group was smoothly reduced by iron powder/acetic acid to the corresponding amine (**11**). Next, was the introduction of the crotonamide Michael acceptor side chain, which was proved to be challenging. Introduction was finally achieved by conversion of commercially available (*E*)-4-(dimethylamino)but-2-enoic acid hydrochloride (**12**) to its corresponding acid chloride *in situ* with oxalylchloride and direct coupling to the amine of **11** in satisfying yield. The final step in the planned precursor synthesis was the chlorination of **13.** Unfortunately, despite the use of several chlorinating reagents, such as thionyl-, phosphoryl- and oxalylchloride, and variation of the reaction conditions we were unable to isolate the desired precursor. Rapid hydrolysis or methanolysis was observed upon work-up/purification, making this compound unsuitable as labeling precursor. Since the desired precursor **14** could not be obtained, it was decided to investigate the possible coupling of cyclic amide **13** to [^{18}F]**15** in order to obtain [^{18}F]afatinib, since cyclic amide **13** proved to be a stable compound

Wan *et al*. recently reported an efficient one step amination of cyclic amides and cyclic ureas using a peptide coupling reagent (BOP, Benzotriazole-1-yl-oxy-tris-(dimethylamino)-phosphonium hexafluorophosphate) for conventional organic synthesis [33]. As this reaction also tolerates anilines and we already had the cyclic amide precursor in hand, we estimated this as a possible alternative for radiolabeling. However, as described by Wan *et al.* the reaction requires prolonged heating and excess amounts of the nucleophile, both of which are unsuitable for radiolabeling. Therefore, we adapted this synthesis method to the unique circumstances that are required for radiochemistry, being the use of low non-stoichiometrical amounts of precursor and the required fluorine-18 synthon as well as short reaction times.

3.2.2 Radiochemistry

In order to adapt the method described by Wan *et al.*, a reliable synthesis of the appropriate fluorine-18 labeled aniline had to be prepared. The synthesis of 3-chloro-4-[^{18}F]fluoroaniline ([^{18}F]**15**) has been described thoroughly in literature and is depicted in Scheme 2 [30, 31].

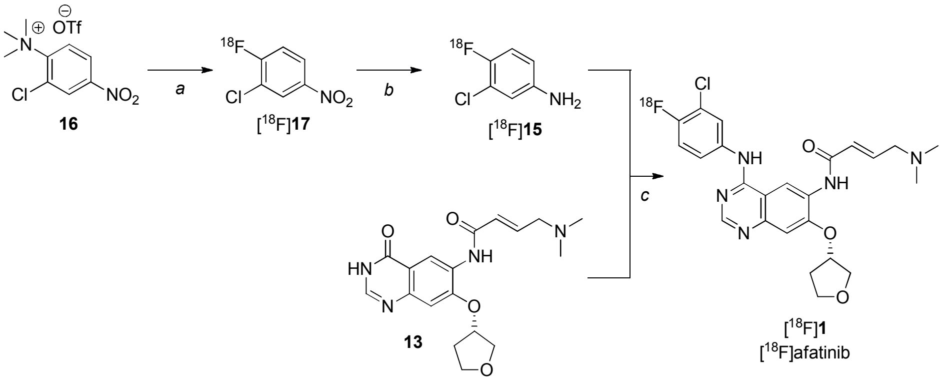

Scheme 2: Synthesis of [^{18}F]**1** ; reagents and conditions: (a) [^{18}F]F$^-$, K_2CO_3, K[2.2.2], MeCN, 25 minutes, 40°C; (b) $NaBH_4$, Pd/C, MeOH, 7 minutes, rt; (c) BOP, DBU, NMP, 30 minutes, 120°C.

The preparation of 3-chloro-4-[^{18}F]fluoronitroaniline (**15**) starts with nucleophilic fluorination of 3-chloro-4-trimethylammonium-nitrobenzene triflate (**16**) using described ^{18}F-fluorination conditions (kryptofix, K_2CO_3) at 40°C for 25 minutes, to afford 3-chloro-4-[^{18}F]fluoronitrobenzene ([^{18}F]**17**) in a radiochemical yield of 82.6% ± 3.6% (corrected for decay) after solid phase extraction purification. The obtained product was subjected to a reduction using $NaBH_4$ in the presence of palladium on activated charcoal to afford 3-chloro-4-[^{18}F]fluoroaniline ([^{18}F]**15**) in 63.2% ± 7.8% radiochemical yield (corrected for decay) and generally a radiochemical purity of >95% without further purification.

After establishing a reliable procedure to prepare 3-chloro-4-[^{18}F]fluoroaniline ([^{18}F]**15**) the stage was set to explore the BOP-mediated condensation with **13**. Initial reaction conditions were screened by variation of solvent, base and temperature. When NMP (*N*-methylpyrrolidine) was used in combination with DBU (1,8-

diazabicyclo[5.4.0]undec-7-een) the desired product could be detected on radio-HPLC. With this encouraging result in hand we set out to optimize the reaction parameters. All reactions were run for a maximum of 30 minutes, with regard to the limited half-life of fluorine-18. The investigation started with the temperature dependence of the reaction. It was found that 120°C provided the highest conversion rates (Table 1, entry 1-4). Higher temperatures than 120°C resulted in the decomposition of the starting materials and product. Next, the need for a base in the reaction mixture was confirmed as discoloration of the precursor solution was observed upon addition of the base (Table 1, entry 5). Furthermore, due to this discoloration it appeared that the BOP, base and cyclic amide precursor solution had to be premixed for a certain period of time to provide higher conversion rates. The preformation was required to form an activated reactive building block, as has been described by Wan *et al.*, which thereby improved the reaction between **13** and [^{18}F]**15.** It was observed that the solution had to be prepared at least 15 minutes prior to addition and remained stable for up to 45 minutes before lower conversion rates were observed. Next, we turned our attention to the stoichiometry of the reaction and optimized for this parameter (Table 1, entry 6-13). To arrive at conditions that reliably provided about 30% conversion to the desired product in the allotted reaction time (Table 1, entry 10). Subsequent semi-preparative HPLC purification provided [^{18}F]afatinib (0.2-3.3 GBq) in excellent purity (>98%) and high specific activity 223 ± 38 GBq/µmol) in an overall yield of 17.0 ± 2.5% (corrected for decay) formulated in an i.v. injectable solution (10% ethanol in saline containing sodium dihydrogenphosphate, pH=5.2) suitable for *in vivo* experiments.

Table 1: Optimization of BOP mediated condensation towards [^{18}F]afatinib

#	**Precursor (µmol)**	**Bop (eq)**	**Base (eq)**	**Preformation time (min)**	**Temperature (°C)**	**Conversion (%)[a]**
1	1.5	8	12	n.d.	100	16
2	1.5	8	12	n.d.	120	22
3	1.5	8	12	n.d.	140	14
4	1.5	8	12	n.d.	160	0
5	1.5	8	0	n.d.	120	2
6	1.5	16	24	30	120	5
7	3	2	3	30	120	16
8	3	4	6	30	120	23
9	3	8	12	30	120	9
10	**6**	**2**	**3**	**30**	**120**	**25-51%**
11	6	4	6	30	120	10
12	9	2	3	30	120	15
13	12	2	3	30	120	18

a: conversion determined by total percentage of activity (product) of the crude reaction mixture determined with analytical HPLC

3.2.3 Metabolite Analysis

In vivo stability of [^{18}F]afatinib was determined by metabolite analysis in Balb/c mice. The animals were injected i.v. (via ocular plexus) with circa 25 MBq of [^{18}F]afatinib and sacrificed at 15 and 45 minutes post injection followed by blood sample collection. Analysis of the plasma (Table 2) revealed good stability of the tracer with >80% of the activity corresponding to the parent tracer. Radioactivity recovery during the work up of the blood samples was >95%.

Table 2: Metabolite analysis

Time (p.i.)	Polar Metabolites (%)	Non-polar metabolites (%)	Parent (%)
15	3.6 ± 0.3	8.9 ± 1.1	87.5 ± 0.8
45	5.6 ± 0.6	11.1 ± 1.9	83.3 ± 1.3

3.2.4 Xenograft Characterization

To evaluate the tumor targeting potential of [^{18}F]afatinib, two clinically relevant NSCLC cell lines were selected and xenografted subcutaneously in nude mice. The cell lines were selected on the basis of EGFR expression and mutation status. Expression of EGFR and HER2 was confirmed through immunohistochemical staining and the EGFR mutations were confirmed by sequencing. For our initial evaluation we selected a responsive and a non-responsive human cancer cell line, both overexpressing EGFR. For the non-responsive model we chose the A549 cell line expressing WT EGFR, which has been reported to show no responsiveness to afatinib [28]. As the responding cell line we chose HCC827 expressing a mutated exon 19 deletion variant of EGFR [28]. Staining results indicated that both cell lines express EGFR, and HCC827 does so to a higher extend (Figure 3). HER2 is equally expressed in both cell lines. Furthermore, the cells were stained for expression of P-gp, a well-known drug efflux transporter associated with drug resistance. Both lines express this efflux-pump, and, based on IHC staining HCC827 tumors showed a higher expression of P-gp.

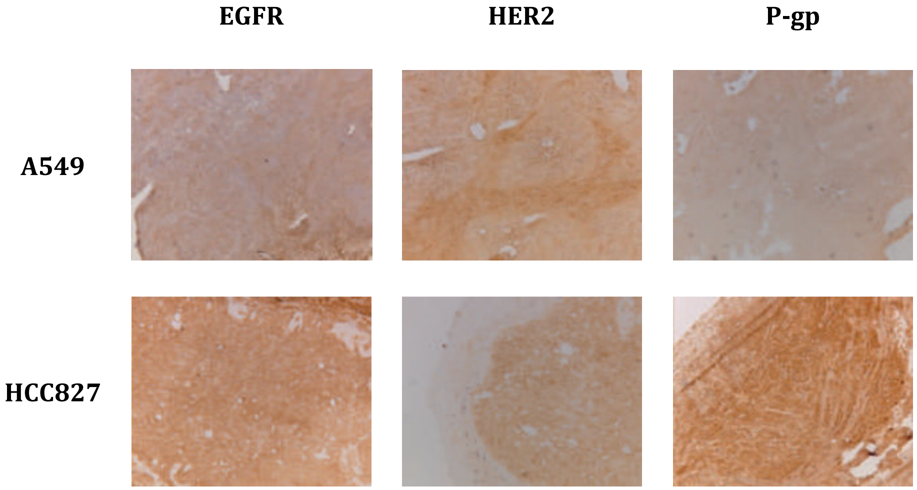

Figure 2: Immunohistochemical staining of tumor lines used in biodistribution studies. Top: EGFR, HER2 and P-gp in tumor line A549; bottom: EGFR, HER2 and P-gp expression in tumor line HCC827.

3.2.5 Biodistribution

In order to assess the tumor targeting potential of [^{18}F]afatinib, an *ex vivo* biodistribution study was performed. Mice bearing tumor xenografts were injected with approximately 25 MBq of [^{18}F]afatinib (specific activity: 223 ± 38 GBq/µmol) and the distribution of the tracer was determined at set time points of 5, 30, 60 and 120 minutes p.i. and results are depicted in Figure 3. [^{18}F]afatinib showed a rapid and high uptake in the metabolic organs (kidney and liver) as is more often observed for small molecule PET-tracers. Furthermore, high initial uptake was observed in well-perfused tissues like the heart and lungs. Due to the rapid excretion the blood level of the tracer was already quite low after 5 minutes p.i. (A549: 2.17 ± %ID/g; HCC827: 1.56 ± %ID/g). Both, A549 and HCC827 tumors showed rapid uptake and after 5 minutes tumor levels were almost at maximum. Interestingly, relevant background tissues such as blood and muscle were rapidly cleared of radioactivity, while the tumors showed good retention of the radioactivity (around 1 %ID/g remained in the tumor at 120 minutes p.i.). This led to moderate/high tumor-to-blood ratios (A549: 2.26 at 120 minutes p.i.; HCC827: 2.59 at 120 minutes p.i.) and high tumor-to-muscle ratios (A549: 6.37 at 120 minutes p.i.; HCC827: 3.83 at 120 minutes p.i.).

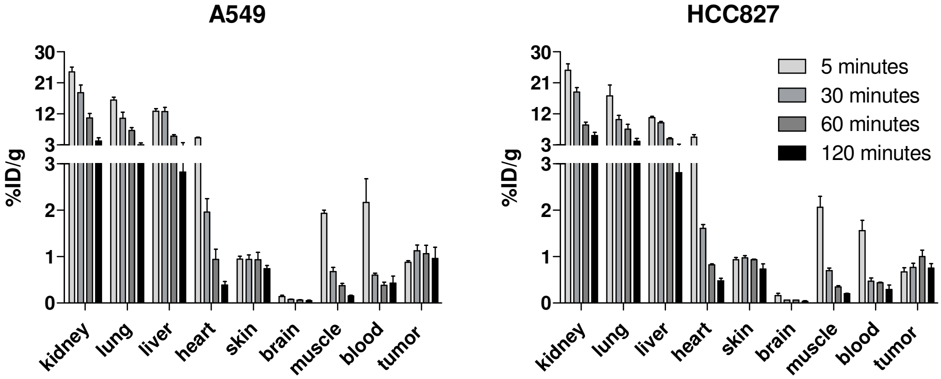

Figure 3: Biodistribution of [^{18}F]afatinib (25 MBq) after 5, 30, 60 and 120 minutes post injection in A549 (n=3, 6 tumors) and HCC827 (n=3, 6 tumors) tumor bearing mice. Columns show the percentage of injected dose per gram (%ID/g) per organ. Errors are standard error of the mean (SEM). Obductions were performed under isoflurane anesthesia.

Uptake of the tracer in the tumor was quick and tumor levels remained constant over time, showing only a little clearance after 2 h. Nevertheless, in absolute numbers the tumor uptake was low in both investigated xenografts. One possible explanation for the low tumor uptake is the intracellular location of the target. Indeed, [^{18}F]afatinib and other TKI-PET tracers first have to cross the cell membrane and have to compete with high intracellular ATP concentration for receptor binding. Another factor might be the P-gp, BCRP and/or other drug efflux pumps that might be involved in clearance of the compound, and which can also take place before EGFR binding. This holds especially true for the HCC827 cells as this line showed high expression levels of P-gp although a larger difference may have been expected based on the relative expression levels. Most likely the combination of a rapid clearance of [^{18}F]afatinib from the blood pool, and the low tracer amounts of [^{18}F]afatinib administered, do explain the relatively low absolute uptake of [^{18}F]afatinib in the targeted tumors. It is also possible that differences in vascularization of the tumor xenografts influences is related to some of the observations. In the end, good clearance of background tissue leads to satisfying tumor to background ratios making [^{18}F]afatinib a suitable agent for future PET-studies.

The uptake in the two different tumor models appeared to be similar and showed no direct significant difference in absolute uptake. This result was somewhat unexpected as afatinib has a higher affinity for mutated EGFR compared to WT EGFR, and because of the relative higher expression of EGFR in HCC827 compared to A549. These data are also deviating from the data Memon *et al.* obtained with [^{11}C]erlotinib in the same xenograft models. In their study, higher uptake levels of [^{11}C]erlotinib in the responsive HCC827 xenograft line (3.66 %ID/g) than in the non-responsive A549 line (1.62 %ID/g) were observed [25]. This apparent difference in the *in vivo* behavior of the [^{18}F]afatinib and [^{11}C]erlotinib tracers, despite comparable biological targets, might among others be due to drug dosing or multi-drug resistance effects and is subject of future comparative studies.

To summarize, a novel BOP-coupling has been described to couple cyclic amides to radiolabeled amidosynthons. Using this method [^{18}F]afatinib was synthesized at a radiochemical yield of 17.0 ± 2.5% calculated from [^{18}F]F^{-}. Furthermore, this method could also be used to synthesize other fluorine-18 labeled PET tracers containing 4-anilinoquinazoline derivatives. The metabolite analysis to investigate the *in vivo* stability revealed a moderate rate of metabolism, with over 80% of intact [^{18}F]afatinib still present in plasma after 45 min. The potential of selective tumor targeting was investigated in 2 tumor xenograft models and tumor accumulation and retention was observed. Nevertheless, future experiments will include multiple PET studies on xenografted mice to assess the optimal imaging conditions for this novel EGFR targeting tracer. Due to the absence of structural modifications we foresee that [^{18}F]afatinib can be readily applied in clinical studies. Translation to the clinic is quickly achieved as toxicity studies are not required, whereby this tracer can provide valuable pharmacokinetic information in patients. This chapter describes the first step in that direction.

3.3 Conclusion

We have developed a method to synthesize [^{18}F]afatinib and related fluorine-18 labeled 4-anilinoquinazolines. [^{18}F]afatinib can be produced efficiently and is stable *in vivo*, however, optimal PET-imaging conditions will be subject of further study to determine its potential as a TKI-PET tracer.

3.4 Materials and methods

3.4.1 General

All reactions were carried out under atmospheric conditions unless otherwise stated and all reagents and solvents were supplied by Sigma-Aldrich (St. Louis, USA) and Biosolve BV (Valkenswaard, the Netherlands) and used as received unless stated otherwise. Reference afatinib was supplied by Axon Medchem BV (Groningen, the Netherlands). Dimethylformamide (DMF) and Tetrahydrofurane (THF) for anhydrous purposes were stored in dry septum capped flasks charged with molecular sieves. Thin Layer Chomatography (TLC) was performed on Merck (Darmstadt, Germany) precoated silica gel 60 F254 plates. Spots were visualized by UV quenching, ninhydrin or anisaldehyde. Column chromatography was carried out either manually by using silica gel 60 Å (Sigma-Aldrich) or on a Buchi (Flawil, Switzerland) sepacore system (comprising of a C-620 control unit, a C-660 fraction collector, 2 C601 gradient pumps and a C640 UV detector) equipped with Buchi sepacore prepacked flash columns. ^{1}H and ^{13}C nuclear magnetic resonance (NMR) spectra were recorded on a Bruker (Billerica, USA) Avance 500 (500.23 MHz and 125.78 MHz, respectively), a Bruker Avance 400 (400.13 MHz and 100.61 MHz, respectively) or a Bruker Avance 250 (250.13 MHz and 62.90 MHz, respectively) with chemical shifts (δ) reported in ppm relative to the solvent. Electrospray ionization mass spectrometry (ESI-MS) was carried out using a Bruker microTOF-Q instrument in positive ion mode (capillary potential of 4500 V). Analytical HPLC was performed on a Jasco PU-2089 pump (Easton, USA) equipped with a Grace (Columbia, USA) C18 Platinum column (5 µm, 250 mm × 4.6 mm) and MeCN/H_2O/DiPA (60:40:0.2, *v*/*v*/*v*) as eluent at a flow rate of 1 mL·min^{-1}, with a Jasco UV-2075 UV detector (λ=254 nm) and a NaI radioactivity detector (Raytest, Straubenhardt, Germany). Chromatograms were acquired using GINA star software (version 5.1, Raytest). Semi-preparative HPLC was carried out on a Jasco PU-2089 pump equipped with a C18 Alltima column (Grace, 5 µm, 250 mm × 10 mm) using MeCN/H2O/DiPA (40:60:0.2, *v*/*v*/*v*) as eluent at a flow rate of

4 mL · min⁻¹, a Jasco UV1575 UV detector (λ=254 nm) and a custom-made radioactivity detector. Chromatograms were acquired using ChromNAV software (version 1.14.01, Jasco). All animal experiments were approved by the local ethics committee.

3.4.2 Chemistry

7-chloroquinazolin-4(3*H*)-one (5) [32].

A mixture of 2-amino-4-chlorobenzoic acid (25.0 g, 146 mmol) and formamide (80 mL) was heated to 130°C for 30 minutes and then heated to 180°C for 4 hours. The mixture was allowed to cool to 20°C and poured onto a mixture of ice and water. A brown precipitate was isolated using vacuum filtration and dried *in vacuo* for 12 hours to obtain 7-chloroquinazolin-4(3*H*)-one as a brown solid (20.6 g, 114 mmol, 78% yield). ^{1}H-NMR (500.23 Mhz, DMSO-D$_6$) δ: 6.65 (dd, J= 1.97, 8.54, 1H, H$_{ar}$), 7.69 (d, J=1.90, 1H, H$_{ar}$), 8.08 (d, J=8.53, 1H, H$_{ar}$), 8.13 (s, 1H, H$_{ar}$), 12.37 (bs, 1H, NH); ^{13}C-NMR (125.78 Mhz, DMSO-D$_6$) δ: 160.74 (C=O), 150.4 (Cq$_{ar}$), 147.5 (CH$_{ar}$), 139.5 (C$_{ar}$Cl), 128.5 (CH$_{ar}$), 127.5 (CH$_{ar}$), 126.9 (CH$_{ar}$), 122.0 (Cq$_{ar}$); HR-MS (ESI, 4500V): m/z calculated for $C_8H_5ClN_2O$: 180.0090, found: 202.9979 (M+Na$^+$)

7-chloro-6-nitroquinazolin-4(3*H*)-one (6) [32].

To a stirred solution of concentrated sulfuric acid (20 mL) and fuming nitric acid (20 mL) was added 7-chloroquinazolin-4(3*H*)-one (5.00 g, 27.7 mmol) portion wise at 0°C. The mixture was allowed to reach 20°C and then stirred at 45°C overnight. The mixture was poured onto ice and water and the precipitate isolated, washed with water and dried *in vacuo*. Recrystallization from acetic acid afforded the desired regioisomer (7-chloro-6-nitroquinazolin-4(3*H*)-one) as yellow crystals (4.26 g, 18.9 mmol, 68% yield). ^{1}H-NMR (500.23 Mhz, DMSO-D$_6$) δ: 12.78 (bs, 1H, NH), 8.66 (s, 1H, H$_{ar}$), 8.27 (s, 1H, H$_{ar}$), 8.00 (s, 1H, H$_{ar}$); ^{13}C-NMR (125.78 Mhz, DMSO-D$_6$) δ: 160.0 (C=O), 152.16 (Cq$_{ar}$), 150.27 (CH$_{ar}$), 145.37 (C$_{ar}$-NO$_2$), 131.0 (CH$_{ar}$-Cl), 130.6 (CH$_{ar}$), 124.9 (CH$_{ar}$), 122.3 (Cq$_{ar}$); HR-MS (ESI, 4500V): m/z calculated for $C_8H_4ClN_3O_3$: 224.9941, found: 247.9827 (M+Na$^+$)

6-nitro-7-(phenylsulfonyl)quinazolin-4(3*H*)-one (8) [32].

7-chloro-6-nitroquinazolin-4(3*H*)-one (2.00 g, 8.87 mmol) and benzenesulfinic acid sodium salt (1.46 g, 8.87 mmol) were suspended in DMF (30 mL) and heated to 90°C for 6 hours. The reaction mixture was diluted with H_2O (30 mL) and the precipitate was collected by vacuum filtration. The resulting solid was dried *in vacuo* to obtain 6-nitro-7-(phenylsulfonyl)quinazolin-4(3*H*)-one as a yellow solid (2.80 g, 8.45 mmol, 95% yield). ^{1}H-NMR (500.23 Mhz, DMSO-D_6) δ: 12.97 (bs, 1H, NH), 8.61 (s, 1H, H_{ar}) 8.52 (s, 1H, H_{ar}), 8.42 (s, 1H, H_{ar}), 8.05 (d. J=7.66, 2xH_{ar}), 7.78 (t, J=7.41, 1 H_{ar}), 7.70 (t, J=7.81, 2 H_{ar}); ^{13}C-NMR (125.78 Mhz, DMSO-D_6) δ: 159.7 (C=O), 151.7 (Cq_{ar}), 150.2 (CH_{ar}), 144.7 (C-NO_2), 140.0 (Cq_{ar}), 138.3 (Cq_{ar}), 135.15 (CH_{ar}), 132.1 (CH_{ar}), 130.2 (2xCH_{ar}), 128.6 (2xCH_{ar}), 127.2 (Cq_{ar}), 124.8 (CH_{ar}); HR-MS (ESI, 4500V): m/z calculated for $C_{14}H_9N_3O_5S$: 331.0263, found: 354.0146 (M+Na^+)

(*S*)-6-nitro-7-((tetrahydrofuran-3-yl)oxy)quinazolin-4(3*H*)-one (10).

To a solution of 6-nitro-7-(phenylsulfonyl)quinazolin-4(3*H*)-one (2.00 g, 6.04 mmol) and (*S*)-tetrahydrofuran-3-ol (0.627 mL, 7.85 mmol), in tert-butanol/DMF (25 mL/5 mL) stirred under argon, was added dropwise potassium tert-butoxide (1M in THF, 21.7 mL, 21.7 mmol) at 20°C. The mixture was stirred for 16 hours at 20°C and then at 45°C until TLC indicated full consumption of 6-nitro-7-(phenylsulfonyl)quinazolin-4(3*H*)-one. All volatiles were removed *in vacuo* to obtain the crude product which was purified by flash column chromatography (MeOH/EtOAc, 5:95 *v/v*) to afford (*S*)-6-nitro-7-((tetrahydrofuran-3-yl)oxy)quinazolin-4(3*H*)-one as a yellow solid (1.25 g, 4.51 mmol, 75% yield). ^{1}H-NMR (500.23 Mhz, DMSO-D_6) δ: 12.55 (bs, 1H, NH), 8.50 (s, 1H, H_{ar}), 8.22 (s, 1H, H_{ar}), 7.40 (s, 1H, H_{ar}), 5.41 (t, J=4.64 Hz, 1H, H_{chiral}), 3.95 (bm, 4H, 2x$CH_{2\text{-tetrahydrofuran}}$), 2.31 (sextet, J=7.86, 13.90, 22.02 Hz, 1H, $CH_{2\text{-tetrahydrofuran}}$), 2.03 (q, J=6.90, 12.45 Hz, 1H, $CH_{2\text{-tetrahydrofuran}}$); ^{13}C-NMR (125.78 Mhz, DMSO-D_6) δ: 160.2 (C=O), 154.4 (C_{ar}-O-C), 153.4 (Cq_{ar}), 149.4 (CH_{ar}), 139.5 (C_{ar}-NO_2), 124.5 (CH_{ar}), 115.9 (Cq_{ar}), 112.3 (CH_{ar}), 80.5 (CH_{chiral}), 72.5 ($CH_{2\text{-tetrahydrofuran}}$), 67.0 ($CH_{2\text{-tetrahydrofuran}}$), 32.9 ($CH_{2\text{-tetrahydrofuran}}$); HR-MS (ESI, 4500V): m/z calculated for $C_{12}H_{11}N_3O_5$: 277.0699, found: 300.0573 (M+Na^+)

(*S*)-6-amino-7-((tetrahydrofuran-3-yl)oxy)quinazolin-4(3*H*)-one (11).

To a refluxing solution (110°C) of (*S*)-6-nitro-7-((tetrahydrofuran-3-yl)oxy)quinazolin-4(3*H*)-one (1.20 g, 4.33 mmol) and acetic acid (1.98 mL, 34.6 mmol) in ethanol/water (27.5 mL, 10:1, *v/v*) was added iron powder (967 mg, 17.3 mmol), the mixture was allowed to reflux (110°C) for 20 minutes. Then the mixture was allowed to cool to 20°C and applied to a celite filter and eluted with ethanol. The product containing fractions were concentrated to obtain the crude product which was purified by flash column chromatography (MeOH/EtOAc, 5:95, v/v) to afford (*S*)-6-amino-7-((tetrahydrofuran-3-yl)oxy)quinazolin-4(3*H*)-one as a an off-white solid (1.06 g, 4.29 mmol, 99% yield). ^{1}H-NMR (500.23 Mhz, DMSO-D$_6$) δ: 12.78 (bs, 1H, NH), 7.79 (s, 1H, H$_{ar}$), 7.23 (s, 1H, H$_{ar}$), 6.93 (s, 1H, H$_{ar}$), 5.31 (s, 2H, NH$_2$), 5.17 (t, J=4.6 Hz, 1H, H$_{chiral}$), 3.96 (m, 1H, CH$_2$), 3.88 (m, 2H, CH$_{2\text{-tetrahydrofuran}}$), 3.77 (m, 1H, CH$_{2\text{-tetrahydrofuran}}$), 2.26 (sextet, J=7.44, 13.70, 21.6 Hz, 1H, CH$_{2\text{-tetrahydrofuran}}$), 2.07 (q, J=6.8, 12.2 Hz, 1H, CH$_{2\text{-tetrahydrofuran}}$); ^{13}C-NMR (125.78 Mhz, DMSO-D$_6$) δ: 160.7 (C=O), 150.4 (C$_{ar}$-O-C), 141.9 (Cq$_{ar}$), 141.8 (CH$_{ar}$), 139.1 (C$_{ar}$-NH$_2$), 117.3 (Cq$_{ar}$), 108.7 (CH$_{ar}$), 106.6 (CH$_{ar}$), 78.5 (C$_{Hchiral}$), 72.8 (CH$_{2\text{-tetrahydrofuran}}$), 67.1 (CH$_{2\text{-tetrahydrofuran}}$), 33.1 (CH$_{2\text{-tetrahydrofuran}}$); HR-MS (ESI, 4500V): m/z calculated for $C_{12}H_{13}N_3O_3$: 247.0957, found: 270.0832 (M+Na$^+$)

(*S,E*)-4-(dimethylamino)-*N*-(4-oxo-7-((tetrahydrofuran-3-yl)oxy)-3,4-dihydroquinazolin-6-yl)but-2-enamide (13).

To a suspension of (*E*)-4-(dimethylamino)but-2-enoic acid hydrochloride (50 mg, 0.4 mmol) in THF (3 mL) containing a catalytic amount of DMF (0.05 mL) under an argon atmosphere was added oxalylchloride (32 µL, 0.36 mmol) at 0°C. When foaming ceased the mixture was heated to 25°C and kept at this temperature for 2 hours. The mixture was then cooled to 0°C and a solution of (*S*)-6-amino-7-((tetrahydrofuran-3-yl)oxy)quinazolin-4(3*H*)-one (50 mg, 0.2 mmol) in *N*-methylpyrrolidine (1 mL) was added in a stream to obtain a yellow suspension. The mixture was allowed to come to room temperature slowly and stirred for 2 hours. When consumption of the amine was observed on TLC the reaction was quenched by the addition of aqueous NaHCO$_3$ (1 mL). The volatiles were removed by rotary evaporation and the remainder was purified by flash column chromatography (Gradient: MeOH:EtOAc = 5:95, *v/v* to MeOH:EtOAc = 20:80, *v/v*) to afford (*S,E*)-4-(dimethylamino)-*N*-(4-oxo-7-((tetrahydrofuran-3-yl)oxy)-3,4-dihydroquinazolin-6-yl)but-2-enamide as a an off-white solid (65 mg, 0.18 mmol, 90% yield). ^{1}H-NMR (500.23 Mhz, DMSO-D_6) δ: 12.22 (s, 1H, NH), 9.32 (s, 1H, H_{ar}), 8.85 (s, 1H, H_{ar}), 8.00 (s, 1H, H_{ar}), 7.13 (s, 1H, H_{ar}), 6.76 (m, 1H, $H_{double\ bond}$), 6.64 (d, 1H, $H_{double\ bond}$), 5.76 (t, J=5.25 Hz, 1H, H_{chiral}), 3.95 (bm, 3H, $CH_{2\text{-}tetrahydrofuran}$), 3.76 (sextet, J=4.9, 8.0, 13.0 Hz, 1H, $CH_{2\text{-}tetrahydrofuran}$), 3.11 (d, J=5.0 Hz, 2H, CH_2), 2.30 (sextet, J=7.2, 13.7, 21.2 Hz, 1H, $CH_{2\text{-}tetrahydrofuran}$), *signals from N-methyl peaks coincide with one of the CH_2-protons:* 2.20 (s, 6H, 2x N-CH_3), 2.16 (m, 1H, $CH_{2\text{-}tetrahydrofuran}$); ^{13}C-NMR (125.78 Mhz, DMSO-D_6) δ: 164.1 (C=O_{amide}), 160.6 (C=$O_{cyclic\ amide}$), 153.7 (C_{ar}-O-C), 147.2 (Cq_{ar}), 145.7 ($CH_{double\ bond}$), 128.0 (Cq_{ar}), 126.9 ($CH_{double\ bond}$), 117.9 (CH_{ar}), 116.2 (Cq_{ar}), 109.2 (CH_{ar}), 79.5 (CH_{chiral}), 72.5 ($CH_{2\text{-}tetrahydrofuran}$), 67.2 ($CH_{2\text{-}tetrahydrofuran}$), 60.11 ($(CH_3)_2N\text{-}\mathit{C}H_2$), 45.5 (2x CH_3), 32.9 ($CH_{2\text{-}tetrahydrofuran}$). HR-MS (ESI, 4500V): m/z calculated for $C_{18}H_{22}N_4O_4$: 358.1641, found: 359.1770 (M+H^+)

3-chloro-*N,N*-dimethyl-4-nitroaniline (19) [30].

To sodiumhydride (60% dispersion in mineral oil, 869 mg, 21.7 mmol) under argon was added a solution of 2-chloro-4-nitroaniline (1.5 g, 8.7 mmol) in THF (15 ml). The mixture was stirred for 5 minutes followed by the addition of a solution of methyliodide (1.14 ml, 18.3 mmol) in THF (5 ml). The mixture was stirred for 24 hours at rt. Upon completion of the reaction as indicated by TLC, the mixture was poured onto a mixture of ice and water. The aqueous solution was extracted with ethylacetate (2 x) and the combined organic layers were washed with brine, dried (Na_2SO_4) and evaporated to afford the crude product, which was purified by flash column chromatography (EtOAc in hexanes, 15:85, *v/v*) to yield an orange solid (1.7 g, 8.4 mmol, 97% yield). ^{1}H-NMR (400.13 Mhz, $CDCl_3$) δ: 8.22 (d, J=2.7 Hz, 1H, H_{ar}), 8.06 (dd, J=9.2, 2.7 Hz, 1H, H_{ar}), 6.97 (d, J=9.0 Hz, 1H, H_{ar}), 3.02 (s, 6H, $H_{methylgroups}$). ^{13}C-NMR (125.78 Mhz, $CDCl_3$) δ: 155.5 (Cq-$(CH_3)_2$), 141.1 (Cq-NO_2), 127.3 (CH_{ar}), 125.1 (Cq-Cl), 123.4 (CH_{ar}), 118.0 (CH_{ar}), 43.1 (2x CH_3). HR-MS (ESI, 4500V): m/z calculated for $C_8H_9ClN_2O_2$: 200.0353, found: 201.0414 (M+H^+)

3-chloro-4-trimethylammonium-nitrobenzene triflate (16) [30].

A solution of 3-chloro-*N,N*-dimethyl-4-nitroaniline (0.6 g, 3.0 mmol) in DCM (5 ml) under argon was treated with methyl trifluoromethanosulfonate (0.66 ml, 6.00 mmol). The mixture was stirred for 24 hours at rt after which a solid was precipitated by the addition of diethylether (20 ml). The solid was collected by vacuum filtration and recrystallized from a mixture of DCM/diethylether (1:1, *v/v*) to obtain the product as a white solid (0.751 g, 2.06 mmol, 69% yield). ^{1}H-NMR (400.13 Mhz, DMSO-D$_6$) δ: 8.62 (d, J=2.7 Hz, 1H, H$_{ar}$), 8.42 (dd, J=9.4, 2.6 Hz, 1H, H$_{ar}$), 8.34 (d, J=9.3 Hz, 1H, H$_{ar}$), 3.85 (s, 6H, H$_{methyl}$). ^{13}C-NMR (125.78 Mhz, DMSO-D$_6$) δ: 148.9 (Cq-NO2), 146.5 (Cq-(CH$_3$)$_2$), 129.5 (CH$_{ar}$), 127.6 (Cq-Cl), 126.6 (CH$_{ar}$), 124.2 (CH$_{ar}$), 43.1 (2x CH$_3$). HR-MS (ESI, 4500V): m/z calculated for $C_8H_{12}ClN_2O_2^+$: 215.0582, found: 215.0578 (M $^+$)

3.4.3 Radiosynthesis

[^{18}F]F$^-$ was produced by the ^{18}O(p,n)^{18}F nuclear reaction using an IBA (Louvain-la-Neuve, Belgium) Cyclone 18/9 cyclotron. Radioactivity levels were measured using a Veenstra (Joure, The Netherlands) VDC-405 dose calibrator. Radiochemistry was carried out in homemade, remotely controlled synthesis units [34]. After irradiation, [^{18}F]fluoride was trapped on a PS-HCO$_3^-$ column (ABX, Radenberg, Germany). It was eluted from the anion exchange column into a screw cap reaction vessel with 1 mL of acetonitrile/water (9/1, v/v) containing Kryptofix 2.2.2 (13.0 mg, 34.6 µmol, 4,7,13,16,21,24-Hexaoxa-1,10-diazabicyclo[8.8.8]hexacosane) and potassium carbonate (2.0 mg, 15 µmol). The solution was evaporated to dryness under a helium flow (50 mL·min^{-1}) and reduced pressure at 90°C. Acetonitrile (0.5 mL) was added and the solution was evaporated to dryness again. To the dried residue was added a solution of 3-chloro-4-trimethylammonium-nitrobenzene triflate (**16**, 3.0 mg, 14 µmol) in acetonitrile (0.7 ml) and the mixture was allowed to react for 25 minutes at 40°C. After the reaction mixture was quenched with water (7 mL), 3-chloro-4-[^{18}F]fluoro-nitrobenzene ([^{18}F]**17**) was trapped on a tC18plus Sep-Pak (Waters, Milford, USA), rinsed with water (10 mL) and subsequently eluted with MeOH (1.5 mL) into a screw cap reaction vessel containing palladium on activated carbon (10%, 3 mg) and sodiumborohydride (10.0 mg, 264 µmol). The reduction was carried out for 7 minutes at 20°C upon which the reaction was quenched by the addition of concentrated hydrochloric acid (37%, 0.1 mL). The thus obtained mixture was passed through a syringe filter (Millex LCR PTFE 0.45 µM / 25 mm, Millipore, Billerica, USA) into a new screw cap reaction vessel. Volatiles were removed *in vacuo* and under a helium stream (100 mL·min^{-1}) at elevated temperatures (90°C for 5 min. and 120°C for 2 min.) to obtain the dry 3-chloro-4-[^{18}F]fluoroaniline-HCl salt [^{18}F]**15**. The product was dissolved in *N*-methylpyrrolidine (0.5 ml) and to this solution was added a solution of (*S,E*)-4-(dimethylamino)-N-(4-oxo-7-((tetrahydrofuran-3-yl)oxy)-3,4-dihydroquinazolin-6-yl)but-2-enamide (**13**, 2 mg, 6 µmol), benzotriazole-1-yl-oxy-tris-(dimethylamino)-phosphonium hexafluorophosphate (BOP, 5.5 mg, 12 µmol), 2,3,4,6,7,8,9,10-octahydropyrimido[1,2-a]azepine (DBU, 2.7 µl, 18 µmol) in anhydrous *N*-methylpyrrolidine (NMP, 0.5 mL), which was dissolved 15 minutes prior to addition. The obtained mixture was heated to 120°C for 30 minutes after which it was cooled to 20°C and quenched by the addition of water (1 mL) and purified by semi-preparative HPLC chromatography. Retention time of the product was 21 minutes. The collected fraction of the preparative HPLC purification containing the product was diluted with 50 mL of water and the total mixture was passed over a tC18 plus Sep-Pak cartridge. The cartridge was then washed with 20 mL of sterile water after which the product was eluted from the cartridge with 1.0 mL of sterile 96% ethanol. The ethanol was diluted to 10 volume percent with formulation solution (7.09 mM NaH_2PO_4 in 0.9% NaCl, w/v in water, pH 5.2) and the complete solution was filtered over a Millex-GV 0.22 µm filter into a sterile 20 mL capped vial. To provide a final solution of 10% ethanol in saline (containing 7.09 mM NaH_2PO_4) containing [^{18}F]afatinib. Analysis of the product was performed by analytical HPLC. Retention time of the product was 9 minutes, radiochemical purity was >98%. The specific activity was calculated against a calibration curve of afatinib using the analytical HPLC system and was found to be 223 ±38 GBq/µmol.

3.4.4 Metabolite Analysis

Eight Balb/C mice were injected with 20-30 MBq of [^{18}F]afatinib, in the ocular plexus under isoflurane anesthesia (2% in 1 L · min^{-1}). The mice were sacrificed at 15 (n = 4) and 45 (n = 4) min post-injection. At these time points, about 1.0-1.5 mL of blood was collected via a heart puncture from each mouse. Blood was collected in a heparin tube and centrifuged for 5 minutes at 4000 r.p.m. (Hettich universal 16, Depex B.V., the Netherlands). Plasma was separated from blood cells and about 1 mL of plasma was diluted with 2 mL of 0.1 M hydrochoric acid and loaded onto a tC2 Sep-Pak cartridge, which was pre-activated by elution with 3 mL of MeOH and 6 mL of water, respectively. The cartridge was washed with 5 mL of H_2O to collect polar radioactive metabolites. Thereafter, the tC2 Sep-Pak cartridge was eluted with 2 mL of MeOH and 1 mL of H_2O to collect the mixture of apolar metabolites. The mixture of apolar metabolites was analyzed using HPLC to determine the percentage of intact [^{18}F]afatinib. HPLC was performed on a Dionex Ultimate 3000 system, equipped with a 1 mL loop. As a stationary phase a Phenomenex Gemini C18, 250 x 10 mm, 5 µm was used. The mobile phase was a gradient of A = acetonitrile and B = 0.1% D*i*PA in H_2O. The HPLC gradient ran for 12.5 minutes increasing the concentration of eluent B from 0% to 10% at a flow rate of 4 ml.min^{-1}.

3.4.5 Immunohistochemical staining

Sections of frozen xenografts (A549, HCC827) were immunostained for assessment of EGFR, HER-2 and P-gp expression. Antibodies were diluted in PBS (phosphate buffered saline) with 1% bovine serum albumin. EFGR was stained with cetuximab (Merck), HER2 with trastuzumab (Roche, Basel, Switzerland), and P-gp with rabbit polyclonal anti-P-gp (AB103477, ITK diagnostics BV, Uithoorn, the Netherlands). As secondary antibodies rabbit anti-human horseradish peroxidase (P0214, Dako, Glostrup, Denmark) or swine anti-rabbit horseradish peroxidase (P0217, Dako) were used. Cryosections (5 µm) of fresh frozen (tumor) tissue were air-dried and subsequently fixed with 2% paraformaldehyde in PBS for 10 minutes. Sections were blocked with normal rabbit serum (in case of trastuzumab or cetuximab) or with normal swine serum (in case of anti-P-gp) and subsequently stained with cetuximab 10 µg/ml (EGFR), trastuzumab 10 µg/ml (HER2) or anti-P-gp 5 µg/ml. Color development was performed with diaminobenzidine (DAB) and counterstaining was done with Hematoxiline.

3.4.6 Sequencing of xenograft material

EGFR mutation analysis was performed on DNA isolated from xenografts using high-resolution melting followed by cycle sequencing of PCR products displaying a suspect melting profile, as described before [35].

3.4.7 Biodistribution studies

Nude mice (Athymic nu/nu, Harlan, Horst, The Netherlands) bearing two tumors (obtained by injection of A549 or HCC827 cells) of the same xenograft line on their left and right flank, received an injection of 15-25 MBq [^{18}F]afatinib via the tail vein. The mice were sacrificed and dissected at 5, 30, 60 and 120 minutes post-injection. Blood, urine, skin, left tumor, right tumor, muscle, heart, lung, liver, kidney and brain were collected, weighed and counted for radioactivity in a Wallac Compugamma 1210 counter (n = 3 for each time point). Biodistribution data are expressed as percentage of injected dose per gram (%ID/g) tissue for each organ.

3.5 References

[1] Ou S-HI. Second-generation irreversible epidermal growth factor receptor (EGFR) tyrosine kinase inhibitors (TKIs): A better mousetrap? A review of the clinical evidence *Crit. Rev. Oncol. Hematol.* **2012**, *83*, 407-421.

[2] Zhang J, Yang PL, and Gray NS. Targeting cancer with small molecule kinase inhibitors *Nat. Rev. Cancer* **2009**, *9*, 28-39.

[3] van Dongen GAMS, Poot AJ, and Vugts DJ. PET imaging with radiolabeled antibodies and tyrosine kinase inhibitors: immuno-PET and TKI-PET *Tumor Biol.* **2012**, *33*, 607-615.

[4] Paez JG, Janne PA, Lee JC, Tracy S, Greulich H, Gabriel S, et al. EGFR mutations in lung cancer: correlation with clinical response to gefitinib therapy *Science* **2004**, *304*, 1497-1500.

[5] Rosell R, Carcereny E, Gervais R, Vergnenegre A, Massuti B, Felip E, et al. Erlotinib versus standard chemotherapy as first-line treatment for European patients with advanced EGFR mutation-positive non-small-cell lung cancer (EURTAC): a multicentre, open-label, randomised phase 3 trial *Lancet Oncol.* **2012**, *13*, 239-246.

[6] Sequist LV, Yang JC-H, Yamamoto N, O'Byrne K, Hirsh V, Mok T, et al. Phase III study of afatinib or cisplatin plus pemetrexed in patients with metastatic lung adenocarcinoma with EGFR mutations *J. Clin. Oncol.* **2013**, *31*, 3327-3334.

[7] Sharma SV, Bell DW, Settleman J, and Haber DA. Epidermal growth factor receptor mutations in lung cancer *Nat. Rev. Cancer* **2007**, *7*, 169-181.

[8] Pao W, Miller VA, Politi KA, Riely GJ, Somwar R, Zakowski MF, et al. Acquired resistance of lung adenocarcinomas to gefitinib or erlotinib is associated with a second mutation in the EGFR kinase domain *Plos Medicine* **2005**, *2*, 225-235.

[9] Poot AJ, Slobbe P, Hendrikse NH, Windhorst AD, and van Dongen GAMS. Imaging of TKI-target interactions for personalized cancer therapy *Clin. Pharmacol. Ther.* **2013**, *93*, 239-241.

[10] Slobbe P, Poot AJ, Windhorst AD, and van Dongen GAMS. PET imaging with small-molecule tyrosine kinase inhibitors: TKI-PET *Drug Discovery Today* **2012**, *17*, 1175-1187.

[11] Tolmachev V, Stone-Elander S, and Orlova A. Radiolabelled receptor-tyrosine-kinase targeting drugs for patient stratification and monitoring of therapy response: prospects and pitfalls *Lancet Oncol.* **2010**, *11*, 992-1000.

[12] Abourbeh G, Dissoki S, Jacobson O, Litchi A, Ben Daniel R, Laki D, et al. Evaluation of radiolabeled ML04, a putative irreversible inhibitor of epidermal growth factor receptor, as a bioprobe for PET imaging of EGFR-overexpressing tumors *Nucl. Med. Biol.* **2007**, *34*, 55-70.

[13] Chen Y, Feng M, Li S, Xu J, Ning H, He Y, et al. Synthesis and evaluation of novel F-18 labeled 4-aminoquinazoline derivatives: Potential PET imaging agents for tumor detection *Biorg. Med. Chem. Lett.* **2012**, *22*, 4745-4749.

[14] Corcoran EB and Hanson RN. Imaging EGFR and HER2 by PET and SPECT: A Review *Med. Res. Rev.* **2014**, *34*, 596-643.

[15] Dissoki S, Eshet R, Billauer H, and Mishani E. Modified PEG-anilinoquinazoline derivatives as potential EGFR PET agents *J. Labelled Compd. Radiopharm.* **2009**, *52*, 41-52.

[16] Hirata M, Kanai Y, Naka S, Matsumuro K, Kagawa S, Yoshimoto M, et al. Evaluation of radioiodinated quinazoline derivative as a new ligand for EGF receptor tyrosine kinase activity using SPECT *Ann. Nucl. Med.* **2011**, *25*, 117-124.

[17] Hirata M, Kanai Y, Naka S, Matsumuro K, Kagawa S, Yoshimoto M, et al. Synthesis and evaluation of radioiodinated phenoxyquinazoline and benzylaminoquinazoline derivatives as new EGF receptor tyrosine kinase imaging ligands for tumor diagnosis using SPECT *Ann. Nucl. Med.* **2012**, *26*, 381-389.

[18] Hirata M, Kanai Y, Naka S, Yoshimoto M, Kagawa S, Matsumuro K, et al. A useful EGFR-TK ligand for tumor diagnosis with SPECT: development of radioiodinated 6-(3-morpholinopropoxy)-7-ethoxy-4-(3 '-iodophenoxy)quinazoline *Ann. Nucl. Med.* **2013**, *27*, 431-443.

[19] Pal A, Balatoni JA, Mukhopadhyay U, Ogawa K, Gonzalez-Lepera C, Shavrin A, et al. Radiosynthesis and initial *in vitro* evaluation of F-18 F-PEG(6)-IPQA-A novel PET radiotracer for imaging EGFR expression-activity in lung carcinomas *Mol. Imaging Biol.* **2011**, *13*, 853-861.

[20] Pantaleo MA, Mishani E, Nanni C, Landuzzi L, Boschi S, Nicoletti G, et al. Evaluation of modified PEG-anilinoquinazoline derivatives as potential agents for EGFR imaging in cancer by small animal PET *Mol. Imaging Biol.* **2010**, *12*, 616-625.

[21] Pisaneschi F, Nguyen Q-D, Shamsaei E, Glaser M, Robins E, Kaliszczak M, et al. Development of a new epidermal growth factor receptor positron emission tomography imaging agent based on the 3-cyanoquinoline core: synthesis and biological evaluation *Biorg. Med. Chem.* **2010**, *18*, 6634-6645.

[22] Yeh HH, Ogawa K, Balatoni J, Mukhapadhyay U, Pal A, Gonzalez-Lepera C, et al. Molecular imaging of active mutant L858R EGF receptor (EGFR) kinase-expressing nonsmall cell lung carcinomas using PET/CT *Proc. Natl. Acad. Sci. U. S. A.* **2011**, *108*, 1603-1608.

[23] van der Veldt AAM, Lubberink M, Mathijssen RHJ, Loos WJ, Herder GJM, Greuter HN, et al. Toward prediction of efficacy of chemotherapy: a proof of concept study in lung cancer patients using [^{11}C]docetaxel and positron emission tomography *Clin. Cancer Res.* **2013**, *19*, 4163-4173.

[24] Van der Veldt Astrid AM, Lubberink M, Bahce I, Walraven M, de Boer Michiel P, Greuter Henri NJM, et al. Rapid decrease in delivery of chemotherapy to tumors after anti-VEGF therapy: implications for scheduling of anti-angiogenic drugs *Cancer Cell* **2012**, *21*, 82-91.

[25] Memon AA, Jakobsen S, Dagnaes-Hansen F, Sorensen BS, Keiding S, and Nexo E. positron emission tomography (PET) imaging with C-11 -labeled erlotinib: a micro-PET study on mice with lung tumor xenografts *Cancer Res.* **2009**, *69*, 873-878.

[26] Bahce I, Smit EF, Lubberink M, van der Veldt AAM, Yaqub M, Windhorst AD, et al. Development of [^{11}C]erlotinib positron emission tomography for *in vivo* evaluation of EGF receptor mutational status *Clin. Cancer Res.* **2013**, *19*, 183-193.

[27] Memon AA, Weber B, Winterdahl M, Jakobsen S, Meldgaard P, Madsen HHT, et al. PET imaging of patients with non-small cell lung cancer employing an EGF receptor targeting drug as tracer *Br. J. Cancer* **2011**, *105*, 1850-1855.

[28] Li D, Ambrogio L, Shimamura T, Kubo S, Takahashi M, Chirieac LR, et al. BIBW2992, an irreversible EGFR/HER2 inhibitor highly effective in preclinical lung cancer models *Oncogene* **2008**, *27*, 4702-4711.

[29] Solca F, Dahl G, Zoephel A, Bader G, Sanderson M, Klein C, et al. Target binding properties and cellular activity of afatinib (BIBW 2992), an irreversible ErbB family blocker *J. Pharmacol. Exp. Ther.* **2012**, *343*, 342-350.

[30] Seimbille Y, Phelps ME, Czernin J, and Silverman DHS. Fluorine-18 labeling of 6,7-disubstituted anilinoquinazoline derivatives for positron emission tomography (PET) imaging of tyrosine kinase receptors: synthesis of F-18-Iressa and related molecular probes *J. Labelled Compd. Radiopharm.* **2005**, *48*, 829-843.

[31] Läppchen T, Vlaming MLH, Custers E, Lub J, Sio CF, DeGroot J, et al. Automated synthesis of [^{18}F]gefitinib on a modular system *Appl. Radiat. Isot.* **2012**, *70*, 205-209.

[32] Schroeder J, Dziewas G, Fachinger T, Jaeger B, Reichel C, and Renner S. Preparing aminocrotonylamino-substituted quinazoline derivatives, comprises reacting chloro-nitro-quinazolinone with amine, converting to quinazoline compound, reducing, converting to phosphonic ester and reacting with hydrogen sulfite. Boehringer Ingelheim Int Gmbh; Boehringer Ingelheim Pharma Gmbh & Co Kg; Schroeder J; Dziewas G; Fachinger T; Jaeger B; Reichel C; Renner S; Boehringer Ingelheim Pharma Gmbh&Co Kg.

[33] Wan Z-K, Wacharasindhu S, Binnun E, and Mansour T. An efficient direct amination of cyclic amides and cyclic ureas *Org. Lett.* **2006**, *8*, 2425-2428.

[34] Windhorst AD, Linden TT, de Nooij A, Keus JF, Buijs FL, Schollema PE, et al. A complete, multipurpose, low cost, fully automated and GMP compliant radiosynthesis system *J. Labelled Compd. Radiopharm.* **2001**, *44*, S1052-S1054.

[35] Heideman DAM, Thunnissen FB, Doeleman M, Kramer D, Verheul HM, Smit EF, et al. A panel of high resolution melting (HRM) technology-based assays with direct

sequencing possibility for effective mutation screening of EGFR and K-ras genes *Cell. Oncol.* **2009**, *31*, 329-333.

Chapter 4

A comparative PET-imaging study with the reversible and irreversible EGFR tyrosine kinase inhibitors [^{11}C]erlotinib and [^{18}F]afatinib in lung cancer bearing mice

P. Slobbe, A.D. Windhorst, M. Stigter-van Walsum, E.F. Smit, H.G.
Niessen, F. Solca, G. Stehle, G.A.M.S van Dongen and A.J. Poot

Published in: *European Journal of Nuclear Medicine and Molecular Imaging: Research,*
2015*,* 5:14

Abstract

Background: Tyrosine Kinase Inhibitors (TKIs) have experienced a tremendous boost in the last years, where more than 22 small molecule TKIs have been approved by the FDA. Unfortunately despite promising clinical successes, a large portion of patients remains unresponsive to these targeted drugs. For non-small cell lung cancer (NSCLC) the effectiveness of TKIs is dependent on the mutational status of EGFR. The exon 19 deletion as well as the L858R point mutation lead to excellent sensitivity to TKIs such as erlotinib and gefitinib, however, despite initial good response, most patients invariably develop resistance against these first generation reversible TKIs, e.g. via T790M point mutation. Second generation TKIs that irreversibly bind to EGFR wild type and mutant isoforms, have therefore been developed and one of these candidates, afatinib, has now reached the market. Whether irreversible TKIs differ from reversible TKIs in their *in vivo* tumor targeting properties is however not known and was subject of the present study.

Methods: Erlotinib was labeled with carbon-11 and afatinib with fluorine-18 without modifying the structure of these compounds. A preclinical PET study was performed in mice bearing NSCLC xenografts with a representative panel of mutations: an EGFR-WT xenograft cell line (A549), an acquired resistance mutant (L858R/T790M) and a treatment sensitive exon 19 deleted mutant (HCC827). PET-imaging was performed in these xenografts with both tracers. Additionally, the effect of drug-efflux transporter P-gp on the tumor uptake of tracers was explored by therapeutic blocking with tariquidar.

Results: Both tracers only demonstrated selective tumor uptake in the HCC827 xenograft line (tumor-to-background ratio: [^{11}C]erlotinib: 1.9 ± 0.5 and [^{18}F]afatinib 2.3 ± 0.4), thereby showing the ability to distinguish sensitizing mutations *in vivo*. No major differences were observed in the kinetics of the reversible and the irreversible tracer in each of the xenograft models. Under P-gp blocking conditions no significant changes in tumor-to-background ratio were observed, however, [^{18}F]afatinib demonstrated better tumor retention in all xenograft models.

Conclusions: TKI-PET provides a method to image sensitizing mutations and can be a valuable tool to compare the distinguished targeting properties of TKIs *in vivo*.

4.1 Introduction

Recent developments in molecular biology have led to an increased understanding of the signal transduction pathways in cancer and crucial molecular targets have been identified that are involved in cancer growth, survival and metastasis. Furthermore, increased structural understanding of proteins and their specific chemical interactions combined with high throughput screening and medicinal chemistry efforts have led to major breakthroughs in drug discovery. Together this has led to the development of tailor-made targeted pharmaceuticals as anti-cancer drugs. Receptor tyrosine kinases (RTKs) form a family of transmembrane proteins that have received a lot of interest as they play a pivotal role in the signal transduction pathways of the cell. RTKs consist of an extracellular domain capable of ligand binding and an intracellular domain for downstream signaling. Prominent members of this family include the epidermal growth factor receptor (EGFR) and the vascular endothelial growth factor receptor (VEGFR)[1, 2].

The development of small molecules targeting kinases has expanded enormously in the last years. 22 small molecule tyrosine kinase inhibitors (TKIs) have been approved by the US Food and Drug Administration with an estimated several hundreds under (pre)clinical development. These TKIs act on the intracellular catalytic kinase domain by competing with ATP and induce inhibition of downstream signaling [3]. Good cell uptake and long-lasting, high affinity binding to the RTK are required to effectively compete with the high intracellular ATP concentration [4]. Although the approval rate of new TKIs is high and substantial patient benefit is achieved, there is a lack of long term efficacy in certain patients with RTK-driven tumors. The underlying cause of this inter-patient variability is best understood for EGFR targeting kinase inhibitors in non-small cell lung cancer (NSCLC) [5].

Activating mutations in the kinase domain of EGFR dictate effectiveness of TKIs that are currently on the market. The most common sensitizing mutations are small in-frame deletions in exon 19 (45%) or the L858R missense mutation (40-45%) in exon 21 leading to favorable response rates of EGFR TKIs [6]. As a result, EGFR-TKI therapy is especially effective in NSCLC patients with tumors displaying an activating EGFR mutation which occurs in 5 to 25% of the Caucasian NSCLC patient population [7, 8]. In clinical practice, mutational status is determined by an invasive biopsy of the tumor tissue, which does not always provide a representative overview of the genomic heterogeneity of the tumor [9]. Unfortunately, despite initial promising response, most patients develop resistance against first generation, reversible, TKIs such as erlotinib and gefitinib [10]. About half of the recurrences are associated with the occurrence of an additional point mutation, i.e. the exon 20 T790M, which compared to the single EGFR mutant displays increased affinity for ATP and thus reduced affinity for first generation reversible inhibitors.

Second generation TKIs such as dacomitinib or afatinib, that covalently bind to EGFR, have been developed and afatinib has recently obtained marketing approval for first line treatment of lung cancer patients with common activating EGFR mutations [11]. This new generation of inhibitors not only binds covalently to their target molecules but also inhibits all kinase competent members of the ErbB receptor family, which are EGFR, HER2 and ERBB4. Most mutant isoforms of these ErbB receptors including EGFR T790M are also inhibited by these new molecules, which therefore bear the potential to delay or even circumvent some of the resistance mechanisms set off by first generation inhibitors.

In recent publications we, amongst others, have demonstrated the use PET imaging with radiolabeled TKIs (TKI-PET) as a tool to address TKI disposition *in vivo*. By labeling the TKI with a positron emitting radionuclide and maintaining its original structure, these PET tracers can be used to assess the *in vivo* biodistribution, pharmacokinetics (at tracer level), off-target binding and more importantly tumor targeting of the therapeutic itself by means of PET [12, 13]. TKI-PET could also become a technique to identify patients who might benefit from treatment, thus providing a non-invasive predictive tool for personalized medicine [3, 12, 13].

However, whether irreversible TKIs differ from reversible TKIs in their *in vivo* tumor targeting properties, is not known and is subject of this study.

Erlotinib (Tarceva ®, Roche, **1**, Figure 1) is a first generation, reversible, 4-anilinoquinazoline inhibitor of EGFR and was approved in 2004 for NSCLC treatment of patients with locally advanced or metastatic NSCLC in combination with chemotherapy. No patient selection based on mutation analysis was performed at the time of approval and all NSCLC patients eligible were treated with erlotinib [14]. In the following years it became clear that EGFR mutations are of great importance for efficacy of erlotinib (and other first generation EGFR TKIs, such as gefitinib) and erlotinib was subsequently approved in 2013 as a first-line treatment for patients whose tumors harbor an exon 19 deletion or an exon 20 point mutation [15]. TKI-PET imaging with the tracer [^{11}C]erlotinib was first reported by Memon *et al.* in a seminal study demonstrating selective uptake in treatment sensitive xenografts with activating mutations of EGFR. In this preclinical study no metabolite analysis was performed [16]. Subsequently clinical evaluation was performed by the same group in NSCLC patients demonstrating uptake in a subgroup of patients, however, in that study mutational status was not reported [17]. The first proof-of-principle in a clinical study was recently published by Bahce *et al.* in which NCSLC patients with responsive EGFR exon 19 deleted tumors showed increased uptake of [^{11}C]erlotinib when compared to patients with non-responsive EGFR wild-type tumors. Furthermore, in these patients a metabolite analysis was performed demonstrating circa 50% intact [^{11}C]erlotinib in plasma and mainly polar metabolites. This was the first study ever demonstrating the predictive potential of an EGFR TKI-PET tracer, therefore this tracer was used as “gold standard” reference in this study [18].

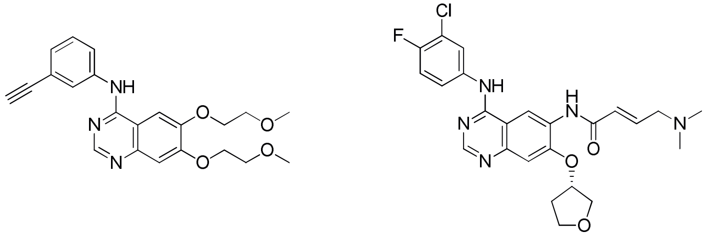

1
Erlotinib

2
Afatinib

Figure 1: Chemical structures of erlotinib and afatinib

Afatinib (Giotrif/Gilotrif®, Boehringer Ingelheim, **2**, Figure 1) is a second generation, irreversible, 4-anilinoquinazoline inhibitor of EGFR [19]. By virtue of its Michael acceptor moiety it is an irreversible inhibitor, which acts by covalent binding to a cysteine residue in the ATP binding domain of EGFR (Cys 797), HER2 (Cys 805) and ERBB4 (Cys 803) [19, 20]. It can be hypothesized that covalent binding of afatinib to EGFR could result in longer retention in the tumor as compared to the reversible TKI erlotinib and thus could provide a PET probe with improved tumor retention. Afatinib has recently gained approval for the treatment of patients with metastatic NSCLC whose tumors harbor common EGFR activating mutations [11].

We recently reported the fluorine-18 labeling of afatinib and initial preclinical evaluation (described in chapter 3) [21]. These studies demonstrated excellent *in vivo* stability of the tracer, with over 80% of intact [^{18}F]afatinib present 45 min p.i. in blood plasma. Uptake in NSCLC xenografted mice was also observed. These achievements now allow for the first time the direct comparison of the tumor targeting potential of the first generation reversible TKI [^{11}C]erlotinib and the second generation irreversible TKI [^{18}F]afatinib, both approved for treatment of NSCLC. The aim of the study described in this chapter was to determine whether irreversible TKIs have improved tumor targeting properties and kinetics and to investigate the influence of drug efflux transporters on the tumor uptake kinetics of these compounds.

4.2 Results and discussion

4.2.1 Radiochemistry

The synthesis of [^{11}C]erlotinib has been described previously and involves a straightforward alkylation employing [^{11}C]MeI on a terminal alcohol (**3**) depicted in scheme 1, providing [^{11}C]erlotinib in high radiochemical yields (up to 4 GBq) and high specific activity (287 ± 63 GBq/µmol) [18].

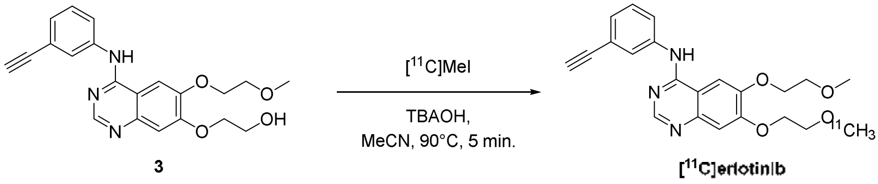

Scheme 1: Radiosynthesis of [^{11}C]erlotinib; Abbreviations: TBAOH: tetrabutylammonium hydroxide; DMF; dimethylformamide.

The synthesis of [^{18}F]afatinib (scheme 2) was recently published by our group and involves a BOP (Benzotriazol-1-yloxy)tris(dimethylamino)phosphonium hexafluorophosphate) mediated coupling of 3-chloro-4-[^{18}F]fluoroaniline ([^{18}F]**6**) with **7** as a key step (chapter 3) [21]. The synthesis of [^{18}F]afatinib starts with nucleophilic fluorination on **4** with ^{18}F$^-$/K[2.2.2] (kryptofix, 4,7,13,16,21,24-Hexaoxa-1,10-diazabicyclo[8.8.8]hexacosane) in the presence of K_2CO_3, for 25 minutes. After a solid phase extraction the resulting 3-chloro-4[^{18}F]fluoro-nitrobenzene ([^{18}F]**5**) is subjected to a reduction using sodium borohydride in the presence of palladium on carbon, thus furnishing the desired 3-chloro-4[^{18}F]fluoro-aniline ([^{18}F]**6**). The final step is a BOP mediated condensation of aniline **6** with **7** to provide [^{18}F]afatinib in high yields (up to 3.5 GBq) and high specific activity (223 ± 38 GBq/µmol) after HPLC purification. Initial *in vivo* stability as well as *ex vivo* biodistribution studies demonstrated excellent *in vivo* stability of the tracer and uptake in NSCLC xenografted mice, although no large differences with regard to uptake between WT and the exon

19 deleted mutant of EGFR were observed in *ex vivo* biodistribution studies, therefore necessitating further PET-studies described in this chapter [21].

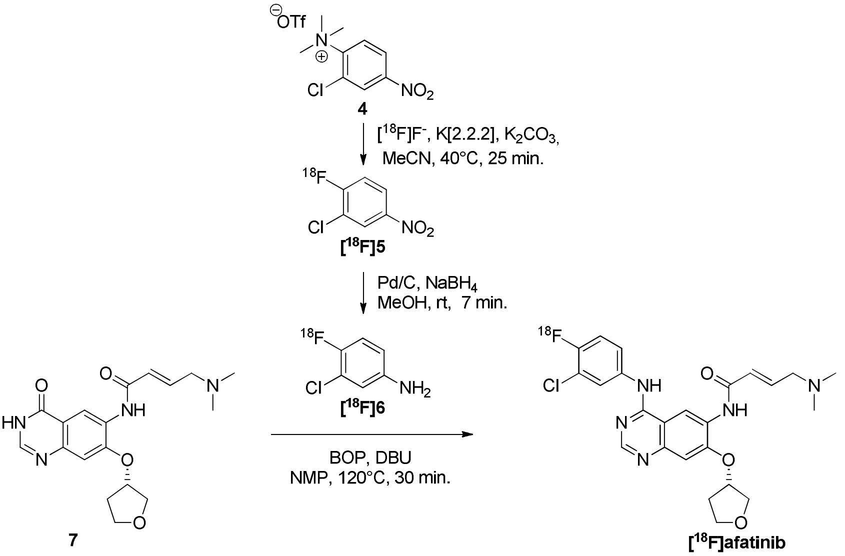

Scheme 2: Radiosynthesis of [^{18}F]**6** and subsequent condensation towards [^{18}F]afatinib. Abbreviations: MeCN: acetronitrile; MeOH: Methanol; DBU: 1,8-diazabicyclo[5.4.0]undec-7-een; NMP: *N*-methylpyrolidone.

4.2.2 Xenograft Characterization

Three NSCLC cell lines were selected for the generation of xenografts and the *in vivo* evaluation of [^{11}C]erlotinib and [^{18}F]afatinib, each expressing a specific EGFR mutation and thus providing a representative overview of mutations found in clinical cases of NSCLC [22]. Firstly, an insensitive reference cell line which expresses EGFR wild-type was selected (A549). Next, a cell line (H1975) which expresses a double mutant of EGFR (L858R/T790M); the first being one of the common sensitizing mutations in exon 21 (L858R) and the second a mutation associated with acquired resistance to erlotinib therapy (T790M in exon 20). Finally, a cell line was selected which is highly sensitive to TKI-treatment, namely the HCC827 cell line which harbors a deletion in exon 19 (delE746-A750). The sensitivity of these cell lines towards the two inhibitors has been clearly described in literature [19, 23, 24]. The results of *in vitro* studies and *in vivo* xenograft experiments demonstrated excellent efficacy of both inhibitors. The double mutant H1975 cells were shown to be resistant to treatment with erlotinib but showed a reduction in tumor growth rate *in vivo* upon afatinib treatment, although significantly less than HCC827. Finally, neither erlotinib nor afatinib showed any *in vitro* or *in vivo* efficacy to the wild-type A549 cells and xenografts, which despite expressing EGFR are not dependent on the ErbB signaling network for proliferation.

To fully characterize these cell lines before the start of PET imaging studies they were xenografted onto athymic nu/nu mice and immunohistochemistry and sequencing was performed on xenograft material. EGFR expression was found in all lines (Figure 2) and although immunohistochemistry is a semi-quantitative technique staining appeared most intense in HCC827 xenografts. EGFR mutations of the xenografts, as described before, were confirmed by sequencing. Finally, the tumors were stained for the expression of P-gp, a drug efflux transporter, for which erlotinib and afatinib are known substrates [25, 26]. Staining indicated that this efflux transporter was most extensively expressed by HCC827 xenografts.

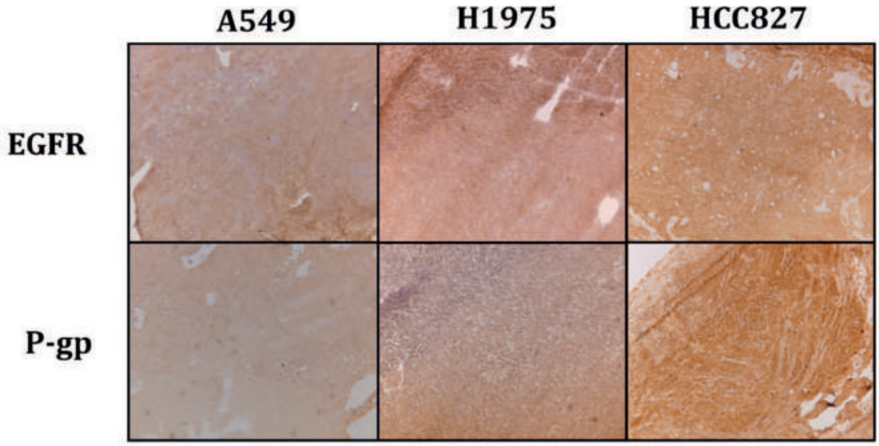

Figure 2: Immunohistochemical staining of NSCLC xenograft lines as used in PET-studies. Images depicted at 5x magnification. Mutations: A549 (wild type), H1975 (L858R/T790M), HCC827 (exon 19 deletion).

4.2.3 PET imaging with [^{11}C]erlotinib and [^{18}F]afatinib in lung cancer xenografts

PET-imaging was performed with both tracers in all three xenograft models to determine whether the irreversible inhibitor shows better tumor targeting. In order to have a proper region for the background tissue, the mice were grafted with a single tumor on the left flank. In this manner the right flank of the animal served as reference region as this contralateral tissue is the same except that it is devoid of tumor cells. Both tumor and background were manually outlined on the basis of an additional [^{18}F]FDG scan, which was performed directly after the TKI-PET scan was finished. Percentage injected dose per gram of tissue (%ID/g) can be directly derived from these PET-scans as a quantitative measure of uptake.

The images and time-activity-curves (TACs, depicting activity concentration over time) of the PET study are shown in Figure 3 and the tumor to background ratios (resulting from a comparison between activity concentration in the tumor and reference tissue) are summarized in Table 1. Since [^{18}F]afatinib has a longer half-life than [^{11}C]erlotinib, [^{18}F]afatinib could be scanned for longer time periods. However, no significant changes were observed in this later frame with regard to uptake. The images shown (Figure 3) are from the last 30 minutes of the scan (60-90 minutes for [^{11}C]erlotinib and 90-120 minutes for [^{18}F]afatinib), representing the highest tumor-to-background ratios. High uptake is observed in the liver and kidneys for both tracers, which is common for IV administered small molecular PET-tracers as these organs represent the major excretion and catabolic routes. The most striking difference between the two tracers is that [^{11}C]erlotinib displays significantly slower kinetics when compared to [^{18}F]afatinib, irrespective of the xenograft line studied. Indeed, [^{11}C]erlotinib (reversible inhibitor) reaches peak uptake in the tumor (HCC827) at 25 min of 3.2 ± 0.3 %ID/g post injection (p.i.), whereas [^{18}F]afatinib (irreversible inhibitor) activity concentration in the tumor (HCC827) is already at a maximum of 1.2 ± 0.2 %ID/g at 10 min p.i., indicating faster kinetics and/or clearance

(Figure 3). This results in a higher activity concentration in the case of [^{11}C]erlotinib in all tissues of interest (tumor and background) when compared to [^{18}F]afatinib.

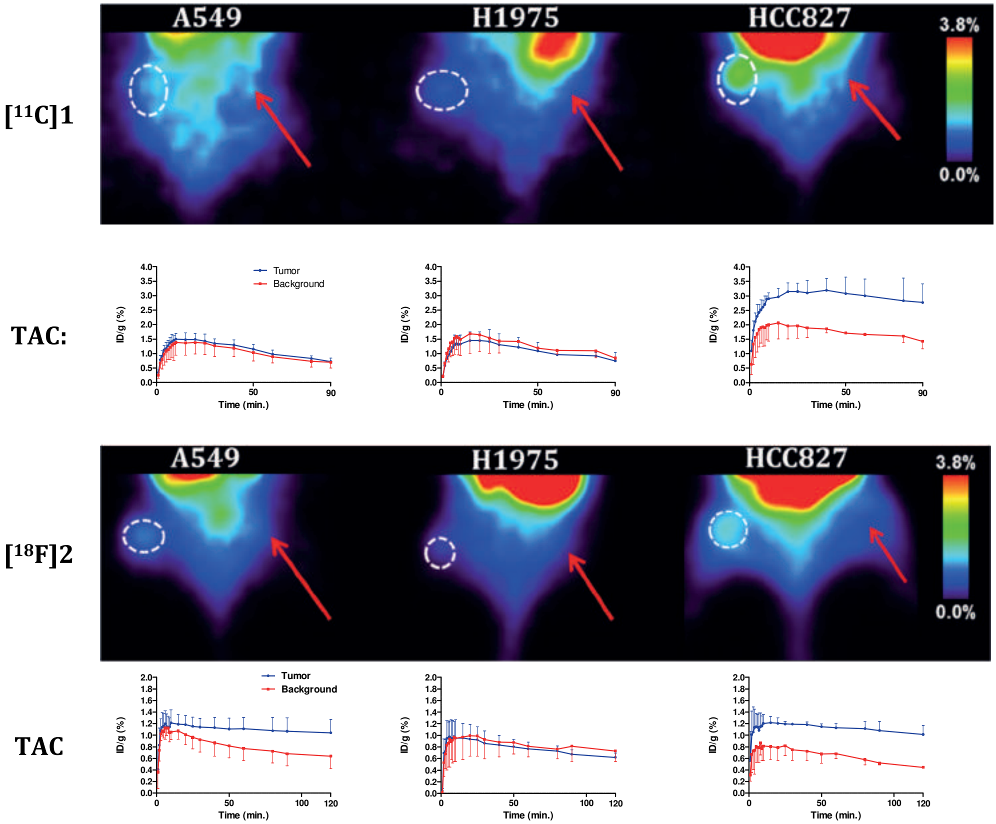

Figure 3: PET-images and time-activity-curves (TACs) of [^{11}C]erlotinib (top) and [^{18}F]afatinib (bottom). Circle indicates tumor position and arrow indicates reference tissue. [^{11}C]erlotinib images summed from 60-90 minutes, [^{18}F]afatinib images from 90-120 minutes. TACs are averaged over 3 animals. Mutations: A549 (wild type), H1975 (L858R/T790M), HCC827 (exon 19 deletion). Tumor and background were manually outlined on the basis of an additional [^{18}F]FDG scan, which was performed directly after the TKI-PET scan was finished.

Regarding the general imaging properties, both tracers appear to have a similar uptake pattern across the various xenograft lines with their distinguished mutational status (Figure 3). In xenografts expressing wild type EGFR (A549), [^{11}C]erlotinib does not show any selective accumulation which is comparable with previous literature reported on this tracer [16]. [^{18}F]afatinib demonstrates a modest, yet statistically significant uptake in A549 cells (Table 1, entry 4).

***Table 1**: Summary of tumor-to-background ratios*

Cell line	#	Tumor-to-background [^{11}C]erlotinib	#	Tumor-to-background [^{18}F]afatinib
		unblocked		
A549	1	1.0 ± 0.3	4	1.5 ± 0.3*
H1975	2	0.9 ± 0.3	5	0.8 ± 0.2
HCC827	3	1.9 ± 0.5*	6	2.3 ± 0.4*
		Tariquidar blocked (15 mg/kg)		
A549	7	1.2 ± 0.3	10	1.3 ± 0.3*
H1975	8	1.0 ± 0.2	11	0.8 ± 0.2
HCC827	9	1.8 ± 0.3*	12	1.9 ± 0.4*

Tumor-to-background ratios in non-blocked (1-6) and blocked situation (7-12), ratios determined in the last frame of the scans (60-90 minutes for [^{11}C]erlotinib and 90-120 minutes for [^{18}F]afatinib) and averaged over 3 animals. P-gp blocking was performed with 15 mg/kg tariquidar. * = Tumor-to-background is statistically significant ($P < 0.05$, Student's t-test for paired data). Mutations: A549 (wild type), H1975 (L858R/T790M), HCC827 (exon 19 deletion).

In the double mutant xenografts (H1975), which harbor a sensitizing mutation (L858R), and an acquired resistance mutation (T790M), no selective uptake was observed for either tracer (Table 1, entry 2 and 5). This result is in good accordance with the efficacy of erlotinib, as it shows no therapeutic effect in this xenograft model. However, afatinib showed a modest but significant reduction in tumor growth rate of H1975 xenografts [20, 24], whereas no significant tumor uptake of [^{18}F]afatinib was observed (Figure 3).

Both [^{11}C]erlotinib and [^{18}F]afatinib demonstrate best uptake in the HCC827 xenografts. [^{18}F]afatinib demonstrates a slightly higher tumor-to-background ratio than [^{11}C]erlotinib (Table 1, entry 3 and 6). This data demonstrates the ability of TKI-PET to image TKI uptake in these tumors in an effective manner. It was previously demonstrated that uptake of [^{11}C]erlotinib in HCC827 xenografts could be blocked by the addition of unlabeled erlotinib [27]. To ascertain whether imaging should be performed at high specific activity in the case of [^{18}F]afatinib (4-6 MBq, 0.017-0.026 nmol of afatinib), PET-imaging with co-administration of unlabeled afatinib (100 ng – 6000 ng) in a bolus IV injection with the tracer was performed in the HCC827 xenograft line. This demonstrated that uptake of the tracer was blocked to background level with a 100 ng addition of afatinib (Table 2).

Table 2: Blocking of [^{18}F]afatinib uptake in HCC827 xenografts

Added dose of afatinib	**Tumor-to-background ratio**
0 ng	2.3 ± 0.4*
100 ng	1.1 ± 0.4
300 ng	1.0 ± 0.3
1000 ng	0.9 ± 0.2
3000 ng	0.9 ± 0.3

Tumor-to-background ratio after a bolus injection of [^{18}F]afatinib with added isotopically unmodified afatinib. Ratios determined in the last frame of the scans (90-120 minutes) and averaged over 3 animals.* = Tumor-to-background is statistically significant ($P < 0.05$, Student‘s t-test for paired data). HCC827 xenografts harbor an exon 19 deleted variant of EGFR.

Several distinct observations can be made from the results described above. Firstly, the absolute uptake (%ID/g, Figure 3) of [^{18}F]afatinib in HCC827 xenografts is lower in comparison with uptake of [^{11}C]erlotinib, where this was expected to be at least comparable, based on the respective affinities of the compounds for EGFR. Immunohistochemistry demonstrated that HCC827 cells have a high P-gp expression and thus there is a possibility that drug efflux is playing a role in this xenograft line. However, differences in biophysical properties such as lipophilicity, basicity or passive permeation may also influence the apparent uptake of these compounds. Secondly, when comparing the reversible [^{11}C]erlotinib with irreversible [^{18}F]afatinib no significant differences are observed with regard to kinetic profile displayed in the TACs for this xenograft model (Figure 3). Thirdly, no differential uptake compared to the background of [^{18}F]afatinib was observed in H1975 tumors despite the fact that afatinib is therapeutically effective in this xenograft line (Figure 3). Finally, in the wild type xenograft line (A549) no uptake of [^{11}C]erlotinib was observed, while [^{18}F]afatinib did show modest uptake (Figure 3). This could be due to differences in retention which might be attributed to biophysical differences between the two tracers, the ability of [^{18}F]afatinib to bind covalently to additional targets (HER2 and ERBB4, next to EGFR) or differences in affinity for efflux transporters. In an attempt to gain further insight into the role of P-gp in PET tracer uptake an imaging study was performed in the presence of an efflux transporter inhibitor.

4.2.4 Influence of drug efflux transporter on tracer uptake

P-glycoprotein (or multidrug resistance protein 1; MDR1) is an ATP-dependent efflux pump that is responsible for the transport of foreign substrates out of the cells and thereby serves as a defense mechanism against these substrates. P-gp expression was previously observed for H1975 and HCC827 using immunohistochemistry and was higher in the latter, indicating that P-gp inhibition could result in an increased uptake of the PET tracers [25, 26].

Dynamic PET-imaging was performed while blocking P-gp using tariquidar (15 mg/kg). Tariquidar was successfully applied in previous PET-studies to block P-gp [28, 29], although it was recently demonstrated that it is also an inhibitor of Breast Cancer Resistance Protein BCRP, another ABC family efflux transporter [30]. Tracer uptake in brain was also monitored as the blood-brain barrier has, amongst other efflux transporters, high P-gp expression. Pretreatment with tariquidar resulted in an increased uptake of both [^{11}C]erlotinib and [^{18}F]afatinib in the brain (Figure 4) thus showing that biodistribution of both compounds (both P-gp substrates) can be influenced by P-gp blockers.

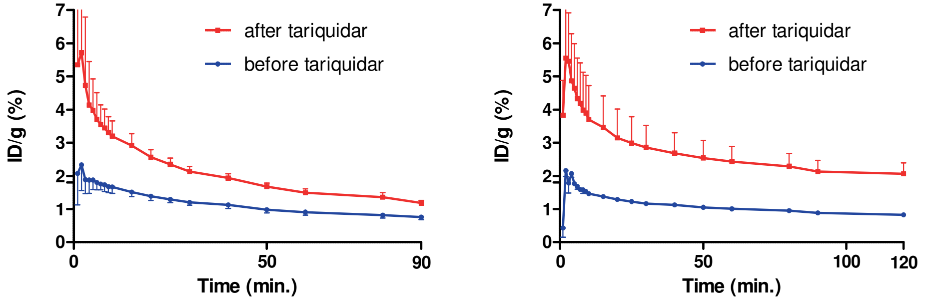

Figure 4: Whole brain time-activity-curves (TACs) of [^{11}C]erlotinib (left) and [^{18}F]afatinib (right) before and after tariquidar pre-treatment. TACs are averaged over 3 animals.

The time-activity-curves of the pre-blocked mice bearing the same tumor models as in the non-blocked condition are depicted in Figure 5. In the wild-type xenograft (A549) a minor increase of [^{11}C]erlotinib tumor accumulation was observed which is also reflected in the tumor-to-background ratio (Table 1, entry 7) although this was not found to be statistically significant. In this xenograft model a higher uptake was observed after treatment with tariquidar in both the tumor and the background (compare Figure 5 with Figure 3). [^{18}F]afatinib also demonstrates a higher absolute uptake of activity (%ID/g) in the tumor and background and no washout was observed in either tissues. Apparently the blocking of the efflux transporter systems with tariquidar resulted in better tissue trapping of [^{18}F]afatinib (Figure 5).

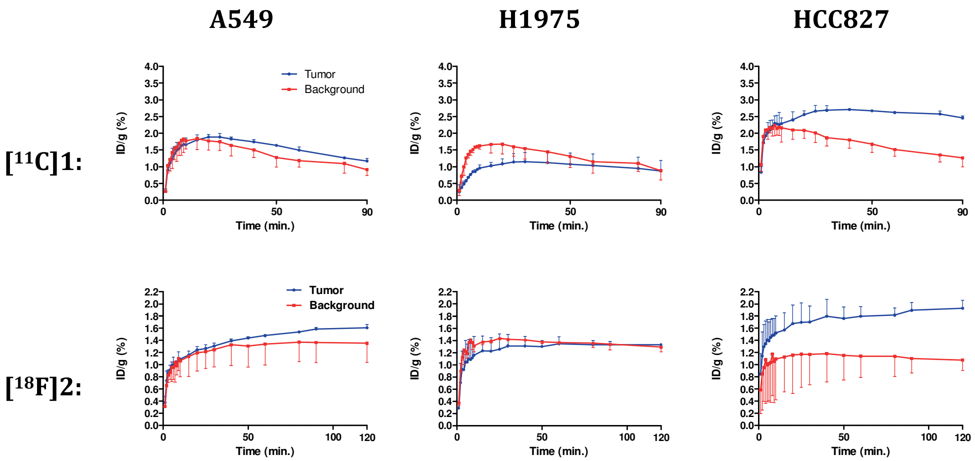

Figure 5: Time-activity-curves (TACs) of [^{11}C]erlotinib (top) and [^{18}F]afatinib (bottom) after tariquidar treatment. TACs are averaged over 3 animals. Mutations: A549 (wild type), H1975 (L858R/T790M), HCC827 (exon 19 deletion). Tumor and background were manually outlined on the basis of an additional [^{18}F]FDG scan, which was performed directly after the TKI-PET scan was finished.

The double mutant (H1975) showed no uptake in the tumor upon P-gp inhibition for [^{11}C]erlotinib (Table 1, entry 8) similar to the unblocked situation (Table 1, entry 2). For [^{18}F]afatinib a higher activity concentration was observed (Figure 5), although the tumor-to-background ratio remained similar to the non-blocked situation (Table 1, entry 5 and 11).

Finally in the HCC827 xenograft no differences were observed for [^{11}C]erlotinib in tumor-to-background ratio (Table 1, entry 3 and 9). In the case of [^{18}F]afatinib a substantial increase of activity concentration was observed (maximal activity concentration: 1.9 ± 0.1 %ID/g vs 1.2 ± 0.2 %ID/g, Figure 3), although this did not lead to higher tumor-to-background ratio, due to a similar increase in the background tissue. It does, however indicate that [^{18}F]afatinib is influenced by efflux transporters to a larger extent than [^{11}C]erlotinib. This is also observed in the kinetics of [^{18}F]afatinib binding, as these are significantly affected. Retention of activity was observed in the HCC827 model in the TAC (Figure 5). This observation is in line with the irreversible mode of binding of afatinib.

An important observation from the blocking study is a moderate increase of activity in all tissues studied for [^{18}F]afatinib (Figure 5). This may be caused by an increase of activity in the blood pool, under P-gp blocking conditions, and hence increased delivery of [^{18}F]afatinib to tissues. This can be explained by the inverse function of P-gp in the intestinal lumen where it normally extracts xenobiotics from the blood [31]. This extraction may be reduced due to the blocking of P-g by tariquidar, resulting in a higher concentration of [^{18}F]afatinib in the blood. The relatively large increase of [^{18}F]afatinib accumulation in the HCC827 tumors indicates that efflux transporters play a significant role in the apparent uptake or efflux of afatinib from these tumors. In the EGFR wild type xenograft A549, showing low P-gp expression, this difference was much less pronounced (Figure 5).

Interestingly the [^{18}F]afatinib time-activity-curves in the A549 and HCC827 xenografts demonstrate an irreversible character with regard to uptake of [^{18}F]afatinib under P-gp blocking conditions (Figure 5). It might well be that efflux by P-gp in the non-blocked situation is relatively fast and quicker than the irreversible binding, resulting in what appears to be reversible kinetics. This effect is not observed for [^{11}C]erlotinib and is in line with a reversible mode of binding. The H1975 xenograft demonstrated no uptake in the blocked or non-blocked situation, which was unexpected on the basis of affinity.

The irreversible binding of afatinib to EGFR-WT and EGFR-T790M, was demonstrated *in vitro* by Solca *et al.* in several experiments, including mass spectrometry and X-ray crystallography of afatinib bound to EGFR-T790M, where a covalent bond between afatinib and EGFR-T790M was demonstrated [19]. The results from the current PET-studies suggest that the *in vivo* tumor uptake of [^{11}C]erlotinib and [^{18}F]afatinib is influenced by P-gp expression levels, and tracer uptake is not completely predictive for the therapeutic efficacy in the H1975 xenograft line. One of the reasons might be that in the current study [^{11}C]erlotinib and [^{18}F]afatinib are administered IV at a tracer dose (µg/kg), while efficacy is tested after oral administration at a therapeutic dose (mg/kg). This justifies further characterization of [^{11}C]erlotinib and [^{18}F]afatinib in PET studies under therapeutic dosage conditions.

4.3 Conclusions

Both [^{11}C]erlotinib and [^{18}F]afatinib are useful TKI-PET tracers for imaging treatment sensitive xenografts harboring exon 19 deletion mutations in EGFR. The good tumor-to-background ratios could in the future be used in clinical decision making for both tracers. The difference between a reversible and irreversible inhibitor could not be demonstrated within a standard PET-imaging situation as both tracers showed similar tumor uptake kinetics. However, when the drug-efflux transporter P-gp is blocked, increased tumor uptake is observed and under those conditions [^{18}F]afatinib reveals different kinetics in the HCC827 model suggestive of irreversible binding. This shows that preclinical TKI-PET imaging can be used to compare tumor targeting properties and tumor kinetics of TKIs, making it a valuable tool for drug design and selection.

4.4 Materials and Methods

Cell lines and reagents

Human lung cancer cell lines A549, H1975 and HCC827 were obtained from the American Type Culture Collection. Erlotinib was obtained from Sequioa Research Products (Pangbourne, United Kingdom) and afatinib was obtained from Axxon Medchem (Groningen, The Netherlands).

4.4.1 Xenografts

Female athymic nude mice (20-25 g) (Harlan, Horst, the Netherlands) were housed in sterile cages under standard conditions (24°C, 60% relative humidity, 12-h light/dark cycles) and provided with water and food *ad libitum*. All reported studies were performed according to national regulation and approved by the local animal experiments ethical committee. Subcutaneous tumors were induced by inoculating approximately $2x10^6$ cells of the A549, H1975 or HCC827 cell lines on the left flank. Approximately 1-2 weeks after tumor cell inoculation, the tumors were of suitable size (100 to 200 mm^3).

4.4.2 Sequencing of xenografts

EGFR mutation analysis was performed on DNA isolated from xenografts using high-resolution melting followed by cycle sequencing of PCR products displaying a suspect melting profile, as described before [32].

4.4.3 Immunohistochemical staining

Sections of frozen xenografts (A549, H1975 and HCC827) were immunostained for assessment of EGFR and P-gp expression. Antibodies were diluted in PBS (phosphate buffered saline) with 1% bovine serum albumin. EFGR was stained with cetuximab (Merck), and P-gp with rabbit polyclonal anti-P-gp (AB103477, ITK diagnostics BV, Uithoorn, the Netherlands). As secondary antibodies rabbit anti-human horseradish peroxidase (P0214, Dako, Glostrup, Denmark) or swine anti-rabbit horseradish peroxidase (P0217, Dako) were used. Cryosections (5 µm) of fresh frozen (tumor) tissue were air-dried and subsequently fixed with 2% paraformaldehyde in PBS for 10 minutes. Sections were blocked with normal rabbit serum (in case of cetuximab) or with normal swine serum (in case of anti-P-gp) and subsequently stained with cetuximab 10 µg/ml (EGFR) or anti-P-gp 5 µg/ml. Color development was performed with diaminobenzidine (DAB) and counterstaining was done with Hematoxiline.

4.4.4 Synthesis of radiotracers

[^{11}C]erlotinib was synthesized as previously described (Scheme 1) [18]. Briefly, cyclotron produced [^{11}C]CO_2 was reduced using $LiAlH_4$ to obtain [^{11}C]CH_3OLi and the latter was subsequently halogenated using hydrogen iodide. The obtained [^{11}C]MeI was distilled to a new vessel containing the hydroxyl labeling precursor **3** (1.0 mg, 2.5 µmol) and TBAOH (tetrabutylammonium hydroxide, 5M aqueous solution, 2 µL, 10 µmol) as a supporting base in acetonitrile (250 µl). The alkylation is performed for 5 minutes at 90 °C. The product was isolated by semi-preparative HPLC, carried out on a Jasco PU-2089 pump equipped with a SymmetryPrep C-18 (Waters, 7 µm, 300 mm × 7.8 mm) using MeCN/25 mM sodium phosphate buffer pH=3.5 (30:70, *v*/*v*) as eluent at a flow rate of 4.3 mL · min^{-1}, a Jasco UV1575 UV detector λ=254 nm) and a custom-made radioactivity detector. Chromatograms were acquired using ChromNAV software (version 1.14.01, Jasco). The collected fraction of the preparative HPLC purification containing the product was diluted with 40 mL of aqueous NaOH (1 mM) and the total mixture was passed over a tC18 plus Sep-Pak cartridge. The cartridge was then washed with 20 mL of sterile water after which the product was eluted from the cartridge with 1.0 mL of sterile 96% ethanol. The ethanol was diluted to 10 volume percent with formulation solution (7.09 mM NaH_2PO_4 in 0.9% NaCl, w/v in water, pH 5.2) and the complete solution was filtered over a Millex-GV 0.22 µm filter into a sterile 20 mL capped vial. To provide a final solution of 10% ethanol in saline (containing 7.09 mM NaH_2PO_4) containing [^{11}C]erlotinib in >99% radiochemical purity as an IV injectable solution in a total synthesis time of less than 30 minutes (from end of isotope production) in high specific activity (287 ± 63 GBq/μmol) and in 13.1 ± 3.7% yield (corrected for decay, up to 3 GBq isolated).

[^{18}F]afatinib was synthesized as previously reported (Scheme 2) [21]. Briefly, cyclotron produced [^{18}F]fluoride was azeotropically dried with acetonitrile/water (9/1, v/v) containing K[2.2.2] (4,7,13,16,21,24-Hexaoxa-1,10-diazabicyclo[8.8.8]hexacosane, 13.0 mg, 34.6 μmol,) and potassium carbonate (2.0 mg, 15 μmol). To the dried residue was added a solution of 3-chloro-4-trimethylammonium-nitrobenzene triflate (**4**, 3.0 mg, 14 μmol) in acetonitrile (0.7 ml) and the mixture was allowed to react for 25 minutes at 40°C. After the reaction mixture was quenched with water (7 mL), 3-chloro-4-[^{18}F]fluoro-nitrobenzene ([^{18}F]**5**) was trapped on a tC18plus Sep-Pak, rinsed with water (10 mL) and subsequently eluted with MeOH (1.5 mL) into a screw cap reaction vessel containing palladium on activated carbon (10%, 3 mg) and sodiumborohydride (10.0 mg, 264 μmol). The reduction was carried out for 7 minutes at 20°C upon which the reaction was quenched by the addition of concentrated hydrochloric acid (37%, 0.1 mL). The thus obtained mixture was passed through a syringe filter (Millex LCR PTFE 0.45 μM / 25 mm) into a new screw cap reaction vessel. Volatiles were removed *in vacuo* and under a helium flow (100 mL•min-1) at elevated temperatures (90°C for 5 min. and 120°C for 2 min.) to obtain the dry 3-chloro-4-[^{18}F]fluoroaniline-HCl salt ([^{18}F]**6**). The product was dissolved in *N*-methylpyrrolidine (NMP, 0.5 ml) and to this solution was added a solution of (*S,E*)-4-(dimethylamino)-*N*-(4-oxo-7-((tetrahydrofuran-3-yl)oxy)-3,4-dihydroquinazolin-6-yl)but-2-enamide (**7**, 2 mg, 6 μmol), BOP (benzotriazole-1-yl-oxy-tris-(dimethylamino)-phosphonium hexafluorophosphate, 5.5 mg, 12 μmol), DBU (1,8-diazabicyclo[5.4.0]undec-7-een, 2.7 μl, 18 μmol) in anhydrous NMP (0.5 mL), which was dissolved 15 minutes prior to addition. The obtained mixture was heated to 120°C for 30 minutes after which it was cooled to 20°C. The product was isolated by semi-preparative HPLC, carried out on a Jasco PU-2089 pump equipped with a C18 Alltima column (Grace, 5 μm, 250 mm × 10 mm) using MeCN/H2O/DiPA

(40:60:0.2, *v*/*v*/*v*) as eluent at a flow rate of 4 mL · min^{-1}, a Jasco UV1575 UV detector (λ=254 nm) and a custom-made radioactivity detector. Chromatograms were acquired using ChromNAV software (version 1.14.01, Jasco). The collected fraction of the preparative HPLC purification containing the product was diluted with 50 mL of water and the total mixture was passed over a tC18 plus Sep-Pak cartridge. The cartridge was then washed with 20 mL of sterile water after which the product was eluted from the cartridge with 1.0 mL of sterile 96% ethanol. The ethanol was diluted to 10 volume percent with formulation solution (7.09 mM NaH_2PO_4 in 0.9% NaCl, w/v in water, pH 5.2) and the complete solution was filtered over a Millex-GV 0.22 μm filter into a sterile 20 mL capped vial. In this way, a final IV injectable solution was provided of 10% ethanol in saline (containing 7.09 mM NaH_2PO_4) containing [^{18}F]afatinib obtained at >98% radiochemical purity, in a total synthesis time of less than 120 minutes (from end of isotope production), at a high specific activity (287 ± 63 GBq/μmol), and in 17.0 ± 2.5% yield (corrected for decay, up to 3.5 GBq isolated).

4.4.5 PET-Imaging

Dynamic PET imaging was performed on three cancer xenograft lines (A549, H1975 and HCC827) in nude mice. Each mouse (n = 3) carried one tumor, which was located on the left flank. Imaging was performed for a duration of 90 ([^{11}C]erlotinib) or 120 min. ([^{18}F]afatinib) using a double-LSO/LYSO layer high-resolution research tomograph (HRRT; CTI/Siemens, Knoxville, TN, USA). The mice were anesthetized with 4% and 2% isoflurane in 1 L.min^{-1} oxygen for induction and maintenance, respectively. First, for attenuation and scatter correction, a transmission scan was acquired using a 740 MBq two-dimensional (2D) fan-collimated ^{137}Cs (662 keV) moving point source. Next, a dynamic emission scan was acquired immediately following administration (IV ocular plexus) of 8-10 MBq [^{11}C]erlotinib (223 ± 38 GBq/μmol) or 4-6 MBq [^{18}F]afatinib (287 ± 63 GBq/μmol) to each animal. Positron emission scans were acquired in list mode and rebinned into the following frame sequence: 10 × 60s, 4 x 300s, and 9 x 600 s. After the TKI scan was finished, [^{18}F]FDG was administered (IV ocular plexus) to the mice followed by scanning for another 60 min. Following corrections for decay, dead time, scatter and randoms, scans were reconstructed using an iterative 3D ordered-subsets weighted least-squares analysis (3D-OSWLS). Point source resolution varied across the field of view from approximately 2.3 to 3.2-mm full width at half maximum in the transaxial direction and from 2.5 to 3.4 mm in the axial direction. Post-filtering was not performed after reconstruction. The PET images were analyzed using the freely available AMIDE-software version 0.9.2 (A Medical Imaging Data Examiner). A box was drawn over the complete animal to obtain the image-derived percentage injected dose per gram (%ID/g). Regions of interest (ROIs) containing the tumor tissue as well as a reference area, which was drawn in the opposite flank of the animal containing exactly the same tissue only devoid of tumor cells, were drawn using the [^{18}F]FDG data, tumor region was defined as FDG positive voxels of the tumor. Subsequently the corresponding images obtained with [^{11}C]erlotinib or [^{18}F]afatinib were overlayed. A time-activity-curve (TAC) was plotted for both the tumor as well as the reference area. The images were smoothed using a Gaussian filter (2 mm).

For PET-imaging studies using mass amounts, afatinib (1.0 mg) was dissolved in DMSO (1.0 ml) and diluted with formulation solution (7.09 mM NaH_2PO_4 in 0.9% NaCl, w/v in water, pH 5.2) to the appropriate concentrations (40 nM, 120 nM, 400 nM and 1200 nM), and after addition of 50 µl [^{18}F]afatinib to 50 µl of these solutions they were injected as a bolus IV injection.

For the P-gp blocking experiments tariquidar for injection (7.5 mg/ml, AzaTrius Pharmaceuticals Pvt. Ltd. Mumbai, India) in saline was diluted to 3.75 mg/ml with saline for injection. In the blocking experiments tariquidar (15 mg/kg) was administered IV 20 minutes prior to tracer injection [29].

4.4.6 Statistical Analysis

Statistical analysis on tumor-to-background ratios was performed using graphpad PRISM (v 5.02, Graphpad Software Inc). Concentration of activity in the tumor (%ID/g, *n* = 3 per group) was compared to concentration of activity in the reference tissue using a one-tailed Student's t-test for paired data.

4.5 References

[1] Ou S-HI. Second-generation irreversible epidermal growth factor receptor (EGFR) tyrosine kinase inhibitors (TKIs): A better mousetrap? A review of the clinical evidence *Crit. Rev. Oncol. Hematol.* **2012**, *83*, 407-421.

[2] Zhang J, Yang PL, and Gray NS. Targeting cancer with small molecule kinase inhibitors *Nat. Rev. Cancer* **2009**, *9*, 28-39.

[3] van Dongen GAMS, Poot AJ, and Vugts DJ. PET imaging with radiolabeled antibodies and tyrosine kinase inhibitors: immuno-PET and TKI-PET *Tumor Biol.* **2012**, *33*, 607-615.

[4] Garuti L, Roberti M, and Bottegoni G. Non-ATP competitive protein kinase inhibitors *Curr. Med. Chem.* **2010**, *17*, 2804-2821.

[5] Kobayashi K and Hagiwara K. Epidermal growth factor receptor (EGFR) mutation and personalized therapy in advanced nonsmall cell lung cancer (NSCLC) *Targeted Oncol.* **2013**, *8*, 27-33.

[6] Sharma SV, Bell DW, Settleman J, and Haber DA. Epidermal growth factor receptor mutations in lung cancer *Nat. Rev. Cancer* **2007**, *7*, 169-181.

[7] Boch C, Kollmeier J, Roth A, Stephan-Falkenau S, Misch D, Grüning W, et al. The frequency of EGFR and KRAS mutations in non-small cell lung cancer (NSCLC): routine screening data for central Europe from a cohort study *BMJ Open* **2013**, *3*.

[8] Marchetti A, Martella C, Felicioni L, Barassi F, Salvatore S, Chella A, et al. EGFR mutations in non–small-cell lung cancer: analysis of a large series of cases and development of a rapid and sensitive method for diagnostic screening with potential implications on pharmacologic treatment *J. Clin. Oncol.* **2005**, *23*, 857-865.

[9] Gerlinger M, Rowan AJ, Horswell S, Larkin J, Endesfelder D, Gronroos E, et al. Intratumor heterogeneity and branched evolution revealed by multiregion sequencing *N. Engl. J. Med.* **2012**, *366*, 883-892.

[10] Pao W, Miller VA, Politi KA, Riely GJ, Somwar R, Zakowski MF, et al. Acquired resistance of lung adenocarcinomas to gefitinib or erlotinib is associated with a second mutation in the EGFR kinase domain *Plos Medicine* **2005**, *2*, 225-235.

[11] Sequist LV, Yang JC-H, Yamamoto N, O'Byrne K, Hirsh V, Mok T, et al. Phase III study of afatinib or cisplatin plus pemetrexed in patients with metastatic lung adenocarcinoma with EGFR mutations *J. Clin. Oncol.* **2013**, *31*, 3327-3334.

[12] Poot AJ, Slobbe P, Hendrikse NH, Windhorst AD, and van Dongen GAMS. Imaging of TKI-target interactions for personalized cancer therapy *Clin. Pharmacol. Ther.* **2013**, *93*, 239-241.

[13] Slobbe P, Poot AJ, Windhorst AD, and van Dongen GAMS. PET imaging with small-molecule tyrosine kinase inhibitors: TKI-PET *Drug Discovery Today* **2012**, *17*, 1175-1187.

[14] Cohen MH, Johnson JR, Chen Y-F, Sridhara R, and Pazdur R. FDA Drug Approval Summary: erlotinib (Tarceva®) Tablets *Oncologist* **2005**, *10*, 461-466.

[15] Wang Y, Schmid-Bindert G, and Zhou C. Erlotinib in the treatment of advanced non-small cell lung cancer: an update for clinicians *Ther. Adv. Med. Oncol.* **2012**, *4*, 19-29.

[16] Memon AA, Jakobsen S, Dagnaes-Hansen F, Sorensen BS, Keiding S, and Nexo E. positron emission tomography (PET) imaging with C-11 -labeled erlotinib: a micro-PET study on mice with lung tumor xenografts *Cancer Res.* **2009**, *69*, 873-878.

[17] Memon AA, Weber B, Winterdahl M, Jakobsen S, Meldgaard P, Madsen HHT, et al. PET imaging of patients with non-small cell lung cancer employing an EGF receptor targeting drug as tracer *Br. J. Cancer* **2011**, *105*, 1850-1855.

[18] Bahce I, Smit EF, Lubberink M, van der Veldt AAM, Yaqub M, Windhorst AD, et al. Development of [^{11}C]erlotinib positron emission tomography for *in vivo* evaluation of EGF receptor mutational status *Clin. Cancer Res.* **2013**, *19*, 183-193.

[19] Solca F, Dahl G, Zoephel A, Bader G, Sanderson M, Klein C, et al. Target binding properties and cellular activity of afatinib (BIBW 2992), an irreversible ErbB family blocker *J. Pharmacol. Exp. Ther.* **2012**, *343*, 342-350.

[20] Li D, Ambrogio L, Shimamura T, Kubo S, Takahashi M, Chirieac LR, et al. BIBW2992, an irreversible EGFR/HER2 inhibitor highly effective in preclinical lung cancer models *Oncogene* **2008**, *27*, 4702-4711.

[21] Slobbe P, Windhorst AD, Walsum MS-v, Schuit RC, Smit EF, Niessen HG, et al. Development of [^{18}F]afatinib as new TKI-PET tracer for EGFR positive tumors *Nucl. Med. Biol.* **2014**.

[22] Janne PA, Engelman JA, and Johnson BE. Epidermal growth factor receptor mutations in non-small-cell lung cancer: Implications for treatment and tumor biology *J. Clin. Oncol.* **2005**, *23*, 3227-3234.

[23] Cha MY, Lee K-O, Kim M, Song JY, Lee KH, Park J, et al. Antitumor activity of HM781-36B, a highly effective pan-HER inhibitor in erlotinib-resistant NSCLC and other EGFR-dependent cancer models *Int. J. Cancer* **2012**, *130*, 2445-2454.

[24] Walter AO, Sjin RTT, Haringsma HJ, Ohashi K, Sun J, Lee K, et al. Discovery of a mutant-selective covalent inhibitor of EGFR that overcomes T790M-mediated resistance in NSCLC *Cancer Discovery* **2013**, *3*, 1404-1415.

[25] Marchetti S, de Vries NA, Buckle T, Bolijn MJ, van Eijndhoven MAJ, Beijnen JH, et al. Effect of the ATP-binding cassette drug transporters ABCB1, ABCG2, and ABCC2 on erlotinib hydrochloride (Tarceva) disposition in *in vitro* and *in vivo* pharmacokinetic

studies employing Bcrp1−/−/Mdr1a/1b−/− (triple-knockout) and wild-type mice *Mol. Cancer Ther.* **2008**, *7*, 2280-2287.

[26] Wind S, Giessmann T, Jungnik A, Brand T, Marzin K, Bertulis J, et al. Pharmacokinetic drug interactions of afatinib with rifampicin and ritonavir *Clin. Drug Invest.* **2014**, *34*, 173-182.

[27] Petrulli JR, Sullivan JM, Zheng MQ, Bennett DC, Charest J, Huang YY, et al. Quantitative analysis of C-11 -erlotinib PET demonstrates specific binding for activating mutations of the EGFR kinase domain *Neoplasia* **2013**, *15*, 1347-1353.

[28] Fox E and Bates SE. Tariquidar (XR9576): a P-glycoprotein drug efflux pump inhibitor *Expert Rev. Anticancer Ther.* **2007**, *7*, 447-459.

[29] Verbeek J, Syvänen S, Schuit RC, Eriksson J, de Lange EC, Windhorst AD, et al. Synthesis and preclinical evaluation of [^{11}C]D617, a metabolite of *(R)*-[^{11}C]verapamil *Nucl. Med. Biol.* **2012**, *39*, 530-539.

[30] Kannan P, Telu S, Shukla S, Ambudkar SV, Pike VW, Halldin C, et al. The “specific” P-glycoprotein inhibitor tariquidar is also a substrate and an inhibitor for breast cancer resistance protein (BCRP/ABCG2) *ACS Chem. Neurosci.* **2010**, *2*, 82-89.

[31] Van Asperen J, Van Tellingen OH, and Beijnen JH. The pharmacological role of P-gp in the intestinal epithelium *Pharmacol. Res.* **1998**, *37*, 429-435.

[32] Heideman DAM, Thunnissen FB, Doeleman M, Kramer D, Verheul HM, Smit EF, et al. A panel of high resolution melting (HRM) technology-based assays with direct sequencing possibility for effective mutation screening of EGFR and K-ras genes *Cell. Oncol.* **2009**, *31*, 329-333.

Chapter 5

Two anti-angiogenic TKI-PET tracers, [^{11}C]axitinib and [^{11}C]nintedanib: radiosynthesis, *in vivo* metabolism and initial tumor targeting potential in rodents

P. Slobbe, R. Haumann, R.C. Schuit, A.D. Windhorst, G.A.M.S van Dongen and A.J. Poot

Published in: *Nuclear Medicine and Biology, **2016**, 43, 612-624*

Abstract

Background: Tyrosine kinase inhibitors (TKIs) are very attractive targeted drugs, although a large portion of patients remains unresponsive. PET imaging with EGFR targeting TKIs ([^{11}C]erlotinib and [^{18}F]afatinib) showed promise in identifying treatment sensitive tumors. The aim of this study was to synthesize two anti-angiogenic TKI tracers, [^{11}C]axitinib and [^{11}C]nintedanib, and to evaluate their potential for PET.

Methods: Following successful tracer synthesis, biodistribution studies in VU-SCC-OE and FaDu xenograft bearing mice were performed. Furthermore, tracer stability studies in mice were performed employing (radio-)HPLC and LC-MS/MS techniques. For [^{11}C]nintedanib an LC-MS/MS method was developed to detect the primary carboxylic acid metabolite, resulting from methylester cleavage, in plasma and tumors, because this metabolite is postulated to be important for nintedanib efficacy. LC-MS/MS was also explored to assess the metabolic fate of [^{11}C]axitinib *in vivo*, since axitinib has an isomerizable double bond.

Results: **:** [^{11}C]axitinib and [^{11}C]nintedanib were successfully synthesized with 10.5 ± 2.6% and 25.6 ± 3.3% radiochemical yield (corrected for decay), respectively. Biodistribution studies only demonstrated tumor uptake of [^{11}C]nintedanib in FaDu xenografts of 1.66 ± 0.02 % ID/g at 60 min. p.i.. *In vivo* stability analysis of [^{11}C]axitinib at 45 min p.i. revealed the formation of predominantly non-polar metabolites (36.6 ± 6.8% *vs* 47.1 ± 8.4% of parent tracer and 16.3 ± 2.1% of polar metabolites), while for [^{11}C]nintedanib mostly polar metabolites were found (70.9 ± 4.1 *vs* 26.7 ± 3.9% of parent tracer and only 2.4 ± 1.6 of a non-polar metabolites). No isomerization of [^{11}C]axtinib was observed *in vivo*, however, a sulfoxide metabolite could be detected using LC-MS/MS. For [^{11}C]nintedanib, LC-MS/MS revealed formation of the reported primary carboxylic acid metabolite when *in vitro* plasma incubations were performed, with large differences in plasmas from different species. *In vivo* metabolite analysis, however, did not demonstrate the presence of the carboxylic acid in plasma or tumor tissue.

Conclusions: Reliable syntheses of [^{11}C]axitinib and [^{11}C]nintedanib were successfully developed. Tumor uptake was observed for [^{11}C]nintedanib, albeit modest. The metabolic profiles of the tracers suggest that rapid metabolism is partly responsible for the modest tumor targeting observed.

5.1 Introduction

One of the hallmarks of cancer is angiogenesis, therefore tyrosine kinases promoting neovascularization in tumors have become important drug targets [1, 2]. This increased understanding of the molecular biology of tumors and their signaling pathways has led to the development of tailor-made targeted pharmaceuticals as anti-cancer drugs [3]. Receptor tyrosine kinases (RTKs) are a particular group of enzymes that act as key players in the signal transduction pathways of growth processes of the cell and are overexpressed in a wide variety of solid malignancies and heavily involved in tumor formation and progression. To date, most prominent members of this family are the epidermal growth factor receptor (EGFR), and the vascular endothelial growth factor receptor (VEGFR). Upon binding of their endogenous ligand (e.g. EGF or VEGF) RTKs oligomerize and transphosphorylation of intracellular tyrosine residues occurs. This activates the downstream signaling and promotes proliferation or angiogenesis and consequently plays an important role in cell survival. As a consequence of aberrant signaling in these pathways tumor formation can occur [4].

There are two main strategies to target kinase receptors involved in angiogenesis; the first option concerns monoclonal antibodies, e.g. ramucirumab, that binds the extracellular domain of the VEGFR2 and competes with the endogenous ligand, or bevacizumab, which binds the signaling ligand VEGF. The second option is small molecule TKIs like sorafenib, which acts intracellularly by competition with ATP for binding at the kinase domain. Of this last category, 9 small molecules that target pro-angiogenic kinases have reached the market and many more are in various stages of clinical development [3]. Despite these apparent successes, response rates can vary dramatically from patient to patient and tools to study this inter-patient variability are therefore of great value.

In recent publications, we and others have demonstrated the use of PET imaging with radiolabeled TKIs (TKI-PET) as a tool to study the *in vivo* behavior of these pharmaceuticals [5, 6]. To perform TKI-PET studies it is important to leave the original structure of the drug unaltered upon radiolabeling, in this manner a representative overview of the behavior of the pharmaceutical (at tracer level) is provided. Furthermore, tracer accumulation can serve as predictive marker when correlation with a therapeutic effect is established. The most prominent example of this concept is found in EGFR imaging in which substantial success was achieved with [^{11}C]erlotinib and [^{18}F]afatinib [7-11].

Contrary to the success obtained in the field of EGFR imaging, the potential of anti-angiogenic TKI-PET has yet to be established. FDA approved anti-angiogenic TKIs have been labeled recently, although preclinical evaluation is sometimes lacking. These analyses might become more complex as anti-angiogenic TKIs are generally promiscuous and have affinity for multiple kinase targets that might be differently expressed in murine and human tissues. Examples include [^{18}F]sunitinib [12], [^{11}C]vandetanib [13] and [^{11}C]sorafenib, of which the latter was most extensively evaluated in preclinical animal models. Broad-spectrum TKI [^{11}C]sorafenib (targeting the RAF-, VEGFR-, PDGFR- and KIT family) was first reported by Asakawa *et al*., who showed the affinity of this TKI for efflux transporters in P-gp/BCRP knock-out mice [14]. Poot *et al*. synthesized [^{11}C]sorafenib as well and investigated its *in vivo* stability and tumor targeting potential in three human cancer xenografts, expressing the main target of sorafenib, RAF1 kinase. Highest uptake (2.52 ± 0.33 %ID/g, 60 min. p.i.) was observed in the xenograft with the highest RAF1 expression [15].

In order to further explore the potential of anti-angiogenic TKI-PET imaging we selected two FDA approved anti-angiogenic TKIs. The aim was to compare a relatively selective TKI with a more promiscuous one with similar kinases as targets, in the same tumor models. Axitinib (AG013736, Inlyta, Pfizer, Figure 1) [16] targeting predominantly VEGFR and to a lesser extent PDGFR and KIT was chosen for comparison with nintedanib (BIBF1120, Vargatef/Ofev, Boehringer Ingelheim, Figure 1), an inhibitor demonstrating similar affinity for VEGFR, PDGFR and FGFR [17]. Apart from the evaluation of the tumor targeting potential of both compounds as PET-tracers, a thorough metabolite analysis was performed using HPLC and LC-MS/MS techniques as both compounds demonstrate a distinguished metabolic profile at a pharmacological dose.

For nintedanib, literature suggests that it is metabolized *via* hydrolysis of the methyl ester moiety to generate a carboxylic acid derivative with affinity for similar therapeutic targets as nintedanib. This metabolism contributes to the cellular retention of the compound and thereby its therapeutic potency [18]. As a consequence of the charge on this carboxylic acid moiety at physiological pH, intracellular trapping of the TKI is improved. Furthermore, this acid is an active inhibitor of the kinase resulting in sustained inhibition. Axitinib comprises a double bond which is susceptible to isomerization. Next to that, several metabolic species are reported for axitinib, such as oxidation at the sulfur atom. For axitinib, most metabolites do not display kinase inhibitory activity. Aforementioned metabolic information has to be taken into account when considering the use of axitinib and nintedanib as PET-tracers [19, 20].

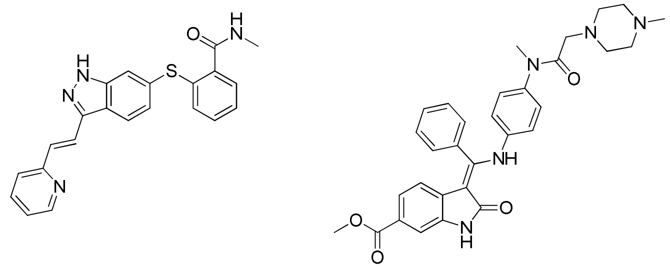

Axitinib (**1**)

Nintedanib (**2**)

Figure 1: Chemical structures of axitinib and nintedanib

5.2 Results and discussion

5.2.1 Chemistry

5.2.1.1 [^{11}C]Axitinib

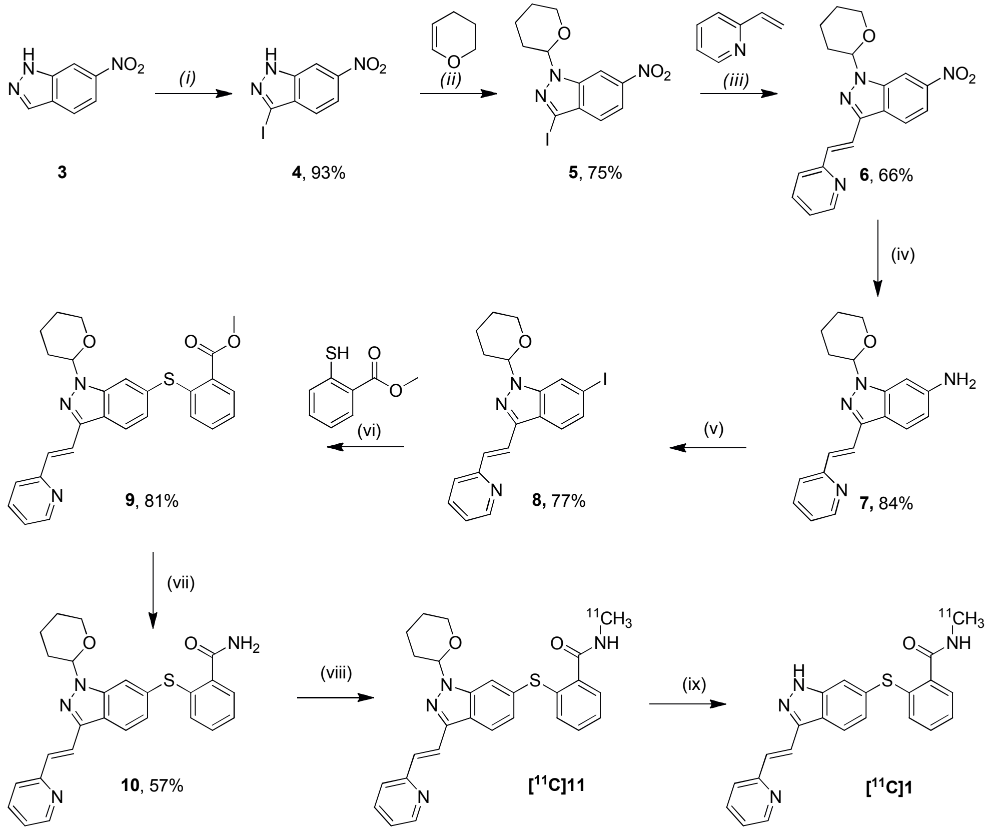

Scheme 1: *(i)* I_2, K_2CO_3, DMF, 2h, rt; *(ii)* $MeSO_3H$, CH_2Cl_2/THF, 16 h, rt; *(iii)* D*i*PEA, Pd(OAC)$_2$ (10 mol%), tri-o-tolylphosphine (30 mol%), DMF, 100°C, 16 h; *(iv)* Fe(s), NH_4Cl, EtOH/H_2O, 2h, 50°C; *(v)* First $NaNO_2$, HCl then CH_2Cl_2, KI/I_2, AcOH/H_2O, 0°C, 4h; (*vi*) Cs_2CO_3, Pd(dppf)$_2$Cl$_2$, DMF, 80°C, 16 h; (*vii*) Formamide, NaOMe, DMF, 2h, 100°C; *(viii)* TBAOH, DMF, 40°C, 5 min; *(ix)* TFA, DMF, 120°C, 3 min

The precursor required to obtain [^{11}C]axitinib, **10**, was synthesized in a 7 step sequence analogous to the patented synthesis procedure for axitinib (Scheme 1) [21]. The first step involves iodination of commercially available 6-nitro-*1H*-indazole in 93% yield. Subsequent protection of the nucleophilic indazole nitrogen is achieved with 3,4-dihydro-*2H*-pyran under acidic conditions in 75% yield. Introduction of the pyridine moiety is achieved via a Heck coupling with 2-vinylpyridine in good yield (66%) and subsequent reduction using iron in ammonium chloride furnished amine **7** in 84% yield. Conversion of amine **7** into aryl iodide **8** was achieved by employing a Sandmeyer reaction in 77% yield. The obtained aryl iodide is reacted with methyl-2-mercaptobenzoate in a palladium catalyzed cross coupling to afford methyl ester **9** in 81% yield. The final step of the precursor synthesis involves the conversion of the methyl ester into the amide functionality required for radiolabeling, which was achieved by reaction with formamide in the presence of sodium methoxide in 57% yield. Due to the nucleophilicity of the indazole nitrogen a protecting group, 3,4-dihydro-*2H*-pyran, was required during the radiolabeling to prevent the formation of undesired side products.

Having precursor **10** in hand, the radiolabeling and deprotection conditions to synthesize [^{11}C]axitinib were explored (Scheme 1). For the carbon-11 methylation, a selection of bases was screened (Table 1, entries 1-6) in DMF at 80°C. This resulted in TBAOH as optimal base. Next the temperature dependance of the reaction was investigated (40-120°C, Table 1, entries 7-10) which did not result in significant changes in HPLC conversion. Subsequently several solvents were evaluated (Table 1, entries 11-13), which demonstrated that DMF was the superior solvent. Finally reducing the amount of solvent and precursor, thereby increasing the [^{11}C]MeI concentration, resulted in a maximal conversion of 51.2%.

Removal of the tetrahydropyran group to obtain the final product is commonly achieved via acidic cleavage. In this case TFA was found to be a suitable deprotection reagent, although elevated temperatures were required (120°C). Complete deprotection to obtain [^{11}C]axitinib was achieved in 3 min. Subsequent semi-preparative HPLC purification provided [^{11}C]axitinib in an overall yield of 10.5 ± 2.6% (corrected for decay), excellent purity (>98%) and high specific activity (206 ± 55 GBq/μmol) in circa 40 min of synthesis time.

Table 1: Optimization of alkylation reaction

#	**Solvent**	**Precursor**	**Base**	**Temp (°C)**	**Volume (μL)**	**HPLC conversion (%)**
1	DMF	1 mg	TBAOH (2 μl)	80	200	33
2	DMF	1 mg	NaH	80	200	2.7
3	DMF	1 mg	K_2CO_3	80	200	1.1
4	DMF	1 mg	NaOH	80	200	14
5	DMF	1 mg	TBAOH (5 μl)	80	200	22.5
6	DMF	1 mg	TBAOH(10 μl)	80	200	24
7	DMF	1 mg	TBAOH (2 μl)	100	200	26
8	DMF	1 mg	TBAOH (2 μl)	120	200	21
9	DMF	1 mg	TBAOH (2 μl)	60	200	29
10	DMF	1 mg	TBAOH (2 μl)	40	200	29
11	DMSO	1 mg	TBAOH (2 μl)	80	200	0.2
12	MeCN	1 mg	TBAOH (2 μl)	80	200	6.7
13	NMP	1 mg	TBAOH (2 μl)	80	200	<0.5
14	**DMF**	**0.5 mg**	**TBAOH (2 μl)**	**40**	**100**	**51.2**

Methylation reactions were performed for 5 min

5.2.1.2 [^{11}C]Nintedanib

The precursor for [^{11}C]nintedanib, desmethyl-nintedanib **21** is prepared from two key building blocks (**15** and **19**) which are both synthesized in three steps and subsequently coupled and deprotected to yield precursor **21** (Scheme 2) [17]. For the first building block *para*-nitromethylaniline is reacted with bromoacetylbromide to yield **13** in 72%. Subsequently **13** is reacted with Boc-piperazine in 87% yield and reduced with Pd/C and hydrogen gas to obtain the amine building block **15**. The synthesis of building block **19** starts with alkylation of methyl 3-nitrobenzoate (**16**) with methyl chloroacetate to yield a mixture of isomers of **17**. After reduction of the nitro functionality to the amine only one of these isomers is able to cyclize to the desired oxindole product **18**, which proceeds in 60% yield. Reaction with (triethoxymethyl)benzene in acetic anhydride provides the exocylic double bond and acetylation in one pot to furnish compound **19.** Coupling of the two building blocks, combined with removal of the acetyl group to provide **20** is achieved in a modest 32% yield. Final cleavage of the Boc-group is achieved by HCl in diethylether to afford the precursor **21** in 78% yield.

Radiosynthesis of [^{11}C]nintedanib involves a straightforward methylation reaction on the piperazine moiety. All alkylation reactions were performed for 5 min at 80°C and subsequently analyzed for conversion with analytical HPLC. After evaluation of a selection of bases in DMF, potassium carbonate was found to be most efficient affording HPLC conversions of 66% (Table 2, entries 1-3). Employing a more reactive methylating agent, methyl triflate did not result in higher incorporation of activity (Table 2, entries 4-7). Using the optimal conditions observed (Table 2, entry 3) and following semi-preparative HPLC purification, [^{11}C]nintedanib was obtained in an overall yield of 25.6 ± 3.3% (corrected for decay), excellent purity (>98%) and high specific activity (213 ± 57 GBq/μmol) in approximately 35 min of synthesis time.

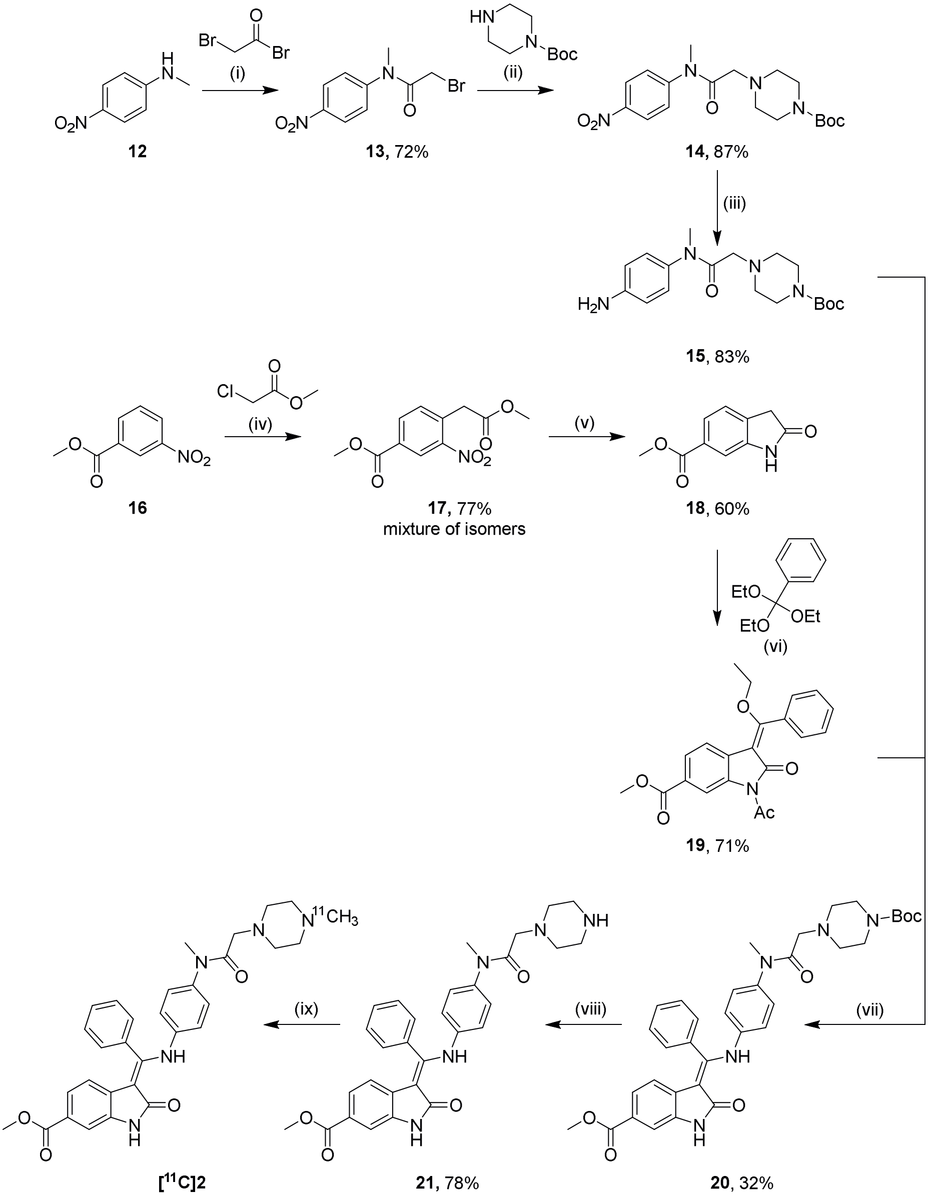

Scheme 2: *(i)* CH_2Cl_2, 2 h, 0°C-rt; (*ii*) K_2CO_3, acetone, 3h, rt; Pd/C, H_2, MeOH, 2h, rt; (*iv*) KOtBu, DMF, 10 min, -10°C; (*v*) Pd/C, H_2, acetic acid, 5h, rt; (*vi*) acetic anhydride, 7h, 130°C; (*vii*) piperidine, DMF, 100°C, 2h; (*viii*) HCl, diethylether, 1h, rt; *(ix)* [^{11}C]MeI, K_2CO_3, DMF, 80°C, 5 min

Table 2: Optimization of alkylation reaction

#	[^{11}C]Synthon	Solvent	Base	HPLC conversion (%)
1	[^{11}C]MeI	DMF	Et_3N	32 %
2	[^{11}C]MeI	DMF	TBAOH	9 %
3	**[^{11}C]MeI**	**DMF**	**K_2CO_3**	**66 %**
4	[^{11}C]MeI	DMSO	K_2CO_3	41 %
5	[^{11}C]MeOTf	DMF	Et_3N	27%
6	[^{11}C]MeOTf	DMF	K_2CO_3	64 %
7	[^{11}C]MeOTf	DMSO	K_2CO_3	38 %

Methylation reactions were performed at 80°C for 5 min

5.2.2 Xenograft selection

To investigate the tumor targeting properties of both [^{11}C]axitinib and [^{11}C]nintedanib, xenografts expressing angiogenic tyrosine kinases which are targeted by axitinib and nintedanib were selected. First, a patient derived head and neck squamous cell carcinoma (HNSCC) xenograft was selected: VU-SCC-OE [22]. As a second cell line we selected another HNSCC cell line, FaDu, and generated xenografts in mice. Expression of angiogenic kinases was demonstrated in these lines by immunohistochemical staining (Figure 2). Both lines express the VEGFR family to variable extent, FaDu demonstrating slightly higher expression. High expression of FGFR was observed in both xenograft lines, while no expression of PDGFR was observed.

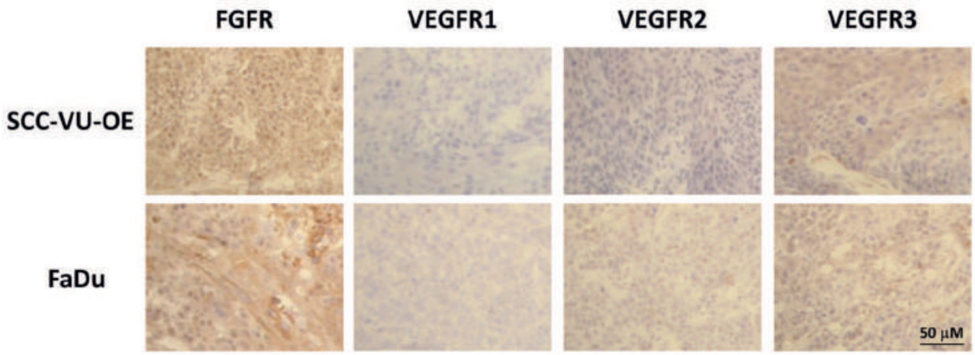

Figure 2: Immunohistochemical staining of xenografts for antiangiogenic target expression

5.2.3 Biodistribution studies

In order to assess the tumor targeting potential of [^{11}C]axitinib and [^{11}C]nintedanib an *ex vivo* biodistribution study was performed. Mice bearing SCC-VU-OE or FaDU xenografts were administered 15-20 MBq of either tracer (corresponding to 0.07 – 0.9 nMol of axitinib or 0.07-0.10 nMol of nintedanib) and were analyzed for biodistribution at 30 and 60 min p.i. (Figure 3). Both tracers demonstrated high liver uptake, as is often observed for small molecular PET tracers. Furthermore, renal uptake of both compounds was observed but was significantly higher for [^{11}C]nintedanib. Uptake in the lung was observed for both compounds, however, uptake was significantly higher for [^{11}C]nintedanib with circa 10% ID/g at 60 min p.i. compared to circa 2.5% ID/g for [^{11}C]axitinib. Tumor uptake was very low for [^{11}C]axitinib in both xenograft lines demonstrating only 0.5% ID/g at 60 min p.i. in FaDu as well as VU-SCC-OE and mimicking the blood values observed. On the other hand [^{11}C]nintedanib demonstrated tumor uptake in FaDu xenografts of 1.66 ± 0.02 % ID/g at 60 min p.i. and this uptake was higher than that observed in the blood. Nevertheless, tumor-to-background ratios remain modest. It should be noted, however, that both compounds target growth factor receptors which are generally expressed on the blood vessels in and around the tumor. While the tumor cells of xenografts are of human origin, the blood vessels are murine and therefore receptors expressed in the blood vessels are also of murine origin. The tracers might have different affinity for these receptors when compared to their human isoforms and therefore tumor targeting can be reduced when compared to the human situation. Furthermore, both [^{11}C]nintedanib and [^{11}C]axitinib after having crossed the cellular membrane, have to compete with high intracellular ATP concentrations (which can be in the micromolar range) for binding at the kinase domain of the targeted receptors [23]. While the affinities are in the picomolar to low nanomolar range for both compounds [16, 18], competition for receptor binding is high. Indeed, in the case of [^{11}C]erlotinib (an EGFR inhibitor) good binding is only observed when mutations of the kinase domain occur which reduce ATP affinity compared to EGFR WT [24].

The accumulation of radioactivity in the tumors might be explained by the presence of radioactive metabolites, similar to the metabolic profile observed after therapeutic dosing of axitinib and nintedanib. In the case of [^{11}C]nintedanib this might be beneficial for tumor targeting, however, in the case of [^{11}C]axitinib this can hamper tumor uptake. Rapid metabolism can result in the loss of the radiolabel and can confound imaging or biodistribution data, tumor uptake included. In order to gain a better understanding of the metabolic profile of these tracers and how they relate to metabolites observed at therapeutic dose, a metabolite analysis was performed for both compounds.

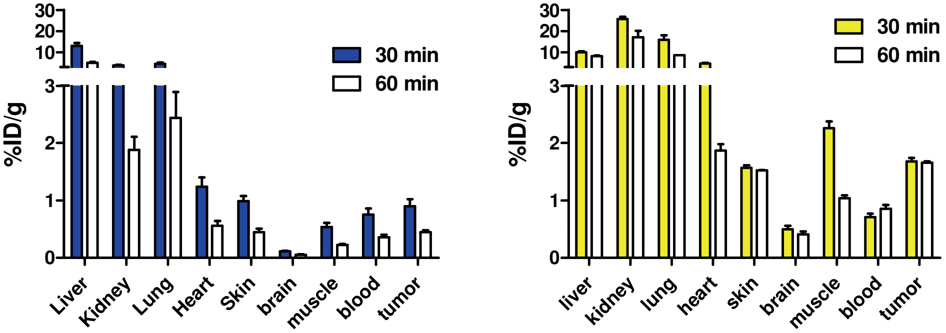

FaDu

[^{11}C]axitinib

[^{11}C]nintedanib

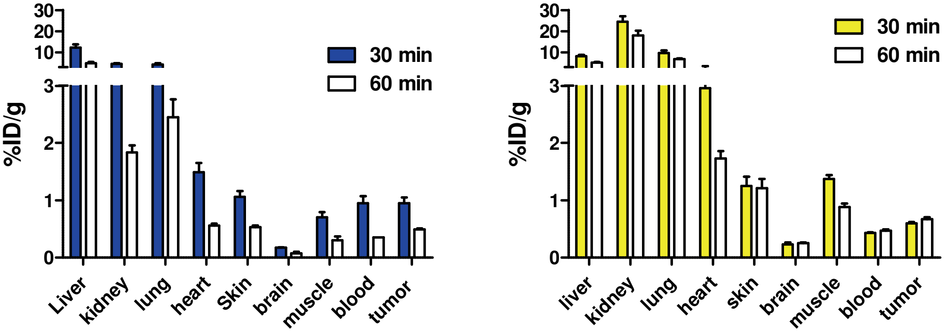

VU-SCC-OE

[^{11}C]axitinib

[^{11}C]nintedanib

Figure 3: Biodistribution studies with [^{11}C]axitinib (left) and [^{11}C]nintedanib (right) 30 and 60 min p.i. in FaDu (top) and VU-SCC-OE (bottom) tumor bearing mice. Mice were administered 15-20 MBq of tracer. Three animals were sacrificed per time point under isoflurane anesthesia

5.2.4 Metabolism

As a first step, the *in vivo* stability of both tracers was determined by a metabolite analysis in non-tumor bearing Balb/c mice. The animals were injected i.v. with 50 MBq of either [^{11}C]axitinib or [^{11}C]nintedanib (corresponding to 0.23 nMol of axitinib or 0.24 nMol of nintedanib) and sacrificed at 15 and 45 min p.i.. Blood samples were collected and analyzed for polar and non-polar metabolites after solid phase extraction of the plasma. [^{11}C]axitinib (Table 3) demonstrated a relatively rapid rate of metabolism with 47.1 ± 8.4% intact 45 min p.i. and predominantly the formation of non-polar metabolites.

Table 3: Metabolite analysis of [^{11}C]axitinib and [^{11}C]nintedanib

Time (p.i.)	**Polar metabolites (%)**	**Non-polar metabolites (%)**	**Parent (%)**
		[^{11}C]axitinib	
15	3.1 ± 0.1	31.9 ± 7.3	65.0 ± 7.3
45	16.3 ± 2.1	36.6 ± 6.8	47.1 ± 8.4
		[^{11}C]nintedanib	
15	35.0 ± 6.6	3.8 ± 3.9	61.2 ± 3.6
45	70.9 ± 4.1	2.4 ± 1.6	26.7 ± 3.9

Plasma of Balb/c mice (*n*=3 per time point)

HPLC analysis of the non-polar fraction revealed one major metabolite with a comparable retention to that of [^{11}C]axitinib (Figure 4). The double bond present in axitinib readily undergoes isomerization from the *trans*- to *cis*-conformation under the influence of light [19] and the retention time of the metabolite is comparable to that of [^{11}C]axitinib. We therefore postulated that the observed metabolite could be *cis*-[^{11}C]axitinib, as this isomerization would only slightly alter the HPLC retention, if at all. In order to test this hypothesis an LC-MS/MS method, capable of detecting the carrier amounts of ions involved in high specific activity PET-tracers, was designed to selectively detect axitinib and its *cis*-isomer.

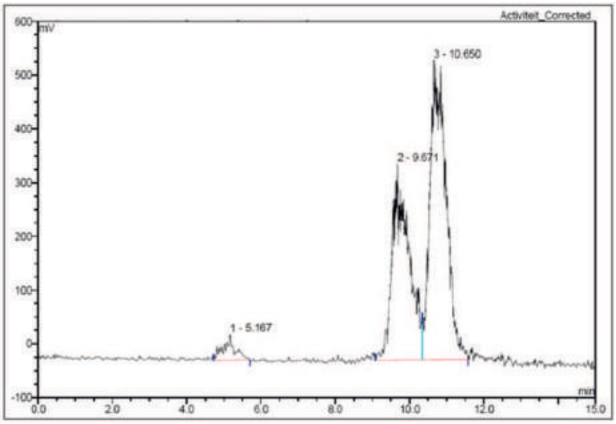

Figure 4: Radio-HPLC chromatogram of the non-polar fraction of the plasma of a Balb/c mouse 45 min p.i. of [^{11}C]axitinib (R_t = 10.65 min) depicting non-polar metabolites (R_t = 5.17 and 9.67 min)

A product ion scan was performed for axitinib, to determine high intensity mass fragments to be used in an MRM method. The transition of 368.9 *m/z* → 356.3 *m/z* was chosen where the fragments correspond to the intact parent ion and loss of a methyl-amine fragment. In this manner, only axitinib and its *cis*-isomer are detected, which can be separated by LC. Analysis of formulated, high specific activity, [^{11}C]axitinib demonstrated a trace amount of *cis*-axitinib present (Figure 5A). Upon exposure of the formulated product to light on the laboratory bench overnight (Figure 5B) and UV light at 365 nM (Figure 5C), isomerization of the double bond was observed, especially when the compound was exposed to UV-light [19]. Finally the non-polar fraction of the plasma was also subjected to the previously described analysis of [^{11}C]axitinib (Figure 5D). This clearly indicated that no *cis*-axitinib was present in this sample, as the ratio of *cis*- to *trans*-axitinib was identical when compared to the purified product. Therefore the observed non-polar radioactive metabolite does not correspond to *cis*-[^{11}C]axitinib. A report on the metabolism of axitinib in humans identifies two major circulating metabolites after administration of [^{14}C]axitinib to healthy volunteers, an *N*-glucuronide derivative and axitinib sulfoxide [20]. Both metabolites showed minimal kinase inhibiting activity. The transition of 403.0 m/z → 372.1 m/z is reported [20] and corresponds to the sulfoxide derivative of axitinib. Using this transition, the sulfoxide could be observed in the plasma samples, indicative of formation of this particular metabolite, providing a possible explanation for the lack of tumor targeting as this particular metabolite lacks affinity for the kinases targeted.

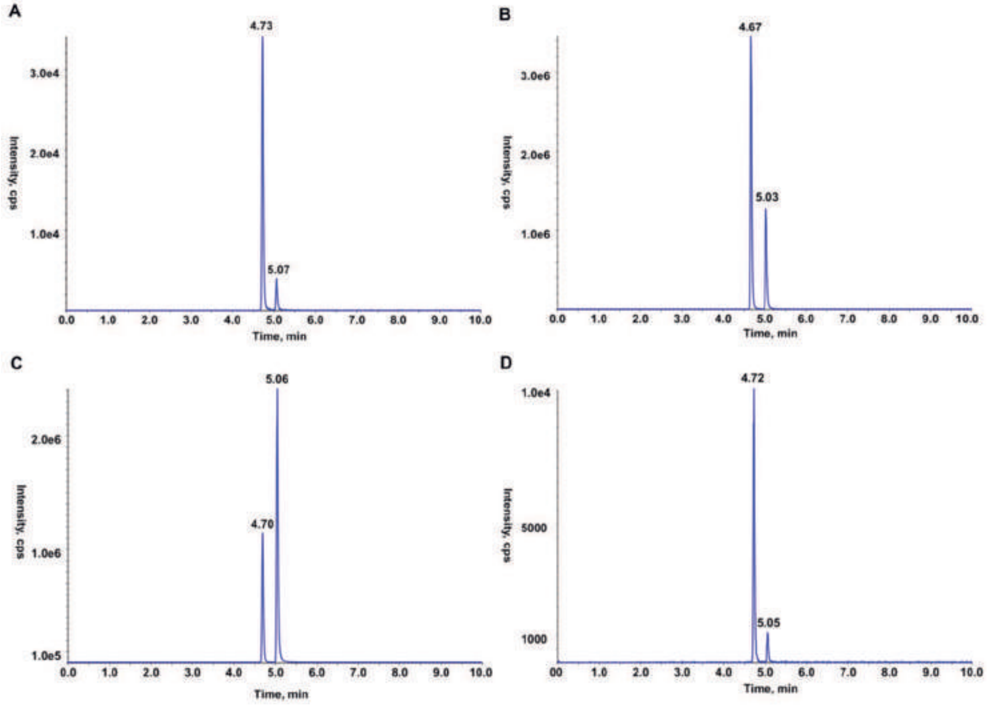

Figure 5: MRM total ion current chromatograms of (transition: 368.9 m/z → 356.3 m/z, trans-axtinib (4.7 min) and cis-axitinib of 5.1 min) depicting A: formulated [^{11}C]axitinib, B: formulated [^{11}C]axitinib exposed to light on the laboratory bench for 16 h, C: formulated [^{11}C]axitinib exposed to UV-light (365 nM) for 15 seconds, D: analysis of the non-polar fraction obtained after solid phase extraction of mouse plasma, 45 min p.i. of [^{11}C]axitinib

A major reported metabolite of nintedanib is its carboxylic acid derivative (**22**), resulting from hydrolysis of the methyl ester by esterases *in vivo* (Scheme 3) [17]. Furthermore, this metabolite is postulated to be formed to a high degree in tumor cells after internalization of nintedanib, and also demonstrates affinity for the kinase. It is of note that this observation holds true for other tissue types as well, due to the ubiquitous expression of esterases. If, however, the trace amounts of [^{11}C]nintedanib are metabolized in plasma before reaching the tumor the tracer will not enter the tumor cells anymore and thereby never reach its intended intracellular target. Initial metabolite analysis of [^{11}C]nintedanib (Table 3) demonstrated a high metabolic rate with circa 25% intact parent left at 45 min p.i. and the formation of predominantly a polar metabolite. This polar metabolite could be resulting from demethylation by which a small polar carbon-11 labeled molecule is formed, or due to the formation of [^{11}C]**22** *in vivo*. The relatively low tumor uptake of [^{11}C]nintedanib could be explained by this high rate of metabolism. This observation prompted further investigation into the metabolic profile of [^{11}C]nintedanib. Metabolite **22**, once formed in plasma, will most likely not pass the cellular membrane anymore and therefore formation of this compound in plasma is detrimental to tumor targeting. To compare the formation of this particular metabolite in plasma *vs* tumor tissue in the same experiment, athymic nu/nu mice (*n*=3) were xenografted with FaDu tumors and injected with [^{11}C]nintedanib. After 45 min the mice were sacrificed and the tumor tissue and plasma were obtained and analyzed via HPLC, after protein precipitation. Two important observations were made: firstly, the tracer itself demonstrated a more moderate rate of metabolism in tumor bearing athymic nu/nu mice when compared to non-tumor bearing Balb/c mice (compare Table 3 with Table 4). Secondly, the tumor tissue contained more parent tracer (75.4 ± 2.0% *vs* 68.2 ± 0.4%) than observed in plasma, indicating a slower metabolic rate in tumor tissue. This might indicate that nintedanib is already metabolized in plasma towards **22**, thereby reducing tumor uptake.

Table 4: Comparison of tumor and plasma metabolites.

	Metabolites (%)	**Parent (%)**
Plasma	31.8 ± 0.2	68.2 ± 0.4
Tumor	24.6 ± 1.8	75.4 ± 2.0

Athymic nu/nu mice bearing two FaDu xenografts at 45 min p.i. of [^{11}C]nintedanib

Finally, in an attempt to identify whether [^{11}C]nintedanib actually metabolizes into [^{11}C]**22**, an LC-MS/MS analysis was performed that could selectively detect the parent (nintedanib) and the carboxylic acid metabolite (**22**) in the previously mentioned tumor and plasma samples. LC-MS/MS was again applied with multiple reaction monitoring [25]. A product ion scan for both pure analytes (nintedanib and **22**) provided two high intensity fragment ions both consisting of the intact parent ion and loss of the dimethylpiperazine fragment. These were used to generate the following MRM-transitions: 540.2 (*m/z*) → 113.1 (*m/z*) for nintedanib and 526.0 (*m/z*) → 112.6 (*m/z*) for **22**, combined with an LC separation (Figure 6) for sensitive detection of both analytes of interest.

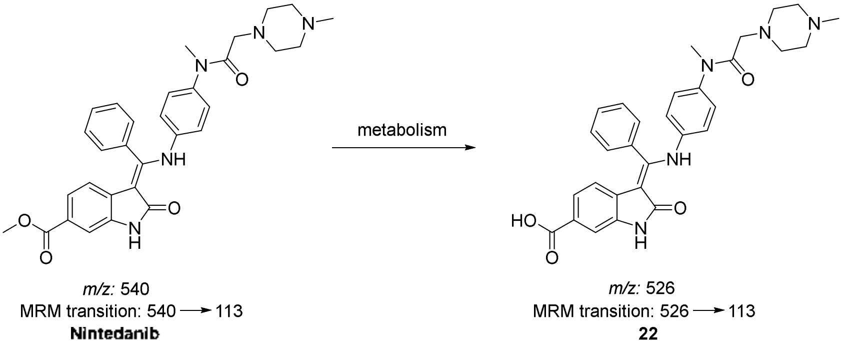

Scheme 3: Metabolic conversion of nintedanib to its carboxylic acid metabolite

To explore the metabolism of nintedanib across different species and to validate the LC-MS/MS method, first plasma analysis was performed. Plasma of several species (athymic nu/nu mouse, Balb/c mouse, rat and human) was incubated with nintedanib (0.4 μM) at 37°C for 3 h and subsequently analyzed using the developed MRM method for the carboxylic acid metabolite and parent nintedanib. Figure 6 depicts the ratio between peak area of **22** and nintedanib. A large difference was observed between the species with regard to formation of the carboxylic acid. The rate of formation of **22** in plasma of athymic nu/nu mice and Balb/c is also in this case significantly different, which is consistent with previous observations *in vivo*. Rat demonstrated the highest conversion to the carboxylic acid metabolite, whereas nintedanib was not metabolized at all in human plasma. This last observation is important for clinical translation of [^{11}C]nintedanib, as tumor targeting might be better in humans as a consequence of higher stability of the tracer in human plasma. The observed differences in formation rate of **22** can be attributed to difference in expression of esterases across the various species, which are responsible for methyl ester hydrolysis [26]. Importantly in the plasma of the animals used for the biodistribution studies carboxylic acid **22** was observed, therefore we performed the same analysis on plasma and tumor tissue obtained from *in vivo* experiments with tumor bearing mice.

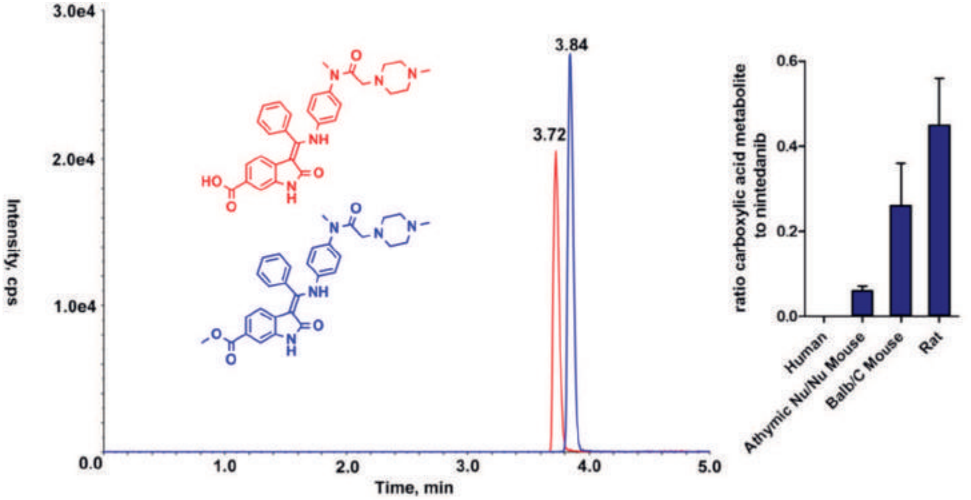

Figure 6: left: MRM total ion current chromatogram of rat plasma sample (**22**: R$_t$ = 3.72; **2**: R$_t$ = 3.84); Right: ratio of **22** to nintedanib observed after incubation of nintedanib for 3 h at 37°C in plasma of various species

Interestingly the LC-MS/MS analysis of the tumor material and plasma from FaDu bearing athymic nu/nu mice did not show the presence of the carboxylic acid metabolite at all. As [^{11}C]nintedanib is administered in high specific activity (213 ± 57 GBq/μmol) and 1.66 ± 0.02% ID/g is found in the tumor (*vide supra*) it might well be that the concentration of the metabolite is under the detection limit of the developed method, although parent nintedanib (carrier) could be clearly detected in these samples without the addition of nintedanib. To confirm this, a therapeutic dose (25 mg/kg) was administered to tumor bearing mice (twice, 24 h and 1 h before the mice were sacrificed) and the same analysis was performed. Also in this case no carboxylic acid metabolite was observed neither in the tumor nor in plasma. It might be that **22** is rapidly cleared from the plasma and therefore was not observed, however, the most striking observation was the lack of carboxylic acid detected in the tumor tissue, indicating that this postulated metabolic process most probably does not occur within the timeframe of analysis of this TKI PET tracer, as clearance from the tumor should be slow due to the low membrane permeability of **22.** Aforementioned results indicate that rapid [^{11}C]nintedanib metabolism might at least be partly responsible for modest tumor targeting.

5.3 Conclusions

Reliable synthesis methods were developed for both [^{11}C]axitinib and [^{11}C]nintedanib to obtain PET tracers of potential value for identifying tumors that are sensitive to these angiogenesis inhibitors. Modest uptake of [^{11}C]nintedanib was observed, however, only in FaDu xenografts. For [^{11}C]axitinib no tumor uptake was observed. To explain *in vivo* biodistribution results an extensive plasma metabolite analysis and characterization was performed. Both tracers showed significant metabolism and therefore the metabolic profile of both tracers was explored.

[^{11}C]axitinib predominantly formed a non-polar metabolite, most likely a sulfoxide derivative that does not show target affinity. This observation is likely to contribute to the absence of tumor targeting. [^{11}C]nintedanib on the other hand demonstrated a relatively large polar metabolite fraction in mice. The reported carboxylic acid metabolite **22** of nintedanib was observed *in vitro* in plasma incubations of various species, however, not in plasma or tumor material *in vivo*. The lack of tumor targeting by [^{11}C]axitinib, and the modest tumor targeting by [^{11}C]nintedanib can in part be attributed to metabolism, however, also other factors might be responsible. Among others, target expression and/or metabolism in nude mice might not be reflecting the human situation, as demonstrated herein for [^{11}C]nintedanib metabolism.

5.4 Materials and Methods

5.4.1 General

All reactions were carried out under atmospheric conditions unless otherwise stated and all reagents and solvents were supplied by Sigma-Aldrich (St. Louis, USA) and Biosolve B.V. (Valkenswaard, the Netherlands) and used as received unless stated otherwise. Nintedanib was purchased from SelleckChem (Houston, TX, USA) and axitinib from LC Laboratories (Woburn, MA, USA). Dimethylformamide (DMF) and tetrahydrofurane (THF) for anhydrous purposes were stored in dry septum capped flasks charged with molecular sieves. Thin Layer Chomatography (TLC) was performed on Merck (Darmstadt, Germany) precoated silica gel 60 F254 plates. Spots were visualized by UV quenching, ninhydrin- or anisaldehyde tlc staining reagents. Column chromatography was carried out either manually using silica gel 60 Å (Sigma-Aldrich) or on a Buchi (Flawil, Switzerland) sepacore system (comprising of a C-620 control unit, a C-660 fraction collector, 2 C601 gradient pumps and a C640 UV detector) equipped with Buchi sepacore prepacked flash columns. ^{1}H and ^{13}C nuclear magnetic resonance (NMR) spectra were recorded on a Bruker (Billerica, USA) Avance 500 (500.23 MHz and 125.78 MHz, respectively), a Bruker Avance 400 (400.13 MHz and 100.61 MHz, respectively) or a Bruker Avance 250 (250.13 MHz and 62.90 MHz, respectively) with chemical shifts (δ) reported in ppm relative to the solvent. Electrospray ionization mass spectrometry (ESI-MS) was carried out using a Bruker microTOF-Q instrument in positive ion mode (capillary potential of 4500 V). Analytical HPLC was performed on a Jasco PU-2089 pump (Easton, USA) equipped with the appropriate column, eluent and flow rate, with a Jasco UV-2075 UV detector (λ=254 nm) and a NaI radioactivity detector (Raytest, Straubenhardt, Germany). Chromatograms were acquired using GINA star software (version 5.1, Raytest). Semi-preparative HPLC was carried out on a Jasco PU-2089 pump equipped with the appropriate column, eluent and flow rate, a Jasco UV1575 UV detector (λ=254 nm) and a custom-made radioactivity detector. Chromatograms were acquired using

ChromNAV software (version 1.14.01, Jasco). All animal experiments were performed according to Dutch national law ('Wet op de proefdieren', Stb 1985, 336) and approved by the local ethics committee.

5.4.2 Chemistry

3-iodo-6-nitro-*1H*-indazole (4).

To a stirred solution of 6-nitro-*1H*-indazole (5.00 g, 30.6 mmol) and potassium carbonate (13.6 g, 98.0 mmol) was added a solution of iodine (8.56 g, 33.7 mmol) in DMF (20 mL) dropwise. The mixture was stirred until TLC indicated full consumption of the starting material (2 h). Then a solution of sodium thiosulfate was added (100 mL, 0.95 M) and the mixture was stirred for 5 min to obtain an orange solution. To this solution was added water (400 mL) to form a precipitate. The precipitate was isolated, washed with water and dried *in vacuo* at 40°C to yield the product as a yellow solid (8.34 g, 28.8 mmol, 94% yield). ^{1}H-NMR (250.13 Mhz, DMSO-D_6) δ: 8.48 (d, J=1.9 Hz, 1H, H_{ar}), (dd, J=8.9, 2.0 Hz, 1H, H_{ar}), 7.67 (d, J=8.8 Hz, 1H, H_{ar}). ^{13}C-NMR (125.8 Mhz, DMSO- D_6) δ: 147.1 ($C_{q,ar}$-NO_2), 139.8 ($C_{q,ar}$), 130.4 ($C_{q,ar}$), 122.4 (CH_{ar}), 116.0 (CH_{ar}), 108.1 (CH_{ar}), 94.4 ($C_{q,ar}$-I). HR-MS (ESI, 4500V): m/z calculated (M^-): 287.9275, found: 287.8873

3-iodo-6-nitro-1-(tetrahydro-*2H*-pyran-2-yl)-*1H*-indazole (5).

To a stirred solution of 3-iodo-6-nitro-*1H*-indazole (3.30 g, 11.4 mmol) and methanesulfonic acid (74.0 µL, 1.2 mmol) in dichloromethane/tetrahydrofurane (3:2, *v/v*, 250 mL) was added a solution of 3,4-dihydro-*2H*-pyran (2.40 g, 28.5 mmol) in dichloromethane (20 mL) dropwise. The mixture was stirred for 16 h at rt after which the reaction mixture was separated between aqueous $NaHCO_3$ (sat.) and dichloromethane. The organic layer was evaporated and the residue was co-evaporated with acetonitrile (3x) and recrystallized from hot acetonitrile. The crystals were isolated, washed with a small amount of cold acetonitrile, dried *in vacuo* at 40°C to afford the product as off-white crystals (3.2 g, 8.6 mmol, 75% yield). ^{1}H-NMR (250.13 Mhz, DMSO-D_6) δ: 8.81 (d, J=1.9 Hz, 1H, H_{ar}), 8.06 (dd, J=8.8, 1.9 Hz, 1H, H_{ar}), 7.71 (d, J=8.8, 1H, H_{ar}), 6.14 (dd, J=9.6, 2.1 Hz, 1H, H_{THP}), 3.81 (m, 2H, H_{THP}), 2.36 (m, 1H, H_{THP}), 2.03 (m, 2H, H_{THP}), 1.74 (m, 1H, H_{THP}), 1.59 (m, 2H, H_{THP}). ^{13}C-NMR (125.8 Mhz, DMSO-D$_6$) δ: 147.6 ($C_{q,ar}$-NO2), 139.1 ($C_{q,ar}$), 131.6 ($C_{q,ar}$), 123.0 (CH_{ar}), 117.0 (CH_{ar}), 108.0 (CH_{ar}), 95.7 ($C_{q,ar}$-I), 84.5 (CH_{THP}), 67.1 ($CH_{2,THP}$), 29.3 ($CH_{2,THP}$), 25.1 ($CH_{2,THP}$), 22.4 ($CH_{2,THP}$). HR-MS (ESI, 4500V): m/z calculated (M+Na$^+$): 395.9816, found: 395.9726

(*E*)-6-nitro-3-(2-(pyridin-2-yl)vinyl)-1-(tetrahydro-*2H*-pyran-2-yl)-*1H*-indazole (6).

A solution of 3-iodo-6-nitro-1-(tetrahydro-*2H*-pyran-2-yl)-*1H*-indazole (2.00 g, 5.36 mmol), 2- vinylpyridine (751 µL, 6.97 mmol) and DiPEA (1.87 mL, 10.7 mmol) in DMF (80 mL) was purged with Argon for 20 min. Palladium(II)acetate (120 mg, 0.536 mmol) and tri-o-tolylphosphine (489 mg, 1.608 mmol) were added and the vial was sealed under an argon atmosphere and heated to 100°C for 16 h. After TLC indicated full consumption of the starting material the reaction mixture was cooled to 20°C and separated between EtOAc and NH_4Cl (aq, sat.) The organic layer was dried (Na_2SO_4) and concentrated. The crude product was purified by column chromatography (EtOAc:Hexane, 3:7, *v/v*) to afford the product as a yellow solid (1.24 g, 3.54 mmol, 66% yield). ^{1}H-NMR (250.13 Mhz, DMSO-D$_6$) δ: 8.79 (d, J=1.7 Hz, 1H, H_{ar}), 8.63 (d, J=4.6 Hz, 1H, H_{ar}), 8.46 (d, J=8.8 Hz, 1H, H_{ar}), 8.08 (dd, J=9 Hz, 1.9 Hz, 1H, H_{ar}), 7.98 (d, J=16.4 Hz, 1H, H_{ar}), 7.84 (td, J=5.8, 1.7 Hz, 1H, H_{ar}), 7.69 (m, 2H, H_{ar}), 7.32 (dd, J=6.9, 5.3 Hz, 1H, H_{ar}), 6.17 (dd, J=9.2, 2.0 Hz, 1H, H_{THP}), 3.86 (m, 2H, H_{THP}), 2.39 (m, 1H, H_{THP}), 2.03 (m, 2H, H_{THP}), 1.77 (m, 1H, H_{THP}), 1.62 (m, 2H, H_{THP}). ^{13}C-NMR (125.8 Mhz, DMSO-D$_6$) δ: 154.9 ($C_{q,ar}$), 150.2 (CH_{ar}), 146.9 ($C_{q,ar}$-NO2), 142.6 ($C_{q,ar}$), 140.1 ($C_{q,ar}$), 137.5 (CH_{ar}), 131.8 (CH_{ar}), 125.7 ($C_{q,ar}$), 123.6 (CH_{ar}), 123.5 (CH_{ar}), 122.8 (CH_{ar}), 122.4 (CH_{ar}), 116.9 (CH_{ar}), 108.3 (CH_{ar}), 84.6 (CH_{THP}), 67.2 ($CH_{2,THP}$), 29.4 ($CH_{2,THP}$), 25.3 ($CH_{2,THP}$), 22.5 ($CH_{2,THP}$). HR-MS (ESI, 4500V): m/z calculated (M+H$^+$): 351.1452, found: 351.1379

(*E*)-3-(2-(pyridin-2-yl)vinyl)-1-(tetrahydro-*2H*-pyran-2-yl)-*1H*-indazol-6-amine (7).

To a suspension of (*E*)-6-nitro-3-(2-(pyridin-2-yl)vinyl)-1-(tetrahydro-*2H*-pyran-2-yl)-*1H*-indazole (3.00 g, 8.56 mmol) in ethanol (50 mL) was added ammonium chloride (50 mL, aq, sat) and iron (1.91 g, 34.2 mmol). The mixture was heated to 50°C for 2 h after which TLC indicated full consumption of the starting material. The reaction mixture was cooled to 20°C, diluted with THF (20 mL) and filtered through celite. The filtrate was concentrated and diluted with water to precipitate a yellow solid. The solid was collected and purified by column chromatography (EtOAc:hexane:Et_3N, 6:4:0.01, *v/v/v*) to afford the product as an off-white solid (2.30 g, 7.18 mmol, 84% yield). ^1H-NMR (250.13 Mhz, DMSO-D_6) δ: 8.59 (d, J=4.7 Hz, 1H, H_{ar}), 7.80 (m, 3H, H_{ar}), 7.65 (d, J=7.9 Hz, 1H, H_{ar}), 7.46 (d, J=16.4 Hz, 1H, H_{ar}), 7.26 (m, 1H, H_{ar}), 6.65 (m, 2H, H_{ar}), 5.59 (dd, J=9.6, 2.4 Hz, 1H, H_{THP}), 5.49 (s, 1H, -NH_2), 3.90 (d, J=11.3 Hz, 1H, H_{THP}), 3.68 (m, 1H, H_{THP}), 2.40 (m, 1H, H_{THP}), 2.04 (m, 1H, H_{THP}), 1.94 (m, 1H, H_{THP}), 1.74 (m, 1H, H_{THP}), 1.74 (m, 1H, H_{THP}), 1.58 (m, 2H, H_{THP}). ^{13}C-NMR (125.8 Mhz, DMSO-D_6) δ: 155.9 ($C_{q,ar}$), 150.0 (CH_{ar}), 146.9 ($C_{q,ar}$-NH_2), 143.3 ($C_{q,ar}$), 141.2 ($C_{q,ar}$), 137.3 (CH_{ar}), 129.5 (CH_{ar}), 124.6 (CH_{ar}), 122.9 (CH_{ar}), 122.8 (CH_{ar}), 121.6 (CH_{ar}), 114.6 ($C_{q,ar}$), 113.8 (CH_{ar}) , 91.6 (CH_{ar}), 84.6 (CH_{THP}), 67.0 ($CH_{2,THP}$), 29.2 ($CH_{2,THP}$), 25.3 ($CH_{2,THP}$), 22.7 ($CH_{2,THP}$). HR-MS (ESI, 4500V): m/z calculated ($M+H^+$): 321.1710, found: 321.1640.

(*E*)-6-iodo-3-(2-(pyridin-2-yl)vinyl)-1-(tetrahydro-*2H*-pyran-2-yl)-*1H*-indazole (8).

(*E*)-3-(2-(pyridin-2-yl)vinyl)-1-(tetrahydro-*2H*-pyran-2-yl)-*1H*-indazol-6-amine (1.65 g, 5.15 mmol) was dissolved in acetic acid (10 mL) and added to a stirring solution of sodium nitrite (577 mg, 8.37 mmol) in water at 0°C. After stirring for 1 h at 0°C, a solution of HCl (6M in water) was added dropwise using a dropping funnel. After continued stirring for 1 h at 0°C , CH_2Cl_2 (7 mL) was added. To this mixture was added a solution of potassium iodide (1.71 g, 10.3 mmol) and iodine (654 mg, 2.58 mmol) in water (20 mL) after 2 h of stirring at 0°C TLC indicated consumption of the starting material. The reaction mixture was poured onto a solution of sodiumthiosulfate (20% in water) and stirred until an orange solution was obtained. The aqueous solution was extracted twice with CH_2Cl_2, made basic with $NaHCO_3$ (sat.) and extracted with CH_2Cl_2 again. The organic layers were dried (Na_2SO_4), filtered and evaporated to dryness to afford the crude product, which was purified by column chromatography (EtOAc:hexane, 1:3, *v/v*) to afford the product as an off-white solid (1.70 g, 5.15 mmol, 77% yield). ^{1}H-NMR (500.23 Mhz, DMSO-D_6) δ: 8.61 (d, J=4.4 Hz, 1H, H_{ar}), 8.26 (s, 1H, H_{ar}), 8.02 (d, J=8.5 Hz, 1H, H_{ar}), 7.91 (d, J=16.4 Hz, 1H, H_{ar}), 7.82 (t, J=7.6 Hz, 1H, H_{ar}), 7.70 (d, J=7.6 Hz, 1H, H_{ar}), 7.59 (m, 2H, H_{ar}), 7.29 (m, 1H, H_{ar}), 5.93 (d, J=9.1 Hz, 1H, H_{THP}), 3.90 (d, *J*=11.3 Hz, 1H, H_{THP}), 3.79 (m, 1H, H_{THP}), 2.41 (m, 1H, H_{THP}), 2.05 (m, 1H, H_{THP}), 1.99 (m, 1H, H_{THP}), 1.74 (m, 1H, H_{THP}), 1.60 (m, 2H, H_{THP}). ^{13}C-NMR (125.8 Mhz, DMSO-D_6) δ: 155.2 ($C_{q,ar}$), 150.2 (CH_{ar}), 142.3 ($C_{q,ar}$), 137.5 (CH_{ar}), 131.0 (2x CH_{ar}), 123.3 (2x CH_{ar}), 121.9 ($C_{q,ar}$), 120.0 (CH_{ar}), 100.1 (CH_{ar}), 94.00 ($C_{q,ar}$-I), 84.4 (CH_{THP}), 67.2 ($CH_{2,THP}$), 29.4 ($CH_{2,THP}$), 25.3 ($CH_{2,THP}$), 22.7 ($CH_{2,THP}$). HR-MS (ESI, 4500V): m/z calculated ($M+H^+$): 432.0567, found: 432.0490.

(*E*)-methyl 3-((3-(2-(pyridin-2-yl)vinyl)-1-(tetrahydro-*2H*-pyran-2-yl)-*1H*-indazol-6-yl)thio)benzoate (9).

In a flame dried flask and under an argon atmosphere (*E*)-6-iodo-3-(2-(pyridin-2-yl)vinyl)-1-(tetrahydro-*2H*-pyran-2-yl)-*1H*-indazole (500 mg, 1.16 mmol) and cesium carbonate (947 mg, 2.91 mmol) were dissolved in DMF (20 mL). In a separate flask, under an argon atmosphere, $Pd(dppf)Cl_2.CH_2Cl_2$ (48 mg, 0.06 mmol) was dissolved in DMF (1 mL) and this solution was added to the reaction mixture. Meanwhile methyl-2-mercaptobenzoate (254 mg, 1.51 mmol) was also dissolved in DMF (5 mL), under argon, in a separate flask and this solution was added to the reaction mixture after it had stirred for 5 min. at rt. The flask was sealed under an argon atmosphere and heated to 80°C for 4.5 h after which full consumption of the starting material was observed on TLC. The mixture was partitioned between water and CH_2Cl_2 and separated. The aqueous layer was acidified (1M HCl, pH = 4) and extracted with CH_2Cl_2. The combined organic layers were dried (Na_2SO_4), filtered and evaporated to obtain the crude product which was purified by column chromatography (EtOAc:hexane, 3:7, *v/v*) to afford the product as a white solid (429 mg, 0.90 mmol, 81%). ^{1}H-NMR (400.13 Mhz, DMSO-D$_6$) δ: 8.63 (d, J=4.2 Hz, 1H, H$_{ar}$), 8.31 (d, J=8.3 Hz, 1H, H$_{ar}$), 8.10 (s, 1H, H$_{ar}$), 7.96 (m, 2H, H$_{ar}$), 7.85 (t, J=7.7 Hz, 1H, H$_{ar}$), 7.73 (d, J=7.8 Hz, 1H, H$_{ar}$), 7.64 (d, J=16.4 Hz, H$_{ar}$), 7.33 (m, 4H, H$_{ar}$), 6.83 (d, J=8.3 Hz, 1H, H$_{ar}$), 5.97 (d, J=9.8 Hz, 1H, H$_{THP}$), 3.92 (m, 1H, H$_{THP}$), 3.78 (m, 1H, H$_{THP}$), 2.43 (m, 1H, H$_{THP}$), 2.03 (m, 2H, H$_{THP}$), 1.73 (m, 1H, H$_{THP}$), 1.59 (m, 2H, H$_{THP}$). ^{13}C-NMR (125.8 Mhz, DMSO-D$_6$) δ: 170.8 (C=O), 162.8 (2 x CH$_{ar}$), 155.04 (C$_{q,ar}$), 150.1 (CH$_{ar}$), 142.3 (2x C$_{q,ar}$), 142.2 (C$_{q,ar}$), 137.4 (CH$_{ar}$), 130.9 (CH$_{ar}$), 130.8 (CH$_{ar}$), 123.3 (CH$_{ar}$), 123.2 (CH$_{ar}$),123.1 (CH$_{ar}$), 123.1 (CH$_{ar}$), 121.8 (C$_{q,ar}$), 119.9 (CH$_{ar}$), 93.8 (C$_{q,ar}$), 84.3 (2 x CH$_{ar}$), 67.1 (CH$_{2,THP}$), 36.2 (CH$_3$), 31.2 (CH$_{THP}$), 29.3 (CH$_{2,THP}$), 25.2 (CH$_{2,THP}$), 22.6 (CH$_{2,THP}$). HR-MS (ESI, 4500V): m/z calculated (M+H$^+$): 472.1689, found: 472.1601

(*E*)-2-((3-(2-(pyridin-2-yl)vinyl)-1-(tetrahydro-*2H*-pyran-2-yl)-*1H*-indazol-6-yl)thio)benzamide (10).

In a flame dried flask under an argon atmosphere (*E*)-methyl 3-((3-(2-(pyridin-2-yl)vinyl)-1-(tetrahydro-*2H*-pyran-2-yl)-*1H*-indazol-6-yl)thio)benzoate (429 mg, 0.90 mmol) was dissolved in DMF (6.5 mL) and to this solution was added formamide (25 %Wt, 119 μL, 2.98 mmol). The mixture was heated to 100°C and methanolic sodium methoxide (145 μL, 0.63 mmol) was added. After 2 h at 100°C full consumption of the starting material was observed and the mixture was cooled, diluted with water, made basic (NaHCO$_3$ (sat.), pH=10) and extracted with EtOAC (2x). The aqueous layer was acidified (1M HCl, pH = 4) and extracted with EtOAC (2x). The combined organic layers were dried (Na$_2$SO$_4$), evaporated to obtain the crude product which was purified by column chromatography (Gradient: EtOAc:hexane, 2:8, *v/v* -> 1:9, *v/v*) to afford the product as a white solid (236 mg, 0.52 mmol, 57%). The product is light sensitive and should be stored in the dark. ^{1}H-NMR (500.23 Mhz, DMSO-D$_6$) δ: 8.61 (d, J=4.4 Hz, 1H, H$_{ar}$), 8.23 (d, J=8.5 Hz, 1H, H$_{ar}$), 7.94 (m, 3H, H$_{ar}$), 7.8 (td, J=7.6, 1.3 Hz, 1H, H$_{ar}$), 7.69 (d, J=7.9 Hz , 1H, H$_{ar}$), 7.60 (m, 2H, H$_{ar}$), 7.52 (s, 1H, H$_{ar}$), 7.26 (m, 4H, H$_{ar}$), 6.95 (d, J=7.9 Hz, 1H, H$_{ar}$), 5.93 (dd, J=9.8, 2.0 Hz, 1H, H$_{THP}$), 3.90 (d, J=11.7Hz, 1H,

H_{THP}), 3.77 (m, 1H, H_{THP}), 2.41 (m, 1H, H_{THP}), 2.04 (m, 2H, H_{THP}), 1.74 (m, 1H, H_{THP}), 1.59 (m, 2H, H_{THP}). ^{13}C-NMR (125.8 Mhz, DMSO-D_6) δ: 169.2 (C=O), 154.6 (CH_{ar}), 149.6 ($C_{q,ar}$), 141.6 (CH_{ar}), 141.11 (CH_{ar}), 136.9 ($C_{q,ar}$), 136.7 (CH_{ar}), 135.6 (CH_{ar}), 132.9 (CH_{ar}), 130.4 ($C_{q,ar}$), 130.3 ($C_{q,ar}$), 129.1 ($C_{q,ar}$), 127.9 ($C_{q,ar}$), 127.0 ($C_{q,ar}$), 125.6 ($C_{q,ar}$), 122.8 ($C_{q,ar}$), 122.8 ($C_{q,ar}$), 122.7 ($C_{q,ar}$), 122.0 ($C_{q,ar}$), 121.7 (CH_{ar}), 115.60 ($C_{q,ar}$), 84.05 (CH_{ar}), 66.6 ($CH_{2,THP}$), 28.9 ($CH_{2,THP}$), 24.7 ($CH_{2,THP}$), 22.1 ($CH_{2,THP}$). HR-MS (ESI, 4500V): m/z calculated ($M+H^+$): 457.1693, found: 457.1563.

2-bromo-*N*-methyl-*N*-(4-nitrophenyl)acetamide (13).

p-nitromethylaniline (0.76 mg, 5.0 mmol) and triethylamine (1.5 mL, 11 mmol) were suspended in $CHCl_3$ (60 mL) and cooled to 0°C. 2-bromoacetylbromide (2.0 g, 10 mmol) in $CHCl_3$ (30 mL) was added dropwise. The mixture was stirred for 2 h at rt, after which full conversion was observed on TLC. The reaction mixture was quenched by the addition of water and the organic layer was separated, washed with $KHSO_4$ (1 M), $NaHCO_3$ (sat) and brine. The organic layer was subsequently dried on Na_2SO_4 and evaporated to dryness to afford the crude product which was purified by column chromatography ($CHCl_3$:MeOH, 98:2, *v/v*) to afford the product as a light brown solid (980 mg, 3.51 mmol, 72%). ^{1}H-NMR (250.13 Mhz, $CDCl_3$) δ: 8.33 (d, J=8.8 Hz, 2H, H_{ar}), 7.51 (m, 2H, H_{ar}), 3.74 (s, 2H, $-CH_2Br$), 3.39 (s, 1H, $-NCH_3$). ^{13}C-NMR (125.8 Mhz, $CDCl_3$) δ: 166.3 (C=O), 148.7 ($C_{q,ar}$), 125.4 (4x CH_{ar}), 38.3 (CH_3), 26.3 (CH_2). HR-MS (ESI, 4500V): m/z calculated ($M+H^+$): 272.9870, found: 272.9888.

***tert*-butyl 4-(2-(methyl(4-nitrophenyl)amino)-2-oxoethyl)piperazine-1-carboxylate (14).**

tert-butylpiperazinecarboxylate (233 mg, 1.25 mmol) and K_2CO_3 (275, 2.00 mmol) were suspended in acetone (10 mL). To this stirred suspension was added 2-bromo-*N*-methyl-*N*-(4-nitrophenyl)acetamide (273 mg, 1.00 mmol) slowly and the mixture was stirred at rt for 3 h. The formed precipitates were removed by filtration and the solvent was removed *in vacuo*. The residue was dissolved in EtOAc, washed with water (3x), dried over Na_2SO_4 and evaporated to afford the product as a yellow solid (328 mg, 0.867 mmol, 87%) ^{1}H-NMR (250.13 Mhz, $CDCl_3$) δ: 8.26 (d, J=8.8 Hz, 2H, H_{ar}), 7.42 (d, J=8.8 Hz, 2H, H_{ar}), 3.34 (s, 8H, $H_{piperazine}$), 3.05 (s, 2H, -CH_2Br), 2.37 (s, 3H, -NCH_3), (s, 9H, H_{Boc}). ^{13}C-NMR (125.8 Mhz, $CDCl_3$) δ: 168.4 (C=O), 154.5 (C=O_{Boc}), 149.3 ($C_{q,ar}$), 124.8 (4x CH_{ar}), 79.7 ($C_{q,Boc}$) 60.3 (CH_2), 52.7 (4x $CH_{2,piperazine}$), 37.4 (CH_3), 28.3 (3x $CH_{3\text{-}Boc}$). HR-MS (ESI, 4500V): m/z calculated ($M+H^+$): 379.1976, found: 379.2009

tert-butyl 4-(2-((4-aminophenyl)(methyl)amino)-2-oxoethyl)piperazine-1-carboxylate (15).

tert-butyl 4-(2-(methyl(4-nitrophenyl)amino)-2-oxoethyl)piperazine-1-carboxylate (1.5 g, 4.0 mmol) and palladium on carbon (43 mg, 0.40 mmol) were dissolved in MeOH (20 mL) and the solution was purged with H_2 gas and subsequently sealed. After vigorous stirring for 2 h TLC indicated full conversion and the mixture was filtered over celite and the filtrate was evaporated to dryness to afford the crude product, which was purified by column chromatography ($CHCl_3$:MeOH, 95:5, *v/v*) to afford the product as an light brown oil (1.15 g, 3.30 mmol, 83%). ^{1}H-NMR (250.13 Mhz, $CDCl_3$) δ: 6.93 (d, J=8.5 Hz, 2H, H_{ar}), 6.67 (d, J=8.7 Hz, 2H, H_{ar}), 3.50 (t, J=5.0 Hz, 4H, $H_{piperazine}$), 3.21 (s, 3H, -NCH_3), 3.05 (s, 2H, -CH_2Br), 2.59 (t, J=4.3 Hz, 4H, $H_{piperazine}$), 1.44 (s, 9H, H_{Boc}). ^{13}C-NMR (125.8 Mhz, $CDCl_3$) δ: 169.3 (C=O), 154.2 (C=O_{Boc}), 148.6 ($C_{q,ar}$), 131.8 ($C_{q,ar}$), 128.2 (2x CH_{ar}), 114.6 (2x CH_{ar}), 79.2 ($C_{q,Boc}$), 58.8 (2x $CH_{2,piperazine}$), 55.4 (CH_2), 52.6 (2x $CH_{2,piperazine}$), 37.5 (CH_3), 28.5 (3x $CH_{3\text{-}Boc}$). HR-MS (ESI, 4500V): m/z calculated ($M+Na^+$): 371.2054, found: 371.1980

methyl 4-(2-methoxy-2-oxoethyl)-3-nitrobenzoate (17).

Potassium *tert*-butoxide (7.85 g, 70.0 mmol) was dissolved in DMF (60 mL) and a solution of methyl chloro-acetate (3.56 g, 2.9 mL, 33 mmol) and methyl 3-nitrobenzoate (5.43 g, 30 mmol) in DMF (10 mL) was added at -10°C and stirred for 10 min after which complete consumption of the starting material was observed on TLC. The mixture was poured into ice-water (100 mL) and HCl (concentrated, 35 mL). The aqueous solution was extracted with EtOAC and the organic layer was washed with $KHSO_4$ (1M), $NaHCO_3$ (sat.) and evaporated to afford the crude product, which was purified by column chromatography (EtOAc: hexane, 2:8, *v/v*) to afford the product as a yellow solid (5.89 g, 23.3 mmol, 77%) and a mixture of isomers (1:0.38, desired:undesired). ^{1}H-NMR (250.13 Mhz, CDCl$_3$) δ: 6.93 (d, J=1.6 Hz, 1H, H$_{ar}$), 8.23 (dd, J=7.9, 1.7 Hz, 1H, H$_{ar}$), 8.23 (d, J=7.9 Hz, 1H, H$_{ar}$), 4.08 (s, 2H, -CH$_{2}$-) 3.97 (s, 3H, -CO2C*H*$_3$) 3.71 (s, 3H, -CH$_2$CO$_2$C*H*$_3$). ^{13}C-NMR (125.8 Mhz, DMSO-D$_6$) δ: 170.4 (C=O, CH$_2$*CO*$_2$CH$_3$), 164.8 (C=O, -*CO*2CH$_3$), 148.6 (C$_{q,ar}$-NO2), 135.2 (C$_{q,ar}$), 135.0 (CH$_{ar}$), 134.3 (CH$_{ar}$), 125.7 (CH$_{ar}$) (130.6 (C$_{q,ar}$), 53.2 (CH$_3$, CH2CO2*C*H3), 52.5 (CH$_3$, CO2*C*H$_3$), 39.0 (CH$_2$). HR-MS (ESI, 4500V): m/z calculated (M+Na$^+$): 276.0479, found: 276.0506

methyl 2-oxoindoline-6-carboxylate (18).

Methyl 4-(2-methoxy-2-oxoethyl)-3-nitrobenzoate (5.06 g, 20 mmol, mixture of isomers) and palladium on carbon were dissolved in acetic acid (100 mL) and the solution was purged with H$_2$ gas and subsequently sealed. After vigorous stirring for 5 h TLC indicated full conversion and the mixture was filtered over celite, the filtrate was evaporated to dryness to afford the crude product. The crude product was dissolved in EtOAc and washed with HCl (1M, 3x), the organic layer was dried (Na$_2$SO$_4$), filtered and evaporated to dryness to afford the product as an brown solid (2.30 g, 12.0 mmol, 60.2%) ^{1}H-NMR (250.13 Mhz, DMSO-D$_6$) δ: 10.54 (s, 1H, -NH), 7.57 (dd, *J*=7.8, 1.3 Hz, 1H, H$_{ar}$), 7.53 (M, 2H, H$_{ar}$), 3.83 (s, 3H, -CO2CH$_3$), 3.56 (s, 2H, -CH$_2$-). ^{13}C-NMR (125.8 Mhz, DMSO-D$_6$) δ: 39.6 (CH$_2$), 52.6 (CH$_3$), 109.4 (C$_{q,ar}$), 123.0 (C$_{q,ar}$), 125.0 (C$_{q,ar}$), 128.3 (CH$_{ar}$), 132.2 (CH$_{ar}$), 144.6 (CH$_{ar}$), 166.6 (C=O), 176.6 (C=O). HR-MS (ESI, 4500V): m/z calculated (M+Na$^+$): 214.0475, found: 214.0490.

(*E*)-methyl 1-acetyl-3-(ethoxy(phenyl)methylene)-2-oxoindoline-6-carboxylate (19).

ethyl 2-oxoindoline-6-carboxylate (466 mg, 2 mmol) was dissolved in acetic anhydride (2.5 mL) and (triethoxymethyl)benzene (1.35 g, 6.0 mmol) was added. The resulting mixture was stirred at 130°C for 7 h. Upon complete conversion (as observed by TLC) the mixture was cooled and diluted with hexanes. The crude product was precipitated, collected by filtration and purified by column chromatography (EtOAc: hexane, 1:1, *v/v*) to afford the product as a light brown solid (516 mg, 1.41 mmol, 71%). ^{1}H-NMR (500.23 Mhz, CDCl$_3$) δ: 8.90 (s, 1H, H$_{ar}$), 8.04 (d, J=8.2 Hz, 1H, H$_{ar}$), 7.95 (d, J=8.2 Hz, 1H, H$_{ar}$), 7.57 (m, 3H, H$_{ar}$), 7.40 (m, 2H, H$_{ar}$), 4.00

(q, J=7.0 Hz (2x), 2H, CH_2), 3.93 (s, 3H, -CO_2CH_3), 2.57 (s, 3H, -$COCH_3$), 1.43 (t, J=7.3 Hz, 3H, -CH_3). ^{13}C-NMR (125.8 Mhz, DMSO-D_6) δ: 171.3 (C=O), 167.2 (C=O), 167.0 (C=O), 136.5 ($C_{q,double\ bond}$), 131.3 ($C_{q,ar}$), 130.6 (CH_{ar}), 128.9 (2x CH_{ar}), 128.4 (CH_{ar}), 128.2 (3x CH_{ar}), 128.1 (CH_{ar}), 126.4 ($C_{q,ar}$), 122.3 (CH_{ar}), 116.5 (CH_{ar}), 105.8 ($C_{q,double\ bond}$), 67.0 (CH_2), 52.1 ($CH_{3,ester}$), 26.9 ($CH_{3,acetate}$) 15.3 (CH_3). HR-MS (ESI, 4500V): m/z calculated (M+Na^+): 388.1155, found: 388.1183.

(*Z*)-methyl-3-(((4-(2-(4-(tert-butoxycarbonyl)piperazin-1-yl)-*N*-methylacetamido)phenyl)amino)(phenyl)methylene)-2-oxoindoline-6-carboxylate (20).

(*E*)-methyl 1-acetyl-3-(ethoxy(phenyl)methylene)-2-oxoindoline-6-carboxylate (237 mg, 0.65 mmol) and *tert*-butyl 4-(2-((4-aminophenyl)(methyl)amino)-2-oxoethyl)piperazine-1-carboxylate (174 mg, 0.5 mmol) were dissolved in DMF (5 mL). The resulting mixture was heated to 100°C for 1 h after which piperidine (2 mL) was added and stirring was continued for 2 h at 100°C. After cooling to room temperature the mixture was diluted with EtOAc, washed with $KHSO_4$ (1M), $NaHCO_3$ (sat.), dried (Na_2SO_4) and evaporated to yield the crude product, which was purified by column chromatography (EtOAc: hexane, 2:8, *v/v*) to afford the product as a light yellow solid (100 mg, 0.16 mmol, 32%). ^{1}H-NMR (500.23 Mhz, $CDCl_3$) δ: 12.17 (s, 1H, -NH), 9.06 (s, 1H, H_{ar}), 7.60 (m, 2H, H_{ar}), 7.53 (t, J=7.4 Hz, 2H, H_{ar}), 7.43 (d, J=6.9 Hz, 2H, H_{ar}), 7.38 (dd, J=8.2, 1.3 Hz, 1H, H_{ar}), 6.97 (d, J=8.2 Hz, 2H, H_{ar}), 6.81 (d, J=8.5 Hz, 2H, H_{ar}), 5.99 (d, J=8.2 Hz, 1H, H_{ar}), 3.85 (s, 3H, -CO_2CH_3), 3.35 (s, 4H, $H_{piperazine}$), 3.18 (s, 3H, -NCH_3), 2.81 (s, 2H, CH_2), 2.31 (s, 4H, $H_{piperazine}$), 1.44 (s, 9H, H_{Boc}). ^{13}C-NMR (125.8 Mhz, DMSO-D_6) δ: 171.1 (C=O), 169.4 (C=O), 167.5 (C=O), 158.4 ($C_{q,double\ bond}$), 154.8 (C=O), 139.9 ($C_{q,ar}$), 138.2 ($C_{q,ar}$), 135.6 ($C_{q,ar}$), 132.4 ($C_{q,ar}$), 130.7 (CH_{ar}), 129.8 (2x CH_{ar}), 129.2 ($C_{q,ar}$), 128.7 (2x CH_{ar}), 127.9 (CH_{ar}), 125.3 ($C_{q,ar}$), 124.1 (CH_{ar}), 122.9 (CH_{ar}), 118.4 (CH_{ar}), 110.5 (CH_{ar}), 98.6 ($C_{q,double\ bond}$), 79.8 ($C_{q,Boc}$), 59.7 (CH_2), 53.0 (4x $CH_{2,piperazine}$), 52.0 (-OCH_3), 37.4 (-NCH_3), 28.5 (3x $CH_{3,Boc}$). HR-MS (ESI, 4500V): m/z calculated (M+H^+): 626.2973, found: 626.2840.

(*Z*)-methyl 3-(((4-(*N*-methyl-2-(piperazin-1-yl)acetamido)phenyl)amino)(phenyl)methylene)-2-oxoindoline-6-carboxylate (21).

(*Z*)-methyl-3-(((4-(2-(4-(tert-butoxycarbonyl)piperazin-1-yl)-*N*-methylacetamido)phenyl)amino)(phenyl)methylene)-2-oxoindoline-6-carboxylate (175 mg, 0.28 mmol) was dissolved in diethylether (10 mL) and to this HCl (102 mg, 85 µL, 2.8 mmol) was added. After TLC indicated full conversion, the mixture was evaporated, taken up in EtOAC, washed with $KHSO_4$ (1M), $NaHCO_3$ (sat.), dried (Na_2SO_4) and evaporated to yield the crude product, which was purified by column chromatography (MeOH: CH_2Cl_2, 1:20, *v/v*) to afford the product as a yellow solid (115 mg, 0.219 mmol, 78%). ^1H-NMR (500.23 Mhz, MeOD-D_4) δ: 7.62 (m, 4H, H_{ar}), 7.55 (d, J=1.3 Hz, 1H, H_{ar}), 7.50 (d, J=7.3 Hz, 2H, H_{ar}), 7.28 (dd, J=8.2, 1.6 Hz, 1H, H_{ar}), 7.13 (d, J=8.5 Hz, 2H, H_{ar}), 6.94 (d, J=8.5 Hz, 2H, H_{ar}), 5.95 (d, J=8.5 Hz, 1H, H_{ar}), 3.84 (s, 3H, -CO_2CH_3), 3.26 (s, 4H, $H_{piperazine}$), 3.22 (s, 2H, CH_2), 3.18 (s, 3H, -NCH_3), 2.87 (s, 4H, $H_{piperazine}$). ^{13}C-NMR (125.8 Mhz, MeOD-D_4) δ: 172.5 (C=O), 169.0 (C=O), 162.4 (C=O), 160.14 ($C_{q,double\ bond}$), 140.2 ($C_{q,ar}$), 140.1 ($C_{q,ar}$), 137.8 ($C_{q,ar}$), 134.0 ($C_{q,ar}$), 132.0 (CH_{ar}), 131.0 (2x CH_{ar}), 130.6 ($C_{q,ar}$), 130.0 (2x CH_{ar}), 129.3 (2x CH_{ar}), 126.5 ($C_{q,ar}$), 125.5 (2x CH_{ar}), 123.5 (CH_{ar}), 119.4 (CH_{ar}), 111.4 (CH_{ar}), 99.9 ($C_{q,double\ bond}$), 59.4 (CH_2), 52.6 (-OCH_3), 50.6 (2x $CH_{2,piperazine}$), 44.0 (2x $CH_{2,\ piperazine}$), 37.9 (-NCH_3). HR-MS (ESI, 4500V): m/z calculated ($M+H^+$): 526.2449, found: 526.2470.

5.4.3 Radiochemistry

5.4.3.1 Synthesis of [¹¹C]axitinib

Carried by a helium stream (10 mL/min), cyclotron produced $[^{11}C]CO_2$ was bubbled through a solution of 100 µL 0.1 M $LiAlH_4$ in THF at 20 °C. The solution was dried by heating the reaction vial to 130°C under a stream of helium and 0.22 mL 60% HI in water was added to the residue. The formed $[^{11}C]CH_3I$ was distilled through a sicapent/NaOH column to a second reaction vial containing a solution of **10** (0.5 mg, 1.1 μmol) and TBAOH (2 μL, 4 μmol, 5M in H_2O) in DMF (100 μL). The reaction mixture was heated at 40°C for 5 min. Subsequently trifluoroacetic acid (50 μL) was added and the reaction vial was heated to 120°C for 3 min after which the reaction vial was cooled to rt and diluted with 2 mL of water and subjected to semi-prep HPLC purification (Alltima C18 column; 10x250; 5μ; eluent: MeCN/H_2O/TFA, 30:70:0.1, v/v/v). The fraction containing [^{11}C]axitinib (R_t = 11.2 min) was collected, diluted with water (40 mL) and trapped on a Sep-Pak tC18+ cartridge. The cartridge was then washed with 20 mL of sterile water after which the product was eluted from the cartridge with 1.0 mL of sterile 96% ethanol. The ethanol was diluted to 10 volume percent with formulation solution (7.09 mM NaH_2PO_4 in 0.9% NaCl, w/v in water, pH 5.2). The decay-corrected radiochemical yield calculated from EOB of [^{11}C]axitnib was 10.5% ± 2.6%. The radiochemical purity was >98% and specific activity was 206 ± 55 GBq/μmol at the end of synthesis. The overall synthesis time from EOB was ± 40 min. Quality control was performed using analytical HPLC (Platinum C18 column; 4.6x250; 10μ; eluent: MeCN/H_2O/TFA, 50:50:0.1, v/v/v) and specific activity was calculated against a calibration curve.

5.4.3.2 Synthesis of [^{11}C]nintedanib

[^{11}C]MeI was synthesized as described above and distilled to a reaction vial containing **21** (1.5 mg, 2.9 μmol) and K_2CO_3 (5 mg, 36.2 μmol) in DMF (200 μL). The reaction mixture was heated and stirred at 80°C for 5 min, after which the reaction vial was cooled to rt and diluted with 2 mL of HPLC eluent and subjected to preparative HPLC purification (Alltima C18 column; 22x250; 10μ; eluent: MeCN/H_2O/TFA, 42.5:47.5:0.1, v/v/v). The fraction containing [^{11}C]nintedanib (R_t = 11.5 min) was collected, diluted with water (60 mL) and trapped on a Sep-Pak tC18+ cartridge. The product was washed with water (20 mL), eluted with EtOH (1 mL) and diluted with 2.5% polysorbatum 80 in saline (9 mL). The decay-corrected radiochemical yield calculated from EOB of [^{11}C]nintedanib was 25.6 ± 3.3%. The radiochemical purity was >98% and the specific activity was 213 ± 57 GBq/μmol at the end of synthesis after formulation. The overall synthesis time from EOB was ± 35 min. Quality control was performed using analytical HPLC (Gracesmart C18 column; 4.6x250; 5µ; eluent: MeCN/H_2O/TFA, 35:65:0.1, v/v/v) and specific activity was calculated against a calibration curve.

5.4.4 Metabolite analysis [^{11}C]axitinib and [^{11}C]nintedanib

5.4.4.1 General method for the work-up of plasma samples with [^{11}C]axitinib/axitinib

Plasma was separated from blood cells and about 1 mL of plasma was diluted with 2 mL of 0.1M hydrochloric acid and loaded onto a tC2 Sep-Pak cartridge, which was pre-activated by elution with 6 mL of MeOH and 12 mL of water, respectively. The cartridge was washed with 3 mL of H_2O to collect polar radioactive metabolites. Thereafter, the tC2 Sep-Pak cartridge was eluted with 1.5 mL of MeOH and subsequently 1.5 mL of H_2O to collect the mixture of nonpolar metabolites.

5.4.4.2 HPLC method for [^{11}C]axitinib metabolites

Samples were subjected to HPLC analysis to determine the percentage of intact [^{11}C]axitinib. HPLC was performed on a Dionex Ultimate 3000 system, equipped with a 1 mL loop. As a stationary phase a Luna C18, 250 x 10 mm, 5 µm was used. The mobile phase was a gradient of A = acetonitrile and B = 0.1% trifluoroacetic acid in H_2O. The HPLC gradient ran for 15.0 min decreasing the concentration of eluent B from 90% to 30% in 11 min, followed by 1 min of elution at 30% B and a decrease to 10% in 3 min at a flow rate of 3 mL.min^{-1}. The eluent was collected with a fraction collector (Teledyne ISCO Foxy Jr., Lincoln, NE, USA) and counted for radioactivity with a Wallac 1470 gamma counter (Perkin Elmer, Waltham, MA, USA).

5.4.4.3 In vivo *plasma metabolite analysis: [^{11}C]axitinib*

Six Balb/c mice were injected with circa 50 MBq of [^{11}C]axitinib (corresponding to 0.24 nMol of axitinib), in the ocular plexus under isoflurane anesthesia (2% in $1\ \mathrm{L}\cdot\mathrm{min}^{-1}$). The mice were sacrificed at 15 ($n = 3$) and 45 ($n = 3$) min p.i.. At these time points, about 1.0-1.5 mL of blood was collected via a heart puncture from each mouse. Blood was collected in a heparin tube and centrifuged for 5 min at 5000 rpm (Hettich universal 16, Depex B.V., The Netherlands). Plasma was separated from blood cells and about 1 mL of plasma was worked up according to the general method described above and analyzed using HPLC according to the method described for [^{11}C]axitinib and metabolites.

5.4.4.4 General method for the work-up of plasma samples with [^{11}C]nintedanib/nintedanib

Plasma was separated from blood cells and about 1 mL was diluted with 2 mL of 0.1 M hydrochoric acid and loaded onto a tC18 Sep-Pak cartridge, which was pre-activated by elution with 6 mL of MeOH and 12 mL of water, respectively. The cartridge was washed with 3 mL of H_2O to collect the polar radioactive fraction. Thereafter, the tC18 Sep-Pak cartridge was eluted with 2 mL of MeOH and 1 mL of H_2O to collect the mixture of non-polar metabolites.

5.4.4.5 HPLC method for [^{11}C]nintedanib metabolites

Samples were subjected to HPLC analysis to determine the percentage of intact [^{11}C]nintedanib. HPLC was performed on a Dionex Ultimate 3000 system, equipped with a 1 mL loop. As a stationary phase a Luna C18, 250 x 10 mm, 5 μm was used. The mobile phase was a gradient of A = acetonitrile and B = 0.1% trifluoroacetic acid in H_2O at 3 $\mathrm{mL.min^{-1}}$ according to the following scheme: 0 min 90% B, 90-30% B in 11 min, 30% B for 1 min, 30-10% B in 3 min. The eluent was collected with a fraction collector (Teledyne ISCO Foxy Jr., Lincoln, NE, USA) and counted for radioactivity with a Wallac 1470 gamma counter (Perkin Elmer, Waltham, MA, USA).

5.4.4.6 In vivo *plasma metabolite analysis: [^{11}C]nintedanib*

Six Balb/c mice were injected with circa 50 MBq of [^{11}C]nintedanib (corresponding to 0.23 nMol of nintedanib), in the ocular plexus under isoflurane anesthesia (2% in 1 L · min^{-1}) and plasma metabolite work up was performed as described in section 2.4.3

5.4.4.7 In vitro *plasma incubations*

Plasma was obtained from athymic nu\nu mice, Balb/c mice and rat by cardiac puncture and stored in heparin tubes. Blood was centrifuged at 5000 rpm for 5 min to separate plasma from blood cells and plasma was directly frozen for storage. Human blood from a healthy volunteer was collected in heparin tubes which were centrifuged at 5000 rpm for 5 min to collect plasma which was directly frozen for storage. Aliquots of 500 µL of plasma (all species) were incubated with [^{11}C]nintedanib (circa 1 MBq, corresponding to 0.005 nMol of nintedanib) for 45 min at 37°C and worked up as described in the previous section, to ascertain the extraction efficiency of activity from these samples, which was found to be >90% in all cases. Aliquots of 400 µL plasma (all species) were incubated with nintedanib (20 µL of a 10 µM solution) for 3 h at 37°C and subsequently worked up according to the general method described above and analyzed using HPLC according to the method described above for [^{11}C]nintedanib and metabolites.

5.4.4.8 In vivo *tumor metabolite analysis*

Nude mice (athymic nu/nu, Harlan, Horst, The Netherlands, *n*=3) bearing two tumors (obtained by injection of FaDu cells) of the same xenograft line on their left and right flanks, received an injection of 50 MBq [^{11}C]nintedanib (corresponding to 0.24 nMol of nintedanib) via the ocular plexus under isoflurane anesthesia (2% in 1 · min^{-1}

oxygen). The mice were sacrificed at 45 min p.i. blood was obtained by cardiac puncture and tumor tissue was obtained by excision. The tumor tissue was first cut into smaller pieces and subsequently homogenized (IKA T18 basic, ultra-turrax), followed by protein precipitation with MeCN/H_2O (1:1, v/v). The supernatant was collected by centrifugation at 5000 rpm for 5 min and subjected to HPLC and LC-MS/MS analysis.

5.4.4.9 LC-MS/MS equipment

LC-MS/MS analysis was performed on a Jasco system (Easton, PA, USA) with an AB Sciex QTRAP 5500 mass spectrometer (Concorde, Ontario, Canada). The Jasco system consisted of two pumps (X-LC 3180PU), a degasser (X-LC 3080DG), a mixer (X-LC 3080MX), a column oven (X-LC 3080CO), and an autosampler (X-LC3159AS). Data was collected with two databoxes (LV 2080-03 and LC-Net II/ACD).

5.4.4.10 LC-MS/MS method for nintedanib/[^{11}C]nintedanib

A Kinetex C18 column (1.7 u, 100 A, 100 x 2.10 mm, Phenomex, Torrance, CA, USA) at 25°C was used for chromatographic separation. A gradient elution was used at a flow rate of 0.4 mL/min. The mobile phase consisted of a mixture of acetonitrile (A) and 0.1% formic acid in water (B) according to the following scheme: 0 min 70% B, 70-10% B in 1.8 min, 10% B for 2.5 min, 10-70% B in 0.05 min, 70% B for .55 min. MS parameters: Capillary potential was set at 5.5 kV, source temperature at 100°C, and desolvation temperature at 750°C. Two scan functions were performed using these conditions: Product ion scan of product peak with *m/z* 540.2 and *m/z* of 526.0 of the metabolite. MRM (multi reaction monitoring mode) Q1 (quadrupole 1) and Q3 (quadrupole 3) set at: 526.0 and 112.6 for carboxylic acid metabolite analysis and 540.2 and 113.1 for parent analysis.

5.4.4.11 LC-MS/MS method for [^{11}C]axitinib/axtinib

A Kinetex Biphenyl column (2.6 u, 100 Å, 100 x 2.10 mm, Phenomex, Torrance, CA, USA) at 25°C was used for chromatographic separation. A gradient elution was used at a flow rate of 0.6 mL/min. The mobile phase consisted of a mixture of acetonitrile (A) and 0.1% formic acid in water (B) according to the following scheme: 0 min 90% B, 90-35% B in 8.5 min, 35% B for 1.5 min, 35-90% B in 0.05 min, 90% B for 0.55 min. MS parameters: Capillary potential was set at 5.5 kV, source temperature at 100°C, and desolvation temperature at 750°C. Two scan functions were performed using these conditions: product ion scan of product peak with *m/z* 368.9 for both *cis* and *trans* axitinib. MRM Q1 and Q3 set at: 368.9 and 356.3 for *cis* and *trans* axitinib detection. MRM Q1 and Q3 set at: 403.00 and 372.1 for axitinib-sulfoxide detection.

5.4.5 Immunohistochemistry

Sections of frozen xenografts (VU-SCC-OE or FaDu, obtained from three individual tumors per cell type) were immunostained for assessment of VEGFR, PDGFR and FGFR expression. Antibodies were diluted in PBS (phosphate buffered saline) with 1% bovine serum albumin. PDGFR was stained with rabbit anti-PDGFR (3169S, Cell Signaling, Leiden, The Netherlands) in a 1/100 dilution. VEGFR1 was stained with rabbit anti-VEGFR1 (AB32152S, Abcam, Cambridge, UK) in a 1/100 dilution, VEGFR2 was stained with rabbit anti-VEGFR2 (AB2349, ITK Diagnostics, Uithoorn, Netherlands) in a 1/50 dilution and VEGFR3 was stained with rabbit anti-VEGFR3/FLT4 (SAB4300609, Sigma Aldrich, St. Louis, USA) in a 1/100 dilution. FGFR4 was stained with rabbit-anti-FGFR (SAB1300019, Sigma Aldrich, St. Louis, USA) in a 1/50 dilution. As secondary antibody swine anti-rabbit horseradish peroxidase (P0217, Dako) was used. Cryosections (5 μm) of fresh frozen (tumor) tissue were air-dried and subsequently fixed with 2% paraformaldehyde in PBS for 10 min. Sections were blocked with normal rabbit serum or with normal swine serum and subsequently incubated with primary antibody for 60 min at rt. After washing the tissue was incubated with the secondary antibody for 60 min at rt. Color development was performed with diaminobenzidine (DAB) and counterstaining was done with hematoxiline.

5.4.6 Biodistribution studies

Nude mice (athymic nu/nu, Harlan, Horst, The Netherlands) bearing two tumors (obtained by injection of VU-SCC-OE or FaDu cells) of the same xenograft line on their left and right flank, received an injection of 15-20 MBq [^{11}C]axitinib or [^{11}C]nintedanib (corresponding to 0.07 – 0.09 nMol of axitinib or 0.07-0.10 nMol of nintedanib) via the tail vein. The mice were sacrificed and dissected at 30 and 60 min p.i.. Blood, urine, skin, left tumor, right tumor, muscle, heart, lung, liver, kidney and brain were collected, weighed and counted for radioactivity in a Wallac Compugamma 1210 counter (n = 3 for each time point). Biodistribution data are expressed as percentage of injected dose per gram (%ID/g) tissue for each organ.

5.5 References

[1] Hanahan D and Weinberg RA. The hallmarks of cancer *Cell* **2000**, *100*, 57-70.

[2] Hanahan D and Weinberg Robert A. Hallmarks of cancer: the next generation *Cell* **2011**, *144*, 646-674.

[3] Zhang J, Yang PL, and Gray NS. Targeting cancer with small molecule kinase inhibitors *Nat. Rev. Cancer* **2009**, *9*, 28-39.

[4] Lemmon MA and Schlessinger J. Cell signaling by receptor tyrosine kinases *Cell* **2010**, *141*, 1117-1134.

[5] Poot AJ, Slobbe P, Hendrikse NH, Windhorst AD, and van Dongen GAMS. Imaging of TKI-target interactions for personalized cancer therapy *Clin. Pharmacol. Ther.* **2013**, *93*, 239-241.

[6] Slobbe P, Poot AJ, Windhorst AD, and van Dongen GAMS. PET imaging with small-molecule tyrosine kinase inhibitors: TKI-PET *Drug Discovery Today* **2012**, *17*, 1175-1187.

[7] Slobbe P, Windhorst AD, Stigter van Walsum M, Schuit RC, Smit EF, Niessen HG, et al. Development of [^{18}F]afatinib as new TKI-PET tracer for EGFR positive tumors *Nucl. Med. Biol.* **2014**.

[8] Slobbe P, Windhorst AD, Stigter van Walsum M, Smit EF, Niessen HG, Solca F, et al. A comparative PET-imaging study with the reversible and irreversible EGFR tyrosine kinase inhibitors [^{11}C]erlotinib and [^{18}F]afatinib in lung cancer bearing mice *Eur. J. Nucl. Med. Mol. Imaging: Res* **2015**, *5*.

[9] Memon AA, Weber B, Winterdahl M, Jakobsen S, Meldgaard P, Madsen HHT, et al. PET imaging of patients with non-small cell lung cancer employing an EGF receptor targeting drug as tracer *Br. J. Cancer* **2011**, *105*, 1850-1855.

[10] Memon AA, Jakobsen S, Dagnaes-Hansen F, Sorensen BS, Keiding S, and Nexo E. Positron Emission Tomography (PET) imaging with C-11-labeled erlotinib: A micro-PET study on mice with lung tumor xenografts *Cancer Res.* **2009**, *69*, 873-878.

[11] Bahce I, Smit EF, Lubberink M, van der Veldt AAM, Yaqub M, Windhorst AD, et al. Development of [^{11}C]erlotinib positron emission tomography for *in vivo* evaluation of EGF receptor mutational status *Clin. Cancer Res.* **2013**, *19*, 183-193.

[12] Wang J-Q, Miller KD, Sledge GW, and Zheng Q-H. Synthesis of [^{18}F]SU11248, a new potential PET tracer for imaging cancer tyrosine kinase *Bioorg. Med. Chem. Lett.* **2005**, *15*, 4380-4384.

[13] Gao M, Lola CM, Wang M, Miller KD, Sledge GW, and Zheng Q-H. Radiosynthesis of [^{11}C]Vandetanib and [^{11}C]chloro-Vandetanib as new potential PET agents for imaging of VEGFR in cancer *Bioorg. Med. Chem. Lett.* **2011**, *21*, 3222-3226.

[14] Asakawa C, Ogawa M, Kumata K, Fujinaga M, Kato K, Yamasaki T, et al. [^{11}C]Sorafenib: Radiosynthesis and preliminary PET study of brain uptake in P-gp/Bcrp knockout mice *Bioorg. Med. Chem. Lett.* **2011**, *21*, 2220-2223.

[15] Poot AJ, van der Wildt B, Stigter-van Walsum M, Rongen M, Schuit RC, Hendrikse NH, et al. [^{11}C]Sorafenib: Radiosynthesis and preclinical evaluation in tumor-bearing mice of a new TKI-PET tracer *Nucl. Med. Biol.* **2013**, *40*, 488-497.

[16] Hu-Lowe DD, Zou HY, Grazzini ML, Hallin ME, Wickman GR, Amundson K, et al. Nonclinical antiangiogenesis and antitumor activities of axitinib (AG-013736), an oral, potent, and selective inhibitor of vascular endothelial growth factor receptor tyrosine kinases 1, 2, 3 *Clin. Cancer Res.* **2008**, *14*, 7272-7283.

[17] Roth GJ, Heckel A, Colbatzky F, Handschuh S, Kley J, Lehmann-Lintz T, et al. Design, synthesis, and evaluation of indolinones as triple angiokinase inhibitors and the discovery of a highly specific 6-methoxycarbonyl-substituted indolinone (BIBF 1120) *J. Med. Chem.* **2009**, *52*, 4466-4480.

[18] Hilberg F, Roth GJ, Krssak M, Kautschitsch S, Sommergruber W, Tontsch-Grunt U, et al. BIBF 1120: Triple angiokinase inhibitor with sustained receptor blockade and good antitumor efficacy *Cancer Res.* **2008**, *68*, 4774-4782.

[19] Sparidans RW, Iusuf D, Schinkel AH, Schellens JHM, and Beijnen JH. Liquid chromatography-tandem mass spectrometric assay for the light sensitive tyrosine kinase inhibitor axitinib in human plasma *J. Chromatogr. B* **2009**, *877*, 4090-4096.

[20] Smith BJ, Pithavala Y, Bu H-Z, Kang P, Hee B, Deese AJ, et al. Pharmacokinetics, metabolism, and excretion of [^{14}C]axitinib, a vascular endothelial growth factor receptor tyrosine kinase inhibitor, in humans *Drug Metab. Dispos.* **2014**, *42*, 918-931.

[21] Babu S, Dagnino R, Quellette MA, Shi B, Tian Q, and Scott EZ. Methods for preparing indazole compounds. WO2006048745; 2006.

[22] Welters MJP, Fichtinger-Schepman AMJ, Baan RA, Hermsen MAJA, van der Vijgh WJF, Cloos J, et al. Relationship between the parameters cellular differentiation, doubling time and platinum accumulation and cisplatin sensitivity in a panel of head and neck cancer cell lines *Int. J. Cancer* **1997**, *71*, 410-415.

[23] Garuti L, Roberti M, and Bottegoni G. Non-ATP competitive protein kinase inhibitors *Curr. Med. Chem.* **2010**, *17*, 2804-2821.

[24] Carey KD, Garton AJ, Romero MS, Kahler J, Thomson S, Ross S, et al. Kinetic analysis of epidermal growth factor receptor somatic mutant proteins shows increased sensitivity to the epidermal growth factor receptor tyrosine kinase inhibitor, erlotinib *Cancer Res.* **2006**, *66*, 8163-8171.

[25] Kuzyk M, Parker C, Domanski D, and Borchers C. Development of MRM-based assays for the absolute quantitation of plasma proteins. In: H Bäckvall and J Lehtiö editors. The low molecular weight proteome: Springer New York; 2013, p. 53-82.

[26] Bahar FG, Ohura K, Ogihara T, and Imai T**.** Species difference of esterase expression and hydrolase activity in plasma *J. Pharm. Sci.* **2012**, *101*, 3979-3988.

Chapter 6

Development of [^{11}C]vemurafenib employing a carbon-11 carbonylative Stille coupling for the *in vivo* detection of V600E mutated BRAF

P. Slobbe, A.D. Windhorst, W.A. Adamzek, M. Bolijn, R.C. Schuit, D.A.M. Heideman, G.A.M.S van Dongen and A.J. Poot

Submitted

Abstract

Over the last decade kinase inhibitors have witnessed tremendous growth as anti-cancer drugs. Unfortunately, despite their promising clinical successes, a large portion of patients does not benefit from these targeted therapeutics. Vemurafenib is a serine/threonine kinase inhibitor approved for the treatment of melanomas specifically expressing the BRAF^{V600E} mutation. The aim of this study was to develop vemurafenib as PET tracer to determine its potential for identification of tumors sensitive to vemurafenib treatment. Therefore, vemurafenib was labeled with carbon-11 and analyzed for its tumor targeting potential in melanoma xenografts Colo829 (BRAF^{V600E}) and MeWo (BRAF^{wt}) using autoradiography on tissue sections, *in vitro* tumor cell uptake studies and biodistribution studies in xenografted athymic nu/nu mice. [^{11}C]vemurafenib was synthesized in 21.3 ± 3.6% yield (decay corrected, calculated from [^{11}C]CO) in > 99% radiochemical purity and a specific activity of 55 ± 18 GBq/µmol. Similar binding of [^{11}C]vemurafenib was shown during autoradiography and cellular uptake studies in both cell lines. Plasma metabolite analysis demonstrated > 95% intact [^{11}C]vemurafenib *in vivo* at 45 minutes after injection, indicating excellent stability. Biodistribution studies confirmed the *in vitro* results, showing similar tumor-to-background ratios in both xenografts models. These preliminary results suggest that identification of BRAF^{V600E} mutations *in vivo* using PET with [^{11}C]vemurafenib will be challenging.

6.1 Introduction

The discovery of driver oncogenes in cancer has paved the way for the development of novel, selective therapies in cancer treatment. The increased understanding of the specific mutations and signaling pathways in tumor formation and proliferation has led to the development of tailor-made targeted therapeutics. One particular type of enzymes, namely kinases, have been particularly well studied over the last few decades and numerous drug discovery programs have been aimed at this class of targets [1].

Kinases comprise a large family of proteins that play an essential role in the signal transduction pathways of cells. Two subcategories can be distinguished, being the receptor kinases and the non-receptor or cytosolic kinases. The receptor kinases are transmembrane complexes which bind extracellular signaling ligands, upon which the receptor oligomerizes and the downstream signaling cascade is activated via the kinase domain. This cascade often consists of various cytosolic kinases. These are phosphorylated sequentially which leads to a cellular response, such as proliferation. A prominent example in this is the RAS-RAF-MEK-ERK pathway [2].

Kinases are heavily involved in cell signaling, growth and differentiation and therefore aberrant activation of kinases often leads to tumor formation. The development of therapeutics targeting kinases has received a lot of interest over the last two decades. An important category of targeted therapeutics comprises the small molecule kinase inhibitors which act intracellularly by competing with ATP for its binding site at the kinase domain of the receptor complex and thereby inhibit downstream signaling. Requirements for kinase inhibitors are good cell uptake and high affinity binding to the kinase domain. A drawback of targeted drugs like kinase inhibitors is a lack of selectivity (cross reactivity with healthy tissue also expressing the targeted receptors) and therefore, currently, the most effective kinase inhibitors are aimed at specific oncogenic mutations in the kinase that are not expressed in healthy tissue. This defines their selectivity over wild type kinase inhibitors. On the other hand if the mutation is not present in the tumor, the kinase inhibitor is less active and therapy is often only marginally successful, while side effects are still induced [3].

As an example, for Tyrosine Kinase Inhibitors (TKIs) targeting the Epidermal Growth Factor Receptor (EGFR), as used in the treatment of non-small cell lung cancer, the underlying reason for this inter-patient variability is best understood. Activating mutations in the kinase domain of EGFR dictate the effectiveness of the TKIs currently on the market (such as: erlotinib, gefitinib and afatinib) [4, 5]. Accordingly, molecular testing in pathology to identify the specific molecular alterations in the tumor has become a critical part of the process of selecting patients for appropriate treatments [6].

In recent publications the use of Positron Emission Tomography (PET) with radiolabeled kinase inhibitors, as a tool to study TKI disposition *in vivo* has been developed by others and us [7-9]. By labeling FDA approved kinase inhibitors with a PET-isotope in an inert manner (i.e., no structural modifications are performed), the *in vivo* biodistribution, pharmacokinetics and tumor targeting can be determined in a noninvasive manner at tracer level. The most successful examples to date include the use of [^{11}C]erlotinib, which was able to distinguish between sensitizing mutations of EGFR and wild type EGFR in non-small cell lung cancer patients, and [^{18}F]afatinib showing a promising similar preclinical targeting profile in tumor bearing mice [10-14]. The aim of this study was to extend this concept to vemurafenib, a serine/threonine kinase inhibitor.

Vemurafenib (**1**, Zelboraf, Roche, Figure 1) is a mutation selective serine/threonine kinase inhibitor developed to specifically inhibit mutated BRAF in the RAS-RAF-MEK-ERK pathway. The V600E mutation of *BRAF* (in which a valine is substituted for a glutamic acid at codon 600) was discovered as an oncogenic driver mutation in 2002 when this mutation was observed in different cancers. This mutation occurs in the activation loop of BRAF and substantially increases kinase activity to drive the proliferation of cancer cells. Expression of mutated BRAF is described for approximately 50% of all melanomas and is also observed in varying prevalence in other types of cancers, e.g. colorectal cancer, non-small cell lung cancer and gastric cancer [15]. Vemurafenib demonstrated good efficacy in various melanoma and colorectal xenografts *in vivo*, which are BRAF^{V600E} positive [16]. Clinical development of vemurafenib started in 2006 and in a phase I trial with 32 patients an unprecedented 81% unconfirmed overall response rate was observed, leading to the pivotal phase III trial that showed a significant improvement in the duration of survival in patients who received vemurafenib *vs* patients treated with dacarbazine, with a 63% reduction in the risk of death [15]. Vemurafenib was approved for treatment of late stage melanoma in 2011. Despite the successes of vemurafenib, patient selection in the case of therapy is of the utmost importance, as in tumors expressing wild type BRAF it has an inverse mode of action. In those cases experimental evidence suggests that vemurafenib actually leads to increased tumor cell proliferation. Accordingly, effective molecular testing for BRAF is in place in pathology laboratories.

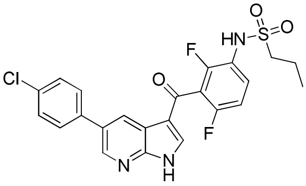

1
vemurafenib

Figure 1: Chemical structure of vemurafenib

Halaban *et al*. demonstrated this dual action mode of vemurafenib in BRAF^{WT} cell cultures isolated from primary or metastatic melanoma tumor tissue [17]. In BRAF^{V600E} cells, treatment with vemurafenib abolished ERK1/2 phosphorylation leading to inhibition of cell growth. Treatment of BRAF^{wt} cells with vemurafenib, however, lead to rapid phosphorylation of ERK1/2 and MEK [17]. These results were confirmed in additional studies using established tumor cell lines (also used in this study) and this was shown also to be the case for structurally unrelated inhibitors targeting BRAF^{V600E}, thereby demonstrating this effect not to be specific for vemurafenib only [18]. It has been hypothesized that RAS-GTP dependent activation of RAF1 (or CRAF) occurs in these cells, likely by heterodimerization with BRAF, resulting in activation of the MEK-ERK signaling cascade and ultimately leading to proliferation.

The aim of this study was to develop [^{11}C]vemurafenib as a PET imaging agent for the identification of BRAF^{V600E} expressing tumors. To this end, a radiolabeling route was developed and preclinical studies with tumor cells and tissues performed. Finally, the *in vivo* targeting potential of [^{11}C]vemurafenib was evaluated in both wild-type and mutant xenografts as a prelude to the use [^{11}C]vemurafenib in clinical PET for patient stratification.

6.2 Results and Discussion

6.2.1 Synthesis of [^{11}C]vemurafenib

Vemurafenib (**1**) can in theory be labeled with a PET-isotope on several positions. For labeling with carbon-11 the carbonyl position is amenable to radiolabeling via a carbonylative cross coupling reaction (Scheme 1). Many palladium cross coupling reactions are suitable for combination with carbon-monoxide insertions (e.g. Heck, Negishi, Sonogashira and others) [19], however, development of these chemical transformations for radiochemistry is still in its early stages. For the synthesis of [^{11}C]vemurafenib two types of palladium mediated cross coupling reactions with [^{11}C]CO-insertion were selected as potential synthesis routes, being the Suzuki and the Stille coupling [20, 21]. Both provide the motif required and examples of radiochemical variants of these reactions have appeared in literature [21]. A major challenge in [^{11}C]carbon monoxide insertion is the substoichiometric amount of [^{11}C]CO present as opposed to the pressurized CO atmosphere in which these reactions are traditionally performed. The retrosynthesis for both routes is depicted in Scheme 1 and involves the cross coupling of an aryl halide (such as **2**) with an aryl boronic acid (Suzuki coupling) or tributylstannane (Stille coupling) as depicted in structure **3**. As aryl halide the aryl iodide was selected, since it is considered to be the most reactive halide with regard to oxidative addition to palladium [22], being the first step in the catalytic cycle. With respect to **3** the tributyl stannane was chosen as this compound could be readily synthesized whereas the boronic acid for the Suzuki coupling has been proven to give problems with respect to isolation in sufficient purity. Therefore, the Stille coupling with [^{11}C]CO insertion was chosen as synthesis route for [^{11}C]vemurafenib. To our knowledge only few reports exist in which these types of radiochemical reactions are described and generally high concentrations of precursors are employed to achieve good radiochemical yields [23, 24]. Finally, literature data suggests that the rate-limiting step in this reaction is the transmetalation of the organostannane with palladium [25, 26].

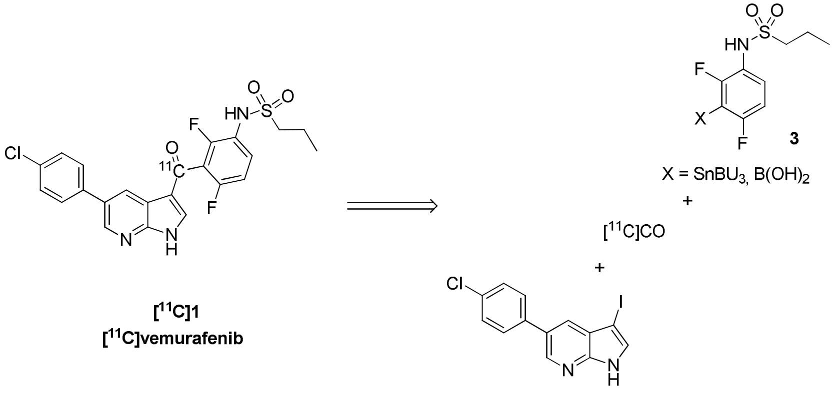

[^{11}C]1
[^{11}C]vemurafenib

3

2

Scheme 1: Retrosynthetic analysis of [^{11}C]vemurafenib via palladium catalyzed carbonylative cross coupling reactions.

As an alternative for [^{11}C]vemurafenib, fluorine-18 labeling of vemurafenib was also considered. The fluorine atoms, however, are in a challenging position to label due to the fact that these are relatively inactivated. Nevertheless, radiofluorination of similar moieties has been reported [27]. Additionally, novel methodology to fluorinate these inactivated positions are being reported and such methods could prove effective in the synthesis of a fluorine-18 derivative of vemurafenib [28]. Initial experiments toward the development of [^{18}F]vemurafenib proved unsuccessful and thus, for tracer feasibility studies, the synthesis of [^{11}C]vemurafenib was first explored.

6.2.2 Precursor synthesis

First the two precursors namely, aryliodide **2** and stannane **3** needed to be synthesized (Scheme 2) prior to the Stille coupling with [^{11}C]CO. The synthesis of aryliodide **2** starts with a Suzuki reaction to couple *para*-chlorophenylboronic acid (**4**) to 5-bromoazaindole (**5**) to yield the cross coupled product **6**. **6** was subjected to iodination with elemental iodine to obtain the desired aryl iodide **2** in a satisfying yield of 64% over 2 steps.

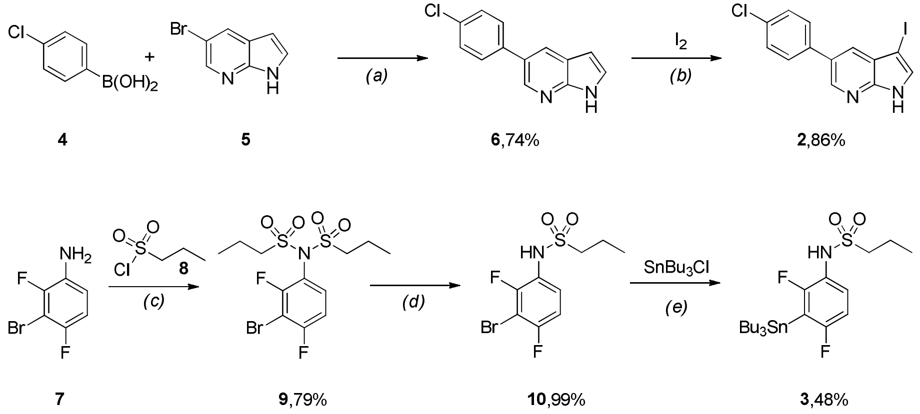

Scheme 2: Synthesis of precursors required for [^{11}C]vemurafenib. Reagents and conditions: *(a)* Pd(dppf)Cl$_2$·CH$_2$Cl$_2$, K$_2$CO$_3$, dioxane/H$_2$O, 80°C, 16h; *(b)* DMF, 20°C, 2h; *(c)* Et$_3$N, CH$_2$Cl$_2$, 20°C, 16h; *(d)* NaOH, MeOH/H$_2$O, 20°C, 2h; *(e)* *n*-BuLi, THF, -78°C-rt, 16h.

The synthesis of the second precursor, **3**, starts with double alkylation of 3-bromo-2,4-difluoro-aniline **7** with propane-1-sulfonylchloride (**8**) affording **9** in 79% yield. One of the introduced propanesulfonyl side chains is subsequently removed under basic conditions to furnish mono-substituted aniline **10** in 99% yield. Introduction of the tributylstannane moiety is achieved via a base promoted halogen lithium exchange and subsequent substitution with tributyltinchloride in 48% yield to provide the second precursor (**3**) required for radiolabeling.

6.2.3 Radiochemistry

[^{11}C]CO was produced by reduction of cyclotron produced [^{11}C]CO$_2$ over molybdenum at 850°C and the obtained [^{11}C]CO was subsequently transferred to a closed reaction vial containing THF, employing xenon as transfer gas by the recently developed method of Eriksson *et al*. [29]. The carbonylation reactions were limited to 5 minutes because of the limited half-life of carbon-11 of 20 minutes.

Our investigation started with the selection of a suitable combination of palladium source and co-ligand which was effective for the synthesis of [^{11}C]vemurafenib (Table 1). After screening a subset of palladium source/ligand combinations the combination of Pd$_2$(dba)$_3$ with triphenylarsine demonstrated promising conversion radiochemical of [^{11}C]CO, as assessed by analytical HPLC (Table 1, entry 4). Therefore this combination of palladium source and ligand was used for further optimization.

First the ratio between Pd$_2$(dba)$_3$ and triphenylarsine was investigated and a substantial increase was observed when 2 equivalents of ligand were used in comparison with palladium, however, no further increase in conversion was observed at a higher ratio (Table 2, entries 1-3). The ratio between precursors aryliodide **2** and stannane **3** was set at 1:3 in favor of the stannane, to promote the transmetalation step. A substantial increase in conversion was observed when the concentration of these reagents were increased 3-fold (Table 2, entry 4), which is in good accordance with data from literature [30]. Further increase of the precursor concentrations of **2** and **3** led to precipitation and solubility issues when preparing the reaction mixture. Additional variation of the stoichiometry did not result in higher conversion towards [^{11}C]vemurafenib (Table 2, entries 5-8). The 3-fold excess of stannane **3** indicates that the rate limiting step in this Stille coupling is indeed the transmetalation, as significantly higher conversions were obtained than when equimolar amounts of both reagents were used or when an excess of aryl iodide was used (compare Table 2, entry 4 with 7 and 8), which is in accordance with data reported on Stille reactions [25, 26]. After HPLC purification and formulation of [^{11}C]vemurafenib, these optimized reaction conditions provided an isolated yield of 21.3 ± 3.6% (corrected for decay, calculated from [^{11}C]CO) in >99% radiochemical purity, sufficient specific activity of 55 ± 18 GBq/µmol in 35 ± 2 minutes of synthesis time as an i.v. injectable solution.

Table 1: selection of palladium/ligand combinations screened for the synthesis of [^{11}C]vemurafenib.

#	Pd-source	Ligand	Solvent	Conversion (%)[a]
1	$PdCl_2(Dppf)\cdot CH_2Cl_2$	-	THF	<1
2	$Pd_2(dba)_3$	Tri-o-tolylphosphine	DMSO[b]	10
3	$Pd_2(dba)_3$	Tri-o-tolylphosphine	THF	13
4	$Pd_2(dba)_3$	Triphenylarsine	THF	16

Reactions performed at 10 µmol of reagents and 1 µmol of catalyst/ligand and at 100°C for 5 minutes. [a] conversion determined from a sample withdrawn from the reaction mixture and analysis by analytical HPLC. [b] Solubility of xenon gas in DMSO is poor and therefore transfer of [^{11}C]CO is limited [29].

Table 2: Optimization of stoichiometry.

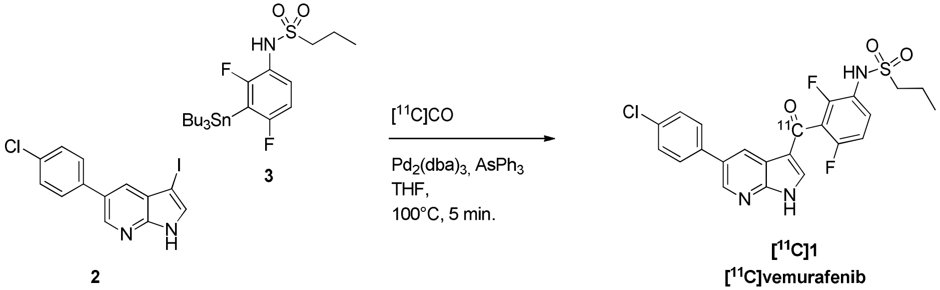

#	2 (μmol)	3 (μmol)	Ratio	$Pd_2(dba)_3$ (μmol)	$AsPh_3$ (μmol)	Ratio	Conversion (%)[a]
1	10	30	3	10	10	1	7
2	10	30	3	10	20	2	17
3	10	30	3	10	30	3	18
4	**33**	**99**	**3.0**	**10**	**20**	**2**	**41**
5	30	60	2.0	10	20	2	35
6	56	70	1.3	10	20	2	23
7	70	70	1.0	10	20	2	27
8	60	45	0.75	10	20	2	14

[a] conversion determined by first purging of excess [11C]CO from the reaction vial and subsequently a sample was withdrawn from the reaction mixture and analyzed by analytical HPLC. Expressed as average of two independent experiments.

6.2.4 Cell lines for evaluation of [^{11}C]vemurafenib binding in vitro *and* in vivo

Having a reliable synthesis route to obtain [^{11}C]vemurafenib, cell lines had to be selected to evaluate the tumor targeting potential of [^{11}C]vemurafenib. Two melanoma cell lines were selected based on reported mutational status of BRAF: Colo829 (BRAF^{V600E}) and MeWo (BRAF^{wt}). Both cell lines were analyzed by Fluorescence Activated Cell Sorting (FACS) using a BRAF antibody (recognizing both WT and BRAF^{V600E}) for assessment of target expression (Figure 2, left) [16, 31]. This demonstrated that BRAF is expressed in both cell lines, with a two-fold higher expression for Colo829 when compared to MeWo (Figure 2, left). Furthermore, both the cells as well as the xenografts derived from the cell lines were sequenced to confirm the reported mutational status of *BRAF*, i.e., Colo829 cells and xenografts contained *BRAF* mutation c.1799T>A; p.(V600E) and MeWo cells and xenografts were wild-type. To determine the sensitivity of the cell lines towards vemurafenib treatment, cell-titer blue assays were performed to determine cell viability. The BRAF^{V600E} expressing cell line (Colo829) was found to be responsive to vemurafenib treatment (IC$_{50}$ = 130 nM), while for the BRAF^{wt} line (MeWo) no IC$_{50}$ was observed (Figure 2, right).

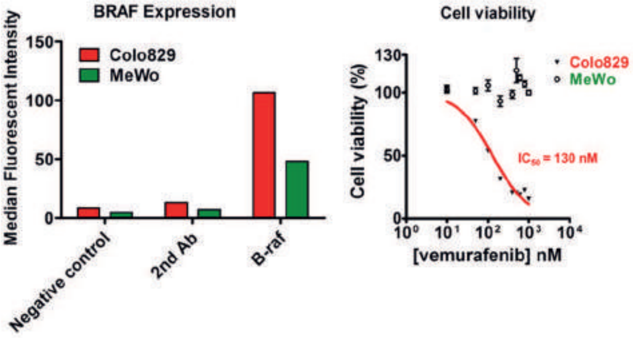

Figure 2: Left: FACS analysis for BRAF expression using a BRAF antibody that recognizes both mutated as well as wild type BRAF; Right: Representative cell viability curve after vemurafenib treatment *in vitro* of MeWo and Colo829 cells.

6.2.5 In vitro evaluation of $[^{11}C]$vemurafenib

To determine the binding potential of $[^{11}C]$vemurafenib to tumor tissue expressing $BRAF^{wt}$ or $BRAF^{V600E}$, autoradiography studies on xenograft sections and *in vitro* cellular uptake studies were performed. Sections of tumor xenografts derived from the aforementioned cell lines were incubated with $[^{11}C]$vemurafenib. This demonstrated similar high binding in both cell types (Figure 3). Upon co-incubation with isotopically unmodified vemurafenib (100 µM), binding decreased significantly although significant non-specific binding remained (Figure 3B). MeWo demonstrated 65.1 ± 3.1% binding when compared to unblocked conditions and Colo829 showed 51.2 ± 11.2% (Figure 3B). These results suggest similar binding of $[^{11}C]$vemurafenib to tissue expressing $BRAF^{wt}$ and $BRAF^{V600E}$.

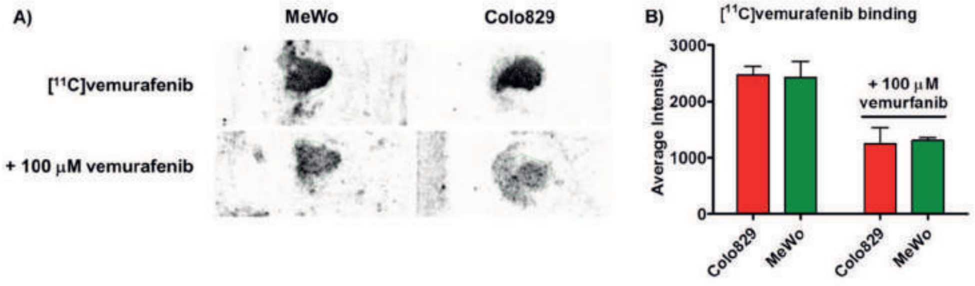

Figure 3: A) Representative autoradiography images of tumor sections of MeWo and Colo829 xenograft tumor sections incubated with $[^{11}C]$vemurafenib (top) and with $[^{11}C]$vemurafenib co-incubated with vemurafenib (100 µM); B) Quantification of blocking experiment.

To determine binding of $[^{11}C]$vemurafenib *in vitro* to intact tumor cells a cell uptake study was performed by incubation of tumor cells in suspension with $[^{11}C]$vemurafenib, followed by removal of the supernatant and washing of the cells with PBS (phosphate buffered saline). High binding was observed in both cell lines, with Colo829 cells demonstrating slightly higher binding when compared to MeWo cells (Figure 4, 74.3 ± 1.5 % vs 61.6 ± 8.2%). Upon pretreatment of the cells with isotopically unmodified vemurafenib a large decrease was observed in cell binding (to

19.3 ± 4.3% for Colo829 and 16.7 ± 6.7% for MeWo cells). These experiments demonstrated that [^{11}C]vemurafenib is able to bind to tumor tissue and is taken up by tumor cells, however, both autoradiography and cellular uptake studies demonstrated similar binding of [^{11}C]vemurafenib to both cell types, prompting further investigation using [^{11}C]vemurafenib in biodistribution studies with xenograft bearing mice.

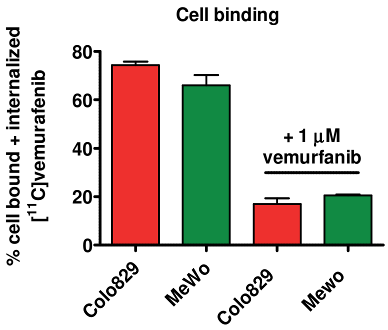

Figure 4: Quantification of cell bound + internalized fraction of [^{11}C]vemurafenib after incubation with tumor cells.

6.2.6 In vivo stability

To determine the *in vivo* stability of [^{11}C]vemurafenib, before the start of *in vivo* experiments, a plasma metabolite analysis was performed in non-tumor bearing athymic nu/nu mice. The mice were injected i.v. (via ocular plexus) with 20-25 MBq of [^{11}C]vemurafenib (corresponding to 0.36-0.45 nmol of vemurafenib) and sacrificed at 15 and 45 minutes post injection followed by blood sample collection. The non-polar and polar fractions were separated using solid phase extraction. Analysis of the blood plasma (Table 3) revealed excellent stability of [^{11}C]vemurafenib with >95% stability 45 minutes after injection. HPLC analysis of the non-polar fraction confirmed the absence of metabolites.

Table 3: Metabolite analysis

Time (p.i.)	Polar Metabolites (%)	Parent (%)
15	2.2 ± 1.9	97.8 ± 1.9
45	4.1 ± 4.4	95.9 ± 4.4

Plasma metabolite analysis after injection of [^{11}C]vemurafenib in non-tumor bearing mice. No non-polar metabolites were observed upon HPLC analysis of the non-polar fraction, which was confirmed by off-line counting of HPLC fractions. Recovery of radioactivity was >95%.

6.2.7 Ex vivo biodistribution studies

To evaluate the *in vivo* tumor targeting potential an *ex vivo* biodistribution study was performed in mice bearing the aforementioned melanoma xenografts. Tumor bearing mice were injected with 20-25 MBq of [^{11}C]vemurafenib (corresponding to 0.36-0.45 nmol of vemurafenib) and sacrificed 60 minutes post injection. Subsequently organs of interest were excised and counted for activity. [^{11}C]vemurafenib accumulation in the different organs and the tumor are depicted in Figure 5 and expressed as injected dose per gram of tissue (%ID/g).

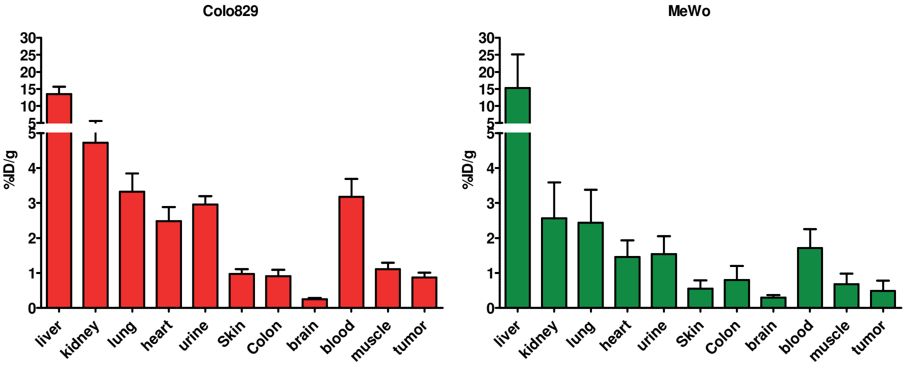

Figure 5: Biodistribution 60 minutes post injection of [^{11}C]vemurafenib in Colo829 (left, BRAF^{V600E}) and MeWo (right, BRAF^{wt}) xenograft bearing mice (*n*=3 per time point) after administration of 20-25 MBq (corresponding to 0.36-0.45 nmol of vemurafenib) under isoflurane anesthesia.

High liver uptake was observed for [^{11}C]vemurafenib, which is more frequently observed for small molecules due to their catabolism in the liver. Uptake in the kidney and urine was observed, indicating renal excretion is a clearance route of [^{11}C]vemurafenib. Highly perfused organs such as heart and lungs also demonstrated high uptake, similar to blood levels. Interestingly, the biodistribution also demonstrated relatively high blood levels of [^{11}C]vemurafenib after 60 minutes (2-3 %ID/g), which is usually lower for small molecules due to rapid blood clearance of this type of PET-tracer. Tumor uptake was modest for both xenograft lines investigated with an uptake of 0.49 ± 0.29 %ID/g in MeWo tumors and 0.87 ± 0.14 %ID/g in Colo829 tumors. While in an absolute sense the sensitive BRAF^{V600E} xenografts demonstrated slightly higher uptake, a comparison of the resulting tumor-to-background ratios clearly demonstrated similar uptake ratios across both xenograft lines (Table 4). The relevant surrounding normal tissues for melanomas being muscle, blood and skin were nearly identical when tumor-to-tissue ratios were calculated for [^{11}C]vemurafenib and in all cases the ratio never exceeded 1. The obtained *in vivo* results, however, are in good accordance with the results observed during the *in vitro* studies, in which also similar uptake was observed in both studied tumor types. This data indicates that [^{11}C]vemurafenib might be unsuitable for the *in vivo* detection of BRAF^{V600E} tumors.

Table 4: Tumor-to-normal tissue ratio

	Colo829 (BRAF^{V600E})	**MeWo (BRAF^{wt})**
Tumor-to-muscle	0.78 ± 0.18	0.72 ± 0.21
Tumor-to-blood	0.27 ± 0.06	0.29 ± 0.19
Tumor-to-skin	0.90 ± 0.19	0.89 ± 0.28

Determined at 60 min p.i.

The low tumor uptake and undesired low tumor-to-normal tissue ratios might be explained by the fact that [^{11}C]vemurafenib is unable to reach its target in the tracer amount administered during biodistribution studies. Therapeutic dosing of vemurafenib is done in the order of 50 mg/kg (corresponding to circa 2.55 μmol of vemurafenib) repeatedly in preclinical efficacy studies leading to constant higher plasma concentrations and subsequently higher tumor exposure. Furthermore, prior to target binding, [^{11}C]vemurafenib first has to cross the cellular membrane and compete with high intracellular ATP concentrations [32], further hampering target engagement. Finally, it was recently reported that vemurafenib is a substrate for ABC-cassette efflux transporters (e.g. P-gp and BCRP) promoting efflux of xenobiotics from the tumors and thereby contributing to multidrug resistance [33, 34]. The trace amounts of [^{11}C]vemurafenib could be readily transported out of the cell in this manner, thereby explaining the low tumor uptake and the relatively high blood values observed in biodistribution studies. Finally as described in the introduction, paradoxical activation of the RAS-RAF-MEK-ERK is observed in BRAF^{wt} cell lines after vemurafenib treatment indicating that uptake in these tumor cells can also be expected providing a possible explanation for the similar tumor-to-normal tissue ratios observed in both BRAF^{wt} and BRAF^{V600E} xenografts.

6.3 Conclusions

We have reported a reliable synthesis to obtain [^{11}C]vemurafenib as PET tracer using a [^{11}C]CO carbonylative Stille coupling. *In vitro* autoradiography on xenograft sections and cell uptake experiments with BRAF^{V600E} Colo829 cells and BRAF^{wt} MeWo cells demonstrated similar binding to the BRAF mutated tumor tissue when compared to wild-type. *In vivo* plasma stability studies demonstrated excellent metabolic stability of [^{11}C]vemurafenib, which is therefore ideally suited for *in vivo* experiments. *Ex vivo* biodistribution studies demonstrated modest uptake of [^{11}C]vemurafenib, not discriminating the BRAF^{V600E} mutation. Altogether, the preliminary data presented herein indicate that PET with [^{11}C]vemurafenib is not suitable as a tool to identify tumors harboring the BRAF^{V600E} mutation.

6.4 Materials and Methods

6.4.1 General

All reactions were carried out under atmospheric conditions unless otherwise stated and all reagents and solvents were supplied by Sigma-Aldrich (St. Louis, USA) and Biosolve BV (Valkenswaard, the Netherlands) and used as received unless stated otherwise. Reference vemurafenib was supplied by LC Labs (Woburn, Massachusetts, USA). Dimethylformamide (DMF, as received) and Tetrahydrofurane (THF, after distillation from $LiAlH_4$) for anhydrous purposes were stored in dry septum capped flasks charged with molecular sieves. Thin Layer Chomatography (TLC) was performed on Merck (Darmstadt, Germany) precoated silica gel 60 F254 plates. Spots were visualized by UV quenching or ninhydrin staining. Column chromatography was carried out either manually by using silica gel 60 Å (Sigma-Aldrich) or on a Büchi (Flawil, Switzerland) sepacore system (comprising of a C-620 control unit, a C-660 fraction collector, two C601 gradient pumps and a C640 UV detector) equipped with Büchi sepacore prepacked flash columns. ^{1}H and ^{13}C nuclear magnetic resonance (NMR) spectra were recorded on a Bruker (Billerica, USA) Avance 500 (500.23 MHz and 125.78 MHz, respectively) with chemical shifts (δ) reported in ppm relative to the solvent. Electrospray ionization mass spectrometry (ESI-MS) was carried out using a Bruker microTOF-Q instrument in positive ion mode (capillary potential of 4500 V). Analytical HPLC was performed on a Jasco PU-2089 pump (Easton, USA) equipped with a Grace (Columbia, USA) C18 Gracesmart column (5 µm, 250 mm × 4.6 mm) and $MeCN/H_2O/TFA$ (65:35:0.1, *v/v/v*) as eluent at a flow rate of 1 $mL{\cdot}min^{-1}$, with a Jasco UV-2075 UV detector (λ=254 nm) and a NaI radioactivity detector (Raytest, Straubenhardt, Germany). Chromatograms were acquired using GINA star software (version 5.1, Raytest). Semi-preparative HPLC was carried out on a Jasco PU-2089 pump equipped with a C18 Alltima column (Grace, 5 µm, 250 mm × 10 mm) using MeCN/H2O/TFA (65:35:0.1, *v/v/v*) as eluent at a flow rate of 4 $mL{\cdot}min^{-1}$, a Jasco UV1575 UV detector (λ=254 nm) and a custom-made radioactivity detector.

Chromatograms were acquired using ChromNAV software (version 1.14.01, Jasco). Athymic nu/nu mice were obtained from Harlan Netherlands B.V. (Horst, the Netherlands). All animal experiments were performed according to Dutch national law ('Wet op de proefdieren', Stb 1985, 336) and approved by the local ethics committee.

6.4.2 Chemistry

5-(4-chlorophenyl)-1H-pyrrolo[2,3-b]pyridine (6).

To a solution of (4-chlorophenyl)boronic acid (563 mg, 3.60 mmol) and 5-bromo-1H-pyrrolo[2,3-b]pyridine (591 mg, 3.00 mmol) in dioxane (8 mL) was added a solution of K_2CO_3 (498 mg, 3.60 mmol) and the mixture was stirred for 30 min. followed by the addition of $Pd(dppf)Cl_2 \cdot CH_2Cl_2$ (220 mg, 0.30 mmol). The mixture was stirred at 80°C overnight, upon which the volatiles were removed *in vacuo*. The obtained solid is suspended in EtOAc and washed with water. The organic layer is separated, dried (Na_2SO_4) and evaporated to afford the crude product, which was purified by column chromatography (Hexane/EtOAc, 6:4, v/v) to afford the product as a tan solid (509 mg, 2.23 mmol, 74%). ^{1}H-NMR (500.23 Mhz, DMSO-D_6) δ: 11.7 (br s, 1H), 8.51 (d, $^4J_{H,H}$ = 1.9 Hz, 1H), 8.21 (d, $^4J_{H,H}$ = 1.9 Hz, 1H), 7.52 (m, 3H), 7.74 (m, 2H), 6.51 (dd, $^3J_{H,H}$ = 3.5 Hz, $^4J_{H,H}$ = 1.9 Hz, 1 H). ^{13}C-NMR (125.78 Mhz, DMSO-D_6) δ: 148.6 (C_q), 141.8 (CH), 138.4 (C_q), 132.2 (C_q), 129.0 (2x CH), 128.9 (2x CH), 127.6 (CH), 127.3 (C_q), 126.7 (CH), 119.7 (C_q), 100.2 (CH). HR-MS (ESI, 4500V): m/z calculated for $C_{13}H_9ClN_4$: 228.0454, found: ($M+H^+$): 229.0518.

5-(4-chlorophenyl)-3-iodo-*1H*-pyrrolo[2,3-b]pyridine (7).

In an evacuated flask, under argon atmosphere 5-(4-chlorophenyl)-*1H*-pyrrolo[2,3-b]pyridine (**6**, 850 mg, 3.72 mmol) and potassium hydroxide (667 mg, 11.9 mmol) were dissolved in DMF (10 mL). To this mixture was added a solution of elemental iodine (1.13 mg, 4.46 mmol) in DMF (6.5 mL). The resulting reaction mixture was stirred for 2 h at room temperature upon which the mixture was poured into ice water and the resulting precipitate was collected by vacuum filtration. The crude product was purified by flash column chromatography (Hexane/EtOAc, 1:1, v/v) to afford the title compound as a tan solid (1.13 g, 3.20 mmol, 86 % yield. ^{1}H-NMR (500.23 Mhz, DMSO-D$_6$) δ: 12.25 (br s, 1H), 8.57 (d, $^4J_{H,H}$ = 1.9 Hz, 1H), 7.88 (d, $^4J_{H,H}$ = 1.9 Hz, 1H), 7.80 (m, 3H), 7.55 (d, $^3J_{H,H}$ = 8.5 Hz, 2H). ^{13}C-NMR (125.78 Mhz, DMSO-D$_6$) δ: 148.2 (C$_q$), 143.1 (CH), 137.8 (C$_q$), 132.6 (C$_q$), 132.1 (CH), 129.4 (2x CH), 129.3 (2x CH), 128.4 (C$_q$), 126.4 (CH), 122.5 (C$_q$), 55.3 (C$_q$). HR-MS (ESI, 4500V): m/z calculated for $C_{13}H_9ClIN_4$: 353.9421, found: (M+H$^+$): 354.9465.

N-(3-bromo-2,4-difluorophenyl)-N-(propylsulfonyl)propane-1-sulfonamide (9).

To a solution of 3-bromo-2,4-difluoroaniline (416 mg, 2 mmol) and triethylamine (585 µl, 4.20 mmol) in CH_2Cl_2 (10 mL) was added propane-1-sulfonylchloride (472 µL, 4.20 mmol) slowly. The mixture was stirred at room temperature under a nitrogen atmosphere overnight. The mixture was evaporated *in vacuo* and taken up in EtOAc. The organic solution was washed with $KHSO_4$ (1 M, aq), $NaHCO_3$ (sat, aq), brine, dried (Na_2SO_4) and evaporated to dryness to afford the crude product. The product was purified by flash column chromatography (Hexane/EtOAc, 9:1, v/v) to afford the title compound as a brown solid (664 mg, 1.58 mmol, 79%). ^{1}H-NMR (500.23 Mhz, CDCl$_3$) δ: 7.36 (m, 1H), 7.05 (ddd, $^3J_{H,F}$ = 9.0 Hz, $^3J_{H,H}$ = 7.4 Hz, $^4J_{H,F}$ = 1.9 Hz, 1H), 3.49 (m, 2H), 1.96 (m, 4H), 1.10 (t, $^3J_{H,H}$ = 7.4 Hz, 6H). ^{13}C-NMR (125.78 Mhz, CDCl$_3$) δ: 162.03 (C$_q$), 160.0 (C$_q$), 157.0 (C$_q$), 132.2 (CH), 119.0 (C$_q$), 112.1 (CH), 99.5 (C$_q$), 57.8 (2x CH$_2$), 16.9 (2x CH$_2$), 12.9 (2x CH$_3$). HR-MS (ESI, 4500V): m/z calculated for $C_{12}H_{16}BrF_2NO_4S_2$: 418.9672, found: (M+Na$^+$): 441.9478.

N-(3-bromo-2,4-difluorophenyl)propane-1-sulfonamide (10).

N-(3-bromo-2,4-difluorophenyl)-*N*-(propylsulfonyl)propane-1-sulfonamide (**9**, 420 mg, 1 mmol) was dissolved in NaOH (2 M, aq, 5 mL) and MeOH (15 mL) and stirred at room temperature for 2 h. The MeOH was evaporated *in vacuo* and the pH was adjusted to 1-2 with HCl (1 M, aq). The aqueous suspension was extracted with CH_2Cl_2 (3x) and the organic layers were combined, dried (Na_2SO_4) and evaporated to yield the title compound as a light brown solid (313 mg, 0.99 mmol, 99%). ^{1}H-NMR (500.23 Mhz, CDCl$_3$) δ: 7.56 (td, $^4J_{H,F}$ = 8.9 Hz (2x), $^3J_{H,H}$ = 5.5 Hz, 1H), 6.99 (ddd, $^3J_{H,F}$ = 9.1 Hz,

$^3J_{H,H}$ = 7.6 Hz, $^4J_{H,F}$ = 1.9 Hz, 1H), 6.47 (s, 1H), 3.06 (m, 2H), 1.88 (sxt, $^3J_{H,H}$ = 7.6 Hz, 2H), 1.06 (t, $^3J_{H,H}$ = 7.4 Hz, 3H). ^{13}C-NMR (125.78 MHz, $CDCl_3$) δ: 158.4 (C_q), 156.4 (C_q), 123.3 (CH), 121.7 (C_q), 112.2 (CH), 96.6 (C_q), 54.2 (CH_2), 17.2 (CH_2), 12.9 (CH_3). HR-MS (ESI, 4500V): m/z calculated for $C_9H_{10}BrF_2NO_2S$: 312.9584, found: (M+Na$^+$): 337.9391.

***N*-(2,4-difluoro-3-(tributylstannyl)phenyl)propane-1-sulfonamide (3).**

A flame dried flask was charged with: *N*-(3-bromo-2,4-difluorophenyl)propane-1-sulfonamide (**10**, 500 mg, 1.59 mmol) and freshly distilled THF (15 mL). The solution was cooled to -80°C and to this was added to *N*-buthyllithium (2.19 ml, 3.50 mmol, 1.6M in hexanes). The obtained reaction mixture was stirred for 30 minutes, after which tributylchlorostannane (518 µL, 1.91 mmol) was added and the mixture was allowed to warm up to RT and stirred overnight. The mixture was quenched by the addition of water and subsequently extracted with CH_2Cl_2. Evaporation of the organic layer afforded the crude product, which was purified by flash column chromatography (Hexane/EtOAc, 9:1, v/v) to afford the title compound as a viscous oil (400 mg, 0.763 mmol, 48% yield). ^{1}H-NMR (500.23 Mhz, $CDCl_3$) δ: 7.53 (td, $^4J_{H,F}$ = 9.1 (2x), $^3J_{H,H}$ = 6.1 Hz, 1H), 6.85 (dd, $^3J_{H,F}$ = 9.0 Hz, $^3J_{H,H}$ = 5.7 Hz, 1H), 6.30 (s, 1H), 3.03 (m, 2H), 1.88 (sxt, $^3J_{H,H}$ = 7.6 Hz, 2H), 1.55 (m, 6H), 1.35 (sxt, $^3J_{H,H}$ = 7.3 Hz, 6H), 1.21 (m, 6H), 1.05 (t, $^3J_{H,H}$ = 7.4 Hz, 3H), 0.91 (t, $^3J_{H,H}$ = 7.3 Hz, 9H). ^{13}C-NMR (125.78 Mhz, $CDCl_3$) δ: 165.6 (C_q), 163.7 (C_q), 159.0 (C_q), 125.9 (CH), 120.0 (C_q), 111.5 (CH), 53.4 (CH_2), 28.9 (3x CH_2), 27.2 (3x CH_2), 17.2 (CH_2), 13.7 (3x CH_3), 12.9 (CH_3), 9.8 (3x CH_2). HR-MS (ESI, 4500V): m/z calculated for $C_{21}H_{37}F_2NO_2SSn$: 525.1535, found: (M+Na$^+$): 548.1502.

6.4.3 Radiochemistry

Production of [^{11}C]CO: [^{11}C]CO_2 was produced by the $^{14}N(p,\alpha)^{11}C$ nuclear reaction performed in a 0.5% O_2/N_2 gas mixture (Linde gas, Schiedam, The Netherlands) using an IBA Cyclone 18/9 cyclotron (IBA, Louvain-la-Neuve, Belgium). Radioactivity levels were measured using a Veenstra (Joure, The Netherlands) VDC-405 dose calibrator. Radiosynthesis was performed using in-house built remotely controlled synthesis units [35]. After irradiation, [^{11}C]CO_2 was transferred to the experimental set-up and concentrated on a silica trap (50 mg silica gel, 100/80 mesh) at -196°C in liquid nitrogen. When the activity reached a maximum, the trap was heated and [^{11}C]CO_2 was passed over a gas purifier column (400 x 4 mm, silica gel, 100/80 mesh) using helium (40 mL.min^{-1}) as a carrier gas. The purified [^{11}C]CO_2 was passed over a molybdenum reductor column (<150μm, 99.99%, Sigma Aldrich) at 850°C after which unreacted [^{11}C]CO_2 was trapped on an ascarite column and [^{11}C]CO was collected on a silica trap (1 mg silica gel, 100/80 mesh) at -196°C. The transfer gas was switched from helium to xenon (Fluka ≥ 99.995, via Sigma Aldrich), [^{11}C]CO was released by heating of the trap and transferred to the capped and closed reagent vial by a gentle xenon flow (2.0 mL.min^{-1}). The reactions were performed after removal of the transfer needle and all experiments were carried out with the same vial type (1 mL, clear crimp vial, 10 x 32 mm, type 27333, Supelco, via Sigma Aldrich) and septum (11-mm aluminum crimp cap, 1.5-mm silicone/PTFE seal, Grace Alltech, Columbia, Maryland, USA) [29].

[^{11}C]Vemurafenib radiosynthesis: $Pd_2(dba)_3$ (2.4 mg, 10 μmol) was dissolved in dry THF (700 μL), and to this solution was added in sequence: triphenylarsine (6.5 mg, 20 μmol), 5-(4-chlorophenyl)-3-iodo-1H-pyrrolo[2,3-b]pyridine (**2**, 10.0 mg, 28.2 μmol) and *N*-(2,4-difluoro-3-(tributylstannyl)phenyl)propane-1-sulfonamide (**3**, 45.0 mg, 85.8 μmol). The vial was capped and connected to the transfer needle for [^{11}C]CO. After transfer of [^{11}C]CO to the reaction mixture (as described above) the vial was heated to 100°C for 5 min. followed by the introduction of a vent needle to the reaction vial and heating for an additional 2 min. at 130°C to evaporate the THF and remove excess gaseous [^{11}]CO. The obtained residue was dissolved in semi-preparative HPLC eluent (3 mL, 65/35/0.1, MeCN/H_2O/TFA, v/v/v*)* and subjected to purification by semi-preparative HPLC chromatography using an Grace Alltima C18 column (5 μ, 250 mm x 10 mm, Columbia, USA) using as eluent: 65/35/0.1, MeCN/H_2O/TFA, v/v/v at a flow of 4 mL.min^{-1}. Retention time of the product was 10.5 minutes. The collected fraction of the preparative HPLC purification containing [^{11}C]vemurafenib was reformulated via solid phase extraction. The fraction was first diluted with 40 mL of water and the total mixture was passed over a preconditioned

(10 mL of ethanol, 10 mL of water) tC18 plus Sep-Pak cartridge (Waters, Milford, Massachusetts, USA). The cartridge was then washed with 15 mL of sterile water and 0.5 mL of sterile 96% ethanol after which the product was eluted from the cartridge with 0.5 mL of sterile 96% ethanol. The ethanol was diluted to 10 volume percent with formulation solution (7.09 mM NaH_2PO_4 in 0.9% NaCl, w/v in water, pH 5.2) and the complete solution was filtered over a Millex-GV 0.22 μm filter into a sterile 20 mL capped vial. To provide a final solution of [^{11}C]vemurafenib in 10% ethanol in saline (containing 7.09 mM NaH_2PO_4). Analysis of the product was performed by analytical HPLC. Retention time of the product was 6 min., radiochemical purity was >99%. The specific activity was calculated against a calibration curve of vemurafenib using the analytical HPLC system and was found to be 55 ± 18 GBq/μmol.

6.4.4 FACS analysis

For FACS analysis of BRAF expression of Colo829 and MeWo cells, the cells were first trypsinized and diluted with PBS to a final volume of 5 mL. Subsequently an aliquot of these cells (100 μL) were counted. The cells were centrifuged (1600 rpm, 4 min.; Hettich Universal 320, Hettich, Buford, Georgia, USA), the supernatant was removed and the pellet was taken up in fresh PBS (500 μL) and was centrifuged again (1600 rpm, 4 min., Eppendorf 5417R Microcentrifuge, Fisher Scientific, Waltman, Massachusetts, USA). The supernatant was removed and the pellet was taken up in icecold PBS (150 μL), cells were treated with paraformaldehyde (16% in water, Brunschwig Chemie, Amsterdam, The Netherlands) and incubated for 20 min. on ice for fixation, followed by washing with PBS (100 μL, twice). Subsequently cells were permeabilized with 0.1% sapponine (in PBS) at room temperature for 30 min. followed by centrifugation (1600 rpm, 4 min.). The cells were blocked by the addition of 0.1% sapponine /2% BSA (in PBS) for 30 min. at room temperature and centrifuged (1600 rpm, 4 min., Eppendorf 5417R Microcentrifuge). The BRAF antibody (purified mouse anti-BRAF, 250 μg/mL, 10 uL diluted with 90 uL 0.1% sapponine/2%BSA, BD Biosciences, San Jose, California, USA) was added and the cells were incubated for 30 min. at room temperature. Upon completion the cells were washed with 0.1% sapponine/2%BSA in PBS (100 µL) and the secondary antibody (Goat anti-mouse Ig FITC, 250 µg/mL, 4 uL in 96 uL 0.1% sapponine/2%BSA in PBS, BD Biosciences systems) was added and the cells were incubated in the dark for 30 min. at room temperature. Upon completion the cells were washed with PBS and taken up in fresh PBS for FACS analysis. Samples were measured by a two laser (488 nm blue laser and 635 nm red laser) Calibur flow cytometer (BD Biosciences) employing the 488 nm blue laser. Data was acquired and analyzed with Cell Quest software (BD Biosciences). Control experiments included treating the cells in the same manner, with exclusion of the primary antibody or the exclusion of both antibodies.

6.4.5 Sequencing analysis of BRAF

For Colo829 and MeWO, the mutational status of *BRAF* exon 15 was assessed by HRM (high-resolution melting) assay followed by Sanger sequencing of HRM-PCR products with an aberrant melting curve, essentially as described previously [36].

6.4.6 Cell Titer Blue assays

Vemurafenib stock solutions of 1 mM in DMSO were prepared and diluted with PBS to a concentration of 10 µM (1% DMSO). Cells (Colo829 or MeWo) were seeded in triplo in a 96 wells plate and treated with increasing concentrations of vemurafenib, from the above mentioned stock solution diluted with medium. After 120 h incubation at 37°C in a CO_2 incubator, CellTiter-Blue (resazurin, Promega, Madesson, WI, USA) was added to the wells and the cells were incubated in the dark for 4 h at 37°C in a CO_2 incubator after which the reaction was stopped by the addition of 3% SDS (50 µL) to each well. Finally the fluorescence was measured using a TriStar^2 LB942 plate reader (Berthold Technologies, Bad Wildbad, Germany). Data was corrected for medium only and normalized to untreated cells (100% viability)

6.4.7 Autoradiography on Colo829 and MeWo xenograft sections

Colo829 and MeWo xenograft sections (10 µm thickness) were pre-treated three times with 5 mM Tris-HCl buffer (pH 7.4) for 5 min.. Sections were dried under a gentle air flow before incubation for 30 min. with [^{11}C]vemurafenib and the following conditions: (A) 5 mM Tris-HCl, pH 7.4; (B) 5 mM Tris-HCl, pH 7.4 and isotopically unmodified vemurafenib at 100 µM (*n* = 4 for each incubation condition). Washing was performed using Tris-HCl (3x) followed by dipping in ice cold water. After drying in an air stream, tumor sections were exposed to a phosphor-imaging screen for 15 min. Data was quantified as average signal intensity per surface area and were represented relative to the tracer only (A) conditions, which was set at 100%. Error bars indicate standard deviations. Quantification of binding was performed using ImageQuantTL v8.1.0.0 (GE Healthcare, Buckinghamshire, UK) by drawing regions of interest around the full tumor sections.

6.4.8 In vitro cell uptake experiments

Colo829 or MeWo cells (1*10^6) suspended in growth medium were incubated in triplicate in centrifuge tubes at 37°C with 1 MBq of [^{11}C]vemurafenib (corresponding to 0.02 nmol of vemurafenib) for 30 min. Upon completion of the incubation period the tubes were centrifuged (5000 rpm, 5 min, 0°C, Hettich universal 16, Depex B.V., the Netherlands) and the supernatant was removed and collected. Subsequently the cells were gently resuspended in PBS and centrifuged again. This procedure was repeated twice and PBS wash steps were collected. All fractions (cells, supernatant and PBS) were counted for radioactivity using a gamma counter (Wallac 1210 Compugamma, PerkinElmer, Waltham, MA, USA) and the cell bound/internalized percentage of [^{11}C]vemurafenib was determined as the fraction of activity in the cell pellet divided by the total activity (cells, supernatant and PBS) corrected for background (medium only) and vehicle treated conditions.

6.4.9 Plasma metabolite analysis

Athymic nu/nu mice were injected with 20-25 MBq of [^{11}C]vemurafenib (corresponding to 0.36-0.45 nmol of vemurafenib), in the ocular plexus under isoflurane anesthesia (2% in 1 L·min^{-1}). The mice were sacrificed at 15 (n = 3) and 45 (n = 3) min. p.i.. At these time points, about 1.0–1.5 mL of blood was collected via a heart puncture from each mouse. Blood was collected in a heparin tube and centrifuged for 5 min. at 4000 r.p.m. (Hettich universal 16, Depex B.V., The Netherlands). Plasma was separated from blood cells and about 1 mL of plasma was diluted with 2 mL of 0.1 M hydrochloric acid and loaded onto a tC18 Sep-Pak cartridge, which was pre-activated by elution with 3 mL of MeOH and 6 mL of water, respectively. The cartridge was washed with 5 mL of H_2O to collect polar radioactive metabolites. Thereafter, the tC18 Sep-Pak cartridge (Waters, Milford, Massachusetts, USA) was eluted with 2 mL of MeOH and 1 mL of H_2O to collect the mixture of non-polar metabolites. The mixture of non-polar metabolites was analyzed using HPLC to determine the percentage of intact [^{11}C]vemurafenib. HPLC was performed on a Dionex (Sunnyville, California, USA) Ultimate 3000 system, equipped with a 1 mL loop. As a stationary phase a Phenomenex (Torrance, California, USA) Gemini C18, 250 × 10 mm, 5 μm was used. The mobile phase was a gradient of A = acetonitrile and B = 0.1% TFA in H_2O. The HPLC gradient ran for 12.0 min. decreasing the concentration of eluent B from 60% to 20% in 10 min. followed by 2 min. of 20% eluent B at a flow rate of 3.5 mL · min^{-1}. Recovery of radioactivity was >95%.

6.4.10 Biodistribution studies

Nude mice (Athymic nu/nu, Harlan, Horst, The Netherlands) bearing two tumors (obtained by injection of MeWo or Colo829 cells, 2*10^6 per site) of the same xenograft line on their left and right flank, received an injection of 25 MBq [^{11}C]vemurafenib (corresponding to 0.45 nmol of vemurafenib) via the ocular plexus. The mice were sacrificed and dissected at 60 min. post-injection. Blood, urine, skin, left tumor, right tumor, muscle, heart, colon, lung, liver, kidney and brain were collected, weighed and counted for radioactivity in a gamma counter (Wallac 1210 Compugamma, PerkinElmer, Waltham, MA, USA). Biodistribution data are expressed as percentage of injected dose per gram (%ID/g) of tissue for each organ.

6.5 References

[1] Morin MJ. From oncogene to drug: development of small molecule tyrosine kinase inhibitors as anti-tumor and anti-angiogenic agents *Oncogene* **2000**, *19*, 6574-6583.

[2] Lemmon MA and Schlessinger J. Cell signaling by receptor-tyrosine kinases *Cell* **2010**, *141*, 1117-1134.

[3] Arora A and Scholar EM. Role of tyrosine kinase inhibitors in cancer therapy *J. Pharmacol. Exp. Ther.* **2005**, *315*, 971-979.

[4] Sharma SV, Bell DW, Settleman J, and Haber DA. Epidermal growth factor receptor mutations in lung cancer *Nat. Rev. Cancer* **2007**, *7*, 169-181.

[5] Kobayashi K and Hagiwara K. Epidermal growth factor receptor (EGFR) mutation and personalized therapy in advanced nonsmall cell lung cancer (NSCLC) *Target. Oncol.* **2013**, *8*, 27-33.

[6] Lindeman NI, Cagle PT, Beasley MB, Chitale DA, Dacic S, Giaccone G, et al. Molecular testing guideline for selection of lung cancer patients for EGFR and ALK tyrosine kinase inhibitors: Guideline from the college of american pathologists, international association for the study of lung cancer, and association for molecular pathology *J. Thorac. Oncol.* **2013**, *8*, 823-859.

[7] Poot AJ, Slobbe P, Hendrikse NH, Windhorst AD, and van Dongen GAMS. Imaging of TKI-target interactions for personalized cancer therapy *Clin. Pharmacol. Ther.* **2013**, *93*, 239-241.

[8] Slobbe P, Poot AJ, Windhorst AD, and van Dongen GAMS. PET imaging with small-molecule tyrosine kinase inhibitors: TKI-PET *Drug Discovery Today* **2012**, *17*, 1175-1187.

[9] van Dongen G, Poot A, and Vugts D. PET imaging with radiolabeled antibodies and tyrosine kinase inhibitors: immuno-PET and TKI-PET *Tumor Biol.* **2012**, *33*, 607-615.

[10] Slobbe P, Windhorst A, Stigter-van Walsum M, Smit E, Niessen H, Solca F, et al. A comparative PET imaging study with the reversible and irreversible EGFR tyrosine kinase inhibitors [^{11}C]erlotinib and [^{18}F]afatinib in lung cancer-bearing mice *EJNMMI Res.* **2015**, *5*, 14.

[11] Bahce I, Smit EF, Lubberink M, van der Veldt AAM, Yaqub M, Windhorst AD, et al. Development of [^{11}C]erlotinib Positron Emission Tomography for *in vivo* evaluation of EGF receptor mutational status *Clin. Cancer Res.* **2013**, *19*, 183-193.

[12] Slobbe P, Windhorst AD, Walsum MS-v, Schuit RC, Smit EF, Niessen HG, et al. Development of [^{18}F]afatinib as new TKI-PET tracer for EGFR positive tumors *Nucl. Med. Biol.* **2014**, *41*, 749-757.

[13] Memon AA, Weber B, Winterdahl M, Jakobsen S, Meldgaard P, Madsen HHT, et al. PET imaging of patients with non-small cell lung cancer employing an EGF receptor targeting drug as tracer *Br. J. Cancer* **2011**, *105*, 1850-1855.

[14] Memon AA, Jakobsen S, Dagnaes-Hansen F, Sorensen BS, Keiding S, and Nexo E. Positron emission tomography (PET) imaging with [^{11}C]-labeled erlotinib: A micro-PET study on mice with lung tumor xenografts *Cancer Res.* **2009**, *69*, 873-878.

[15] Bollag G, Tsai J, Zhang J, Zhang C, Ibrahim P, Nolop K, et al. Vemurafenib: the first drug approved for BRAF-mutant cancer *Nat. Rev. Drug. Discov.* **2012**, *11*, 873-886.

[16] Yang H, Higgins B, Kolinsky K, Packman K, Go Z, Iyer R, et al. RG7204 (PLX4032), a selective BRAFV600E inhibitor, displays potent antitumor activity in preclinical melanoma models *Cancer Res.* **2010**, *70*, 5518-5527.

[17] Halaban R, Zhang W, Bacchiocchi A, Cheng E, Parisi F, Ariyan S, et al. PLX4032, a selective BRAFV600E kinase inhibitor, activates the ERK pathway and enhances cell migration and proliferation of BRAFWT melanoma cells *Pigm. Cell Melanoma Res.* **2010**, *23*, 190-200.

[18] Hatzivassiliou G, Song K, Yen I, Brandhuber BJ, Anderson DJ, Alvarado R, et al. RAF inhibitors prime wild-type RAF to activate the MAPK pathway and enhance growth *Nature* **2010**, *464*, 431-435.

[19] Wu X-F, Neumann H, and Beller M. Palladium-catalyzed carbonylative coupling reactions between Ar-X and carbon nucleophiles *Chem. Soc. Rev.* **2011**, *40*, 4986-5009.

[20] Långström B, Itsenko O, and Rahman O. [^{11}C]Carbon monoxide, a versatile and useful precursor in labelling chemistry for PET-ligand development *J. Labelled Compd. Radiopharm.* **2007**, *50*, 794-810.

[21] Rahman O. [^{11}C]Carbon monoxide in labeling chemistry and positron emission tomography tracer development: scope and limitations *J. Labelled Compd. Radiopharm.* **2015**, *58*, 86-98.

[22] Vikse K, Naka T, McIndoe JS, Besora M, and Maseras F. Oxidative additions of aryl halides to palladium proceed through the monoligated complex *Chemcatchem* **2013**, *5*, 3604-3609.

[23] Karimi F, Barletta J, and Långström B. Palladium-mediated ^{11}C-carbonylative cross-coupling of alkyl/aryl iodides with organostannanes: An efficient synthesis of unsymmetrical alkyl/aryl [^{11}C-carbonyl]ketones *Eur. J. Org. Chem.* **2005**, *2005*, 2374-2378.

[24] Nader MW and Oberdorfer F. Syntheses of [carbonyl-^{11}C]2-(2-benzoylphenoxy)-N-phenylacetamide from [^{11}C]carbon monoxide by the Suzuki and the Stille reactions *Appl. Radiat. Isot.* **2002**, *57*, 681-685.

[25] Farina V and Krishnan B. Large rate accelerations in the stille reaction with tri-2-furylphosphine and triphenylarsine as palladium ligands: mechanistic and synthetic implications *J. Am. Chem. Soc.* **1991**, *113*, 9585-9595.

[26] Stille JK. The palladium-catalyzed cross-coupling reactions of organotin reagents with organic electrophiles *Angew. Chem. Int. Ed.* **1986**, *25*, 508-524.

[27] Wang M, Gao M, Miller KD, Sledge GW, and Zheng Q-H. [^{11}C]GSK2126458 and [^{18}F]GSK2126458, the first radiosynthesis of new potential PET agents for imaging of PI3K and mTOR in cancers *Bioorg. Med. Chem. Lett.* **2012**, *22*, 1569-1574.

[28] Tredwell M, Preshlock SM, Taylor NJ, Gruber S, Huiban M, Passchier J, et al. A general copper-mediated nucleophilic ^{18}F fluorination of arenes *Angew. Chem. Int. Ed.* **2014**, *53*, 7751-7755.

[29] Eriksson J, van den Hoek J, and Windhorst AD. Transition metal mediated synthesis using [^{11}C]CO at low pressure – a simplified method for ^{11}C-carbonylation *J. Labelled Compd. Radiopharm.* **2012**, *55*, 223-228.

[30] Nader MW and Oberdorfer F. Syntheses of carbonyl-C-11 2-(2-benzoylphenoxy)-N-phenylacetamide from C-11 carbon monoxide by the Suzuki and the Stille reactions *Appl. Radiat. Isot.* **2002**, *57*, 681-685.

[31] Sapkota B, Hill CE, and Pollack BP. Vemurafenib enhances MHC induction in BRAFV600E homozygous melanoma cells *OncoImmunology* **2013**, *2*, e22890.

[32] Garuti L, Roberti M, and Bottegoni G. Non-ATP competitive protein kinase inhibitors *Curr. Med. Chem.* **2010**, *17*, 2804-2821.

[33] Mittapalli RK, Vaidhyanathan S, Sane R, and Elmquist WF. Impact of P-Glycoprotein (ABCB1) and Breast Cancer Resistance Protein (ABCG2) on the brain distribution of a novel BRAF inhibitor: Vemurafenib (PLX4032) *J. Pharmacol. Exp. Ther.* **2012**, *342*, 33-40.

[34] Durmus S, Sparidans RW, Wagenaar E, Beijnen JH, and Schinkel AH. Oral availability and brain penetration of the B-RAF(V600E) inhibitor vemurafenib can be enhanced by the P-Glycoprotein (ABCB1) and Breast Cancer Resistance Protein (ABCG2) inhibitor elacridar *Mol. Pharmaceutics* **2012**, *9*, 3236-3245.

[35] Windhorst AD, Linden TT, de Nooij A, Keus JF, Buijs FL, Schollema PE, et al. A complete, multipurpose, low cost, fully automated and GMP compliant radiosynthesis system *J. Labelled Compd. Radiopharm.* **2001**, *44*, S1052-S1054.

[36] Heideman DAM, Lurkin I, Doeleman M, Smit EF, Verheul HM, Meijer GA, et al. KRAS and BRAF mutation analysis in routine molecular diagnostics: Comparison of three testing methods on formalin-fixed, paraffin-embedded tumor-derived DNA *J. Mol. Diagn.* **2012**, *14*, 247-255.

Chapter 7

Reflections and future perspectives

7.1 Reflections

TKI-PET imaging with FDA approved kinase inhibitors, as described in this thesis, has demonstrated its initial value in a preclinical setting as well as in early phase clinical studies. These studies, however, are not straightforward and require a tailor made approach per TKI of interest. It is of critical importance that the radiolabeled TKIs chemical structure is unchanged and that they are labeled in an inert way for two major reasons: firstly, only when the chemical structure is unchanged a representative biodistribution of the pharmaceutical of interest is obtained. Secondly, rapid translation of preclinical results to the clinic are possible with FDA approved radiolabeled TKIs as no further toxicological studies are required. For TKI-target interaction studies, especially the selection of an appropriate model system to evaluate the novel radiotracers was found to be of great importance. Currently the most successful TKI-PET tracer is without doubt [^{11}C]erlotinib, followed closely by [^{18}F]afatinib. Both compounds have demonstrated their value in the field of imaging sensitizing mutations of EGFR (Epidermal Growth Factor Receptor). This is, in part, owed to the excellent availability of NSCLC (Non-Small Cell Lung Cancer) cell lines and their proper characterization with regard to receptor expression, mutational status and sensitivity. On the other hand the clinically observed mutations are also well defined. The exon 19 deletion of EGFR is readily imaged using TKIs specific for this mutation, where substantial tumor-to-background ratios for [^{11}C]erlotinib and [^{18}F]afatinib are observed in xenografted mice [1]. [^{11}C]Erlotinib was clinically validated in a proof-of-principle study in NSCLC patients demonstrating the same trend of uptake in exon 19 deleted EGFR expressing tumors and not in patients whose tumor expressed wild type EGFR [2]. [^{18}F]afatinib is currently also being evaluated in NSCLC patients and early results are encouraging in patients harboring activating mutations of EGFR. Depicted in Figure 1 is a PET-image of the first patient ever scanned with [^{18}F]afatinib, the tumor expressed a treatment sensitive exon 19 deletion as confirmed by sequencing of biopsy material [3]. Uptake of [^{18}F]afatinib can be seen in the tumor (indicated by the crosshair). Uptake matches the viable tumor tissue (dependent on EGFR for proliferation), as confirmed by [^{18}F]FDG PET (Figure 1-C) and the necrotic central core of the tumor showed no uptake. High uptake could be observed in the catabolic organs such as the liver and also in the heart (resulting from blood pool activity, which can be related to intact tracer as well as metabolites). The best tumor-to-background ratios from initial results obtained in patients appear to be in the later time-points after injection, after clearance of background tissue. This observation, while preliminary, is in good agreement with the results observed with [^{18}F]afatinib in preclinical mice xenograft studies. The good correlation observed between preclinical and clinical studies is encouraging for the field of TKI-PET. This observation indicates that, at least in case of EGFR inhibitors, valuable information with regard to tumor targeting and prediction of treatment sensitivity can be obtained from preclinical imaging studies in mice bearing the appropriate tumor model. In this respect PET studies might provide support in drug discovery to validate inhibitors with regards to biodistribution and tumor targeting, possibly facilitating go/no-go decisions in preclinical development and even in early phase clinical trials.

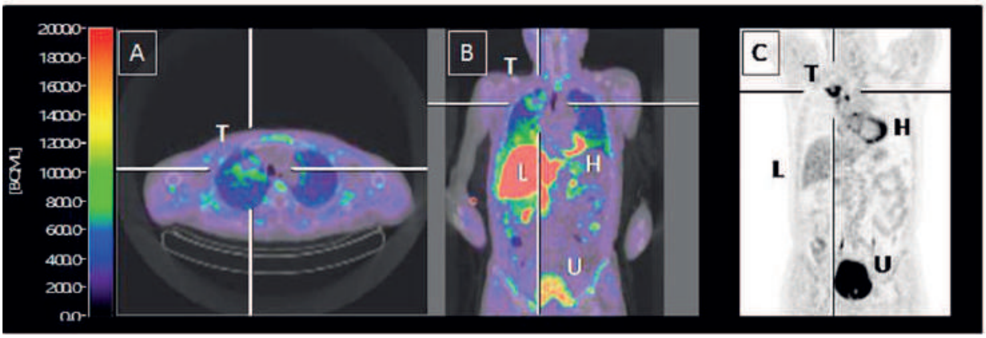

Figure 1: Axial (A) and coronal (B) CT-fused [^{18}F]afatinib PET scan of a NSCLC patient harboring an exon 19 deletion of EGFR. The patients was administered a low dose CT-scan for anatomical reference, followed by 4 whole body PET scans (head to pelvis), 3 min per bed position, 18cm field of view with 50% overlap, at time points 1, 30, 60, and 90 min). Images depicted were obtained 90 min p.i.; (C) [^{18}F]FDG PET image of the same patient. T = tumor, L = liver, H = heart, U = urinary bladder; Figure adapted from [3].

The success of both [^{11}C]erlotinib and [^{18}F]afatinib is related to the high affinity of the compounds for mutated EGFR on one hand, but also due to reduced ATP binding at the kinase domain of mutated EGFR. Activating mutations moderate the affinity of ATP for the ATP binding site and especially the exon 19 deletion hampers ATP binding, thereby allowing small molecules to bind to the kinase domain more efficiently [4]. The intracellular concentration of ATP is in the order of micromolars and such concentrations will never be reached with small molecules without unacceptable toxicity, indicating that developing ATP competitive inhibitors for wild type kinases is very challenging and requires excellent affinity of the kinase inhibitor or the presence of unique mutations rendering the kinase less suited towards ATP binding. Furthermore, this indicates that the use of PET-tracers when targeting kinases is not only dependent on affinity alone but also these types of factors and especially the competition with ATP should be considered, by for example determining the affinity of ATP for the kinase when selecting a suitable TKI and target for imaging.

Another important factor in the development of new TKI-PET tracers, is the drug efflux transporters, heavily expressed by tumors. The ATP binding cassette is a family of transmembrane transporter proteins and are ATP-dependent efflux pumps that are responsible for the transport of foreign substrates out of the cells and thereby serves as a defense mechanism against these substrates. In general TKIs are good substrates for transport by these types of pumps (e.g. P-gp and BCRP), resulting in lower intracellular levels of TKI, and in lower tumor uptake. Especially the tracer amounts used in high specific activity PET imaging studies can be rapidly removed from the tumors via this mechanism. Blocking of these transporters has been shown to influence tracer uptake in other studies as well as the study described in chapter 4 and is therefore an important parameter to be considered when evaluating new TKI-PET tracers [1].

A significant variable in the determination of tracer uptake in TKI-PET studies, apart from absolute values (such as %ID/g or SUV) is the tumor-to-background ratio, which hinges on the selection of suitable background tissue. In general, muscle and blood are taken as background regions and image contrast with these tissues has to be achieved. Both reference tissues can be easily quantified using *ex vivo* biodistribution data, however this only provides limited information over time as only static time points can be analyzed. Dynamic PET-imaging on the other hand can provide an accurate picture of activity concentration over time in several tissues at once, but especially blood values are difficult to determine in tumor bearing mice from imaging data. It is challenging to delineate a major artery in mice for this purpose as a consequence of the spatial resolution of the preclinical PET-camera and partial volume effects. Repetitive blood sampling from mice during a PET-scan is technically challenging and is burdensome for the mice. Combined with anesthesia this can lead to death of the mice during scanning sessions. As a solution a suitable background tissue containing relevant components (blood and muscle) can be selected in the same region as the tumor xenograft is located. For instance a region of interest contralateral to the xenografted tumor might provide a more realistic value in dynamic scans as was demonstrated in the comparative imaging study described in chapter 4. In this case the background region was devoid of high uptake organs and xenografted tumor cells, but was located on the contralateral flank. In this case the mice were xenografted only with one tumor on one flank, thereby leaving the other flank of the mouse available for background determination. This could thereby provide an accurate measure on non-specific uptake in tissue, providing realistic tumor-to-background ratios.

In this thesis the development of additional TKI-PET tracers is described, with as a main goal to image other TKI-target interactions then mutated EGFR. A two-fold approach was taken with on the one hand anti-angiogenic kinase inhibitors (axitinib and nintedanib), which generally demonstrate a more promiscuous target profile, when compared to the mono-specific EGFR inhibitors. On the other hand a kinase inhibitor targeting a mutated cytosolic kinase downstream of growth factor receptors was selected. These studies have taught us that the promising results obtained with [^{11}C]erlotinib and [^{18}F]afatinib could not be directly translated to other targets and kinases, and that these other targets require a different, unique approach and a more in depth knowledge of the tumors biology. It is therefore important that also these kinase inhibitors are translated to the clinic, to determine the accuracy of the preclinical validation studies currently being performed (reverse translation).

The [^{11}C]axitinib and [^{11}C]nintedanib study demonstrated that imaging of tumors with these type of broad spectrum inhibitors is very challenging. The selection of suitable cell lines and model system becomes even more difficult than when a single target is being studied and target expression is no guarantee for tumor uptake of a TKI-PET tracer. The target profile of both axitinib and nintedanib is comparable (VEGFR, PDGFR and FGFR), however axitinib demonstrates a more selective character towards the VEGFR family and this allowed for a direct comparison in the same tumor models. The more promiscuous inhibitor [^{11}C]nintedanib demonstrated uptake in one of the cell lines used, whereas [^{11}C]axitinib did not. An important factor to consider in this case is the cross reactivity of the molecule of interest with the native receptor expressed in the species in which the studies are being performed. The growth factor receptors involved in angiogenesis are normally overexpressed on the blood vessels of a tumor to supply oxygen, nutrients and energy to support its growth. The affinity of kinase inhibitors can vary between the human receptor and its murine homolog and while the cells used for xenograft formation are of human origin, the blood vessels formed are murine and therefore the receptors expressed are also murine. In the case of nintedanib the affinity for human and murine VEGFR2 is similar, making this a more suitable tracer for the tumor model used. This explains, at least in part, why tumor uptake was observed in this case and not for [^{11}C]axitinib [5].

At the outset of the project the aim was to evaluate the tumor targeting potential of both [^{11}C]axitinib and [^{11}C]nintedanib, however, it was soon observed that these compounds were metabolized rapidly and this prompted the question whether the metabolism of the PET tracers was comparable to that observed after therapeutic dosing. To this end a thorough metabolite study was performed, which led to the development of sensitive LC-MS/MS methodology able to detect the carrier amounts of tracer employed in high specific activity PET tracers in plasma samples obtained from *in vivo* experiments. This demonstrated that in the case of [^{11}C]axitinib significant amount of an inactive metabolite was formed, providing a possible explanation for the lack of tumor uptake as well. In the case of [^{11}C]nintedanib a carboxylic acid has been reported as a primary metabolite which is also an active inhibitor of the kinase and by virtue of its charge demonstrates longer cellular retention. This metabolite was observed upon incubation of the tracer in plasma of various species, but was not observed *in vivo* even not after therapeutic dosing. Estimation of species dependent metabolism is applicable to other PET-tracers as well and might prove valuable in the future for other PET tracer development projects.

[^{11}C]vemurafenib was the first kinase inhibitor explored in this study that does not target a membrane bound kinase, but a downstream serine/threonine kinase instead: B-RAF. B-RAF is involved in the pivotal RAS-RAF-MEK-ERK signaling pathway, which plays a prominent role in proliferation. Comparable to the EGFR inhibitors described in this thesis, vemurafenib binds a mutated variant of B-RAF (V600E, where a valine is substituted for a glutamic acid in the activating region of the kinase, exon 15) and therefore was seen as a promising and selective target for imaging. Contrary to the EGFR situation, in which there is a drastically reduced affinity of the developed inhibitors for wild type EGFR, vemurafenib also has an effect on cells expressing wild type B-RAF. Paradoxically, enhanced proliferation is observed in these wild type cells after stimulation with vemurafenib *in vitro*. We were therefore interested if imaging with [^{11}C]vemurafenib could provide a tool to navigate this complex biological system. An innovative Stille coupling employing a [^{11}C]CO insertion was developed to radiolabel vemurafenib on the carbonyl position. Experiments with [^{11}C]vemurafenib *in vitro* and *in vivo* all demonstrated similar binding in both wild-type and mutated cells. In *in vitro* assays, high binding was observed to wild type B-RAF expressing tumors and mutated B-RAF expressing tumors in both xenograft sections as well as intact cells. *In vivo* tumor uptake of [^{11}C]vemurafenib was relatively low, indicating that other factors might interfere with tumor targeting. The tumor-to-background ratios derived from *ex vivo* biodistribution studies were similar in both cell lines investigated, indicating comparable uptake in both the mutated and wild type cell line and that selecting tumors sensitive to treatment will be challenging with [^{11}C]vemurafenib.

Combining the results of aforementioned studies leads to the conclusion that currently the EGFR system is best understood and future studies in the TKI-PET might focus on a better understanding of why these tracers are so effective or why this is such a suitable imaging target. Determining the key factors involved in erlotinib/afatinib binding might provide valuable insight into other tracers and the development of kinase inhibitors as therapeutics itself. Translation of other TKI-PET tracers to the clinic remains of the utmost importance as this might shed light on the question whether or not the preclinical studies are representative for the clinical situation and can thereby show if the proper model systems are being used. The successes achieved in the imaging of EGFR mutated tumors prompted us to investigate emerging, novel third generation kinase inhibitors as TKI-PET tracers.

7.2 [^{11}C]rocelitinib (CO-1686), a third generation TKI-PET tracer

7.2.1 Introduction

Overexpression of activating mutations of EGFR render NSCLC tumors uniquely sensitive to treatment with small molecule tyrosine kinase inhibitors (e.g. erlotinib, gefitinib and afatinib) which occur between 5-25% of the Caucasian patient population [6]. There are two major activating mutations observed in NSCLC patients, first is a deletion in exon 19, which represent approximately 45% of the activating mutations, and second is an L858R point mutation occurring in exon 21 (approximately 40%) [7]. Despite the initially encouraging treatment results observed in these cases, patient with these tumors often develop resistance to therapy in the form of a secondary mutation [8]. About half of recurrences are associated by the occurrence of an additional point mutation, i.e. the exon 20 T790M point mutation, for which no targeted therapy was available until recently (2015). Several inhibitors have entered clinical trials that were specifically designed to target this mutation of EGFR and spare wild-type EGFR, with prominent examples including CO-1686 (rocelitinib, Clovis oncology), EGF816 (nazartinib, Novartis), AZD9291 (osimertinib, Astra Zenenca). The latter was recently approved (tradename: Tagrisso) for the treatment of metastatic EGFR T790M mutation positive NSCLC patients whose disease has progressed during or after EGFR-TKI therapy (e.g. erlotinib or gefitinib).

The successful results obtained with first and second generation EGFR inhibitors was the incentive to pursue these novel generation inhibitors as potential TKI-PET tracers. One of the inhibitors currently in clinical trials is rocelitinib (CO-1686, Clovis oncology, **1**) and in 2014 it was granted breakthrough therapy status by the FDA. Current clinical trials include patients who have had prior EGFR directed mono therapy (e.g. erlotinib or gefitinib) but developed resistance to therapy by expression of the T790M mutation. A direct comparison between erlotinib and rocelitinib in TKI naïve patients is also being studied clinically in a registration trial. At the start of this study only preliminary results were disclosed in abstracts on clinical efficacy but initial results were encouraging in a class of patients that is to date untreatable. This was the motivation for developing [^{11}C]CO-1686 as 3rd generation EGFR inhibitor. A compelling but unconfirmed 60% ORR (overall response rate, reduction in tumor burden) was reported in 2015 and 90% disease control rate in patients who developed resistance on prior TKI therapy in the form of T790M in an intermediate analysis. The confirmed results disclosed recently, however, showed dramatically different results with a confirmed objective response rate of between 28% and 34% reported at the end of 2015 from a larger patient cohort [9].

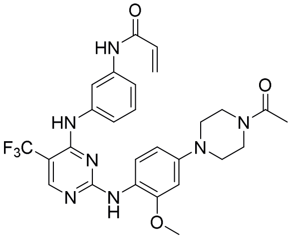

1
Rociletinib
(CO-1686)

Figure 1: Chemical structure of rociletinib (CO-1686)

The success and predictive value with regard to sensitivity demonstrated by [^{11}C]erlotinib and [^{18}F]afatinib encouraged investigation into third generation EGFR inhibitors. The hypothesis being that with radiolabeled CO-1686 good uptake would be observed in both exon 19 deleted and T790M mutated EGFR expressing tumors, but not in wild type. Furthermore, the well-defined biology of EGFR and available tumor cell lines should allow rapid *in vivo* evaluation and when successful pave the way for clinical evaluation of this third generation TKI-PET tracer. It should be noted that other third generation EGFR inhibitors with a more promising clinical profile are better suited for this purpose.

7.2.3 Precursor synthesis

The strategy for the synthesis of [^{11}C]CO-1686 involves a methylation on phenolic precursor **12**. The synthesis for **12** entails a convergent synthesis with a key coupling step between two building blocks depicted in Scheme 1 (**6** and **11**). The first building block, containing the Michael acceptor for irreversible EGFR binding is synthesized in two steps. First dichloropyrimidine **2** is coupled with *N*-Boc-*m*-phenylenediamine (**3**) in the presence of a base in 68% yield to obtain **4**. The product (**4**) is subsequently deprotected and coupled with acryloyl chloride in a one pot procedure to obtain the first building block (**6**) in a modest 37% yield over 2 steps. The second building block is synthesized in three steps, starting with the coupling of acetyl piperazine (**8**) to 4-

fluoro-2-hydroxynitrobenzene (**7**) in good yield. Next a suitable protecting group for the alcohol had to be selected, which should be able to withstand the reductive and acidic conditions of the following steps. The tri-isopropyl silyl group was selected for its excellent stability towards reduction and its relatively high acid tolerance. Introduction of the protecting group was achieved by reacting phenol **9** with tri-isopropylsilyl triflate to obtain the protected nitrobenzene derivative **10** in 73% yield. Subsequent reduction was achieved by palladium on carbon and hydrogen gas in high yield, furnishing the desired aniline building block **11**. The final coupling was achieved under acidic conditions to afford the protected precursor, which was deprotected to furnish **12**. Deprotection of **11**, however, resulted in unexpected dimerization of the precursor molecule, regardless of variation of the conditions, most likely via Michael addition of the deprotected phenol moiety with the acrylamide functionality. Fortunately the desired precursor could be readily separated from the dimerized side-product by preparative HPLC to afford the desired precursor in 23% yield over 2 steps.

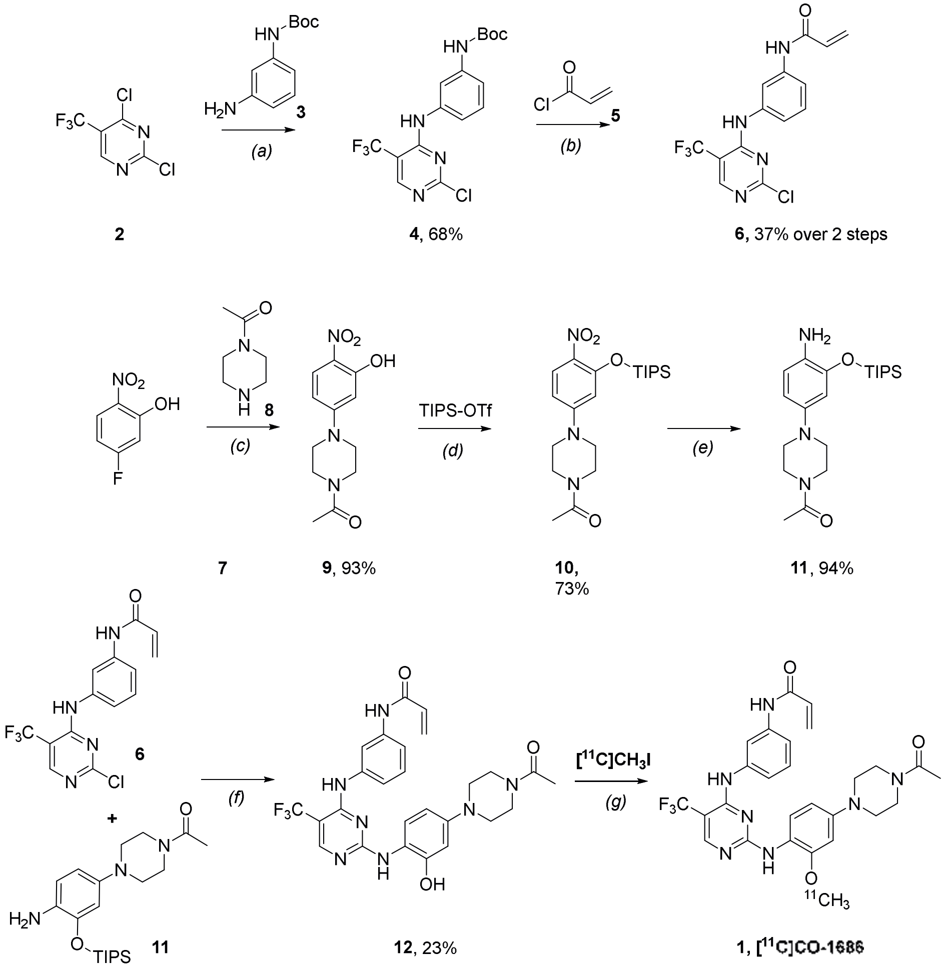

Scheme 1: precursor synthesis and radiolabeling of [^{11}C]CO-1686. Reagents and conditions: *(a)* DiPEA, *t*-BuOH, 0-20°C, 4h; *(b)* TFA, CH_2Cl_2, 0°, 15 min. then **5**, CH_2Cl_2, -30°C, 1h; *(c)* Dioxane, reflux, 2h; (*d*) CH_2Cl_2, 0°C, 2h; *(e)* Pd/C. H_2, EtOH, rt, 2h; *(f)* HCl, BuOH, reflux, 2h then TBAF, THF, 0°C-rt, 2.5h; *(g)* K_2CO_3, DMF, 20-80 °C, 5 min..

7.2.4 Radiosynthesis

To synthesize [^{11}C]CO-1686 precursor **12** was subjected to carbon-11 methylation in the presence of a base (Scheme 1). Initial labeling experiments in DMF with potassium carbonate as a supporting base provided satisfying HPLC conversion of 59% ± 4% (*n*=3). Subsequent semi-preparative HPLC purification provided [^{11}C]CO-1686 (0.3-2.2 GBq) in excellent purity (>98%) and high specific activity (183 ± 68 GBq/µmol) in an overall isolated yield of 7.8 ± 2% (corrected for decay, calculated from [^{11}C]CO2) in a total synthesis time of 28.2 ± 2.6 min formulated in an i.v. injectable solution.

7.2.5 Metabolite analysis

To determine the *in vivo* stability of [^{11}C]CO-1686, before starting *in vivo* experiments, a plasma metabolite analysis was performed in non-tumor bearing athymic nu/nu mice. The animals were injected i.v. (via ocular plexus) with circa 15 MBq of [^{11}C]CO-1686 (corresponding to 0.08 nmol of CO-1686) and sacrificed at 15 minutes post injection followed by blood sample collection. The non-polar and polar fractions were separated using solid phase extraction. Analysis of the plasma (Table 1) revealed excellent stability of the tracer with >90% of the activity corresponding to the parent tracer after 15 minutes and almost no metabolites were observed. Combined with the fact that these types of small molecules distribute quite rapidly, these preliminary stability data indicate that tumor uptake is related to parent tracer and not a metabolite.

Table 1: Plasma metabolite analysis 15 min p.i. of [^{11}C]CO-1686

Time (min)	Parent	Non-polar metabolite	Polar metabolite
15	93.0 ± 1.3%	4.6 ± 4%	2.4% ± 0.1%

7.2.6 Xenograft selection

To evaluate the tumor targeting potential of [^{11}C]CO-1686 three NSCLC cell lines were selected for the generation of xenografts and *in vivo* evaluation in tumor bearing mice. The cell lines were selected based on the expression of a specific EGFR mutation and thus provide a representative overview of mutations found in clinical cases of NSCLC [7]. Moreover, the xenografts had been used for the studies described in chapter 3 and 4 and therefore were well characterized before the start of *in vivo* experiments, and could be used for comparisons with [^{11}C]erlotinib and [^{18}F]afatinib. Firstly, an insensitive cell line which expresses EGFR wild type was selected (A549). Next, a cell line (H1975) which expresses a double mutant of EGFR (L858R/T790M); the first being a common sensitizing point mutation in exon 21 (L858R) and the second a mutation associated with acquired resistance to erlotinib therapy (T790M in exon 20), for which CO-1686 and related inhibitors were designed. Finally, a cell line was selected which is highly sensitive to TKI treatment, namely the HCC827 cell line harboring a deletion in exon 19 (delE746-A750). The sensitivity of these cell lines towards CO-1686 has been clearly described in literature [10-12].

7.2.7 Biodistribution studies

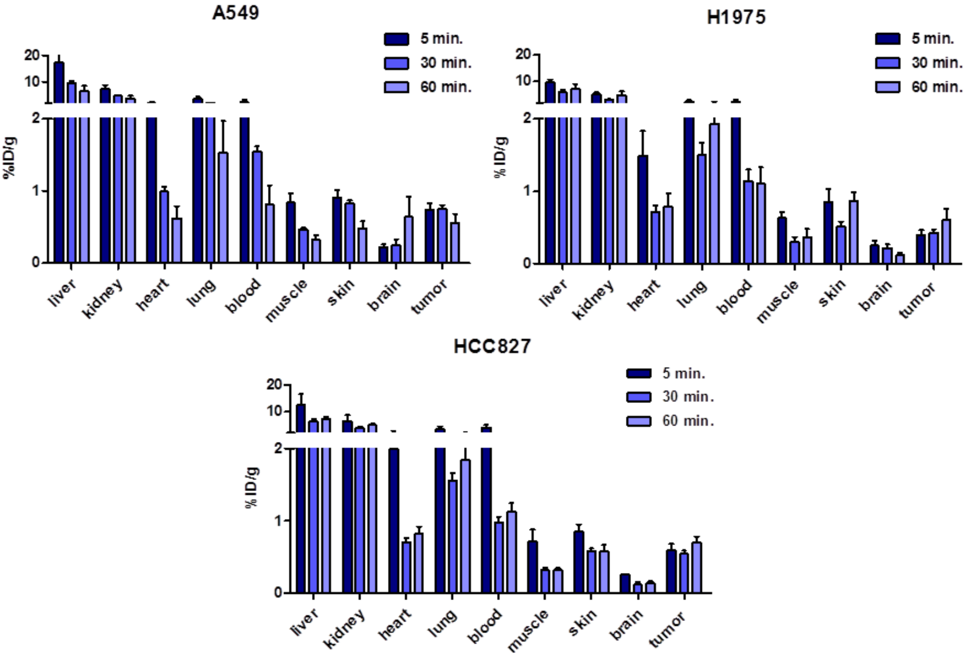

Figure 2: Biodistribution studies with [^{11}C]CO-1686 5, 30 and 60 min. p.i. in A549 (wild type, top-left), H1975 (l858r/T790M, top-right) and HCC827 (exon 19 del., bottom) tumor bearing mice. Mice were administered 15 MBq of tracer. Three animals were sacrificed per time point under isoflurane anesthesia, tumor data is averaged over 6 tumors (2 per mouse).

Xenografted tumor bearing mice were injected with approximately 15 MBq of [^{11}C]CO-1686 (corresponding to 0.08 nmol of CO-1686) and the distribution of the tracer was determined at set time points of 5, 30 and 60 minutes p.i. and results are depicted in Figure 2. [^{11}C]CO-1686 showed a rapid and high uptake in the metabolic organs (kidney and liver) as is more often observed for small molecule PET-tracers. Furthermore, high initial uptake was observed in well-perfused tissues like the heart and lungs. Blood clearance was observed, which was quite rapid, and blood levels were around 1 %ID/g, 60 min. p.i.. The relevant tumor-to-background ratios have been summarized in Table 2. This demonstrates that in all cases the tumor-to-blood ratios remained modest and lower then 1 indicative of lower tumor uptake. The tumor-to-muscle ratios however do increase steadily over time, as a consequence of clearance, with the highest ratio being observed in the HCC827 xenografts. All three investigated tumor types demonstrated modest tumor uptake in an absolute sense, which was quite rapid. The sensitive xenografts H1975 and HCC827 appeared to demonstrate a trend of radioactivity retention in an absolute sense (%ID/g) while the wild type tumors (A549) appeared to show clearance at 60 min. p.i.. This is, however, not reflected in the tumor-to-background ratios which are comparable across the three xenografts. One of the sensitive xenografts (HCC827) demonstrated substantial tumor-to-muscle ratio of 2.22 at 60 min. p.i. The observed increasing tumor-to-background ratios would suggest that that imaging or biodistribution studies at later time points might lead to better tumor-to-background ratios. The previous experience with other EGFR targeting tracers would also suggest imaging at later time point might be valuable. To this end CO-1686 could be labeled at the trifluoromethyl position using fluorine-18 in order to perform studies several hours p.i., owing to the longer half-life of fluorine-18. Methodology to label this position has been recently reported [13, 14] and this might be subject of future studies.

Table 2: tumor-to-background ratios resulting from biodistribution studies with [^{11}C]CO-1686

Tissue	A549			H1975			HCC827		
	5 min.	*30 min.*	*60 min.*	*5 min.*	*30 min.*	*60 min.*	*5 min.*	*30 min.*	*60 min.*
Blood	0.32	0.49	0.70	0.16	0.38	0.55	0.15	0.56	0.63
Muscle	0.88	1.60	1.75	0.63	1.43	1.64	0.83	1.72	2.22

7.2.8 Conclusions

The synthesis of [^{11}C]CO-1686 was successfully achieved in good yields, high purity and specific activity suitable for *in vivo* studies. Initial metabolite analysis revealed excellent stability of [^{11}C]CO-1686 and therefore is suitable for *in vivo* studies. Tumor uptake was observed in all cell lines and an indication of retention was observed in the sensitive xenografts, that imaging at later time points might prove more informative. Tumor-to-background ratios are comparable, with HCC827 demonstrating the highest ratio at 60 min p.i.. Future research will show the potential of third generation EGFR TKIs as PET-tracers, for which the first results have been described in this study.

7.3 Future Perspectives

We see a bright future for TKI-PET. In order for this class of tracers to become validated as precision medicine tools, translation to clinical studies is of vital importance. The preclinical studies performed in mice are very informative, but it is unclear if they can be translated directly to the patient situation. Current experience with [^{11}C]erlotinib shows that in the case of imaging exon 19 deleted EGFR expressing tumors the translation from mice to patient is straightforward and the clinical results observed could be predicted based on the preclinical tumor targeting studies. It would appear that the same holds true for [^{18}F]afatinib, although clinical evaluation is ongoing and results are preliminary. Investigation into other targets in a clinical setting is limited. To our knowledge one of the few examples is [^{11}C]lapatinib which was evaluated in patients presenting with brain metastases of HER2-positive breast cancer. In this study uptake was demonstrated in these metastasis, which was not related to increased perfusion as a consequence of BBB disruption by the metastasis (this study is discussed in chapter 2) [15]. Unfortunately no details were provided on uptake in the primary HER2-postive breast cancer lesions. Hopefully this will be reported in the near future as HER2 was shown to be an attractive imaging target with for example ^{89}Zr-trastuzumab [16]. Finally the evaluation of for example [^{11}C]sorafenib, [^{11}C]axitinib, [^{11}C]nintedanib and [^{11}C]vemurafenib in their respective oncological indications will provide valuable information for the TKI-PET field and validate the manner in which preclinical evaluations of these tracers are being performed. This might also prove valuable for drug discovery, when preclinical targeting studies predict *in vivo* tumor targeting of novel therapeutics. It is clear however that PET imaging of every TKI-target combination requires a unique approach.

Additional future preclinical studies might include a more detailed investigation into the binding of [^{11}C]erlotinib to mutated EGFR. These studies could include kinetic studies with regard to receptor occupancy or pharmacodynamical studies. Furthermore the influence of ATP on binding of TKI-PET tracer could be investigated as this clearly plays a very important role. Especially the dosing aspects of TKI-PET tracers is of interest, as these therapeutics are commonly dosed at several tens of milligrams per kilogram as opposed to the tracer dose that is administered at high specific activity. Moreover, the route of administration is a very important parameter. TKIs are dosed orally and thereby have a slower release into circulation when compared to PET tracers. The latter are administered as a bolus I.V injection, leading to rapid high blood levels. The fast blood clearance observed for almost all small molecular PET tracers may influence effective delivery to the tumor. Orally administered pharmaceuticals generally release much more slowly into circulation and are dosed repeatedly resulting in stable plasma concentrations of the drug and as a consequence higher tumor exposure. In the case of radiolabeled antibodies for example, the long circulation times and thus tumor exposure are beneficial for high tumor uptake. Increasing the circulating tracer concentration might also improve image quality and tumor to non-tumor ratios. To our knowledge no studies have been reported with oral administration or repeated injections of a radiolabeled TKI and these studies might provide novel and valuable insight into the use of TKI-PET tracers.

7.4 Experimental

7.4.1 General

All reactions were carried out under atmospheric conditions unless otherwise stated and all reagents and solvents were supplied by Sigma-Aldrich (St. Louis, USA) and Biosolve BV (Valkenswaard, the Netherlands) and used as received unless stated otherwise. Reference CO-1686 was supplied by Selleckchem (Houston, Texas, USA). Dimethylformamide (DMF, as recieved) and tetrahydrofurane (THF, after distillation from $LiAlH_4$) for anhydrous purposes were stored in dry septum capped flasks charged with molecular sieves. Thin Layer Chomatography (TLC) was performed on Merck (Darmstadt, Germany) precoated silica gel 60 F254 plates. Spots were visualized by UV quenching or ninhydrin staining. Column chromatography was carried out either manually by using silica gel 60 Å (Sigma-Aldrich) or on a Büchi (Flawil, Switzerland) sepacore system (comprising of a C-620 control unit, a C-660 fraction collector, two C601 gradient pumps and a C640 UV detector) equipped with Büchi sepacore prepacked flash columns. ^1H and ^{13}C nuclear magnetic resonance (NMR) spectra were recorded on a Bruker (Billerica, USA) Avance 500 (500.23 MHz and 125.78 MHz, respectively), a Bruker Avance 400 (400.13 MHz and 100.61 MHz, respectively) or a Bruker Avance 250 (250.13 MHz and 62.90 MHz, respectively) with chemical shifts (δ) reported in ppm relative to the solvent. Electrospray ionization mass spectrometry (ESI-MS) was carried out using a Bruker microTOF-Q instrument in positive ion mode (capillary potential of 4500 V). Analytical HPLC was performed on a Jasco PU-2089 pump (Easton, USA) equipped with a Grace (Columbia, USA) C18 Gracesmart column (5 µm, 250 mm × 4.6 mm) and $MeCN/H_2O/TFA$ (70:30:0.1, *v*/*v*/*v*) as eluent at a flow rate of 1 $mL{\cdot}min^{-1}$, with a Jasco UV-2075 UV detector (λ=254 nm) and a NaI radioactivity detector (Raytest, Straubenhardt, Germany). Chromatograms were acquired using GINA star software (version 5.1, Raytest). Semi-preparative HPLC was carried out on a Jasco PU-2089 pump equipped with a C18 Alltima column (Grace, 5 µm, 250 mm × 10 mm) using MeCN/H2O/TFA (32.5:62.5:0.1, *v*/*v*/*v*) as eluent at a flow rate of 4 mL · min^{-1}, a Jasco UV1575 UV detector (λ=254 nm) and a custom-made radioactivity detector. Chromatograms were acquired using ChromNAV software (version 1.14.01, Jasco). Athymic nu/nu mice were obtained from Harlan Netherlands B.V. (Horst, the Netherlands). All animal experiments were performed according to Dutch national law ('Wet op de proefdieren', Stb 1985, 336) and approved by the local ethics committee.

7.4.2 Chemistry

***tert*-butyl (3-((2-chloro-5-(trifluoromethyl)pyrimidin-4-yl)amino)phenyl)carbamate (4).**

A 3-neck flask charged with $CaCl_2$ and *N*-Boc-1,3-diaminobenzene (960 mg, 4.61 mmol) and 1-butanol (7.0 mL) under a flow of nitrogen gas. The reaction mixture was cooled to 0°C after which 2,4-dichloro-5-trifluoromethylpyrimidine (622 µL, 4.61 mmol) was added followed by dropwise addition of DiPEA (936 µL, 5.53 mmol). The reaction mixture was stirred at 0°C for 1h after which it was allowed to warm to room temperature slowly after which it was stirred for 4 h until TLC indicated full conversion. The precipitated white solid was collected by filtration and purified by flash column chromatography (Hexane/EtOAc, 8:2, *v/v*) to afford the title compound as a white solid (1.22 g, 3.14 mmol, 68%). ^{1}H-NMR (500.23 Mhz, DMSO-D$_6$) δ: 9.56 (s, 1H), 9.50 (s, 1H), 8.58 (s, 1H), 7.59 (s, 1H), 7.27 (m, 2H), 7.03 (m, 1H), 1.48 (s, 9H). ^{13}C-NMR (125.78 Mhz, DMSO-D$_6$) δ: 162.8 (Cq), 161.1 (Cq), 158.5 (Cq), 157.1 (CH), 153.2 (Cq), 140.4 (Cq), 138.9 (Cq), 137.6 (Cq), 129.1 (CH), 129.0 (CH), 120.1 (CH), 106.2 (CH), 79.7 (Cq), 28.6 (3x CH_3). HR-MS (ESI, 4500V): m/z calculated for $C_{16}H_{16}ClF_3N_4O_2$: 388.0914, found: (M+Na$^+$): 411.0786

***N*-(3-((2-chloro-5-(trifluoromethyl)pyrimidin-4-yl)amino)phenyl)acrylamide (6).**

To a solution of tert-butyl (3-((2-chloro-5-(trifluoromethyl)pyrimidin-4-yl)amino)phenyl)carbamate (400 mg, 1.03 mmol) in CH_2Cl_2 (3.0 ml) was added trifluoroacetic acid (1.5 mL) slowly at 0°C. The reaction mixture was allowed to warm up to room temperature and stirred for 10 min. after which all volatiles were directly evaporated *in vacuo* and the obtained oil was redissolved in fresh CH_2Cl_2 (3.0 mL), cooled to -30°C and DiPEA (430 µL, 2.47 mmol) was added. To the obtained reaction mixture was added acryloyl chloride (201 µL, 2.47 mmol) and the mixture was stirred for 1 h. The reaction was quenched by the addition of H2O (5 mL) and the organic layers was separated, evaporated and purified by flash column chromatography (Hexane/EtOAc, 7:3, *v/v*) to afford the title compound as a white semi-solid (131 mg, 0.38 mmol, 37%). ^{1}H-NMR (250.13 Mhz, DMSO-D_6) δ: 10.26 (s, 1H), 9.61 (s, 1H), 8.59 (S, 1H), 7.98 (s, 1H), 7.31 (t, J=8.2 Hz, 1H), 7.14 (d, J=7.9 Hz, 1H), 6.47 (m, 1H), 6.24 (dd, J=17.2 Hz, 1H), 5.76 (dd, J=2.8, 9.2 Hz, 1H). ^{13}C-NMR (125.78 Mhz, DMSO-D_6) δ: 166.5 (Cq), 163.4 (Cq), 161.0 (Cq), 160.5 (Cq), 140.5 (CH), 139.5 (Cq), 139.1 (CH), 132.0 (CH), 130.5 (Cq), 129.4 (CH), 128.0 (CH2), 127.4 (CH), 118.9 (Cq), 116.5 (CH). HR-MS (ESI, 4500V): m/z calculated for $C_{14}H_{10}ClF_3N_4O$: 342.0495, found: (M+Na$^+$): 365.0382.

1-(4-(3-hydroxy-4-nitrophenyl)piperazin-1-yl)ethanone (9).

5-Fluoro-2-nitrophenol (2.02 g, 12.86 mmol) was dissolved in dioxane (5 mL), to this solution was added acetylpiperazine (5.00 mL, 39.0 mmol) and the resulting mixture was refluxed for 4 h. After cooling to room temperature the mixture was poured into water to afford a yellow precipitate which was collected by vacuum filtration and dried *in vacuo* at 40°C to afford the title compound as a yellow solid (3.21 g, 12.1 mmol, 93%). ^{1}H-NMR (500.23 Mhz, DMSO-D_6) δ: 10.73 (br s, 1H), 7.89 (d, J= .8 Hz, 1H), 6.64 (dd, J=9.6, 2.7 Hz, 1H), 6.41 (d, J=2.5 Hz, 1H), 3.56 (d, J=5.0 Hz, 4H), 3.48 (m, 2H), 3.34 (br. s, 2H), 2.03 (s, 3H). ^{13}C-NMR (125.78 Mhz, DMSO-D_6) δ: 173.8 (Cq), 161.9 (Cq), 161.1 (Cq), 132.4 (CH), 129.6 (Cq), 112.1 (CH), 104.4 (CH), 51.1 (CH2), 49.9 (CH2), 26.5 (CH_3). HR-MS (ESI, 4500V): m/z calculated for $C_{12}H_{15}N_3O_4$: 265.1063, found: (M+Na$^+$): 288.0942

1-(4-(4-nitro-3-((triisopropylsilyl)oxy)phenyl)piperazin-1-yl)ethanone (10).

1-(4-(3-Hydroxy-4-nitrophenyl)piperazin-1-yl)ethanone (3.20 g, 12.1 mmol) was dissolved in dry CH2Cl2 (45 mL) at 0°C. 2,6-lutidine (1.40 mL, 12.1 mmol) was added to this solution, followed by the dropwise addition of tri-isopropylsilyl triflate (3.24 mL, 12.1 mmol) and the reaction mixture was kept at 0°C for 2h after which TLC indicated full consumption of the starting material. The reaction mixture was quenched with water and the layers were separated. The organic layer was separated, dried (Na_2SO_4) and purified by flash column chromatography (Hexane/EtOAc, 1:1, *v/v*) to afford the title compound as a yellow solid. ^1H-NMR (500.23 Mhz, DMSO-D_6) δ: 7.87 (d, J=9.5 Hz, 1H), 6.67 (dd, J=9.3, 1.7 Hz, 1H), 6.21 (s, 1H), 3.52 (m, 4H), 3.42 (m, 2H), 3.35 (m, 2H), 2.03 (s, 3H), 1.33 (septet, J=7.5 Hz, 3H), 1.07 (d, J=7.6 Hz, 18H). ^{13}C-NMR (125.78 Mhz, DMSO-D_6) δ: 168.9 (Cq), 155.1 (Cq), 152.4 (Cq), 130.1 (Cq), 128.3 (CH), 107.3 (CH), 104.2 (CH), 46.6 (2x CH_2), 45.1 (2x CH_2), 21.7 (CH_3), 18.2 (6x CH_3), 12.9 (3x CH). HR-MS (ESI, 4500V): m/z calculated for $C_{21}H_{35}N_3O_2Si$: 421.2397, found: (M+Na^+): 444.2293.

1-(4-(4-amino-3-((triisopropylsilyl)oxy)phenyl)piperazin-1-yl)ethanone (11). 1-(4-(4-Nitro-3-((triisopropylsilyl)oxy)phenyl)piperazin-1-yl)ethanone (1.39 g, 3.30 mmol) was suspended in EtoH (30 mL) and to this suspension was added palladium on carbon (10%, 140 mg). The solution was purged with hydrogen gas for 10 min., sealed and vigorously stirred at room temperature for 2 h. The reaction mixture was subsequently loaded onto a celite column and eluted with EtOAc. Evaporation of the product containing fractions afforded the title compound as a white solid (1.22 g, 3.12 mmol, 94%). ^1H-NMR (500.23 Mhz, DMSO-D_6) δ: 6.59 (d, J=8.5 Hz, 1H), 6.38 (dd, J=8.4, 2.0 Hz, 1H), 6.33 (s, 1H), 4.17 (s, 2H), 3.54 (m, 4H), 2.86 (m, 2H), 2.79 (m, 2H), 2.01 (s, 3H), 1.27 (septet, J=7.5 Hz, 3H), 1.07 (d, J=7.6 Hz, 18H). ^{13}C-NMR (125.78 Mhz, DMSO-D_6) δ: 173.3 (Cq), 148.0 (Cq), 147.7 (Cq), 138.1 (Cq), 102.5 (CH), 116.3 (CH), 113.44 (CH), 56.3 (CH_2), 55.7 (CH_2), 50.1 (CH_2), 46.1 (CH_2), 26.4 (CH_3), 23.09 (6x CH_3), 17.5 (3x CH). HR-MS (ESI, 4500V): m/z calculated for $C_{21}H_{37}N_3O_2Si$: 391.2655, found: (M+H^+): 392.2727.

_N_-(3-((2-((4-(4-acetylpiperazin-1-yl)-2-((triisopropylsilyl)oxy)phenyl)amino)-5-(trifluoromethyl)pyrimidin-4-yl)amino)phenyl)acrylamide (12).

1-(4-(4-amino-3-((triisopropylsilyl)oxy)phenyl)piperazin-1-yl)ethanone (176 mg, 0.45 mmol) and *N*-(3-((2-chloro-5-(trifluoromethyl)pyrimidin-4-yl)amino)phenyl)acrylamide (140 mg, 0.41 mmol) were dissolved in 1-butanol (4 mL). To this solution was added HCl (1M in H_2O, 102 µL) and it was heated to reflux and stirred for 2 h at this temperature. The volatiles were evaporated *in vacuo* and the crude product was filtered over a short column of silica gel and used the product containing fractions were collected and evaporated to dryness. The obtained oil was used as obtained in the subsequent deprotection step. The product was dissolved in THF (4 mL) and to this was added a solution of TBAF (118 mg, 0.45 mmol) in THF (1 mL) and the obtained mixture was stirred at 0°C for 30 min., followed by stirring at room temperature for 2h. The volatiles were evaporated and the crude product was separated from its dimerized variant using preparative HPLC performed on a C18 Alltima column (Grace, 10 µm, 250 mm × 22 mm) using MeCN/H2O/TFA (20:80:0.1, *v*/*v*/*v*) as eluent at a flow rate of 10 mL · min^{-1} and the product containing fractions were lyophilized to afford the product as a light grey solid (51 mg, 0.10 mmol, 23%). ^{1}H-NMR (400.13 Mhz, DMSO-D_6) δ: 10.25 (s, 1H), 7.78 (br s, 1H), 7.57 (t, J=7.8 Hz, 2H), 7.33 (t, J=8.1 Hz, 2H), 7.17 (br s, 1H), 6.45 (m, 2H), 6.26 (dd, J=16.9, 1.8 Hz, 1H), 5.78 (m, 1H), 3.56 (m, 4H), 3.01 (m, 4H), 2.05 (s, 3H). ^{13}C-NMR (125.78 Mhz, DMSO-D_6) δ: 168.2 (Cq), 163.1 (Cq), 158.4 (Cq), 139.1 (Cq), 131.8 (CH), 128.8 (CH), 127.1 (CH), 75.6 CH_2), 63.8 (CH_2), 48.8 (CH_2), 45.3 (CH_2), 21.2 (CH_3). HR-MS (ESI, 4500V): m/z calculated for $C_{26}H_{26}F_3N_7O_3$: 542.2122, found: (M+H$^+$): 542.2108.

7.4.3 Radiochemistry

[^{11}C]CO2 was produced by the ^{14}N(p,α)^{11}C nuclear reaction performed in a 0.5% O_2/N_2 gas mixture using an IBA Cyclone 18/9 (IBA, Louvain-la-Neuve, Belgium). Carried by a stream of helium (10 mL/min), the produced [^{11}C]CO2 was bubbled through a solution of 100 µL 0.1 M $LiAlH_4$ in THF at 20 °C. The THF was evaporated by heating the reaction vial to 130 °C under a stream of helium. To the dry residue was added 0.25 mL 60% HI in water. The formed [^{11}C]CH$_3$I was distilled through a sicapent/NaOH column to a second reaction vial containing a solution of **12** (0.1 mg, 0.2 μmol) and K$_2$CO$_3$ (5 mg, 36 μmol) in DMF (100 μL). The reaction mixture was kept at 20°C for 1 min., heated to 40°C for 2 min. and finally heated at 80°C for 2 min., while stirring. Subsequently the reaction vial was cooled to room temperature and diluted with 1.5 mL of HPLC eluent and subjected to semi-prep HPLC purification (Alltima C18 column; 10x250; 5μ; eluent: MeCN/H2O/TFA, 32.5:67.5:0.1, v/v/v). The fraction containing [^{11}C]CO-1686 (Rt = 11.0 min) was collected, diluted with water (40 mL) and trapped on a Sep-Pak tC18+ cartridge. The cartridge was then washed with 20 mL of sterile water after which the product was eluted from the cartridge with 1.0 mL of sterile 96% ethanol. The ethanol was diluted to 10 volume percent with formulation solution (7.09 mM NaH2PO4 in 0.9% NaCl, w/v in water, pH 5.2). [^{11}C]CO-1686 (0.3-2.2 Gbq) was obtained in excellent purity (>98%) and high specific activity (183 ± 68 GBq/μmol) in an overall yield of 7.8 ± 2% (corrected for decay, calculated from [^{11}C]CO$_2$) in a total synthesis time of 28.2 ± 2.6 min. formulated in an i.v. injectable solution (10% ethanol in saline containing sodium dihydrogenphosphate, pH = 5.2) suitable for *in vivo* experiments. Quality control was performed using analytical HPLC (Gracesmart C18 column; 4.6x250; 5μ; eluent: MeCN/H2O/TFA, 30:70:0.1, v/v/v) and specific activity was calculated against a calibration curve.

7.4.4 Metabolite Analysis

Six nu/nu athymic mice were injected with 15 MBq of [^{11}C]CO-1686 (corresponding to 0.08 nmol CO-1686), in the ocular plexus under isoflurane anesthesia (2% in 1 L · min^{-1}). The mice were sacrificed at 5 (n = 3) and 45 (n = 3) min post-injection. At these time points, blood was collected via a heart puncture from each mouse. Blood was collected in a heparin tube and centrifuged for 5 min. at 4000 r.p.m. (Hettich universal 16, Depex B.V., the Netherlands). Plasma was separated from blood cells and about 1 mL of plasma was diluted with 2 mL of 0.1 M hydrochloric acid and loaded onto a tC2 Sep-Pak cartridge, which was pre-activated by elution with 3 mL of MeOH and 6 mL of water, respectively. The cartridge was washed with 5 mL of H_2O to collect polar radioactive metabolites. Thereafter, the tC2 Sep-Pak cartridge was eluted with 2 mL of MeOH and 1 mL of H_2O to collect the mixture of apolar metabolites. The mixture of apolar metabolites was analyzed using HPLC to determine the percentage of intact [^{11}C]CO-1686. HPLC was performed on a Dionex Ultimate 3000 system, equipped with a 1 mL loop. As a stationary phase a Phenomenex Gemini C18, 250 x 10 mm, 5 µm was used. The mobile phase was a gradient of A = acetonitrile and B = 0.1% DiPA in H_2O. The HPLC gradient ran for 12.5 min. increasing the concentration of eluent B from 0% to 10% at a flow rate of 4 ml.min^{-1}.

7.4.5 Biodistribution studies

Nude mice (Athymic nu/nu, Harlan, Horst, The Netherlands) bearing two tumors (obtained by injection of A549, H1975 and HCC827 cells) of the same xenograft line on their left and right flank, received an injection of 15 MBq [^{11}C]CO-1686 (corresponding to 0.08 nmol of CO-1686) via the ocular plexus. The mice were sacrificed and dissected at 5, 30 and 60 min. post-injection. Blood, urine, skin, left tumor, right tumor, muscle, heart, lung, liver, kidney and brain were collected, weighed and counted for radioactivity in a Wallac Compugamma 1210 counter (*n* = 3 for each time point). Biodistribution data are expressed as percentage of injected dose per gram (%ID/g) tissue for each organ

7. 5 References

[1] Slobbe P, Windhorst AD, Stigter-van Walsum M, Smit EF, Niessen HG, Solca F, et al. A comparative PET imaging study with the reversible and irreversible EGFR tyrosine kinase inhibitors [^{11}C]erlotinib and [^{18}F]afatinib in lung cancer-bearing mice*. EJNMMI Res.* **2015**;*5*:14.

[2] Bahce I, Smit EF, Lubberink M, van der Veldt AAM, Yaqub M, Windhorst AD, et al. Development of [^{11}C]erlotinib Positron Emission Tomography for *in vivo* evaluation of EGF receptor mutational status*. Clin. Cancer Res.* **2013**;*19*:183-93.

[3] Bahce I, Yaqub M, Smit EF, Lammertsma AA, van Dongen GAMS, and Hendrikse NH. Personalizing NSCLC therapy by characterizing tumors using TKI-PET and immuno-PET*. Lung Cancer*.

[4] He M, Capelletti M, Nafa K, Yun C-H, Arcila ME, Miller VA, et al. EGFR exon 19 insertions: A new family of sensitizing EGFR mutations in lung adenocarcinoma*. Clin. Cancer Res.* **2012**;*18*:1790-7.

[5] Hilberg F, Roth GJ, Krssak M, Kautschitsch S, Sommergruber W, Tontsch-Grunt U, et al. BIBF 1120: Triple angiokinase inhibitor with sustained receptor blockade and good antitumor efficacy*. Cancer Res.* **2008**;*68*:4774-82.

[6] Boch C, Kollmeier J, Roth A, Stephan-Falkenau S, Misch D, Gruning W, et al. The frequency of EGFR and KRAS mutations in non-small cell lung cancer (NSCLC): routine screening data for central Europe from a cohort study*. BMJ Open* **2013**;*3*.

[7] Sharma SV, Bell DW, Settleman J, and Haber DA. Epidermal growth factor receptor mutations in lung cancer*. Nat Rev Cancer* **2007**;*7*:169-81.

[8] Pao W, Miller VA, Politi KA, Riely GJ, Somwar R, Zakowski MF, et al. Acquired resistance of lung adenocarcinomas to gfitinib or erlotinib is associated with a second mutation in the EGFR kinase domain*. PLoS Med* **2005**;*2*:e73.

[9] Sequist LV, Goldman JW, Wakelee HA, Camidge DR, Yu HA, Varga A, et al. Efficacy of rociletinib (CO-1686) in plasma-genotyped T790M-positive non-small cell lung cancer (NSCLC) patients *J. Clin. Oncol.* **2015**;*33*:1.

[10] Cha MY, Lee K-O, Kim M, Song JY, Lee KH, Park J, et al. Antitumor activity of HM781-36B, a highly effective pan-HER inhibitor in erlotinib-resistant NSCLC and other EGFR-dependent cancer models*. Int. J. Cancer* **2012**;*130*:2445-54.

[11] Solca F, Dahl G, Zoephel A, Bader G, Sanderson M, Klein C, et al. Target binding properties and cellular activity of afatinib (BIBW 2992), an irreversible ErbB family blocker*. J. Pharmacol. Exp. Ther.* **2012**;*343*:342-50.

[12] Walter AO, Sjin RTT, Haringsma HJ, Ohashi K, Sun J, Lee K, et al. Discovery of a mutant-selective covalent inhibitor of eGFR that overcomes T790M-mediated resistance in NSCLC*. Cancer Discovery* **2013**;*3*:1404-15.

[13] Huiban M, Tredwell M, Mizuta S, Wan Z, Zhang X, Collier TL, et al. A broadly applicable [^{18}F]trifluoromethylation of aryl and heteroaryl iodides for PET imaging. *Nat Chem* **2013**;*5*:941-4.

[14] van der Born D, Sewing C, Herscheid JDM, Windhorst AD, Orru RVA, and Vugts DJ. A universal procedure for the [^{18}F]trifluoromethylation of aryl iodides and aryl boronic acids with highly improved specific activity. *Angew. Chem. Int. Ed.* **2014**;*53*:11046-50.

[15] Saleem A, Searle GE, Kenny LM, Huiban M, Kozlowski K, Waldman AD, et al. Lapatinib access into normal brain and brain metastases in patients with Her-2 overexpressing breast cancer. *EJNMMI Res.* **2015**;*5*:30.

[16] Nagengast WB, de Vries EG, Hospers GA, Mulder NH, de Jong JR, Hollema H, et al. *In vivo* VEGF imaging with radiolabeled bevacizumab in a human ovarian tumor xenograft. *J. Nucl. Med.* **2007**;*48*:1313-9.

Chapter 8

Summary

P. Slobbe, A.J. Poot, A.D. Windhorst and G.A.M.S. van Dongen

Radiolabeled Tyrosine Kinase Inhibitors for Drug Development and Cancer treatment:

TKI-PET

In this thesis the development of clinically approved (tyrosine) kinase inhibitors (TKIs) as Positron Emission Tomography (PET) imaging agents is described. PET is a unique, non-invasive *in vivo* imaging technique that enables the visualization and quantification of the distribution of molecules labeled with positron-emitting isotopes at a picomolar level. This method enables the evaluation of cellular biochemical and physiological processes *in vivo* by monitoring the distribution and kinetics of a radiolabeled molecule. Nowadays, PET has found broad application in clinical practice for personalized treatments, in research and pharmaceutical development. PET with radiolabeled drugs can serve as a tool to answer vital questions during drug development, such as assessing the distribution of a drug in the body quantitatively and over time, indicating if the desired target is present (target expression), whether the target site is reached by the drug, and how the kinetics of binding are *in vivo*. Discrepancy between tumor uptake of a drug and the therapeutic response might be indicative for the presence of resistance mechanisms. Furthermore, uptake in off-target tissue might be predictive for toxicity during treatment. Inter-patient variation of tumor targeting can be assessed, providing a method to preselect patients which will or will not benefit the most from treatment. The societal relevance of this is becoming increasingly important with the economic burden of cancer treatment increasing at an alarming rate. The cost of cancer care in the United States alone was $125 billion in 2010 and is estimated to reach $173 billion dollars in 2020 [1]. In 2011 an estimated 63% of these expenses were associated with the use of targeted therapies, indicating that these drugs currently dominate the anti-cancer spending. Moreover, this is only expected to increase with novel targeted therapies under heavy development by the pharmaceutical industry. On average the cost of intravenous targeted therapy was $65.000 dollars per patient per year and for oral targeted therapy $88.800 per patient per year in 2011. Combining this with the fact that a large portion of patients does not even respond to the therapy used, the need for patient selection becomes of the utmost importance. Imaging with targeted drugs can play a large role in this regard, identifying the right drug for the right patient at the right time.

This concept of image guided personalized medicine has already been well established in the use of antibodies as imaging agents, the immuno-PET concept, where a monoclonal antibody is inertly labeled with a PET-radionuclide and can be used to study the *in vivo* behavior of the antibody. This technique has demonstrated its value in various preclinical- and clinical studies [2]. **Chapter 1** describes the current status of cancer drug development with an emphasis on targeted therapy and the increasingly important role that immuno-PET has played in this regard. Furthermore examples are provided of successes achieved with immuno-PET targeting growth factor receptors exerting kinase activity, raising the question whether or not the other class of kinase targeting drugs, namely the small molecule kinase inhibitors can also be used as imaging agents in the same way. The research described in this thesis was focused on the preclinical validation of PET-imaging with small molecule (tyrosine) kinase inhibitors nowadays known as the TKI-PET concept.

It is estimated that, next to the 30 (end of 2015) approved small molecule kinase inhibitors several hundreds are currently at the various stages of (pre)clinical development. **Chapter 2** describes the status of TKI-PET in the year 2011, when this research project was launched, and the novel insights that appeared in the literature during the project [3]. This overview serves as an introduction to the research performed. At the outset of this project the TKI-PET field was in its infancy and while nowadays an increasing number of reports is appearing in the literature the arsenal of labeled kinase inhibitors is still relatively small. It is however, encouraging that an increased clinical interest can be observed in the use of TKI-PET. The research in this thesis focusses on clinically approved kinase inhibitors only, as these provide rapid translation to clinical TKI PET studies. But a more important reason, this class of drugs suffers from a rather substantial lack of clinical efficacy in certain patient populations. The role that TKI-PET can play in this case is elegantly demonstrated by the landmark studies performed with [^{11}C]erlotinib in non-small cell lung cancer (NSCLC). Erlotinib is only clinically effective in patients that harbor activating mutations of EGFR (e.g. the exon 19 deletion) in their tumors, which occurs in only 10 – 30% of NSCLC cases. PET-imaging with [^{11}C]erlotinib demonstrated good uptake in mouse models with tumors harboring these mutations, but not in wild type [4, 5]. This result was later confirmed in a landmark clinical PET-study in NSCLC patients [6].

There are important requirements for de development of PET tracers based on FDA approved TKIs: First, to avoid a difference in their *in vivo* behavior it is of vital importance that the radiotracer and the parental compound have exactly the same chemical structure. Only when the native chemical structure is employed as a tracer, the results of the PET study will represent the behavior of the corresponding drug. Second, the labeling of TKIs requires a drug-specific strategy. Usually a TKI can be labeled with carbon-11 and sometimes with fluorine-18, but this is dictated by the molecular structure of the approved TKI. The challenge in the radiosynthesis of PET-tracers lies in the short half-life of PET-isotopes, being 20 min for carbon-11 and 110 min for fluorine-18. The third important consideration in the design of a TKI-PET tracer is the metabolism of the drug. It is therefore vital to know whether or not metabolism occurs, which biologically active metabolites are formed within the time-frame of the PET study, and whether or not metabolism of a tracer amount of drug is significantly different from the metabolism after therapeutic dosing.

Chapter 3 describes the development of fluorine-18 labeled afatinib, a second generation TKI irreversibly targeting a mutated variant of the epidermal growth factor receptor (EGFR) in NSCLC. In essence afatinib is a successor of erlotinib. For the radiosynthesis of [^{18}F]afatinib, a novel peptide coupling reagent mediated reaction was developed. Subsequently the metabolism and initial tumor targeting properties of [^{18}F]afatinib were explored in tumor bearing mice [7]. It was observed that [^{18}F]afatinib was metabolically stable, which was encouraging for the tumor targeting studies. Two clinically relevant NSCLC cell lines were selected for the initial evaluation in xenograft bearing mice. A cell line expressing wild type EGFR (A549) was used next to a treatment sensitive cell line expressing exon 19 deleted EGFR (HCC827). Unfortunately while good uptake was expected in the exon 19 deleted tumors, based on the [^{11}C]erlotinib data reported in literature, biodistribution studies indicated comparable uptake across the two investigated xenograft types. A variety of factors could be responsible for this lack of selectivity, one being for example involvement of multi-drug resistance, in the form of drug efflux from tumor cells by ABC transporters (such as P-gp and BCRP). It has been well established that most TKIs are also substrates for these types of drug efflux pumps.

To gain further insight into this and to perform a direct comparison between [^{11}C]erlotinib (a reversible EGFR inhibitor) and [^{18}F]afatinib (an irreversible EGFR inhibitor), **chapter 4** describes a comparative pre-clinical imaging study in tumor bearing mice [5]. In this study three tumor types were investigated all expressing a different variant of the EGF receptor, the aforementioned two cell lines (A549 and HCC827) and the newly explored H1975 cell line that expresses two point mutations, namely one sensitizing point mutation (L858R) and one mutation associated with acquired resistance (T790M) to first generation EGFR targeting TKIs (e.g. gefitinib and erlotinib). Furthermore, the effect of blocking the important drug efflux transporters P-gp and BCRP was explored by administering a blocker (tariquidar) prior to imaging. Both tracers only demonstrated selective tumor uptake in the HCC827 xenograft line (tumor-to-background ratio, [^{11}C]erlotinib 1.9 ± 0.5 and [^{18}F]afatinib 2.3 ± 0.4), thereby showing the ability to distinguish sensitizing mutations *in vivo*. No major differences were observed in the kinetics of [^{11}C]erlotinib, the reversible binder and [^{18}F]afatinib, the irreversible tracer, in each of the xenograft models. Under P-gp blocking conditions, no significant changes in tumor-to-background ratio were observed; but, [^{18}F]afatinib demonstrated better tumor retention in all xenograft models and thereby displayed the characteristics of an irreversible inhibitor. The described synthesis for [^{18}]afatinib was also translated to a GMP (Good Manufacturing

Practice) compliant procedure and this tracer has now entered into a clinical trial in NSCLC patients with a mutation of EGFR. The preliminary results of this study show that uptake is observed in tumor expressing a sensitizing mutation in the EGF receptor, similar to the clinical results observed with [^{11}C]erlotinib.

The effectiveness of inhibitors of mutated EGFR is offset by the fact that in almost every case patients on TKI therapy develop resistance to the drug they are taking. Usually this resistance is induced by a secondary mutation located in the ATP binding site of EGFR. One of the most common mutations clinically observed is the T790M mutation, also known as the gatekeeper mutation. In response to this the pharmaceutical industry is developing inhibitors that target this specific variant of EGFR whilst sparing the wild type receptor to avoid side effects. One of these inhibitors, rociletinib (CO-1686), was also explored as PET tracer for its tumor targeting potential in pilot experiments. The preliminary results, including metabolism and biodistribution studies are described in the **Reflections and future perspectives** chapter of this thesis. Rociletinib is a third generation, irreversible inhibitor of activating mutations of EGFR (e.g. exon 19 deletions) and the acquired resistance T790M mutation. Rocelitionib was successfully labeled via a carbon-11 methylation and initial metabolite analysis demonstrated excellent *in vivo* stability. Biodistribution studies in tumor bearing mice demonstrated uptake in the mutated cell lines (HCC827 and H1975) but also in the wild type xenograft (A549). The tumor-to-background ratios were similar across the investigated xenografts but did appear to increase over time and were most optimal in the HCC827 (exon 19 deleted) xenografts. The subject of future work might include the development of a fluorine-18 labeled variant to determine the complete potential of this third generation TKI-PET tracer.

Having established that imaging with kinase inhibitors targeting mutated EGFR was feasible in lung cancers models, the question occurred if this kind of PET imaging was specific for this particular signal transduction cascade or could be expanded toward other signal transduction cascade inhibitors as well. The study presented in

chapter 5 was aimed at the development of PET tracers of TKIs targeting pro-angiogenic receptors and thereby a different type of TKI-target interaction. Importantly, these TKIs usually have a more broad target profile then the selective EGFR inhibitors discussed previously. Angiogenesis is the formation of new blood vessels and particularly in proliferating tumors this process is very important. Blood vessels provide actively dividing tumor cells with required nutrients, energy and oxygen. This process is heavily mediated via several kinase receptor families (e.g. vascular endothelial growth factor receptor (VEGFR) or fibroblast growth factor receptor (FGFR) and these have become attractive drug targets over the last decade. Two TKIs developed for angiogenesis inhibition were selected for evaluation as PET-imaging agents, being axitinib and nintedanib. The target profile of both TKIs is comparable (VEGFR, PDGFR and FGFR), however, axitinib demonstrates a more selective character towards the VEGFR family. This allowed for a direct comparison in the same tumor model systems.

Both axitinib and nintedanib were successfully labeled via carbon-11 methylation reactions and the biodistribution and tumor targeting were assessed in two head-and-neck cancer xenograft models in mice (FaDu and VU-SCC-OE) expressing the desired anti-angiogenic targets as assessed by immunohistochemistry. This demonstrated, surprisingly, only selective tumor uptake of [^{11}C]nintedanib in FaDu xenografts of 1.66 ± 0.02 % ID/g at 60 min. p.i.. As previously mentioned tracer uptake can be substantially influenced by the formation of (radio-)metabolites and the metabolism after therapeutic dosing describes metabolites for both compounds on interest. Axitinib has a variety of known metabolites, resulting from therapeutic dosing, most of which are inactive with regard to kinase inhibition. Furthermore, the structure of axitinib comprises a readily isomerizable double bond, which could result in additional metabolites *in vivo*. In the case of nintedanib a carboxylic acid metabolite is reported resulting from methylester cleavage, in plasma and tumors. This particular metabolite is an active inhibitor of the kinase and due to the charge present on the carboxylic acid moiety is unable to pass the cellular membrane. This can be advantageous when this metabolite is formed inside tumor cells as longer exposure is achieved. However, when formed in plasma it will no longer be able to enter tumor cells, and therefore will lead to reduced tumor uptake.

To explain the observed biodistribution results a thorough metabolite analysis was performed, as initial *in vivo* stability analyses demonstrated rapid metabolism for both tracers. Using LC-MS/MS, methods were developed to detect metabolites of interest at tracer level using multi reaction monitoring (MRM). For [^{11}C]axitinib a sulfoxide metabolite was observed and it was demonstrated that the double bond was not isomerized *in vivo*. The observed sulfoxide derivative is inactive *vis-à-vis* the primary target(s) of axitinib (the VEGFR family) and this can be a possible explanation for the lack of tumor targeting observed. In the case of [^{11}C]nintedanib the carboxylic acid metabolite was observed upon incubation in plasma of various species, including the mice used in the xenograft studies, however, not in human plasma. Plasma and tumor tissue samples obtained from xenografted mice, however, did not demonstrate the carboxylic acid after tracer administration or therapeutic dosing (25 mg/kg). A substantial polar fraction was observed during metabolite analysis indicative of the loss of small polar fragments of radioactivity which could be explained by demethylation *in vivo*. While these results do not provide an unambiguous explanation for the lack of tumor targeting observed, they do indicate that metabolism is at least partly responsible.

The study described in **chapter 6** was also aimed at another type of kinase, in this case a cytosolic kinase, downstream from the membrane growth factor receptors discussed in the previous studies. The BRAF kinase is a pivotal member of the RAS-RAF-MEK-ERK pathway involved in the growth processes of the cell. The *BRAF* V600E mutation is a known driver oncogene in melanoma and other types of solid tumors. Vemurafenib is a selective serine/threonine kinase inhibitor approved for the treatment of late stage melanoma, which are positive for V600E mutated BRAF. In patients positive for this mutation treatment with vemurafenib is very effective, however in wild type it is not. Paradoxically preclinical experiments even suggest that vemurafenib leads to increased proliferation in non-mutated tumor cells. PET-imaging with radiolabeled vemurafenib can therefore be a valuable tool to study this *in vivo* and has the potential to be used as a patient stratification tool.

The labeling of vemurafenib is radiochemically challenging and a synthesis route employing an innovative Stille coupling with [^{11}C]carbon monoxide insertion was developed to prepare [^{11}C]vermurafenib in sufficient yields for *in vivo* experiments. [^{11}C]vemurafenib was analyzed for its tumor targeting potential in melanoma xenografts Colo829 (BRAF^{V600E}) and MeWo (BRAF^{wt}) using autoradiography, cell uptake studies, and *ex-vivo* biodistribution studies. BRAF expression was determined by FACS analysis and sensitivity to vermurafenib was determined by cell viability assays. Finally, sequencing of the xenograft material confirmed the mutational status of the xenografts being BRAF^{V600E} for Colo829 and BRAF^{wt} for MeWo. Furthermore, the *in vivo* stability was determined by a plasma metabolite analysis and excellent stability of [^{11}C]vemurafenib was observed which makes this PET tracer suitable for *in vivo* studies. Both autoradiography and cellular uptake studies showed binding to the tumor tissue which was high, but similar binding was observed in both investigated tumor types. *Ex vivo* biodistribution studies confirmed the *in vitro* experiments demonstrating the same tumor to background ratios (when compared to muscle, skin and blood) for both xenograft types investigated. The uptake in the relevant background tissue was also higher than the uptake observed in the tumors. Therefore selecting vemurafenib-sensitive tumors based on [^{11}C]vemurafenib uptake is very challenging and thusfar appears not feasible based on the current results.

References

[1] Shih Y-CT, Smieliauskas F, Geynisman DM, Kelly RJ, and Smith TJ. Trends in the cost and use of targeted cancer therapies for the privately insured nonelderly: 2001 to 2011 *J. Clin. Oncol.* **2015**.

[2] van Dongen GAMS, Poot AJ, and Vugts DJ. PET imaging with radiolabeled antibodies and tyrosine kinase inhibitors: immuno-PET and TKI-PET *Tumor Biol.* **2012**, *33*, 607-615.

[3] Slobbe P, Poot AJ, Windhorst AD, and van Dongen GAMS. PET imaging with small-molecule tyrosine kinase inhibitors: TKI-PET *Drug Discovery Today* **2012**, *17*, 1175-1187.

[4] Memon AA, Jakobsen S, Dagnaes-Hansen F, Sorensen BS, Keiding S, and Nexo E. Positron emission tomography (PET) imaging with [^{11}C]-labeled erlotinib: A micro-PET study on mice with lung tumor xenografts *Cancer Res.* **2009**, *69*, 873-878.

[5] Slobbe P, Windhorst AD, Stigter-van Walsum M, Smit EF, Niessen HG, Solca F, et al. A comparative PET imaging study with the reversible and irreversible EGFR tyrosine kinase inhibitors [^{11}C]erlotinib and [^{18}F]afatinib in lung cancer-bearing mice *EJNMMI Res.* **2015**, *5*, 14.

[6] Bahce I, Smit EF, Lubberink M, van der Veldt AAM, Yaqub M, Windhorst AD, et al. Development of [^{11}C]erlotinib Positron Emission Tomography for *in vivo* evaluation of EGF receptor mutational status *Clin. Cancer Res.* **2013**, *19*, 183-193.

[7] Slobbe P, Windhorst AD, Stigter-van Walsum M, Schuit RC, Smit EF, Niessen HG, et al. Development of [^{18}F]afatinib as new TKI-PET tracer for EGFR positive tumors *Nucl. Med. Biol.* **2014**.

Chapter 9

Samenvatting (Summary in Dutch)

P. Slobbe, A.J. Poot, A.D. Windhorst and G.A.M.S. van Dongen

Radioactief Gelabelde Kinaseremmers voor Geneesmiddelontwikkeling en Kankertherapie:

TKI-PET

In dit proefschrift wordt de ontwikkeling van klinisch goedgekeurde tyrosinekinaseremmers (TKIs) als Positron Emissie Tomografie (PET) tracers beschreven. PET is een unieke, non-invasieve, beeldvormende techniek die de visualisatie en kwantificatie mogelijk maakt van de distributie van een molecuul voorzien van een positron uitzendend isotoop in picomolaire concentraties *in vivo*. Met deze methode is het mogelijk om de cellulaire, fysiologische en biochemische processen *in vivo* te bestuderen door het vastleggen van de distributie en kinetiek van een radioactief gelabeld molecuul. In de huidige klinische praktijk heeft PET brede toepassing gevonden in diagnostiek en behandeling op maat. Ook in het onderzoek en in de geneesmiddelontwikkeling speelt PET tegenwoordig een sleutelrol. PET met radioactief gelabelde geneesmiddelen kan als hulpmiddel worden gebruikt om belangrijke vragen te beantwoorden tijdens de geneesmiddelontwikkeling, bijvoorbeeld: wat is de distributie van het geneesmiddel in het lichaam op kwantitatieve wijze over tijd? Op deze manier kan er bekeken worden of a) het biologische doel (target, een receptor of enzym) van het geneesmiddel aanwezig is (target expressie), b) de locatie van het target bereikt wordt door het geneesmiddel en c) hoe de kinetiek van geneesmiddel is en of er binding aan het target is. Discrepanties tussen de opname van een geneesmiddel in de tumor en het therapeutisch effect kan duiden op de aanwezigheid van resistentiemechanismen. Daarnaast kan opname in gezond weefsel voorspellend zijn voor toxiciteit en dus voor bijwerkingen tijdens een behandeling. De variatie in tumoropname tussen verschillende patiënten kan bepaald worden en op deze manier kunnen patiënten die het meeste profijt zullen hebben van de behandeling geselecteerd worden. Het maatschappelijke belang hiervan wordt steeds belangrijker als men de stijgende kosten voor de oncologische zorg in ogenschouw neemt. De kosten voor oncologische zorg in de Verenigde Staten waren

125 miljard dollar in 2010 en worden geschat te stijgen naar 173 miljard dollar in 2020. Naar schatting was 63% van deze kosten in 2011 toe te schrijven aan de zogenaamde “targeted therapies” ofwel doelgerichte therapieën, hetgeen aangeeft dat deze categorie van kankergeneesmiddelen de uitgaven domineren. De verwachting is dat deze kosten exponentieel zullen gaan stijgen, omdat nieuwe doelgerichte therapieën onder hevige ontwikkeling zijn in de farmaceutische industrie. Gemiddeld kost een intraveneus toegediende doelgerichte therapie ongeveer 65.000 dollar per patiënt per jaar en voor orale therapieën is dit zelfs 88.000 dollar per patiënt per jaar (in 2011). Belangijker dan de kosten is dat een groot deel van de patiëntenpopulatie die een dergelijk middel voorgeschreven krijgt hier nauwelijks of zelfs helemaal niet op reageert en slechts de bijwerkingen van het middel ondervindt. Beide factoren maken het extra belangrijk dat er een adequate selectie is om de juiste patiënt op de juiste tijd het juiste middel te geven. PET met doelgerichte geneesmiddelen kan hier een grote rol in spelen.

Het concept van *door beeldvorming gestuurde therapie op maat* is inmiddels gevestigd in het veld van de antilichaamtherapie; het zogenaamde “immuno-PET concept”. Hierbij wordt een monoclonaal antilichaam gelabeld met een PET-isotoop op een manier waarbij het onveranderd gedrag vertoond in het lichaam. Deze techniek heeft zijn waarde bewezen in verschillende preklinische- en klinische studies [1]. **Hoofdstuk 1** beschrijft de huidige status van de oncologische geneesmiddelontwikkeling met een nadruk op de doelgerichte therapieën en de steeds groter wordende rol die immuno-PET hierin speelt. Spraakmakende voorbeelden worden in dit hoofdstuk uitgelicht waarbij antilichamen die gericht zijn tegen groeifactor receptoren in beeld gebracht worden middels immuno-PET. Naast de antilichamen is er nog een categorie doelgerichte therapie die op dezelfde receptoren aangrijpt, namelijk de klein moleculaire kinaseremmers. De vraag die centraal staat in dit proefschrift is of dezelfde voorspellende werking als die van het immuno-PET concept ook toepasbaar is op deze klasse van geneesmiddelen, een concept dat inmiddels TKI-PET genoemd wordt.

Eind 2015 waren er 30 van dit soort kleine moleculen goedgekeurd voor gebruik in patiënten en er wordt geschat dat er nog honderden in verschillende stadia van ontwikkeling zijn. In **Hoofdstuk 2** wordt de status van het TKI-PET-veld beschreven bij de start van dit onderzoeksproject, aangevuld met de nieuwe kennis die in de literatuur is verschenen tijdens dit onderzoek. Dit hoofdstuk dient als algemene inleiding voor het beschreven werk in de rest van het proefschrift [2]. Aan de start van dit project stond het TKI-PET-veld in haar kinderschoenen, maar tegenwoordig verschijnt er steeds meer wetenschappelijke literatuur omtrent dit onderwerp, echter blijft het arsenaal aan gelabelde kinaseremmers beperkt. Het is bemoedigend dat er een groeiende klinische interesse waar te nemen is in deze klasse van PET-tracers en dat er steeds meer van deze moleculen in patiënten getest worden. Juist daarom richt het onderzoek dat in dit proefschrift beschreven staat zich op de klinisch goedgekeurde kinaseremmers omdat deze enerzijds een snelle vertaling naar de kliniek bieden en anderzijds in een substantieel deel van patiëntenpopulatie niet effectief zijn. De rol die TKI-PET hierin kan vervullen is op elegante wijze gedemonstreerd in een baanbrekende klinische studie met [^{11}C]erlotinib in patiënten met niet-kleincellig longkanker (NSCLC). In dit type longkanker is erlotinib alleen therapeutisch effectief in patiënten wiens Epidermale Groeifactorreceptor (EGFR) een zogenaamde activerende mutatie herbergt. Deze mutatie staat bekend als de exon 19 deletie en komt voor in 10-25% van de niet-kleincellig longkanker patiënten. In preklinisch onderzoek bleek dat PET-beeldvorming met [^{11}C]erlotinib goede tumoropname liet zien in tumor-dragende muizen met deze specifieke mutatie, maar niet als deze mutatie afwezig was (wild type EGFR) [3, 4]. Dit resultaat werd vervolgens bevestigd in een belangrijke klinische studie in niet-kleincellig longkanker patiënten, waarbij op basis van [^{11}C]erlotinib PET, gevoeligheid voor therapie voorspeld kon worden [5].

Er zijn een aantal eisen waar rekening mee gehouden moet worden bij het ontwikkelen van PET-tracers op basis van klinisch goedgekeurde kinaseremmers. Ten eerste: om afwijkend biologisch gedrag van het molecuul te voorkomen, is het van het hoogste belang om geen wijzigingen aan te brengen in de chemische structuur van het geneesmiddel. Slechts wanneer de ongewijzigde structuur gebruikt wordt als tracer geeft de resulterende PET-scan een beeld van de distributie van het corresponderende geneesmiddel. Per TKI is er dus een geneesmiddel specifieke synthesestrategie nodig. In het algemeen kan een kinaseremmer gelabeld worden met koolstof-11 en in sommige gevallen met fluor-18, dit is afhankelijk van de moleculaire structuur. De grootste uitdaging in radiosynthese van PET-tracers ligt in de korte halfwaardetijd van het gekozen PET-isotoop, welke 20 minuten is voor koolstof-11 en 110 minuten voor fluor-18. Ten derde is het van belang om rekening te houden met het metabolisme van de TKI-PET-tracer. Het is daarom van belang om het metabolisme van het geneesmiddel te kennen en om te weten of er biologisch actieve verbindingen kunnen ontstaan als gevolg van dit metabolisme binnen het tijdsbestek van de PET-scan. Het is hierbij ook van belang om te weten of dit metabolisme verschilt op tracerniveau of na toediening van een therapeutisch dosis.

Hoofdstuk 3 beschrijft de ontwikkeling van fluor-18 afatinib, dit is een tweede generatie TKI welke irreversibel bindt aan gemuteerd EGFR in NSCLC. In essentie is afatinib de opvolger van erlotinib. Voor de radiosynthese van [^{18}F]afatinib is er een nieuwe reactie ontwikkeld, gebaseerd op een reagens dat is bedoeld voor het vormen van peptidebindingen. Vervolgens is het metabolisme en de initiële tumoropname bekeken in tumor-dragende muizen [6]. [^{18}F]afatinib bleek metabool stabiel, wat belangrijk is voor een goede tumoropname. Twee klinisch relevante NSCLC cellijnen zijn vervolgens gekozen voor de eerste evaluatie in tumor-dragende muizen. De eerste (A549) betrof een cellijn die wild type EGFR tot expressie brengt en de tweede (HCC827) betrof een behandel gevoelige tumor die een exon 19 deletie van EGFR tot expressie brengt. Hoewel op basis van de literatuur rondom [^{11}C]erlotinib een hogere tumoropname werd verwacht in de gevoelige lijn (HCC827), bleek de opname in beide tumor types gelijk. Er zijn een aantal factoren die verantwoordelijk kunnen zijn voor deze observatie, bijvoorbeeld de (ontwikkelde) resistentie tegen geneesmiddelen van tumoren, dit vindt plaats via de zogenaamde “efflux” pompen (zoals de ABC pompen

P-gp en BCRP). Deze pompen verwijderen xenobiotica, zoals geneesmiddelen, uit de tumorcel. Het is bekend dat TKIs goede substraten zijn voor dit soort efflux pompen.

Om hier beter inzicht in te verkrijgen en om een directe vergelijking te maken tussen [^{11}C]erlotinib (een reversibel EGFR remmer) en [^{18}F]afatinib (een irreversibele EGFR remmer) is de studie gedaan die beschreven staat in **hoofdstuk 4**. In dit deel van het proefschrift wordt een vergelijkende preklinische beeldvormende studie beschreven in tumor-dragende muizen [4]. In dit onderzoek zijn drie verschillende tumor typen met elkaar vergeleken, elk van deze brengt een unieke mutatie van de EGF receptor tot expressie. Twee van de lijnen die gebruikt zijn in het vorige hoofdstuk (A549 en HCC827) en een derde: H1975. Deze laatste cellijn brengt twee punt mutaties van EGFR tot expressie, te weten één die gevoeligheid teweeg brengt (L858R) en één die geassocieerd is met resistentie tegen eerste generatie TKIs (zoals gefitinib en erlotinib). Daarnaast is het effect van het blokkeren van belangrijke efflux pompen bekeken door een remmer (tariquidar) van deze pompen toe te dienen alvorens er een PET-scan uitgevoerd werd. Beide bestudeerde tracers lieten goede opname zien in de HCC827 tumor lijn (tumor-tot-achtergrond ratio, [^{11}C]erlotinib 1.9 ± 0.5 en [^{18}F]afatinib 2.3 ± 0.4), waarmee de tracers lieten zien dat ze behandel gevoelige mutaties *in vivo* kunnen identificeren. Er werden geen grote verschillen gezien tussen de reversibel bindende tracer [^{11}C]erlotinib en de irreversibel bindende tracer [^{18}F]afatinib in de bestudeerde tumor types. Als er eerst een efflux pomp remmer toegediend werd waren er geen significante verschillen te zien met betrekking tot tumor-tot-achtergrond ratios, maar de irreversibele remmer [^{18}F]afatinib liet betere tumor retentie zien in de verschillende tumoren, waarmee het irreversibele karakter van deze tracer aan het licht kwam.

De ontwikkelde synthese van [^{18}F]afatinib is daarnaast vertaald naar een procedure die geschikt is voor GMP (Good Manufacturing Practice) en deze tracer wordt momenteel klinisch geëvalueerd in niet-kleincellig long kanker patiënten die gemuteerd EGFR tot expressie brengen. De eerste resultaten van deze studie laten zien dat er opname van de tracer te zien is in de tumor van een patiënt die een mutatie (exon 19 deletie) tot expressie brengt. Deze mutatie is gevoelig voor behandeling met afatinib. Deze resultaten zijn vergelijkbaar met de klinische resultaten die verkregen werden met [^{11}C]erlotinib.

In bijna alle gevallen waarbij patiënten behandeld worden met een TKI die selectief gemuteerd EGFR remt, ontstaat er na enige tijd op behandeling resistentie tegen de gebruikte therapie. Over het algemeen wordt dit veroorzaakt door een secundaire mutatie in de EGF receptor op de positie waar ATP normaal bind. Een van de klinisch meest voorkomende resistentie mutaties is de T790M puntmutatie, ook wel bekend als de "gatekeeper" mutatie. De farmaceutische industrie doet veel onderzoek naar remmers die specifiek deze variant van EGFR remmen, terwijl ze de niet gemuteerde receptor ongemoeid laten. Een van deze remmers, rociletinib (CO-1686), is ook ontwikkeld als PET-tracer en de tumoropname is in verkennende experimenten bestudeerd.

Deze eerste resultaten, inclusief een metabolieten analyse en biodistributie in tumor-dragende muizen zijn opgenomen in **Hoofstuk 7: Reflections and future perspectives**. Rocelitinib is een derde generatie, irreversibele remmer van activerende mutaties van EGFR (bijvoorbeeld de exon 19 deletie) en de mutatie geassocieerd met resistentie: T790M. Rocelitinib is succesvol gelabeld met koolstof-11 door middel van een methylerings reactie en de initiële metabolieten analyse liet uitstekende stabiliteit *in vivo* zien. Biodistributie studies in tumor-dragende muizen lieten opname zien in de gemuteerde cellijnen (HCC829 en H1975) maar ook in de wild type lijn (A549). De tumor-tot-achtergrond ratio's waren vergelijkbaar in de verschillende tumor modellen, maar leken wel toe te nemen over tijd. De beste ratio werd verkregen in de HCC827 cel lijn (exon 19 deletie van EGFR). Toekomstige studies kunnen de ontwikkeling van een fluor-18 variant van deze tracer omvatten om de potentie van deze verbinding te kunnen bepalen door middel van beeldvorming op latere tijdstippen.

Nadat er vastgesteld was dat de beeldvorming met kinaseremmers die zich richten op gemuteerd EGFR succesvol was in longkanker modellen, rees de vraag of dit soort PET-diagnostiek specifiek was voor de EGFR signaaltransductiecascade of dat dit ook naar andere kinaseremmers uitgebreid kon worden. Het onderzoek dat beschreven wordt in **hoofdstuk 5** was gericht op het ontwikkelen van TKIs die receptoren remmen die betrokken zijn bij angiogenese in een tumor, wat een ander type TKIs betreft. De remmers hebben over het algemeen een breder "target" profiel, wat betekend dat ze aangrijpen op meerdere receptoren in tegenstelling tot de selectieve EGFR remmers die tot nu toe besproken zijn. Angiogenese is het proces van de vorming van nieuwe bloedvaten en in agressief groeiende tumoren is dit een belangrijk proces. Nieuwe bloedvaten voorzien de groeiende tumor van voedingstoffen, energie en zuurstof. Kinase receptoren zijn sterk betrokken in het reguleren van dit proces, voorbeelden hiervan zijn de vasculair endothelial growth factor receptor familie (VEGFR) of de fibroblast growth factor receptor (FGFR) en deze receptoren zijn daarom belangrijke aangrijpingspunten voor nieuwe geneesmiddelen geworden.

Twee TKIs, die speciaal ontwikkeld zijn voor de remming van angiogenese, zijn ontwikkeld als PET-tracers, namelijk: axtinib en nitedanib. De beide verbindingen grijpen aan op dezelfde receptoren (VEGFR, PDGFR en FGFR), maar axitinib is selectiever voor de VEGFR familie. Hierdoor was het mogelijk een directe vergelijking tussen de twee te maken in dezelfde tumor modellen.

Zowel axtinib als nintedanib zijn succesvol gelabeld met koolstof-11 via methyleringsreacties en de biodistributie van beide verbindingen is bepaald in twee hoofd-hals carcinoom lijnen in tumor-dragende muizen (FaDu en VU-SCC-OE). De expressie van de receptoren is bepaald met immunohistochemie op het tumor materiaal. De biodistributies lieten slechts opname zien van $[^{11}C]$nintedanib in de FaDu tumoren (1.66 ± 0.02 %ID/g op 60 min. na injectie) en er werd geen opname waargenomen voor $[^{11}C]$axitinib. Zoals eerder genoemd kan het metabolisme een belangrijke rol spelen in de traceropname en voor beide verbindingen zijn er belangrijke metabolieten gerapporteerd na toediening van therapeutische hoeveelheden van de geneesmiddelen. Voor axitinib zijn er een aantal metabolieten bekend die geen of een zeer lage affiniteit hebben voor de receptor, daarnaast omvat de structuur een dubbele binding die snel een isomeer kan vormen. Deze verbindingen kunnen ook als radiometaboliet gevormd worden wat invloed heeft op de tumoropname. De methyl ester functionaliteit van nintedanib kan *in vivo* verzeept worden tot het vrije carbonzuur, zowel in plasma als in tumorcellen. Dit specifieke metaboliet is een actieve remmer van het kinase en als gevolg van de lading op het carbonzuur kan het niet meer over celmembranen diffunderen. Dit is een voordeel als de vorming van het zuur plaatsvindt in de tumor cel, omdat hierdoor langere retentie ontstaat. Als het zuur echter in plasma ontstaat zal de nintedanib niet meer in de tumorcel opgenomen kunnen worden en daardoor de bindingsplaats op de receptor niet meer kunnen bereiken.

Ter aanvulling op de biodistributie studies is er een uitgebreide metabolieten analyse uitgevoerd. De initiële *in vivo* stabiliteit resultaten liet zien dat er sprake was van een snel metabolisme van beide tracers. Met LC-MS/MS zijn er methodes opgezet om de eerdergenoemde metabolieten te detecteren op tracer niveau, hierbij werd gebruikt gemaakt van multi reaction monitoring (MRM). Een sulfoxide metaboliet van [^{11}C]axitinib is op deze manier gevonden en het bleek dat de dubbele binding niet werd geïsomeriseerd *in vivo*. Het geobserveerde sulfoxide metaboliet heeft geen affiniteit voor de receptoren waar axitinib op aangrijpt en dit kan deels verklaren waarom er voor [^{11}C]axitinib geen tumoropname geobserveerd werd. In het geval van [^{11}C]nintedanib werd het carbonzuur gevonden na incubatie van de tracer in plasma van verschillende soorten: naakte muis, muis, rat en mens. Een belangrijke observatie was dat zowel in het muizen- als het rattenplasma het carbonzuur aangetroffen werd, maar niet in plasma van menselijke afkomst.

In de plasmamonsters en het tumorweefsel verkregen uit de tumor-dragende muizen is het carbonzuur niet gevonden na toediening van [^{11}C]nintedanib als tracer of na toediening van een therapeutische dosis nintedanib (25 mg/kg). In de metaboliet analyse werd een substantiële polaire fractie gevonden wat kan duiden op verlies van kleine polaire, radioactieve moleculen, welke verklaard kunnen worden door demethylering *in vivo*. Hoewel de metaboliet analyse geen doorslaggevend bewijs leverde voor het gebrek aan tumoropname, impliceert de data wel dat het metabolisme in ieder geval deels hiervoor verantwoordelijk is.

Het onderzoek dat in **hoofdstuk 6** beschreven staat was gericht op weer een andere klasse kinase receptoren, namelijk een niet membraan gebonden kinase receptor, maar één die tot expressie komt in het cytosol. Dit kinase is onderdeel van de signaaltransductiecascade van de eerdergenoemde groeifactor receptoren. Het B-RAF kinase speelt een sleutel rol in de RAS-RAF-MEK-ERK cascade, welke zeer belangrijk is in de groei- en deelprocessen van de cel. De V600E mutatie in het BRAF kinase is een bekende oncogene mutatie in melanomen en andere type tumoren. Vemurafenib is een serine/threonine kinaseremmer goedgekeurd voor melanomen, welke V600E gemuteerd BRAF tot expressie brengen. In deze patiëntenpopulatie is vemurafenib dan ook zeer effectief, echter als er niet gemuteerd BRAF tot expressie wordt gebracht niet. In preklinische experimenten is er zelfs aangetoond dat vemurafenib extra proliferatie teweeg brengt in deze tumoren. PET-beeldvorming met vemurafenib als tracer kan daarom een waardevol hulpmiddel zijn om dit fenomeen *in vivo* te bestuderen en kan dienen als selectie middel om de juiste patiënten voor behandeling te identificeren.

Het labelen van vemurafenib is een radiochemische uitdaging en hiervoor is een Stille koppeling met [^{11}C]CO insertie ontwikkeld. [^{11}C]vemurafenib is vervolgens geanalyseerd *in vitro* en *in vivo* voor de tumoropname in de melanoom cellijnen Colo829 (BRAF^{V600E}) en MeWo (BRAF^{wt}) middels autoradiografie studies, cel binding studies en biodistributies in tumor-dragende muizen. De expressie van BRAF is bepaald met een FACS-analyse en de gevoeligheid van de tumorcellen door viabiliteits assays. De mutaties van het tumormateriaal, verkregen uit de muizen, zijn bevestigd middels sequentiebepaling. Ten slotte is ook de *in vivo* stabiliteit van [^{11}C]vemurafenib bepaald in een metabolietanalyse en deze bleek uitstekend te zijn. Zowel de autoradiografie studies als de experimenten in tumorcellen wezen er op dat er hoge binding was aan het tumorweefsel, maar dat deze vergelijkbaar was in beide tumor typen. Biodistributie experimenten in tumor-dragende muizen bevestigde dit resultaat. In beide lijnen werden vergelijkbare tumor-tot-achtergrond ratio's waargenomen. De resultaten uit dit hoofdstuk laten zien dat selectie van tumoren die gevoelig zijn voor behandeling op basis van de opname van [^{11}C]vemurafenib in de tumor uitdagend is en wellicht niet haalbaar.

Referenties

[1] van Dongen GAMS, Poot AJ, and Vugts DJ. PET imaging with radiolabeled antibodies and tyrosine kinase inhibitors: immuno-PET and TKI-PET *Tumor Biol.* **2012**, *33*, 607-615.

[2] Slobbe P, Poot AJ, Windhorst AD, and van Dongen GAMS. PET imaging with small-molecule tyrosine kinase inhibitors: TKI-PET *Drug Discovery Today* **2012**, *17*, 1175-1187.

[3] Memon AA, Jakobsen S, Dagnaes-Hansen F, Sorensen BS, Keiding S, and Nexo E. Positron emission tomography (PET) imaging with [^{11}C]-labeled erlotinib: A micro-PET study on mice with lung tumor xenografts *Cancer Res.* **2009**, *69*, 873-878.

[4] Slobbe P, Windhorst AD, Stigter-van Walsum M, Smit EF, Niessen HG, Solca F, et al. A comparative PET imaging study with the reversible and irreversible EGFR tyrosine kinase inhibitors [^{11}C]erlotinib and [^{18}F]afatinib in lung cancer-bearing mice *EJNMMI Res.* **2015**, *5*, 14.

[5] Bahce I, Smit EF, Lubberink M, van der Veldt AAM, Yaqub M, Windhorst AD, et al. Development of [^{11}C]erlotinib Positron Emission Tomography for *in vivo* evaluation of EGF receptor mutational status *Clin. Cancer Res.* **2013**, *19*, 183-193.

[6] Slobbe P, Windhorst AD, Walsum MS-v, Schuit RC, Smit EF, Niessen HG, et al. Development of [^{18}F]afatinib as new TKI-PET tracer for EGFR positive tumors *Nucl. Med. Biol.* **2014**.

Chapter 10

About the author

Curriculum Vitae

Paul Slobbe was born on the 14th of January 1988 in the city of Amstelveen, The Netherlands. After completing his pre-university education (gymnasium) at the Herman Wesselink College in Amstelveen he obtained his Bachelor's degree in Pharmaceutical Sciences in 2009 from the VU University, during which he did an internship in the medicinal chemistry group of Iwan de Esch and Rob Leurs. Pursuing his synthetic interest he then went on to obtain a Master's degree in Organic Chemistry from the VU University and perform an internship in the Synthetic Organic Chemistry group of Romano Orru and Koop Lammertsma. In 2011 he performed an internship in the Chemical Biology group of Huib Ovaa at the Dutch Cancer Institute. Combining his interest in oncology research with synthetic organic chemistry he then started his PhD research at the VU university medical center on the topic of radiolabeled kinase inhibitors as a PET imaging tool in drug development and personalized medicine. The results of which are described in this thesis. Following completion of the practical part of his PhD work he joined LinXis to develop their novel antibody-drug-conjugate platform. In 2016 he moved to Boehringer Ingelheim to join the medical affairs department as Medical Manager Oncology.

List of Publications

[1] **Slobbe P**, Windhorst AD, Adamzek WA, Bolijn M, Schuit RC, Heideman DAM, et al. Development of [^{11}C]vemurafenib employing a carbon-11 carbonylative Stille coupling for the *in vivo* detection of V600E mutated BRAF. *submitted* **2016**.

[2] **Slobbe P**, Haumann R, Schuit RC, Windhorst AD, van Dongen GAMS, and Poot AJ. Two anti-angiogenic TKI-PET tracers, [^{11}C]axitinib and [^{11}C]nintedanib: radiosynthesis, *in vivo* metabolism and initial tumor targeting potential in rodents. *Nuclear Medicine and Biology* **2016**; *43*: 612-24.

[3] **Slobbe P**, Windhorst AD, Stigter-van Walsum M, Smit EF, Niessen HG, Solca F, et al. A comparative PET imaging study with the reversible and irreversible EGFR tyrosine kinase inhibitors C-11 erlotinib and F-18 afatinib in lung cancer-bearing mice. *European Journal of Nuclear Medicine and Molecular Imaging: Research* **2015**; *5*.

[4] **Slobbe P**, Windhorst AD, Stigter-van Walsum M, Schuit RC, Smit EF, Niessen HG, et al. Development of F-18 afatinib as new TKI-PET tracer for EGFR positive tumors. *Nuclear Medicine and Biology* **2014**; *41*: 749-57.

[5] **Slobbe P**, Poot AJ, Van D, G.A.M.S., Niessen H, and Windhorst AD. Radiolabeled quinazoline derivatives. WO 2014118197 A1; **2014**.

[6] Janssen GV, **Slobbe P**, Mooijman M, Kruithof A, Ehlers AW, Guerra CF, et al. Diastereoselective one-pot synthesis of tetrafunctionalized 2-imidazolines. *Journal of Organic Chemistry* **2014**; *79*: 5219-26.

[7] Poot AJ, **Slobbe P**, Hendrikse NH, Windhorst AD, and van Dongen GAMS. Imaging of TKI-target interactions for personalized cancer therapy. *Clinical Pharmacology & Therapeutics* **2013**; *93*: 239-41.

[8] **Slobbe P**, Ruijter E, and Orru RVA. Recent applications of multicomponent reactions in medicinal chemistry. *Medchemcomm* **2012**; *3*: 1189-218.

[9] **Slobbe P**, Poot AJ, Windhorst AD, and van Dongen GAMS. PET imaging with small-molecule tyrosine kinase inhibitors: TKI-PET. *Drug Discovery Today* **2012**; *17*: 1175-87.

[10] Merkx R, Burns KE, **Slobbe P**, El Oualid F, El Atmioui D, Darwin KH, et al. Synthesis and evaluation of a selective fluorogenic pup derived assay reagent for Dop, a potential drug target in mycobacterium tuberculosis. *Chembiochem* **2012**; *13*: 2056-60.

Dankwoord

Zonder twijfel het meest gelezen deel van dit (en daarbij elk) proefschrift is het dankwoord. Waarschijnlijk ben je zelf ook als eerste naar dit deel gebladerd om te controleren of je er in staat en zo ja, of er voldoende woorden aan je gewijd zijn? Een slordige 250+ pagina's wetenschap of 4 jaar hard (en soms minder hard) werken, worden haastig doorgebladerd om bij dit deel van het werkje uit te komen. Wees gerust ik heb mijn best gedaan om iedereen te vernoemen en de nodige lof toe te dichten. Dit laat echter onverlet dat ik mensen vergeten kan zijn waarvoor mijn excuses!

Beste ***Guus***, ik heb je leren kennen als een gepassioneerd wetenschapper, maar ook als een echte marketing man. Immers je kan nog zulke mooie resultaten hebben, maar vervolgens moet je die nog wel verkopen! Jouw bevlogenheid voor het vak werkt aanstekelijk. Altijd kritisch naar resultaten kijkend en niet bang om te zeggen dat het manuscript toch een andere insteek nodig had. Voor mijn gevoel zitten er in jouw dag een aantal uur extra. Ik ga er van uit dat binnenkort het "Guus van Dongen" laboratorium in het imaging gebouw geopend wordt. De vraag is alleen nog of de buste bij de ingang van het gebouw komt of op de derde verdieping bij Tracer Center Amsterdam. Hartelijk dank voor de mogelijkheid om mijn promotieonderzoek in jouw groep te doen en dat je altijd klaar stond met wijze raad.

Mr President, Sir! (voor de niet ingewijden: Beste ***Bert***,) in de vier jaar dat ik in jouw kelder (lees: het RNC) heb gewerkt ben je een van mijn lievelings bazen geworden. Altijd klaar om in een voortgangsgesprek te zeggen: Ja, maar het zijn geen antilichamen en de opname is daar ook niet mee te vergelijken! Aan het begin van mijn promotie periode, zijn we op bezoek geweest bij Boehringer Ingelheim in

Biberach. Aldaar moest ik een presentatie geven over het afatinib project. Bij het terugwandelen naar het hotel zei je de volgende, wat mij betreft, onsterfelijke woorden tegen mij: Zo, jij bent ook niet vies van een beetje bluffen. Die opmerking is me bijgebleven omdat ik denk dat die ons beide goed kenmerkt. Wetenschappers met een gezonde dosis zelfvertrouwen. Ik heb je leren kennen als een groot voorvechter van de radiochemie en PET. Het RNC zoals we dat nu kennen is voor een groot deel jouw verdienste. Ik ben je dankbaar dat ik in jouw radiochemie groep vier jaar onderzoek heb mogen doen en dat ik ook altijd bij je aan kon kloppen voor advies over wat dan ook.

De man die die mij vanaf het begin af aan wegwijs heeft gemaakt in onze radioactieve kelder, is zonder twijfel ***Alex*** geweest. Naast het schrijven van de beurs waar ik vier jaar onderzoek van heb mogen doen, stond je altijd klaar om het onderzoek te bespreken. Samen hebben we TKI-PET op de kaart te gezet (of in ieder geval een goede poging gewaagd), ondanks dat de “antilichaam-lui” het toch soms maar wat magertjes vonden. Het is geweldig dat ik er naast een uitstekende begeleider tijdens mijn promotie, er ook een goede vriend aan heb overgehouden. Dat we nog maar vaak mogen memoreren over de wetenschap, het leven, de politiek of wat dan ook onder het genot van een goed glas wijn of whisky.

I would like to thank ***Prof. Dr. Antony Gee*** or ***Tony*** for reading and correcting the contents of this thesis and participating in my PhD defense. I have come to know you as one of the most foremost experts on carbon-11 chemistry and therefore I am pleased to have you on my PhD committee.

Dear ***Flavio***, I would like to thank you for participating in my defense and for reading and correcting my thesis but also for your contributions to the two manuscripts we co-authored on afatinib, which form a substantial part of this thesis.

Beste ***Philip***, tijdens mijn promotie hebben we elkaar, vanaf het begin, al regelmatig getroffen. Hetzij op een congres of tijdens een NKRV dag. Van die laatste staat mij nog een opmerking van je bij, na afloop van een presentatie van mij: “goede presentatie, goed Engels en fijn om te horen dat je afatinib lekker op z’n Hollands uitspreekt”. Hartelijk dank voor je deelname aan mijn lees commissie en oppositie.

Beste ***Egbert***, ik wil je bedanken voor je deelname aan mijn lees- en promotiecommissie en voor het kritisch kijken naar de twee manuscripten die we samen geschreven hebben. Daarnaast voor je geduld als ik aan het uitweiden was over problemen met de synthese van [^{18}F]afatinib, dat snel de patiënt in moest!

Beste ***Harry***, hartelijk dank voor je voorzitterschap van mijn leescommissie en je deelname aan de oppositie. Daarnaast ook voor je bijdrage tijdens de afgelopen vier jaar, bijvoorbeeld in de vorm van de TKI-overleggen. Deze waren mijns inziens belangrijk voor het translationele karakter van het onderzoek op dit gebied.

Beste ***Iwan***, mijn eerste echte chemie ervaring heb ik opgedaan tijden mijn bachelor stage in jouw medicinal chemistry groep. Vandaaruit ben ik via de organische chemie en het NKI op mijn promotieplek beland. Ik vind het geweldig dat je deelneemt aan mijn lees- en promotiecommissie en wil je daarvoor hartelijk bedanken.

Beste ***Dr. Menke***, beste ***Willemien***, ook jou wil ik hartelijk bedanken voor je deelname aan mijn lees- en promotiecommissie.

Tijdens mijn vier jaar in het VUmc/RNC heb ik een hoop mensen leren kennen die op een of andere manier bijgedragen hebben aan de totstandkoming van dit proefschrift. Ik zou verstek laten gaan als ik niet zou beginnen bij mijn collega’s van M-136 of labje D1/D1sco, de Fab-Four, de vier musketiers en mijn favoriete radiochemische ridders! Samen zijn we de weg van de wetenschap ingeslagen, om vervolgens er een georganiseerd zooitje van te maken.

Berend, de jut bij mijn jul, de knabbel bij mijn babbel, de Ernie bij mijn Bert. Of om het een beetje chemisch te houden, mijn onzin katalysator. Onze liefde is begonnen onder de warmte lampen op het terras van la Cabana en onder het genot van meerdere “girafes” in Tours te Frankrijk. Van het oprichten van onze succesvolle horeca onderneming tot de meest legendarische quiz op het RNC weekend, alles wat wij samen aanraakten veranderde spontaan in goud. Wellicht niet alle syntheses die ingezet werden, maar de tracers zaten altijd toch maar weer in het potje aan het einde van de rit en uiteraard meer dan 98% radiochemische zuiverheid en hoge specifieke activiteit, eerlijk! Het zal niemand verassen dat jij één van mijn twee paranimfen bent, waarvoor dank!

Dear miss Jody Jackson, ***Bieneke,*** voorvechter van het correcte gebruik van de Nederlandse taal en regelmatig voorgesteld als ons debiele zusje. Ik heb er van genoten om grapjes met je uit te halen, want daar trapte je altijd zo lekker in. Heel veel succes met het afronden van je proefschrift, beursvoorstellen en met je tijd in Sydney! Daarnaast bedankt voor het nakijken van het eerste stukje van de Nederlandse samenvatting, als er verderop nog foutjes in staan wil ik er niets over horen!

Renske, mijn bureau- en zuurkastbuurvrouw en (in ieder geval zoals ik het graag zou zien) m'n secretaresse (of Donna), ons gedeeld fanatisme voor series heeft ertoe geleid dat we vaak uitgebreide analyses van afleveringen maakten, maar vooral dat ik een hoop gespoiled heb voor je. Ik weet redelijk zeker dat Derek toch niet doodgaat dus maak je geen zorgen. Een laatste tip: pas op het gooien van waterflesjes want je zou zomaar eens de verkeerde kunnen raken.

Ik moet natuurlijk ook de favoriete doofstomme Oeigoer van de groep bedanken, ***Lonneke***, we zijn samen gestart aan de studie farmaceutische wetenschappen en uiteindelijk zijn we ook in het zelfde lab, beland om promotie onderzoek te doen, uiteraard heb jij je plekje aan mij te danken, waarvoor graag gedaan!

Grote, maar dan ook echt uit de kluiten gewassen, stuiterbal op speed: ***Gerrie!*** In het eerste jaar van onze studie hebben we elkaar leren kennen en man wat een bak drukte kan één mens produceren! Uiteindelijk ben je ook in de radiochemie beland, op het RNC en heb je daar consequent een 10 liter erlenmeyer gebruikt om 3 microgram van een verbinding in te bewaren, waarvoor hulde. Ik hoop dat we nog vaak een avond aan de bier, wijn en whisky gaan, want daar zijn we toch wel erg goed in! Onze vrouwen rijden wel!

Pe-Ko-sak! Or our resident slovenian princess and my only fellow oncologist, ***Alexandra***, I wish you luck on your quest to work in radiochemistry on every continent of the world and good luck with finishing your own thesis, which I expect to be finished in about two weeks.

Ulrike, Ulei! I think together with Robert you have the biggest collection of scotch I have seen outside of a liquor store. Good luck with the last part of your PhD!

Marion**,** starting out as our French intern taking her first baby-steps in radiochemistry, now also a PhD student in the RNC. Bonne Chance!

De metabolieten koning, ***Robert***, bedankt voor al je hulp bij de verschillende analyses, LC-MS/MS werkzaamheden en andere afhaalchinees diensten. Op de cowboy laarzen en met muziek aan die, denk ik, iedereen uit je lab wegjoeg werkte je altijd met een aanstekelijke relaxtheid de experimentjes af. ***Marissa***, jij ook bedankt voor de hulp bij de metaboliet analyses.

Mooijer, gekke volendammer, zoe gaal gezellig om met jou gewerkt te hebben, zelfs ondanks zoe gaal veel gezeik over logboeken, schoonmaak, regels en andere ellende! Loopt de [^{18}F]afatinib synthese nog? Mocht je ooit nog een slaapplaats zoeken in Amstelveen heb je m'n nummer, Oe eh jej ju aai?!

Kevin, Nee-luister-het-volgende, Adamzek, aan jou laat ik mijn plaats in de koffiehoek na, het is nu aan jou om je mening aan de mensen op te gaan dringen. Dank voor al het muizen werk wat je over de jaren heen voor me hebt gedaan. Kooidier! ***Esther*** ook jou wil ik bedanken voor de ondersteuning bij de verschillende experimenten en de gezelligheid van de afgelopen jaren. De PET-scans, biodistributies, cel experimenten, etc. waren niet mogelijk geweest zonder de ondersteuning van de sectie (sexy) biologie. **Inge (erelid), Carla, Mariska en Ricardo**, bedankt! ***Marijke,*** in de eerste jaren van mijn promotie was jij verantwoordelijk voor het dieren werk. De eerste keer dat we samen een biodistributie hebben uitgevoerd heb ik met verbazing staan kijken hoe snel en kundig je dat werk deed. Hartelijk dank voor je hulp tijdens mijn promotie onderzoek! ***Marije***, mijn FACS heldin! De beste experimenten zijn die waar iemand ze helemaal voor je doet en je er zelf geen omkijken naar hebt, dank voor jouw bijdrage aan dit proefschrift!

Danielle, mede via jou (en Remco) ben ik aan mijn promotie plek op het RNC gekomen en daarvoor ben ik erg dankbaar, want het is een mooie tijd geweest! Ook dank voor de nuttige discussies rondom de verschillende projecten.

Beste **Gerard**, ik denk dat je de 5b cursus al verzorgt sinds zo ongeveer rond de tijd dat radioactiviteit ontdekt werd, de passie waarmee je dit nog steeds doet is geweldig. Daarnaast is het geruststellend dat dezelfde grapjes in de cursus op hetzelfde moment terug komen! Ook wil ik je bedanken voor je bijdrage aan het onderzoek, elke werkbespreking stond je klaar om in discussie te gaan over de experimenten of de vervolg onderzoeken die mogelijk waren!

Mr GMP***, Rob***, de man van de oneindige stroom van papieren met blauwe balken er op. Ik zweer dat ik de afgelopen vier jaar trouw alle logboeken heb ingevuld!

De regelgeving rond stralingsbescherming in het RNC is in de capabele handen van onze stralingspolitie. Die gelukkig niet alles weten van wat we beneden knoeiden en uitspookten onder het nom van: ach, morgen is het wel vervallen. **Gertrüd** ik zal de KiWi-law nooit meer vergeten, dank voor het regelen van die enorme stapel papierwerk rondom stralingsbescherming zodat wij redelijk ongestoord onze gang konden gaan. **Jan**, ook jou wil ik bedanken voor je hulp de afgelopen jaren onder andere voor het bestellen van de activiteit maar ook voor de goede gesprekken en gezelligheid over de jaren heen. **Tjaard**, een van de beste klanten van snackbar “echte vrienden” met een aanstekelijke lach die regelmatig door de koffiehoek schalde. Ik heb het altijd een traktatie gevonden om samen de verschillende cursussen te verzorgen en de etentjes bij everything on a stick waren altijd een feest, dank van Slobstra.

In het SVD aquarium zaten de “omroep dames” die essentieel waren voor de communicatie, eerst ***Greet*** daarna ***Annelies***, bedankt voor alle secretariële ondersteuning!

Uiteraard zou het werk op het RNC niet mogelijk zijn zonder de producten en inspanningen van onze handy-men, toolboys, ICTers of instrumentatie dienst: ***Fred, Arjen, Maarten, Peter, Wesley*** en ***Roy***. Met terugwerkende kracht mijn excuses voor het slopen van tientallen synthese units en de armgat afsluiting van hotcell 6, hoewel dat laatste toch wel een unieke prestatie was. Dank voor al jullie harde werk en ondersteuning wat ons vak mogelijk maakt.

Het werk op het RNC zou een stuk minder stralend zijn zonder de radioactiviteit die geproduceerd werd bij Cyclotron BV. Ik wil daarom alle medewerkers van Cyclotron BV bedanken voor de koolstof-11 en fluor-18 bundeltjes! ***Maria***, jij was de vertrekkende AIO toen ik binnenkwam maar bent gelukkig nooit ver uit de buurt geweest, bedankt voor je hulp in het prille begin!

Alle andere mensen binnen het RNC die allemaal klaar stonden om te helpen, of om een bakkie koffie te drinken onder het genot van een slap verhaal en een stuk taart (na de welbekende lokroep: "wij gaan koffie drinken!"). ***Frank, Sjoerd, Dennis, Rolph, Annemieke, Kanar, Cinzia, Wissam, Jos, Johan, Clifford, Anneloes, Iris, Claudia, Ab en Anna*** allemaal hartelijk bedank voor de leuke tijd!

Elke AIO krijgt op een zeker moment een stagiair te begeleiden wat een hoop tijd kost maar ontzettend leuk werk is, **Marc** en **Paul** bedankt voor jullie chemische inzet, het werk wat jullie hebben gedaan heeft dan misschien (nog) niet tot een publicatie geleid, maar staat wel in hoofdstuk 7 van dit boekje. **Rianne**, samen met Robert hebben we denk ik een mooi stuk werk afgeleverd in LC-MS/MS project rondom nintedanib en dat heeft dan ook geleid tot een mooie, gedeelde publicatie, die in hoofdstuk 5 beschreven staat.

Pieter, heel veel succes met de afronding van je promotie en bedankt voor je hulp door de jaren heen en zeker toen ik mijn weg nog aan vinden was in onze bunker. ***Joost,*** de master Yoda van fluor-18, jij hebt me wegwijs gemaakt in de fluor-18 chemie waarvoor dank! Ook jij heel veel succes met het afronden de promotie. ***Dion,*** de CF_3 man, en een zeer nauwkeurig wetenschapper, ik denk dat je inmiddels een bloedhekel hebt aan phosphazene basen? ook voor jou is het einde van de promotie in zicht, dus reden voor nog een feestje! Sehr geehrte Frau Funke! Beste ***Uta,*** de vrouw van Gemütlichkeit en veel en lekker eten. Altijd als je terugkwam uit Duitsland lagen er weer koekjes of chocolaatjes klaar in de koffiehoek! Danke Schon!

Na het aflopen van mijn promotietijd heb ik bij LinXis gewerkt, eveneens in het RNC. ***Joey***, de ADO-fan met een gezonde dosis Haagse bluf (gebakken lucht), samen met ***Niels*** regeerden jullie over de koffiehoek als het ging om sport en dan met name voetbal. ***Eugen***, one of the most talented chemists I met in my career, I enjoyed working with you on the Lx project. Good luck as head of chemistry! ***Veronica*** the single female member of the company, I think that almost all conversations involving a problem in the lab with you included an Ai-Ai-Ai before getting to the issue, thank you for the good times with LinXis and good luck with all the boys! Ik wil daarnaast ook het senior management board bedanken: ***HendrikJan, Gerro en Paul***, bedankt voor de leuke tijd die ik heb gehad bij LinXis!

Tjøstil, allereest bedankt dat je mij op mijn verdediging bij wilt staan als mijn paranimf. We kennen elkaar sinds het prille begin van mijn studie van "the dark side" en voor een korte tijd hebben Anass en jij mij weten te bekeren tot het zuiver pad van de organische chemie. Altijd klaar met wijze raad en in voor een grap. Mochten onze carrières stranden dan hebben we altijd nog ons maandelijks-een-nieuwe-frituurpan-aan-huis-inclusief-olie-en-snacks bedrijfsplan wat niet anders dan een eclatant succes kan worden. ***Sara*** ook you and I go way back, samen op het duistere pad van de farmaceutische wetenschappen begonnen en aangepakt door de organische chemie profeten Znabet en Vlaar. Wat we gelukkig wel goed konden relativeren als we in het donker balletjes aan het uitdelen waren. Ik zou willen zeggen mijn oprechte excuses voor pest-de-Brabander-dag, maar dan zou ik liegen, Put troost uit het feit dat de tennisvereniging van vlierenkut nog steeds bestaat!

Al eerder genoemd, de koning, de man die van een welpje, een leeuw maakt. De man van voor wat hoort wat, de man van Wild FM en de man die de bijnaam Slobske en Slobé in het leven heeft geroepen: ***Anass***, bedankt voor je vriendschap en je gastvrijheid die zich zelfs tot Marrokko heeft uitgestrekt! En nee, zo rijk ben ik nou ook weer niet! YO ***Daantje!*** Binnen het VCSVU bestuur hebben we elkaar leren kennen, wat mij misschien nog wel het meeste is bijgebleven is dat elk persoon waar we contact mee hadden, omschreven werd als: Yo, die chick van … ! Veel succes met de afronding van je eigen promotie onderzoek!

Daarnaast wil ik de mensen om mij heen bedanken, waarvan het merendeel waarschijnlijk totaal niet begrepen heeft waar ik nu vier jaar aan gewerkt heb, maar toch altijd wel interesse hadden! ***Mitchell en Simone, Rens en Ineke, Lisanne en Maurice, Roxanne en Dimitri, Johan en Mandy, Erik en Imke, Glenn, Marnix, David***

en Carola, Danielle en Dingeman, Irene en Danilo, Kirsten en Rob, Yvonne, Ben en Ursula, Bas en Anna, Chris, Marc, Vincent, Robert-Jan, Koos, Arthur.

Mirjam en Dylan, hopelijk is het na het bijwonen van de promotie iets duidelijker geworden waar ik me al die tijd mee bezig heb gehouden! Alle andere familie en vrienden: bedankt voor de interesse over de jaren heen!

Tot slot drie mensen die ik in het bijzonder wil bedanken:

Pa en Ma, ik denk dat ik in 4 jaar wel honderd keer de vraag van mam heb gekregen: wil je nou nog één keer zeggen wat je voor onderzoek doet? Om vervolgens, moedig, maar tevergeefs de titel proberen te onthouden. Dit ritueel ging steevast gepaard met een diepe zucht van Pa. Ik wil jullie bedanken voor alles, zonder jullie was dit proefschrift, maar nog belangrijker, ik, er niet geweest. Jullie hebben mij alle kansen te geven om te doen wat ik leuk vond en hebben mij daarin altijd gesteund!

Lieve ***Shel***, wij zijn inmiddels bijna het grootste deel van ons leven samen en zijn samen de mensen geworden die we nu zijn. Het kan dan ook bijna geen toeval zijn dat ik op 17 november promoveer, de dag dat wij twaalf jaar geleden een relatie kregen. Jij hebt van start tot finish dit hele promotie traject meegemaakt en was er altijd voor me. Van een luisterend oor voor gezeur als ik thuis kwam tot ongeremd enthousiasme als ik na een (paar) jaar werk enkele a4-tjes in één of ander wetenschappelijk tijdschriftje had weten te publiceren. Jij kunt dingen relativeren op een manier waar ik alleen maar bewondering voor kan hebben! Wat er in de toekomst ook op ons pad komt, we gaan er samen iets mooi van maken: *“the good things in life are better with you!”*

Paul